# ELASTIC DYNAMICS OF SLIDING ELECTRICAL CONTACTS UNDER EXTREME CONDITIONS

A Dissertation
Presented to the Faculty of the Graduate School
of Cornell University
in Partial Fulfillment of the Requirements for the Degree of
Doctor of Philosophy

by

Anthony Joseph Johnson

January 2008

# ELASTIC DYNAMICS OF SLIDING ELECTRICAL CONTACTS UNDER EXTREME CONDITIONS

Anthony Joseph Johnson, Ph.D.

Cornell University 2008

The goal of this dissertation is to explore the effects of structural deformations on high speed, high current density, sliding electrical contacts. The specific technologies studied in this body of work are the the homopolar motor and electromagnetic launcher, with an emphasis towards the latter.

The coupled motion of the guide rails and armature of an electromagnetic launcher are modeled by a Timoshenko beam on an elastic foundation. Using reduced order finite element simulations, it is found that elastic waves are generated in the guide rails. These waves are radiated from the armature when it passes through a characteristic wave speed of the rails called the critical velocity. The critical velocity depends on the stiffness of the foundation and is below the bar and shear wave speeds. It is found that as the armature accelerates beyond the critical velocity, the magnitude of the stress in the rails can reach values beyond the yield stress of the rail material. It is also shown that the contact pressure between the armature and guide rails is changed dramatically by the presence of the stress waves in the guide rails. The changes in the contact pressure are significant enough to cause interruption of the electric current and potentially damage the rails or armature.

Experiments show that the reduced order computational model captures much of the dynamics of the rails during launch. The presence of elastic waves and the phenomena associated with a critical wave speed are verified experimentally

using a fiber optic strain system that is insensitive to electromagnetic interference. Many of the wave effects seen in the simulations are seen in these experiments. This includes the transition from quasi-static deformation states to wave radiation states at the critical velocity. Other effects shown in the experiments are wave reflections, strain amplification and jerk effect waves. There is also experimental and theoretical evidence for a lateral instability of the armature as it rides along the guide rails.

For electrical contacts in homopolar motors, it is found that structural deformations of the brush fibers can affect the ability of the brushes to conduct electricity by changing the resistance of the contacts. This can affect the performance of the motor and may contribute to the wear of the brushes. Large variations in the structural properties of different commercial brushes are found and it is conjectured that the electromechanical measurements in this dissertation could be used as a quality control test for the large number of brushes necessary for the full-scale motor.

A statistical model for these brush deformations is also developed and compared to the experimental data. It is found that the model can be made to fit the experimental data, but more brush samples and a controlled atmosphere would be needed to verify this model.

## BIOGRAPHICAL SKETCH

The author was born in 1980 in Canon City Colorado. He was raised in the small town of Penrose Colorado and he attended secondary school in the nearby town of Florence. While attending Florence High school, his main passion was the sport of wrestling. His wrestling career concluded in qualifying for the Colorado State Wrestling Championships in 1999.

After high school, the author began his studies at the University of Colorado in Boulder. While in Boulder, he performed computational research in the field of high energy particle physics under the direction of Prof. Uriel Nauenberg. This research culminated in an honors thesis on a data reduction technique for detecting supersymmetric particles in a future particle accelerator. In the spring of 2003 he graduated Cum Laude with a B.S. in Engineering Physics.

In the 2003, the author began his graduate work in the School of Applied and Engineering Physics. For the first year he was a teaching assistant for Introduction to Electrodynamics and Introduction to Quantum Mechanics under Professors Chris Xu and Alexander Gaeta respectively. In the Spring of 2004, he was awarded the Trevor R. Cuykendall Memorial award for his efforts as in teaching.

For the rest of his time at Cornell, the author worked with Prof. Francis C. Moon on the research contained in this dissertation. Some of this research was presented at the 13th Electromagnetic Launch Symposium, an international conference in Berlin. The author was awarded the Peter J. Kemmey scholarship to attend this conference and was then given the best presentation award by a vote of the conference attendees.

Dedicated to the memory of

John R. Johnson and

Jason M. Mahlberg

## ACKNOWLEDGEMENTS

I would like to extend my deepest gratitude to Prof. Francis C. Moon. His continuous stream of ideas and insights made the research in this dissertation possible. He has pushed me to explore scientific issues using experimental, theoretical and computational techniques and I am eternally grateful to him.

I would also like to thank Prof. Chris Xu, Prof. Alexander Gaeta, and Prof. Subrata Mukherjee for being members of my thesis committee. I am particularly grateful to Prof. Xu for our discussions on research and teaching my first year at Cornell.

The research reported in this dissertation was supported in part by a grant to Cornell University from the U.S. Office of Naval Research, Multi-University Research Initiative with the Georgia Institute of Technology as the lead university. I would like to extend my thanks to the researchers at the Georgia Institute of Technology who developed the instrument that made the strain measurements possible. Specific thanks to Dr. Richard Cowan, Steven Sheffield, Dr. Scott Bair and Terence Haran for their help in putting these experiments together.

Finally, I would like to thank my fiancée Tiara Myers for her continual support throughout my time at Cornell. This dissertation would not have been possible without her patience and encouragement.

TABLE OF CONTENTS

## LIST OF TABLES

## LIST OF FIGURES

# Part I

# Introduction and Background

# Chapter 1
# Introduction

This dissertation explores the structural deformations associated with electrical contacts in two high power electric machines; the electromagnetic launcher and the superconducting homopolar motor. With high current densities and high sliding contact speed, these technologies are pushing the limits of present understanding of electrical contact interfaces. This chapter will give a general overview of the work in this dissertation as well as a basic technical description of the electromagnetic launcher, homopolar motor, present day challenges with implementing these technologies and their histories. Both of these technologies are part of a Navy program to build an all electric ship. There are also studies in both the United States and Europe to use electromagnetic launchers for suborbital micro-sattelites.

Each of these technologies can be classified as an extreme contact but for slightly different reasons. The reason for this is shown in Figure 1.1. The plots in this figure show the current density and contact pressure versus the relative sliding velocity of the electrical contacts in some actual electromagnetic launchers and homopolar motors/generators. Two electromagnetic launchers are shown in this plot, the Medium Caliber Launcher at the institute for Advanced Technology [76] and the launcher at the Georgia Institute of Technology. Various homopolar motors/generators are also plotted. Most of this data came from a review paper on homopolar generators written by Ian McNab [63]. The remaining data is from the General Atomics homopolar motor [96] that is directly related to the research in this dissertation.

The extreme nature of the electromagnetic rail launcher is relatively obvious from the plots in Figure 1.1. Typical launchers have sliding velocities in the range of $1-3\,km/s$, current densities in the range of $0.1\,MA/cm^2$ and contact pressures

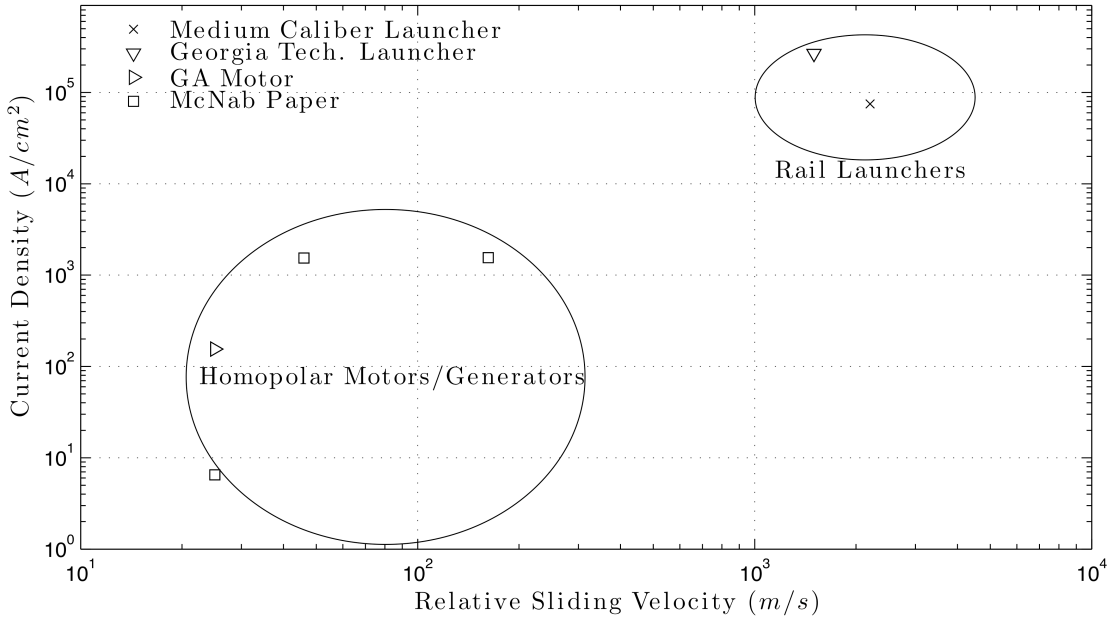


(a) Current Density Versus Sliding Velocity

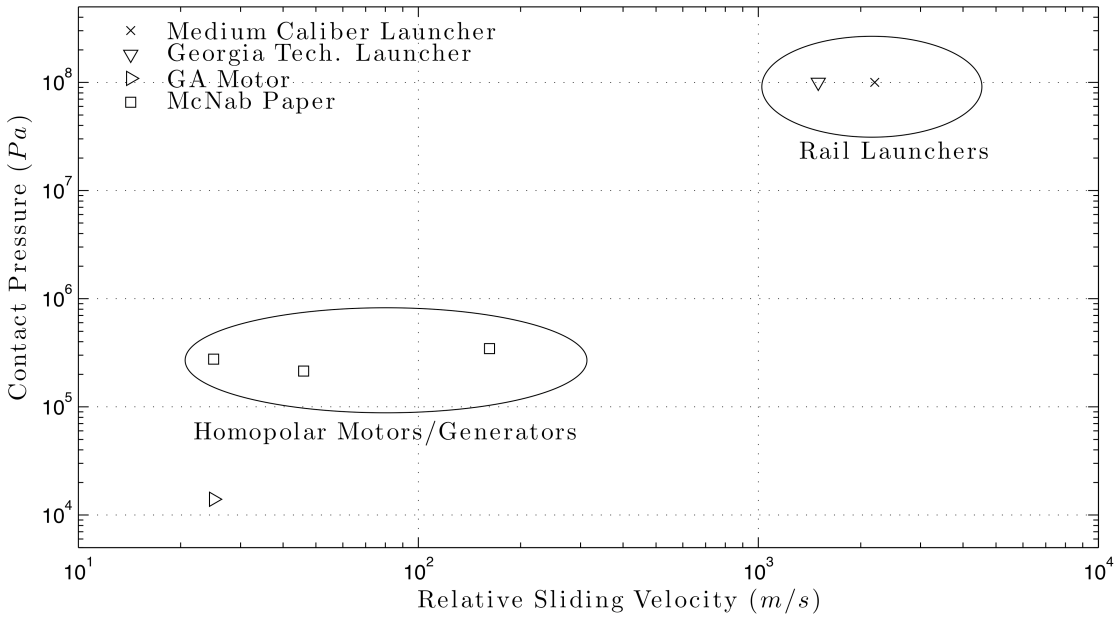


(b) Contact Pressure Versus Sliding Velocity

Figure 1.1: Contact Properties for Rail Launchers and Homopolar Devices

in the range of $100\,MPa$. The combination of these three all happening at once pushes modern understanding of the electrical, thermal and mechanical properties of the contact interface to its limit.

The superconducting homopolar motor associated with the research in this dissertation is extreme in a different way. The General Atomics motor operates at much smaller contact pressures than the others. This is because this motor uses metal fiber brushes instead of the more standard monolithic carbon brushes typically used in these devices. The primary problem with these metal fiber brushes is wear during use. Asymmetric wear is seen between the positive and negative brushes and the exact source of this is not well understood.

## 1.1 Electromagnetic Launcher

The contact interface of an electromagnetic launcher is subject to current densities in the range of 0.1 $MA/cm^2$ and contact pressures in the range of 10 to 500 $MPa$ [95]. This occurs while the relative velocity between the two surfaces increases from zero to the speed of sound in the rail material ($1 - 3$ $km/s$) in a few milliseconds. These current densities, pressures and relative sliding velocities occurring simultaneously at a contact interface is essentially unheard of in any other technology.

One of the primary technical challenges associated with this technology is the extension of the lifetime of the rails. Moderate velocity shots (1-2 $km/s$) suffer a phenomenon called armature transitioning; where the armature loses contact with the rails during launch [7]. High velocity ($> 2$ $km/s$) shots suffer a phenomenon called gouging [60]. These two mechanisms cause micro and macro-scale wear and damage to the rails during launch and, as such, the rails typically only last for a few shots. While electromagnetic and thermal sources of wear have been explored

extensively in the literature (e.g. [8],[4], [78] and [84]),there is only a small amount of published work on the structural dynamics of these devices.

The work in this dissertation begins from a theoretical perspective by exploring the wave character of the rails in electromagnetic launchers. This is done by exploring the classic problem of a beam on an elastic foundation. A number of *characteristic wave speeds* exist in the rails. These include the *critical velocity, shear velocity and bar velocity*. These speeds represent the lower and upper wave speed limits in a beam on an elastic foundation and they are all near the typical sliding velocity of an electromagnetic launcher. This introduces the possibility of these waves interfering with the contact interface.

Finite element simulations are then used to explore how these waves interfere with the contact interface. It is found that several phenomenon occur at the characteristic wave speeds of the rails. The rails change from a quasi-static strain state to a transient wave radiation state at the critical velocity. When this transition occurs, dramatic spatial shifts and changes in the amplitude of the contact pressure also occur. After the shear velocity is reached, the contact interface begins to skip over the waves in the rails. The pressures that occur at this point are large enough to case severe damage to the rails.

To verify the computational model, stress waves generated during launch were measured using a fiber optic strain measurement device. These experiments were carried out on a moderate size electromagnetic launcher at the Georgia Institute of Technology. These measurements give a picture of the strains present during launch and confirm the wave radiation phenomenon seen in the simulations. Other wave phenomena are also seen, these include wave reflections, strain amplification and jerk effect waves.

In addition to the work on structural dynamics, a small scale electromagnetic

launcher was also constructed and a low-cost technique for measuring the velocity of the projectile was developed and tested. This was done to help expand the number of sensors available for researchers in this field.

### 1.1.1 Brief History of Research

The scientific study of electromagnetic launchers dates back to 1901 to a Norwegian Professor at the University of Oslo named Kristian Birkeland. Two good historical reviews of his work have been written by Alv Egeland [24],[23]. His electromagnetic launcher was of the coil gun variety. It used a homopolar generator to propel 10 kg iron projectiles to velocities nearly 100 m/s [87]. His vision was to construct a launcher that would fire projectiles very long distances (100-1000 km). His research was ultimately limited by the fact that there were no pulsed power supplies available to achieve the high launch velocities necessary for these long distance launches.

The next major attempt at an electromagnetic launcher was made by a frenchman named Fauchon-Villeplee in 1917. His launcher was similar to a modern day rail launcher except that it used external static magnetic fields to propel the projectile. It was powered by a bank of batteries. A thorough review of his work can be found in the literature [66]. Fauchon-Villeplee also designed a large-scale launcher that would have been theoretically capable of launching a 100 kg projectile to 1600 m/s. This launcher was never built and would have required a power supply significantly larger than any that have been built to date.

During World War II the Germans explored electromagnetic launchers as a potential weapon with applications as anti-aircraft guns or long range artillery. This research was spearheaded by Dr. Joachim Hänsler and an in-depth review of it can be found in the literature [66]. The electromagnetic launchers built during

this period fired small ($\approx 10g$) projectiles at speeds in excess of 1 km/s. The work in Germany was stopped at the end of the war.

Modern study of electromagnetic launchers began at the Australian National University in Canberra [58] in the early 1970's. This launcher was powered by a 500 MJ homopolar generator and used plasma armatures to propel small 3 gram LEXAN cubes to nearly 6 $km/s$. Studies continued on plasma armature launchers for the next 15-20 years (e.g. [13], [41], [86], [77], [97], [62],[38]). While plasma armatures can push projectiles to very high velocities, they generate very high temperatures at the rail surface and this can cause significant damage to the rails. They are also very inefficient because of the high resistance across the armature [59]. It is for these reasons that present day studies have focused on solid armature launchers.

The recent study of electromagnetic launchers has been reviewed very well in a series of papers by Dr. Harry D. Fair of the Institute for Advanced Technology [27], [28], [29], [30]. These papers cover the major advances for the last 10 years. The primary advances that have been made involve the development and use of coupled-field finite element simulations. These simulations have led to better armature designs and a better understanding of the thermal and electric aspects of electromagnetic launcher design. In addition to scientific advancements, a good review of patents in electromagnetic rail launchers has been put together by Chadee Persad [79].

The major shift in the field in recent years has been the involvement of the U.S. Navy. The Navy is pursuing electromagnetic launchers as a long-range weapon on their all-electric ship concept. These vessels will have enough space and the power capabilities to house a pulsed power supply capable of firing a large-scale electromagnetic launcher (see [68]). This change has shifted the research focus

from the power supply to the barrel of the launcher. The primary goals of this research have been to understand the wear and damage phenomena that are seen in laboratory launchers. Lifetime of the rails is now considered the major technical hurdle to jump to get a tactically useful weapon.

The major phenomena associated with bore lifetime can be split into two different groups; high velocity and low velocity. The primary low velocity damage mechanism is referred to as startup damage. This occurs at the beginning of the launch because the current in the low velocity regions is very high and the current is transmitted from the same point on the rail for a relatively long time. This causes heat to build up and melting can occur. High velocity damage mechanisms include transitioning and gouging. Many thermal and electric effects have been studied with respect to these phenomena, but the source of these mechanisms is still not well understood (see [7], [8] [60], [78], [93]).

This dissertation explores the structural dynamics of the rails as a possible contributor to the high velocity damage mechanisms. Previous work in this aspect of electromagnetic launchers has approached it from a design point of view. A number of papers have been written that model the cross-section of the launcher containment under static and dynamic loads [20],[95]. Three dimensional simulations of the structural deformations have also been developed [104]. This research has focused on the deformations of the containment and the relative deformations of the individual components inside the containment. Some work has also been done that focuses in on the vibrations of the armature during launch [105].

Application of the Bernoulli-Euler beam model to a rail launcher was first considered by Jerome T. Tzeng [100],[101]. While not a dynamic simulation, Tzeng's work first introduced the possibility of resonant railway dynamics in rail launchers. Some of Tzeng's colleagues have also looked at the beam dynamics using

three dimensional simulations of a nominal bore geometry [55]. The work in this dissertation continues the application of basic beam theory by exploring how the vibrations in the rails are generated and how they interact with the armature during launch. This gives an indication of the impact that these waves can have on the contact interface between the armature and the rails.

### 1.1.2 Applications

Electromagnetic launchers offer many advantages over conventional propulsion techniques and so they have a wide array of potential applications. The major advantage is the ability to generate very high accelerations. Some of these applications include weapons, fusion research, space launch and impact/materials research.

Some of the military applications of electromagnetic launchers that have been considered include missile defense systems, anti-aircraft, anit-armor and extended-range artillery [26]. The velocities that can be obtained with these devices could extend Naval ship bombardment ranges to 300 $km$ [68]. They also allow for dramatic increases in penetration ability for anti-armor applications [46].

Space launch is another interesting application for this technology. Electromagnetic launchers could be used to fire micro/nano-satellites from the ground [54] or from on-board an aircraft [67]. The technical challenge associated with earth-to-space launch is heating of the satellite as it passes through the atmosphere [12]. These devices have even been considered for use on a lunar base for firing mined materials back to the earth [87]. One other possibility could be to put a launcher in orbit for firing micro-satellites out of the earth's gravitational pull. The limitation for this application would be the energy density of the power supply.

Finally, electromagnetic launchers could be used in fusion research. They have

been presented as a potential method for temperature control and refueling of Tokomak fusion reactors [81],[43]. It has also been proposed that they could offer a potential method for attaining impact fusion [52]. This particular application is a bit more far-fetched though because it would require very high velocity launches in the range of $130\,km/s$. Velocities this high have never been obtained with an electromagnetic launcher.

### 1.1.3 Principle of Operation and Equations of Motion

Electromagnetic launchers are devices that use electromagnetic forces to accelerate mass to high velocities. The main types of launcher are coil launchers, rail launchers and linear induction motors. Rail launchers are the focus of this dissertation, so the basic principles behind this technology will be discussed in this section. Information on all of these technologies can be found in the proceedings of the biennial Electromagnetic Launch Symposium in the IEEE Transactions on Magnetics. Information specific to coil/induction launchers can be found in a number of different papers and books (e.g. [72] and [22]).

The basic geometry of a rail launcher is shown in Figure 1.2. The major components are the rails, armature, insulators and containment. The rails are typically made of a copper alloy. The insulators are made of a fiberglass material called G-10 (also known as garolite) and the containment is made out of laminated steel plates. The lamination is necessary to reduce losses due to eddy currents [9]. The armature in modern launchers is made out of a solid metal, usually aluminum, but plasma armatures have also been used to propel non-conducting projectiles.

A pulsed current power supply is attached to the breech of the launcher. This power supply usually consists of a large capacitor bank, but any power supply capable of generating a large enough current pulse will also work. Examples of

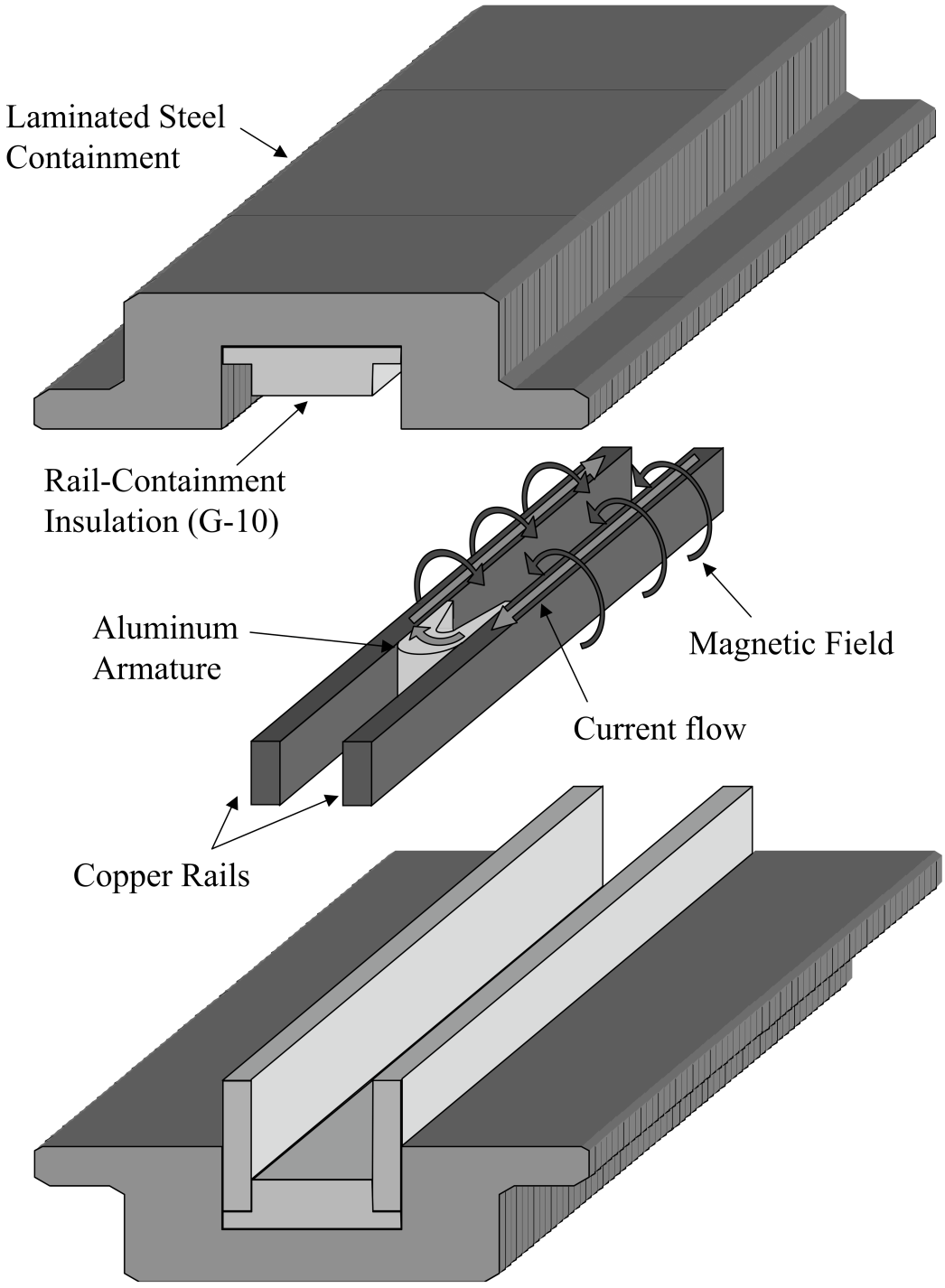


Figure 1.2: Rail Launcher Geometry

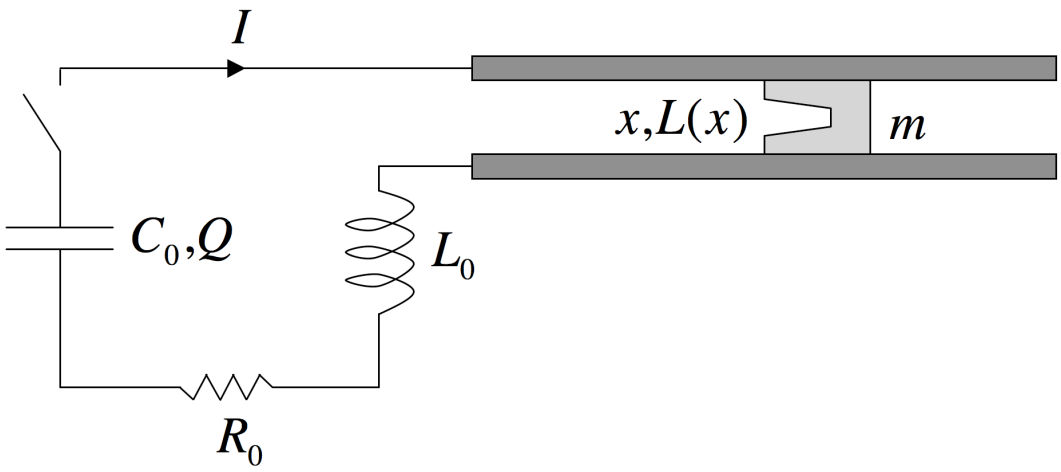


(a) Electromechanical Model of Launcher

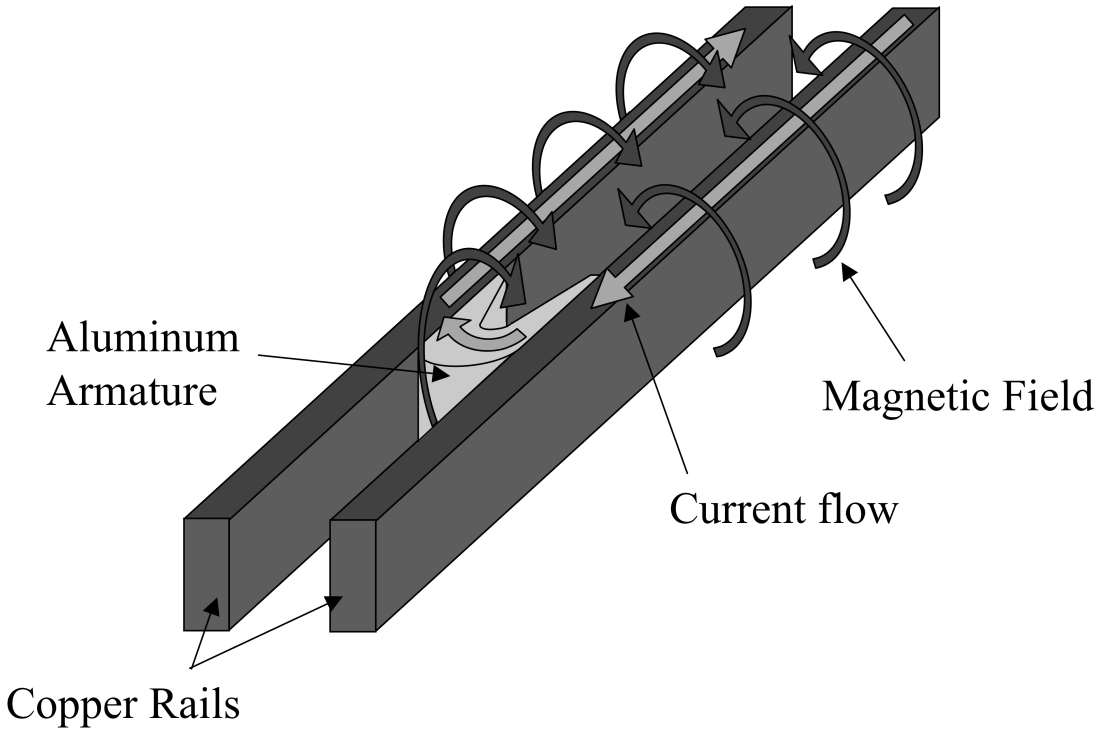


(b) Magnetic Field Lines in Electromagnetic Launcher

Figure 1.3: Electromechanical model (top) and magnetic field (bottom) of an electromagnetic rail launcher.

alternatives are homopolar generators, batteries, inductive storage and flux compressors [65]. Capacitors are the most common of these technologies and are used in laboratory launchers primarily because of their reliability and flexibility. Typical peak currents for electromagnetic launchers range from 100 kA to 5 MA depending on the size of the launcher.

As the current flows, a magnetic field is generated behind the armature (See Figure 1.1.3) and this pushes the armature down the length of the launcher. The electromagnetic force on the armature is generated by the $\vec{J} \times \vec{B}$ force where $\vec{J}$ is the current density in the armature and $\vec{B}$ is the magnetic field generated by the rails as shown in Figure 1.1.3. In typical rail launchers these forces produce launch accelerations that can range anywhere from 10 kGee up to 1 MGee. These accelerations allow for launch velocities in the range of 1-3 km/s in a very short distance.

The fundamental equations of motion for a capacitor driven electromagnetic launcher can be derived using an electromechanical Lagrangian. This is accomplished by treating the launcher barrel as a variable inductor whose inductance depends on the position of the armature. This system can drawn as a simple circuit, which is pictured in Figure 1.1.3. This circuit consists of a capacitor with a capacitance of $C_0$, an inductor with an inductance of $L_0$ and an overall resistance $R_0$. The armature is described by its mass $m$ and position $x$. A model which assumes that the inductance of the barrel is just a linear function of the position of the armature agrees well with experiments.

$$L(x) = L'x \quad \text{where} \quad L' = \text{constant} \tag{1.1}$$

Where $L'$ is referred to as the inductance gradient of the launcher. The equations for calculating an approximate value of $L'$ can be found in a text by Frederick Grover [37]. An example calculation of $L'$ for a rail launcher with rectangular rails

can also be found in Chapter 6 of this dissertation. With this assumption, it is possible to write down the electromechanical Lagrangian $\mathcal{L}$ for a capacitor driven rail launcher as shown in Figure 1.1.3 [73].

$$\mathcal{L} = \frac{1}{2}m\dot{x}^2 - \frac{Q^2}{2C_0} + \frac{1}{2}(L_0 + L'x)\dot{Q}^2 \tag{1.2}$$

Where $x$ and $Q$ are the generalized coordinates for the position of the armature and the stored charge on the capacitor bank. It is important to point out that this formulation assumes that the mass of the armature is constant. This assumption is often violated in actual rail launchers. Energy dissipation terms such as resistance and friction can be taken into account by considering a Rayleigh dissipation function $\mathcal{R}$ [72].

$$\mathcal{R} = \frac{sign(\dot{x})\mu N\dot{x}}{2} + \frac{R_0\dot{Q}^2}{2} \tag{1.3}$$

This simple model assumes a constant resistance and a constant friction force. The Lagrangian and Rayleigh dissipation functions satisfy Lagrange's equation.

$$\frac{d}{dt}\left(\frac{\partial\mathcal{L}}{\partial\dot{q}}\right) - \frac{\partial\mathcal{L}}{\partial q} + \frac{\partial\mathcal{R}}{\partial\dot{q}} = 0 \tag{1.4}$$

Plugging $\mathcal{L}$ and $\mathcal{R}$ into Lagrange's equation and simplifying gives the equation of motion for an armature in a capacitor driven electromagnetic rail launcher.

$$m\ddot{x} = \frac{1}{2}\dot{Q}^2L' - sign(\dot{x})\mu N \tag{1.5}$$

$$(L_0 + L'x)\ddot{Q} + (R_0 + L'\dot{x})\dot{Q} + \frac{Q}{C_0} = 0 \tag{1.6}$$

One of the most useful things about this equation is that it gives a quantitative measure of the propulsion force in an electromagnetic launcher.

$$F_{prop} = \frac{L'I^2}{2} \tag{1.7}$$

This means that the propulsion force is simply proportional to the square of the current $I$. A typical value of $L'$ for a laboratory launcher is approximately $0.5 \times$

$10^{-7} H/m$. This simple approximation works surprisingly well when compared to experimental data. Equations 1.6 and 1.7 will be referred to throughout this dissertation.

## 1.2 Superconducting DC Homopolar Motor

The second electrical contact technology explored in this dissertation is the superconducting DC homopolar motor. The contact interfaces in the homopolar motor are not subject to conditions as extreme as the electromagnetic launcher but they can still be classified as extreme because of the electrical transfer brushes that they use. The homopolar motor studied in this dissertation uses metal fiber brushes to transfer current. This is in contrast to the monolithic carbon or metal carbon brushes that are used in conventional electric motors. Current densities for brushes in a homopolar motor are in the range of $200 - 600\, A/cm^2$ and sliding velocities can range from $25\, m/s$ to above $300\, m/s$ [63]. Monolithic carbon brushes can only be run efficiently up to about $25\, m/s$ [85]. Above this limit, large contact pressures must be used to maintain contact. This increases friction and wear and decreases electrical and mechanical efficiency.

The technical challenges associated with using metal fiber brushes include atmospheric control and tight control of the contact pressure (see Chapter 20 of [85]). These are necessary to minimize corrosion and wear. These complications in implementation are offset by a large (potentially 10-fold [85]) increase in efficiency over conventional brushes. This comes from the fact that fiber brushes offer more contact spots at lower contact pressures. This increases the electrical efficiency while reducing the amount of loss due to friction.

It is interesting to note that in addition to sharing technological challenges with the electromagnetic launcher, homopolar generators have been used as power

supplies for rail launchers [58],[64].

### 1.2.1 Principle of Operation

The specific device associated with this body of research is being constructed by General Atomics for the United States Navy for the their future all-electric ship concept [96]. This device is intended to be a drive motor, but many have also been designed to operate as generators [6], [61]. A detailed description of the actual motor associated with this research and comparison of it with other motor technologies can be found in the literature [96]. Just some of the basic technical details of this motor will be presented here.

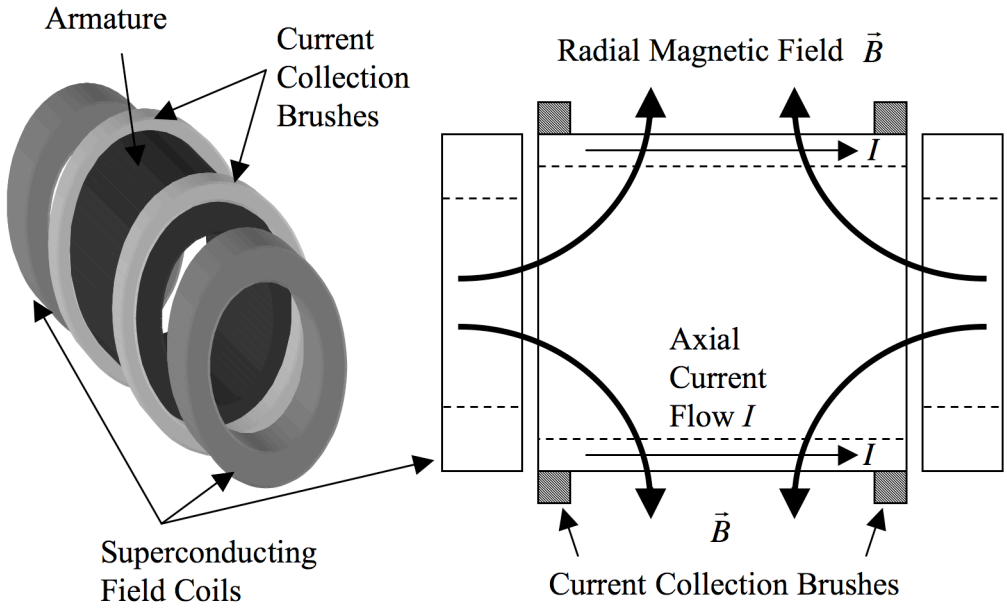


Figure 1.4: Basic Geometry of the Superconducting DC Homopolar Motor

The basic geometry of this motor is pictured in Figure 1.4. The General Atomics homopolar motor uses superconducting electromagnets with current flowing in opposite directions to generate a magnetic field that is perpendicular to the axis of

rotation. This field penetrates a copper cylinder, called the armature, which has current flowing through it along the axis of rotation. The average magnitude of the field at the armature is nearly 2 Tesla [96]. The current flow perpendicular to the magnetic field gives a torque that rotates the armature. The current is collected from sliding electrical brushes on either side of the armature. The General Atomics motor has 1600 metal fiber brushes that carry a current density of $155\,A/cm^2$ at a sliding velocity in the range of $25\,m/s$. This motor is a 1/4 scale prototype with a power output of $3.7\,MW$ (5000 horsepower). As one can imagine, the number of brushes necessary for the full scale motor will be very large and uniformity of mechanical and electrical characteristics between the individual brushes should be maintained.

### 1.2.2 Brief History and Literature Review

While the motor associated with this dissertation is intended for propulsion of a naval ship, most modern homopolar motor research has focused on their use as high power generators for pulsed power applications. These applications have varied from fusion research [103] to power supplies for electromagnetic launchers [58]. In all of these applications, the mechanical and electrical performance of the electric brushes has been a concern.

The use of metal fiber brushes dates back to Thomas A. Edison [2]. These brushes fell out of favor in the early 1900's because of cost and wear issues. Interest has been revitalized because of the dramatic increases in efficiency that these brushes offer, but wear is still a problem. Increased wear is seen when current is flowing and asymmetric wear has been seen between the positive and negative brushes. Much of the modern research has focused on atmospheric conditions [85].

The deflections of the fibers have been considered in the design of metal fiber

brushes form the point of view of surface tracking [85]. The research in this dissertation explores how these fiber deflections affect the compliance of the brush as well as its contact resistance under load in static conditions. It has been found that the individual fibers buckle easily. This leads to nonlinear compliance of the brush as a whole. This nonlinear nature also extends to the electrical resistance of the contact and should be considered in the analysis/design of a system using these brushes.

# Part II

# Elastic Waves in Electromagnetic Launchers

# Chapter 2
# Elastic Beam Dynamics

The electrical contact problems explored in this dissertation involve the contact between an elastic object and another elastic structure. In the electromagnetic rail launcher, one of the main structural elements is a simple beam on an elastic foundation. Understanding the dynamics of these systems requires a foray into the theory of elastic beam deflections. This chapter will cover the basics of Bernoulli-Euler and Timoshenko beam theory and their application to dynamic problems. This will establish the theoretical background necessary to understand the implications of the computational and experimental work described in later chapters of this dissertation.

## 2.1 Brief History and Literature Review

The specific problems encountered in this dissertation are closely related to the problem of a moving load on a beam on an elastic foundation. The classical problem of a structure supporting a moving load has been studied extensively since the 1850's. Much of the early research grew out of the railroad industry and was related to the analysis of bridges. The review in this section does not cover the history of the study of this problem in great detail, instead the primary sources that relate directly to the studies in this dissertation are presented. For a more thorough summary of the history of this research, the reader is referred to the books by Ladislav Frýba [34] and Stephen Timoshenko [99].

Some of the research in the 1930's and 1940's was dedicated to the study of beam deflections as a function of load velocity [57]. For the case of a constant velocity load moving on a Bernoulli-Euler beam on an elastic foundation, theoreti-

cal calculations show that the deflection of the beam diverges at a certain velocity called the critical velocity [51]. Much of this research was affiliated with the design of high-speed rocket test tracks. In the 1960's these studies were extended to the case of the Timoshenko beam on an elastic foundation [33], [90],[91],[92] and [1]. Finite element techniques for modeling Timoshenko beams were also developed in this period [50],[21].

More recent studies have focused on computational research, but some theoretical work is still being conducted. Of particular interest to the studies of electromagnetic launchers is the case of a moving step load [31],[32]. This particular problem is interesting because of its similarity to the electromagnetic repulsion force between the rails of an electromagnetic launcher.

In contrast to earlier work on moving loads on elastic beams, in this dissertation the moving load is calculated in response to a given displacement acceleration of a slider on contact with the beam. This research focuses on transient accelerations of the slider from rest to velocities beyond the critical and shear velocities of the beam. The impact of resonant phenomena of the beam on the contact between the slider and the beam are explored computationally and the wave dynamics of the beam are explored experimentally on an electromagnetic launcher.

## 2.2 Equations of Motion

The first step in understanding the dynamics of an elastic beam is to present the model and the equation of motion. A general theory would involve applying the continuum theory of elasticity to both the elastic guide way and its supporting structure. Such detailed studies are important at the armature interface but often miss the overall wave dynamics of the entire system. Instead, reduced order models using Bernoulli-Euler and Timoshenko beam models are used to describe three-

dimensional beams using a one-dimensional continuum. The relevant coordinate system for this description is pictured in Figure 2.1. The deflection $w(x,t)$ of the beam is represented by the deflection of the neutral axis, which is shown as a dotted line in Figure 2.1. There are a number of beam models, but the two of interest for this dissertation are the Bernoulli-Euler model and Timoshenko model. The equations representing both will be presented here. Just some of the basic assumptions behind these models will be presented here but full derivations of these equations are also included in Appendix A for the sake of completeness.

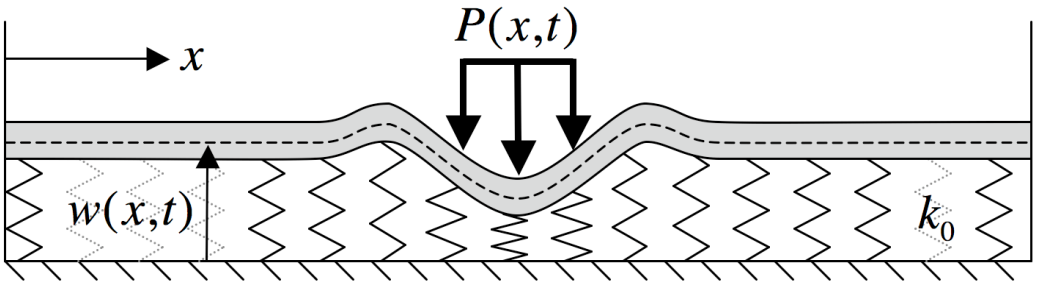


Figure 2.1: Beam on Elastic Foundation Under Load

Figure 2.2(a) shows an element of a Bernoulli-Euler beam under bending. The dotted line in this figure represents the neutral axis, and the lines perpendicular to it are called the shear planes. In the Bernouilli-Euler model, the shear planes are assumed to remain perpendicular to the neutral axis of the beam. In the Timoshenko model, this restriction is lifted and the result is an additional degree of freedom $\psi(x,t)$, pictured in 2.2(b). This additional degree of freedom gives the Timoshenko model a more realistic response at higher frequencies. For the problems discussed in this body of work, this improvement in the model is vital.

The deflection of the beam can be described using a partial differential equation which can be derived using Newton-Euler or Lagrangian methods [39],[98]. The Newton-Euler derivations of the Bernoulli-Euler and Timoshenko models are

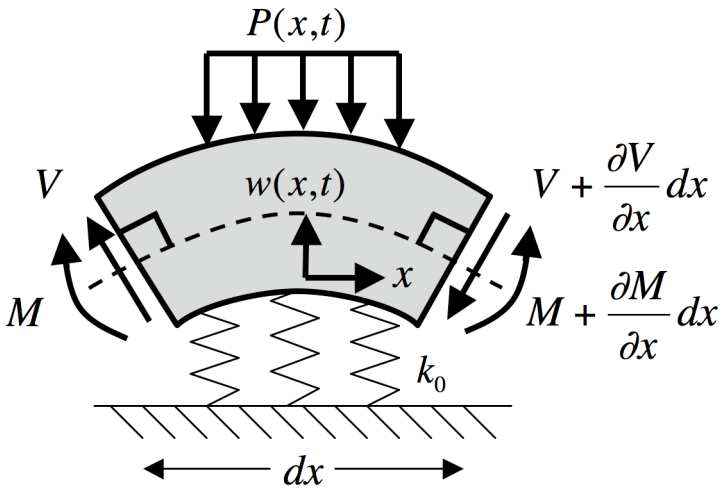


(a) Bernoulli-Euler Degrees of Freedom

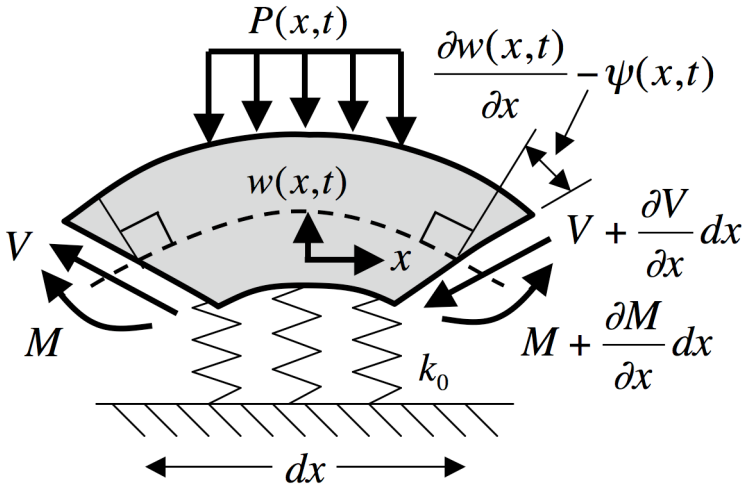


(b) Timoshenko Degrees of Freedom

Figure 2.2: Beam Equation Degrees of Freedom

included in Appendix A. For the Bernoulli-Euler beam on an elastic foundation this partial differential equation is as follows.

$$EJ\frac{\partial^4 w(x,t)}{\partial x^4} + \rho A\frac{\partial^2 w(x,t)}{\partial t^2} + k_0 B w(x,t) = P(x,t) \tag{2.1}$$

Where the description of the parameters of this equation are outlined in Table 2.1. This model assumes that the shear planes remain perpendicular to the neutral axis and it neglects rotary inertia and nonlinear geometric effects. These assumptions

Table 2.1: Beam Equation Parameters

| Symbol | Description | Units |
|---|---|---|
| $E$ | Elastic Modulus for Rail Material | $N/m^2$ |
| $G$ | Shear Modulus for Rail Material | $N/m^2$ |
| $\kappa$ | Timoshenko Shear Coefficient | N/A |
| $\rho$ | Density of Rail Material | $kg/m^3$ |
| $J$ | Cross-Sectional Moment of Inertia of Rail | $m^4$ |
| $A$ | Cross-sectional Area of Rail | $m^2$ |
| $h$ | Height of Rail | $m$ |
| $B$ | Width of Rail | $m$ |
| $k_0$ | Areal Stiffness of Foundation Material | $N/m^3$ |

are outlined in the derivation in Appendix A. As one can see, the dynamics of the beam have been reduced to the dynamics of the neutral axis through $w(x,t)$.

The differential equation for the Timoshenko model can be written in two different ways. The first representation includes both the deflection $w(x,t)$ and cross-sectional rotation due to shear deformation $\psi(x,t)$ degrees of freedom [39],[98].

$$\kappa AG\left(\frac{\partial\psi(x,t)}{\partial x}-\frac{\partial^2 w(x,t)}{\partial^2 x}\right)+\rho A\frac{\partial^2 w(x,t)}{\partial t^2}+k_0 Bw(x,t)=P(x,t) \tag{2.2}$$

$$\kappa AG\left(\frac{\partial w(x,t)}{\partial x}-\psi\right)+EJ\frac{\partial^2\psi(x,t)}{\partial x^2}=\rho J\frac{\partial^2\psi(x,t)}{\partial t^2} \tag{2.3}$$

These equations can then be simplified in to one higher-order differential equation for the deflection of the beam.

$$\begin{aligned} EJ\frac{\partial^4 w(x,t)}{\partial x^4}-\rho J\left(1+\frac{E}{\kappa G}\right)\frac{\partial^4 w(x,t)}{\partial x^2\partial t^2} &+ \rho A\frac{\partial^2 w(x,t)}{\partial t^2} \\ +\frac{\rho^2 J}{\kappa G}\frac{\partial^4 w(x,t)}{\partial t^4} &+ k_0 Bw(x,t)=P(x,t) \end{aligned} \tag{2.4}$$

This model allows shear deformation and does not neglect rotary inertia, but it does still neglect geometric nonlinearities (see Appendix A). In both of these reduced order models the transverse strains in the beam are not treated and the wave and vibration motions of the foundation are neglected. As with the Bernoulli-Euler model, the end result is a major simplification of a full three dimensional

continuum model. When these simplified models are used in a finite element simulation they can considerably reduce the number of elements and computation time necessary as compared to a three-dimensional model of the same system.

## 2.3 Wave Dispersion and Wave Velocities of Beam Models

### 2.3.1 Derivation

The relationship needed for understanding the wave nature of a problem is the dispersion relationship. The dispersion relationship relates the wave number $k$ to the angular frequency $\omega$ of a wave ($k = 1/\lambda$ where $\lambda$ is the wavelength of the wave[1]). The dispersion relationship can be used to describe the velocity of waves in a medium described by a linear mathematical model. In wave propagation problems there are two important velocities; the phase velocity and the group velocity [36]. The phase velocity represents the speed at which individual wave components travel. In other words, each wave with a particular wavelength travels at a particular velocity and this velocity is given by the phase velocity. The mathematical definition of the phase velocity is as follows:

$$v_{ph} = \frac{\omega}{k} \tag{2.5}$$

The group velocity represents the speed at which modulations in the amplitude of the wave travel. This is the speed at which energy and information can travel in a medium. The mathematical definition of the group velocity is as follows.

$$v_{gr} = \frac{d\omega}{dk} \tag{2.6}$$

Since the dispersion relationship relates $\omega$ to $k$ it can be used to calculate the group and phase velocities for a particular wave problem. For the Bernoulli-Euler

[1]See [25] or [36] for in-depth description of basic wave theory

and Timoshenko beam models, it is possible to derive the dispersion relationship by simply ignoring the loading terms in Equations 2.1 and 2.4 and assuming a wave solution of the form $w(x,t) = Sin(kx - \omega t)$. Plugging this solution into Equation 2.1 gives the following dispersion relationship for the Bernoulli-Euler Beam.

$$EJk^4 - \rho A\omega^2 + k_0 B = 0 \tag{2.7}$$

Analysis of this equation can be simplified by non-dimensionalization. This can be accomplished by using the following substitutions.

$$\bar{k}^4 = Jk^4, \quad \bar{\omega}^2 = \frac{\rho A\omega^2}{E} \quad \text{and} \quad \bar{k}_0 = \frac{k_0 B}{E} \tag{2.8}$$

Substituting Equation 2.8 into Equation 2.7 gives the non-dimesnional form of the dispersion relationship for the Bernoulli-Euler Beam.

$$\bar{k}^4 - \bar{\omega}^2 + \bar{k}_0 = 0 \tag{2.9}$$

The $\bar{k}_0$ term introduces a cut-off frequency below which no pure waves can propagate. This cut-off frequency comes from the foundation supporting the rail and is discussed in detail in the next section. The process for calculating the dispersion relationship for the Timoshenko beam is the same and it gives the following relationship.

$$EJk^4 - \rho J\left(1 + \frac{E}{\kappa G}\right)k^2\omega^2 - \rho A\omega^2 + \frac{\rho^2 J}{\kappa G}\omega^4 + k_0 B = 0 \tag{2.10}$$

Non-dimensionalization is accomplished by the following additional substitutions.

$$\bar{r}^2 = \frac{J}{A^2} \quad \text{and} \quad \bar{v}^2 = \frac{E}{\kappa G} \tag{2.11}$$

Substituting Equation 2.8 and Equation 2.11 into Equation 2.10 gives the non-dimesnional form of the dispersion relationship for the Timoshenko beam.

$$\bar{k}^4 - \bar{\omega}^2 - (1 + \bar{v}^2)\bar{r}\bar{k}^2\bar{\omega}^2 + \bar{v}^2\bar{r}^2\bar{\omega}^4 + \bar{k}_0 = 0 \tag{2.12}$$

These dispersion relationships capture the wave character of beams quite well even up to very high frequency vibrations. This will be discussed in the following sections using plots of the dispersion relationships and phase and group velocities.

### 2.3.2 Bernoulli-Euler Beam Wave Velocities

It is a bit easier to understand the Bernoulli-Euler dispersion relationship so that is where this analysis will begin. Solving Equation 2.9 for $\omega$ gives the following.

$$\omega(k) = \pm\sqrt{\bar{k}^4 + \bar{k}_0} \tag{2.13}$$

Where one solution is for positive frequencies and the other is for negative frequencies. The negative solution is just a reflection of the positive solution. Plotting the positive equation as a function of $k$ gives the plot in Figure 2.3 for the free beam ($\bar{k}_0 = 0$, thin line in Figure 2.3) and for the beam on an elastic foundation ($\bar{k}_0 = 1$, thick line in Figure 2.3). These plots were generated by assuming that $\bar{\omega}$ is real and solving for complex values of $\bar{k}$.

For the free beam there is no imaginary part of $\bar{k}$ . This means that unattenuated waves can exist for any frequency. In contrast to this, the beam on an elastic foundation does have imaginary parts. This indicates that both attenuated and unattenuated waves can exist when an elastic foundation is present. This observation has very serious implications for the electromagnetic launcher and will be returned to repeatedly throughout this dissertation.

One other important observation is the high frequency behavior. Both the free beam and the beam on and elastic foundation approach a quadratic in high frequency regions. This has very important consequences for the wave velocities. This can be studied by calculating the group and phase velocities. The equations

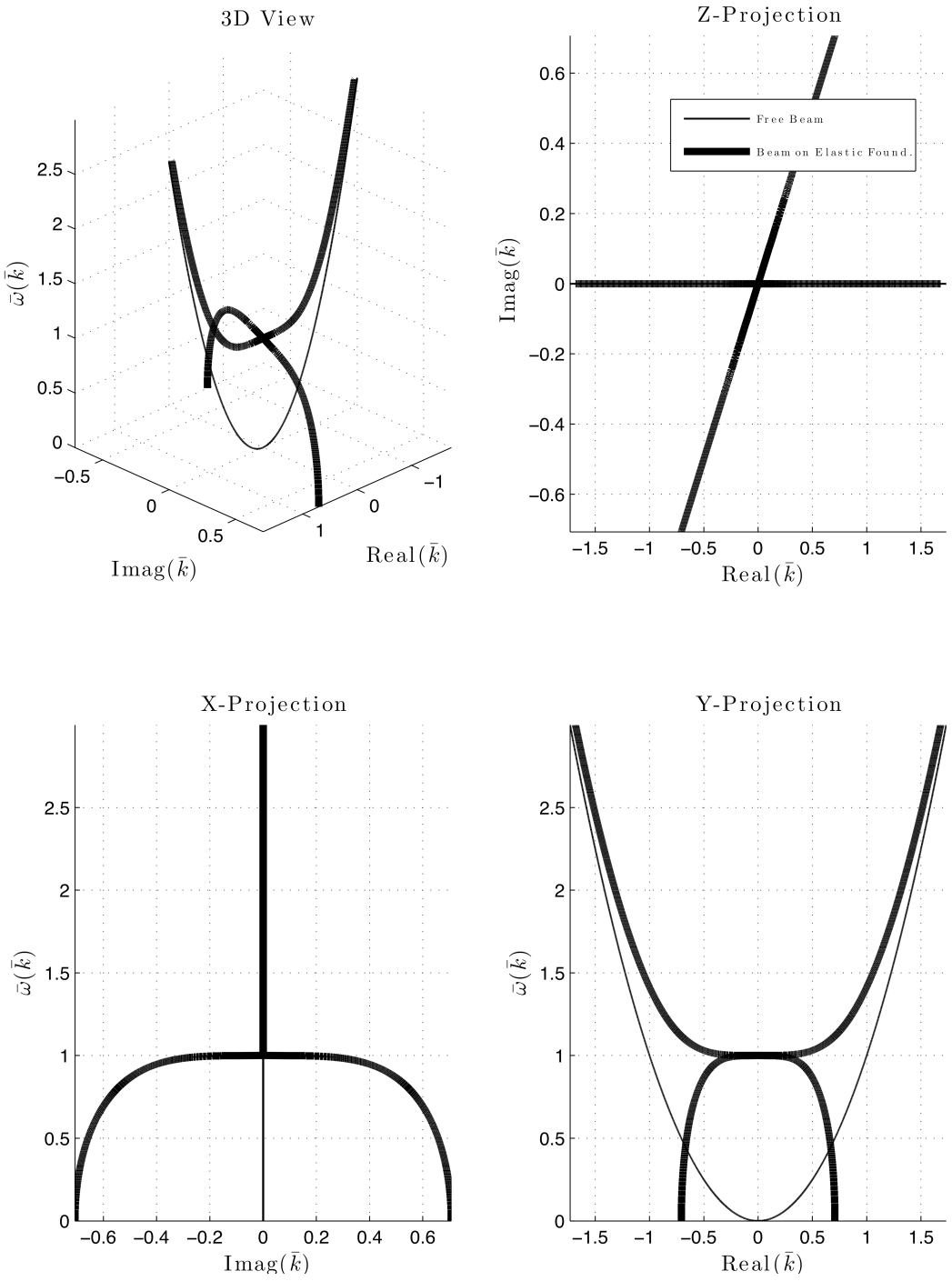


Figure 2.3: Dispersion Relationship $\omega(k)$ for the Bernoulli-Euler beam for the foundation-free beam (thin lines) and beam with a foundation (heavy lines).

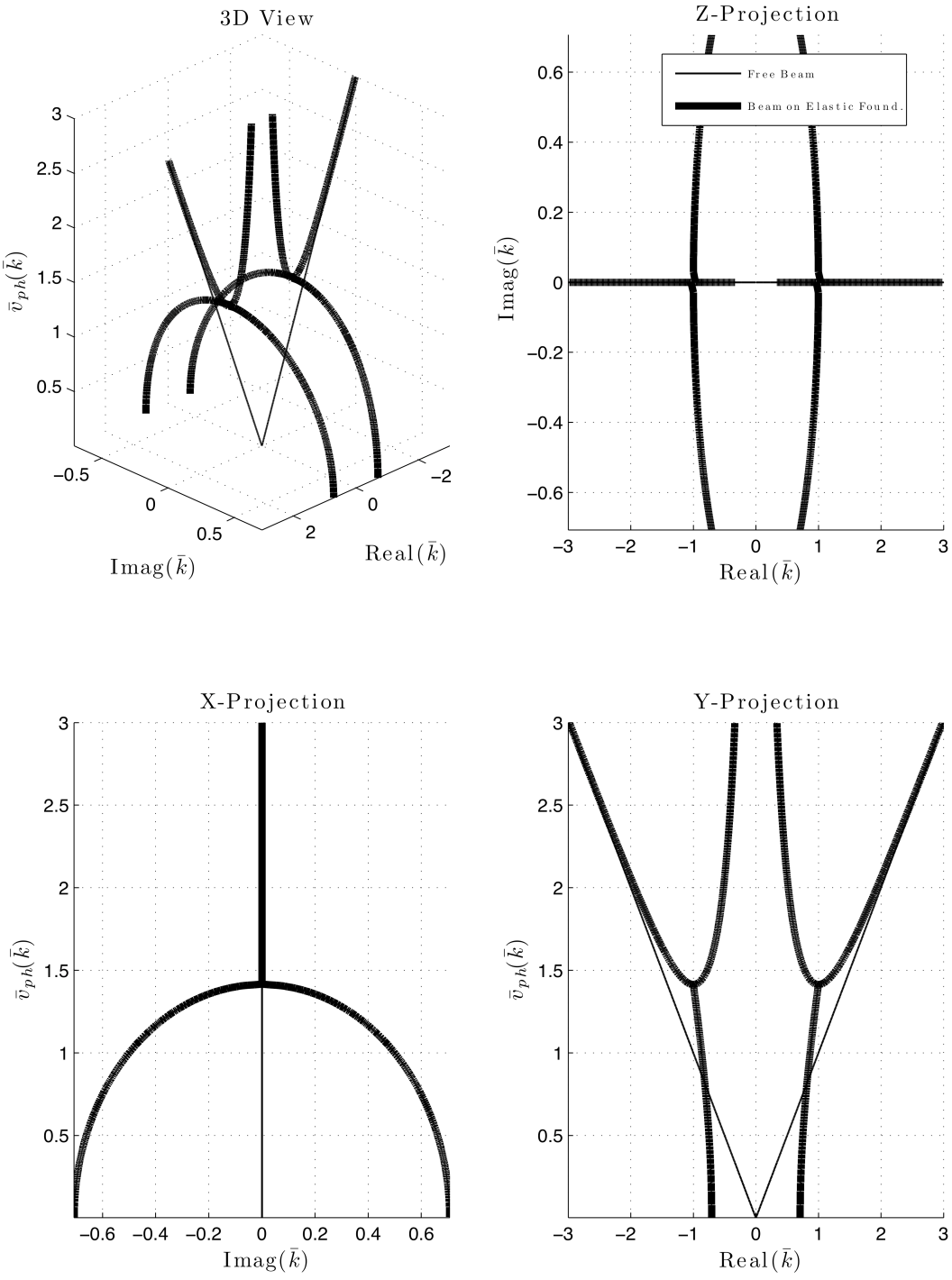


Figure 2.4: Phase velocity for the Bernoulli-Euler beam for the foundation-free beam (thin lines) and beam with a foundation (heavy lines).

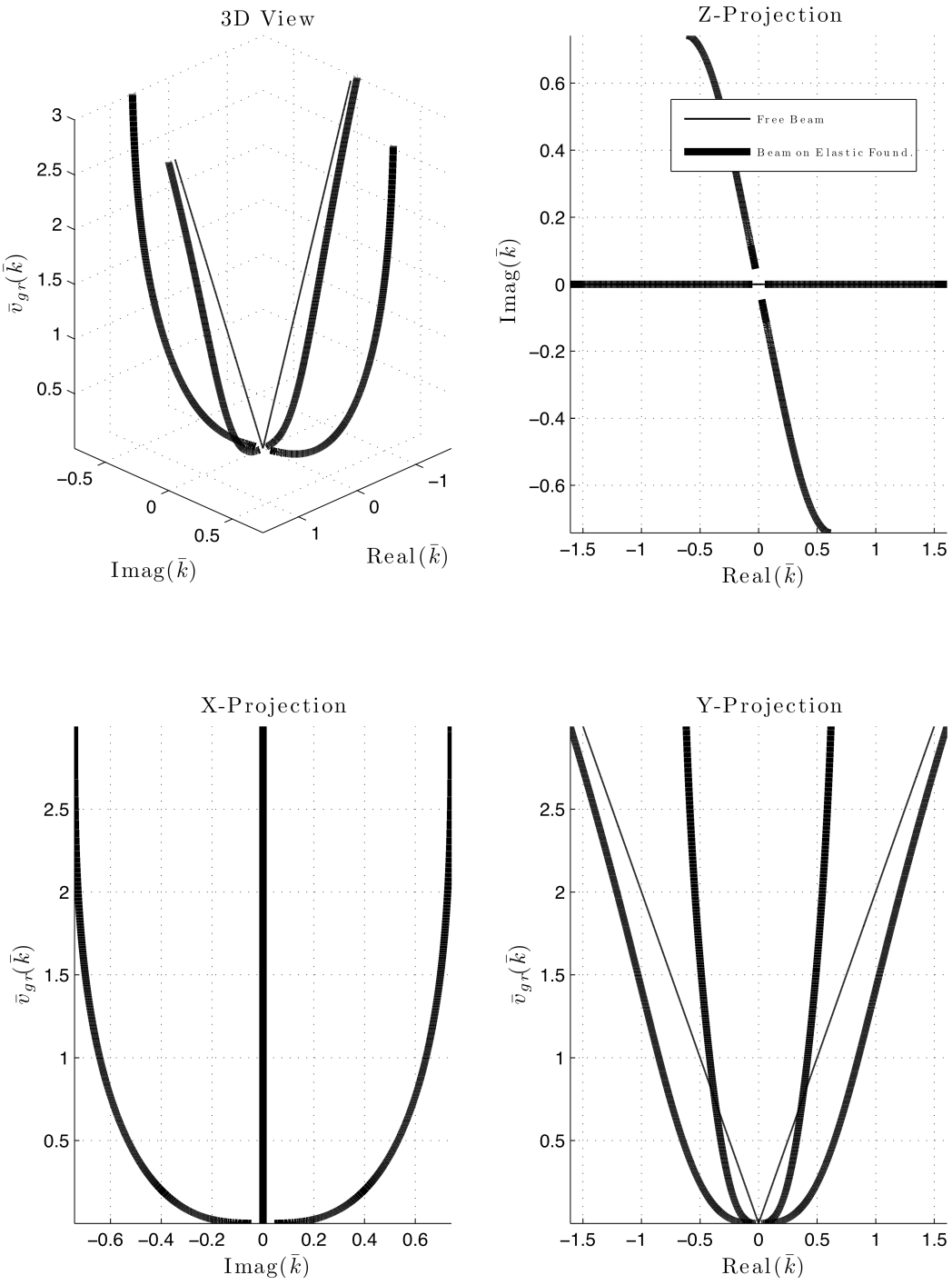


Figure 2.5: Group velocity for the Bernoulli-Euler beam for the foundation-free beam (thin lines) and beam with a foundation (heavy lines).

for the wave velocities for the Bernoulli-Euler beam are as follows:

$$\bar{v}_{gr}^{BE} = \pm \frac{2\bar{k}^3}{\sqrt{\bar{k}^4 + \bar{k}_0}} \tag{2.14}$$

$$\bar{v}_{ph}^{BE} = \pm \frac{\sqrt{\bar{k}^4 + \bar{k}_0}}{\bar{k}} \tag{2.15}$$

The group and phase velocities for the Bernoulli-Euler beam are plotted in Figures 2.4-2.5. The plot is shown for both a free beam and a beam on an elastic foundation. In the free case, the phase and group velocities extend over the full range of possible velocities (i.e. from zero to infinity). In the case of the beam on an elastic foundation, the phase velocity has a minimum. This minimum is generated because of the offset seen in the real solutions in Figure 2.3 and it is referred to as the *critical velocity* [51]. This velocity is vital to the computational research in this dissertation and as such will be discussed in detail in Section 2.4. For now, it is sufficient to point out that it represents the *minimum possible unattenuated wave velocity*. It is a lower limit on the speed of waves in a beam on an elastic foundation.

Another important thing to point out in Figures 2.4-2.5 is that for the Bernoulli-Euler beam, the phase and group velocities extend out to infinity. This means that, at least theoretically, waves could travel on a Bernoulli-Euler beam at infinite speed. This violates the laws of relativity and points out the fundamental limitation of this model. For very high frequency problems, the Bernoulli-Euler model is inaccurate. This is the primary justification for using the Timoshenko model.

### 2.3.3 Timoshenko Beam Wave Velocities

As already stated, the Timoshenko dispersion relationship is a bit more difficult to interpret. The major reason for this is because the dispersion relationship in

Equation 2.12 is fourth order. This gives rise to four solutions.

$$\omega(k) = \pm\sqrt{\frac{1+\bar{r}\bar{k}^2(1+\bar{v}^2) \pm \sqrt{(1+\bar{r}\bar{k}^2(1+\bar{v}^2))^2 - 4\bar{r}^2\bar{v}^2(\bar{k}^4+\bar{k}_0)}}{2\bar{r}^2\bar{v}^2}} \tag{2.16}$$

The positive solutions are displayed in Figure 2.6 for the free beam and the beam on an elastic foundation. These plots were made with the parameters set to $\bar{v} = 0.5$ and $\bar{r} = 0.5$ for the two cases $\bar{k} = 0$ and $\bar{k} = 1$. As with the Bernoulli-Euler beam, Figure 2.6 was generated by assuming a real value of $\omega$ and solving for complex values of $k$. In this case, the free beam only has imaginary parts when the real part is zero. This is reflected in the ellipse in Figure 2.6. The pure real parts of the free beam dispersion consist of two different modes. One mode represents bending waves and the other represents shear waves.

As with the Bernoulli-Euler beam, the Timoshenko beam on an elastic foundation allows the possibility of both attenuated and unattenuated waves. This has implications for the wave velocities that can be studied by looking at plots of the group and phase velocities. The equations for these velocities for the Timoshenko beam are as follows

$$\bar{v}_{gr}^T = \pm\frac{\bar{k}(1+\bar{v}^2 \pm \frac{1+\bar{v}^2+\bar{r}\bar{k}^2(\bar{v}^2-1)^2}{\sqrt{(1+\bar{r}\bar{k}^2(1+\bar{v}^2))^2-4(\bar{k}^4+\bar{k}_0)\bar{r}^2\bar{v}^2}})}{\sqrt{2\bar{v}(1+\bar{r}\bar{k}^2(1+\bar{v}^2) \pm \sqrt{(1+\bar{r}\bar{k}^2(1+\bar{v}^2))^2 - 4(\bar{k}^4+\bar{k}_0)\bar{r}^2\bar{v}^2})}} \tag{2.17}$$

$$\bar{v}_{ph}^T = \pm\sqrt{\frac{1+\bar{r}\bar{k}^2(1+\bar{v}^2) \pm \sqrt{(1+\bar{r}\bar{k}^2(1+\bar{v}^2))^2 - 4\bar{r}^2\bar{v}^2(\bar{k}^4+\bar{k}_0)}}{2\bar{r}^2\bar{k}^2\bar{v}^2}} \tag{2.18}$$

Plots of the phase and group velocity for the Timoshenko beam are shown in Figures 2.7-2.8. As with the Bernoulli-Euler model, the free beam has only real solutions and the beam on an elastic foundation has complex and pure real solutions. The point where these complex and pure real modes join represents the critical velocity for the Timoshenko beam on an elastic foundation. The equation for this velocity will be shown in Section 2.4

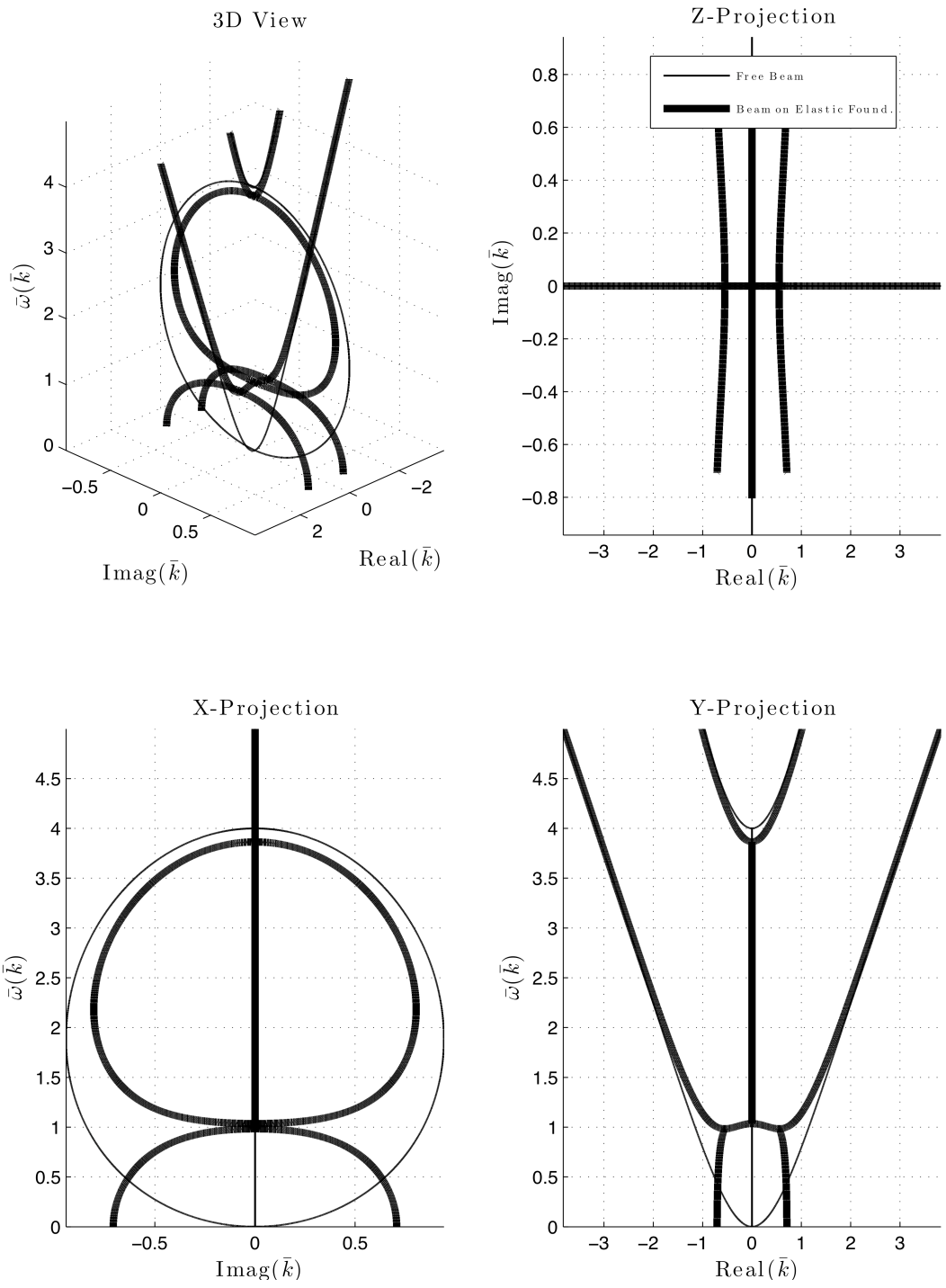


Figure 2.6: Dispersion Relationship $\omega(k)$ for the Timoshenko beam for the foundation-free beam (thin lines) and beam with a foundation (heavy lines).

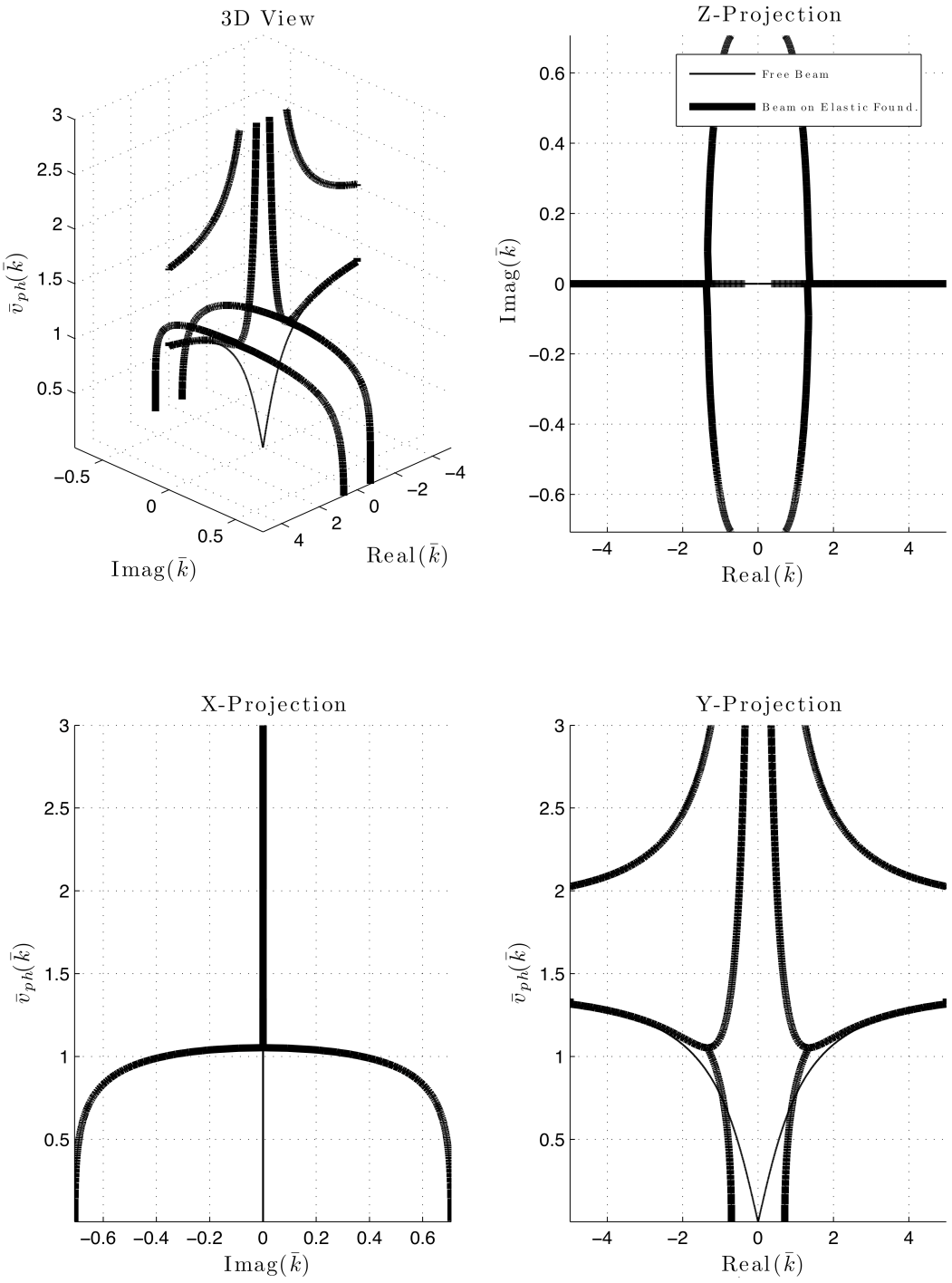


Figure 2.7: Phase velocity for the Timoshenko beam for the foundation-free beam (thin lines) and beam with a foundation (heavy lines).

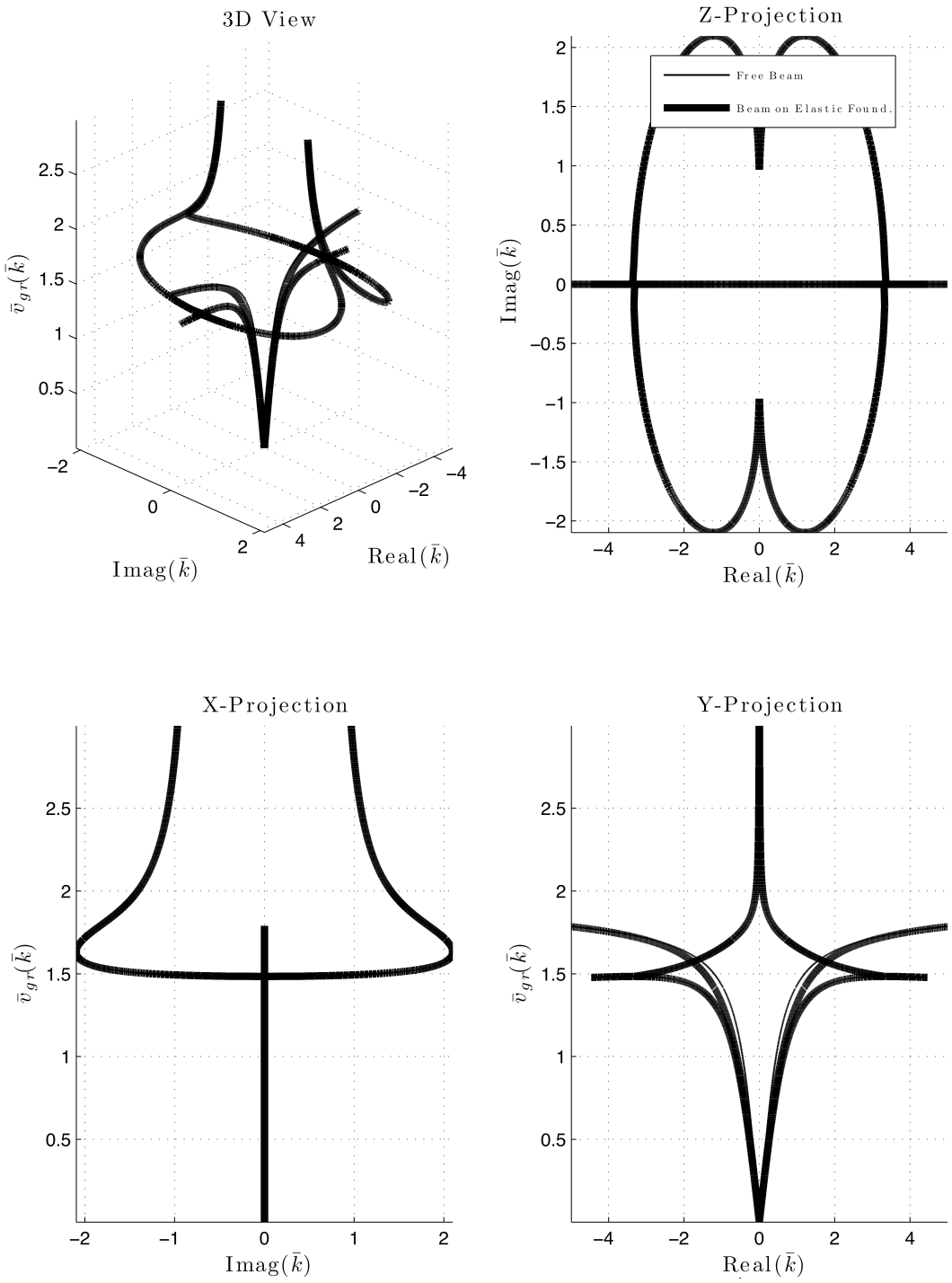


Figure 2.8: Group velocity for the Timoshenko beam for the foundation-free beam (thin lines) and beam with a foundation (heavy lines).

Probably the most important difference between the Timoshenko and Bernoulli-Euler models is the high-frequency behavior. In the high frequency limits, the two pure real modes of the Timoshenko beam asymptotically approach two different velocities, these are referred to as the shear and bar velocities and their expressions are as follows.

$$v_{bar} = \sqrt{\frac{E}{\rho}} \tag{2.19}$$

$$v_{sh} = \sqrt{\frac{\kappa G}{\rho}} \tag{2.20}$$

The bar velocity represents the highest possible wave speed for a traveling wave in a beam. This is the speed of a compressional wave. The shear speed represents the upper limit for a bending wave. These two velocities are characterized primarily by the material properties of the rail. It should be noted that the shear coefficient $\kappa$ is dependent on the shape of the cross-section of the rail, but is usually near its value for a rectangular beam ($\kappa \approx 5/6$) [70],[45]. These upper speed limits are the reason for choosing this model over the Bernoulli-Euler model. The Bernoulli-Euler model allows for unattenuated wave solutions with velocities extending out to infinity(see Figures 2.4-2.5). The Timoshenko model limits the waves to more realistic propagation velocities. It is important to note that in the three dimensional theory of elasticity for isotropic materials there are two non-dispersive elastic waves associated with compression (dilatation) and shear [25], [36]. The speed of these waves are close to, but slightly different from the Timoshenko beam waves $v_{bar}$ and $v_{sh}$.

## 2.4 Critical Velocities

As shown in the previous sections, the free beam dispersion relationships and wave velocities change considerably when one adds in an elastic foundation. The primary

difference is in an offset in the point where the dispersion relationship crosses the vertical axis. This offset spawns a branch of complex wave numbers that pushes the minimum phase velocity from zero up to a finite number.

The minimum in the phase velocity curve corresponds to the critical velocity. As stated in the previous section, the critical velocity represents the minimum possible unattenuated wave speed. The equation for the critical velocity for a Bernoulli-Euler beam on an elastic foundation is [51]:

$$v_{cr} = \left( \frac{4Bk_0EJ}{\rho^2 A^2} \right)^{1/4} \tag{2.21}$$

The equation for the critical velocity of a Timoshenko Beam is a bit more complicated. It is defined by the following relationship (see [15] for the derivation).

$$v_{cr} = \sqrt{\frac{\sqrt{r_2^2 - 4r_1r_3}}{2r_1} - \frac{r_2}{2r_1}} \tag{2.22}$$

Where the parameters are defined as follows.

$$r_1 = \left( \rho A - \frac{k_0 BJ}{\kappa AG} \right)^2 \tag{2.23}$$

$$r_2 = 2\left( \rho A - \frac{k_0 BJ}{\kappa AG} \right) \frac{EJk_0 B}{\kappa AG} + 4k_0 BJ \tag{2.24}$$

$$r_3 = \left( \frac{EJk_0 B}{\kappa AG} \right)^2 - 4EJk_0 B \tag{2.25}$$

While the equation for the Timoshenko critical velocity is different, the interpretation is the same. It represents the point where the branch for unattenuated modes joins the branch for attenuated modes in $k$-space. For the parameter values for a typical electromagnetic launcher (see Chapter 3, Table 3.1) the two critical velocities given by Equations 2.21-2.22 only differ by 6%. It is because of this small difference that throughout the remainder of this dissertation, when the critical velocity is calculated or referred to, Equation 2.21 will be used for the sake of simplicity.

### 2.4.1 Foundation Mass Effects

One effect that is not taken into account in the models presented so far is the mass and inertia of the foundation. In an electromagnetic launcher, the containment is typically made of steel laminates and fiberglass and it is very heavy. For a better model the dynamics of the launcher the kinetic energy of this foundation should be taken into account. The translational kinetic energy in a length $L$ of the beam can be written in the following way.

$$KE_{Trans}^{Beam} = \frac{1}{2}\int_0^L \eta_r \left(\frac{\partial w(x,t)}{\partial t}\right)^2 dx \tag{2.26}$$

Where $\eta_r = \rho A$ is the mass per unit length of the rail. The mass of the foundation can also be considered using a similar relationship which will be demonstrated in this section. It should be noted that one could potentially include rotational effects as well, but these will not be considered in this section.

Figure 2.9 shows the geometry of the foundation and the rail for this calculation. The foundation is assumed to have a width $B$ that is equal to the width of the rail, and a height of $h_f$. It is also assumed to have a density of $\rho_f$ that translates to a mass per unit length of $\eta_f = \rho_f B h_f$. The foundation is pictured as connecting the rail to an immovable surface and it has a stiffness per unit area of $k_0$. Also pictured in Figure 2.9 is the deflection of the mass in the foundation $w_f(y,x,t)$ at a distance $y$ from the immovable surface. The translational kinetic energy of the foundation can be written in terms of this deflection in the following way.

$$KE_{Trans}^{Found} = \frac{1}{2}\int_0^L \left(\int_0^h \rho_f B \left(\frac{\partial w_f(x,y,t)}{\partial t}\right)^2 dy\right) dx \tag{2.27}$$

For this calculation, the velocity of the foundation at $y$ is assumed to be equal to the velocity of the rail on the side that connects to the rail at $y = h$ and equal to zero on the opposite side at $y = 0$. It is assumed to be linear in between. This

means that the velocity of the foundation can be written in terms of the velocity of the rail in the following way.

$$\frac{\partial w_f(x,y,t)}{\partial t} = \frac{y}{h_f}\frac{\partial w(x,t)}{\partial t} \tag{2.28}$$

This assumption allows one to rewrite the translational kinetic energy of the foundation in terms of the deflection of the rail.

$$KE_{Trans}^{Found} = \frac{1}{2}\int_0^L \left( \int_0^h \rho_f B \left( \frac{y}{h_f}\frac{\partial w(x,t)}{\partial t} \right)^2 dy \right) dx \tag{2.29}$$

Carrying out the integration over $y$ gives the following.

$$KE_{Trans}^{Found} = \frac{1}{2}\int_0^L \frac{\eta_f}{3} \left( \frac{\partial w(x,t)}{\partial t} \right)^2 dx \tag{2.30}$$

Where the substitution $\eta_f = \rho_f B h_f$ has been used. Adding this to the translational kinetic energy of the beam in Equation 2.26 gives the total translational kinetic

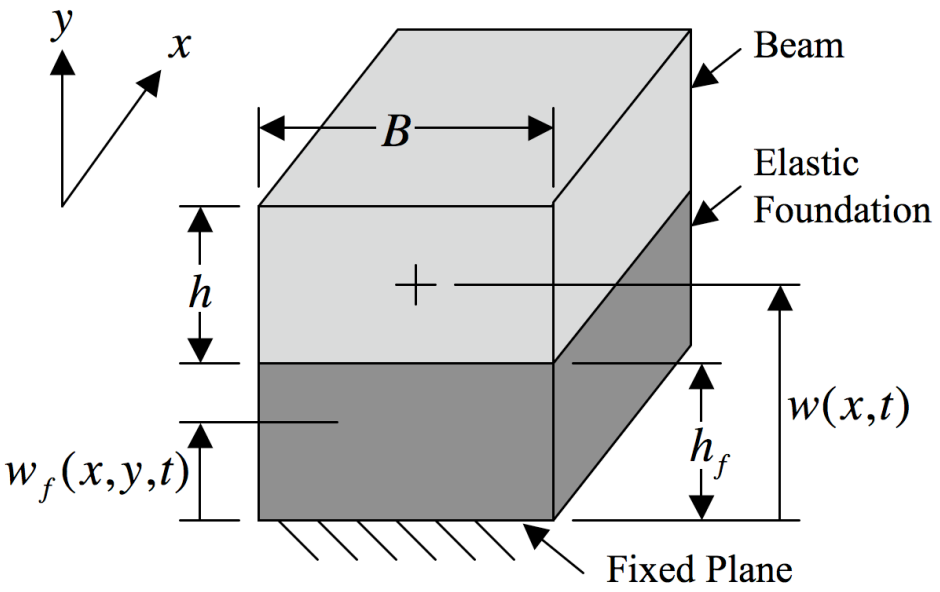


Figure 2.9: Effective Mass of Foundation

energy.

$$KE_{Trans}^{Tot} = \frac{1}{2}\int_0^L \left(\eta_r + \frac{\eta_f}{3}\right)\left(\frac{\partial w(x,t)}{\partial t}\right)^2 dx \tag{2.31}$$

This means that when the translational kinetic energy of the foundation is considered, the effective mass per unit length of the rail is increased. This effective mass per unit length is as follows.

$$\eta_{eff} = \eta_r + \frac{\eta_f}{3} \tag{2.32}$$

This can be taken a step further by observing that the translational kinetic energy is the only place that the mass per unit length appears in the derivation of the equation of motion for the Bernoulli-Euler beam (e.g. see [39]). This allows one to write, without loss of generality, the modified Bernoulli-Euler equation of motion.

$$EJ\frac{\partial^4 w(x,t)}{\partial x^4} + \eta_{eff}\frac{\partial^2 w(x,t)}{\partial t^2} + k_0 B w(x,t) = P(x,t) \tag{2.33}$$

The corresponding critical velocity for this system can then be written as follows.

$$v_{cr} = \left(\frac{4Bk_0EJ}{\eta_{eff}^2}\right)^{1/4} \tag{2.34}$$

This indicates that the critical velocity of a beam on an elastic foundation can be affected by the mass of the foundation. A heavy foundation will effectively lower the critical velocity. Evidence of this lowering of the critical velocity is seen in the experimental analysis done in Chapter 4.

# Chapter 3
# Rail Launcher Dynamics

## 3.1 The Model

Electromagnetic launchers offer difficult challenges for simulation using finite elements. Their coupled nature and large aspect ratios cause the number of necessary nodes to become large very quickly. In addition to this, the high frequency nature of the electromagnetic fields and structural vibrations make the necessary time steps very small. The combination of these two requirements makes fully-coupled three-dimensional simulations intractable in a reasonable amount of time. In this section, the basic geometry and the simplifications that have been employed to simulate the electromagnetic launcher will be presented.

The first simplification is to model the launcher in two dimensions. This reduces the number of nodes so that the problem can become solvable in a reasonable amount of time. The major consequence of modeling this system in two dimensions is that it is not possible to properly model the electromagnetic field. This means that the mechanical effects of the field have to be approximated in a self consistent way. The rails of the electromagnetic launcher repel each other just like two current carrying wires. The force per unit length between the two rails is proportional to the square of the flowing current $I$ and inversely proportional to the distance $r$ between the two [72].

$$\frac{F_{mag}}{L} = \frac{\mu_0 I^2}{2\pi r} \tag{3.1}$$

The propulsion force on the armature is also proportional to the square of the current (see Equation 1.7). This means that the repulsive pressure on the rails and the acceleration of the armature will be linearly proportional to each other.

$$a \propto \frac{F_{mag}}{L} \tag{3.2}$$

In some of the simulations in this dissertation, the armature was moved by applied displacements and repulsive pressures were applied to the rails. In these simulations, Equation 3.2 was followed so that the repulsive forces on the rails would be consistent with the acceleration of the armature.

The source of the mechanical forces is the interaction of the magnetic field with the flowing current. The magnetic pressure on a current carrying surface is proportional to the square of the magnetic field [72].

$$P_{mag} = \frac{B^2}{2\mu_0} \tag{3.3}$$

This equation comes from the the Maxwell stress tensor. For the problems in this chapter, it is simply used to give a rough approximation and scaling law.

The second major simplification is to model the rails using one-dimensional beam elements. This is done by using Timoshenko beam elements. The justification for this simplification of the model is covered in detail in Chapter 2.

Finally, some of the research in this chapter has been previously published in the IEEE Transactions on Magnetics. These portions are reprinted, with permission, from [48]  and [49] 

## 3.2 Classification of Foundation

The first step in modeling the rails of an electromagnetic launcher as a Timoshenko beam on an elastic foundation is to put together reasonable estimates of all of the parameters in Equation 2.4. The majority of these parameters are simply defined

by the materials being used for the rails. The stiffness, $k_0$ of the foundation is more difficult to obtain. It was found by using a simplified static two-dimensional model of the containment. This calculation will be shown for two different laboratory launchers.

### 3.2.1 Institute for Advanced Technology Launcher

The Medium Caliber Launcher (MCL) at the Institute for Advanced Technology (IAT) is arguably the most studied rail launcher in the world. It is for this reason that this launcher was modeled. A drawing of the approximate cross-section of the launcher is shown in Figure 3.1(a). The firing capabilities of this launcher can be found in the literature [76].

Table 3.1: Medium Caliber Launcher Parameters

| Symbol | Description | Value |
|---|---|---|
| $E$ | Elastic Modulus for Rail Material | 120 $GPa$ |
| $G$ | Shear Modulus for Rail Material | 47 $GPa$ |
| $\kappa$ | Timoshenko Shear Coefficient | 0.833 |
| $\rho$ | Density of Rail Material | 8320 $kg/m^3$ |
| $J$ | Cross-Sectional Moment of Inertia of Rail | $2.5 \times 10^{-9}$ $m^4$ |
| $A$ | Cross-sectional Area of Rail | $3 \times 10^{-4}$ $m^2$ |
| $h$ | Height of Rail | 0.01 $m$ |
| $B$ | Width of Rail | 0.03 $m$ |
| $k_0$ | Areal Stiffness of Foundation Material | $8.44 \times 10^{11}$ $N/m^3$ |
| $v_{cr}$ | Bernoulli-Euler Critical Velocity | 1486 $m/s$ |
| $v_{sh}$ | Shear Velocity | 2170 $m/s$ |
| $v_{cr}$ | Bar Velocity | 3797 $m/s$ |

For this simulation, the rails were removed and a pressure was applied to the insulation material behind the rail and the deflection was calculated for various static pressures. The boundary conditions and applied pressures are shown in Figure 3.1(b). The final result of this calculation is shown in Table 3.1. The stiffness shown in this table is calculated at the point of maximum deflection of

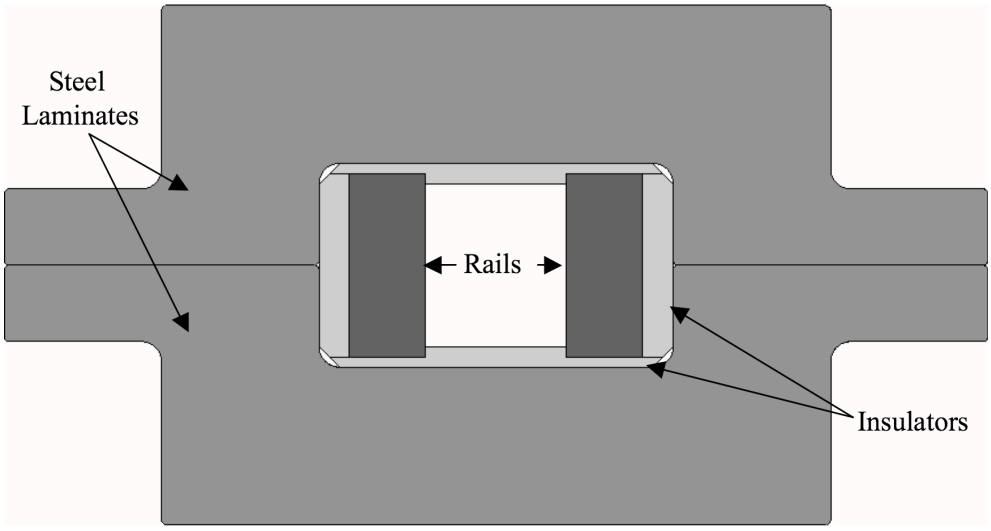


(a) Cross Section Sketch

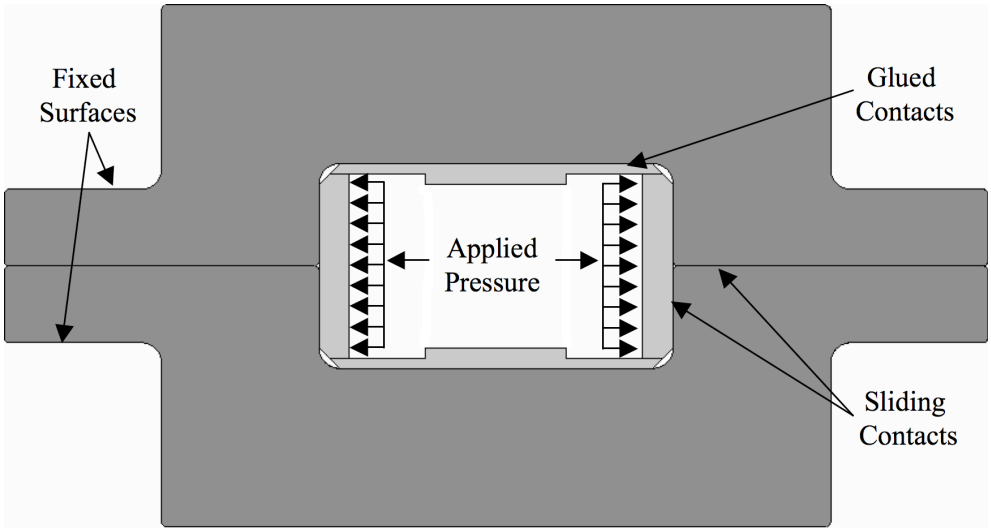


(b) Boundary Conditions and Applied Loads

Figure 3.1: Approximate Cross Section of Medium Caliber Launcher

the insulator surface directly behind the center of the rail. The maximum deflection was taken to give a 'worst case' number for the stiffness (i.e. the softest value for the stiffness). In addition to the stiffness, the important material and geometric parameters for the MCL are summarized in Table 3.1. These numbers are not intended to be the exact values for the MCL specifically. They are only meant to capture the basic parameters of a laboratory launcher of that scale.

### 3.2.2 Georgia Institute of Technology Launcher

The Georgia Institute of Technology launcher was constructed under an Office of Naval Research Multidisciplinary University Research Initiative (ONR-MURI) grant. This launcher was designed for studies of friction and wear in the bore of the launcher. The majority of the research in this dissertation was funded under this grant, much of it is related to this launcher so it is necessary to present the stiffness calculation for it as well.

Before describing the stiffness calculation, this is an appropriate place to introduce the capabilities of this launcher. The Georgia Tech. launcher is relatively small by laboratory launcher standards. It is 1.5 m in length and fires armatures that weigh approximately 10 g to velocities in excess of 2 km/s. The capacitor power supply stores 200 kJ of energy distributed over six different banks. Each bank can be fired individually and the delay between each bank is programmable. Pictures of the launcher are shown in Figure 3.2. The containment is made of electrically isolated stainless steel laminates. These laminates are also isolated from the rails with G-10 insulators. The launcher is housed in an acoustic chamber and fires into an evacuated catch chamber to reduce noise.

A drawing of the cross-section of the foundation used in the simulation is shown in Figure 3.3 (see Figure 3.2(d) for a photograph). The real launcher is held

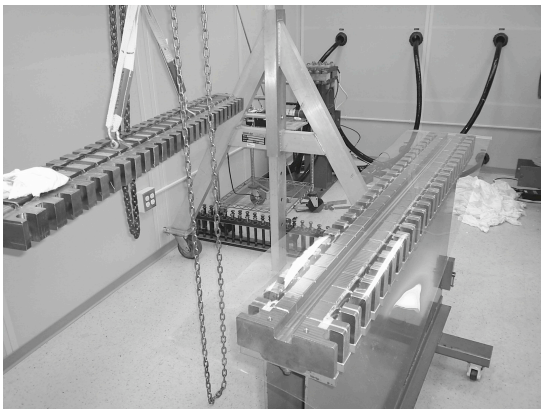

(a) Dismantled Launcher Containment

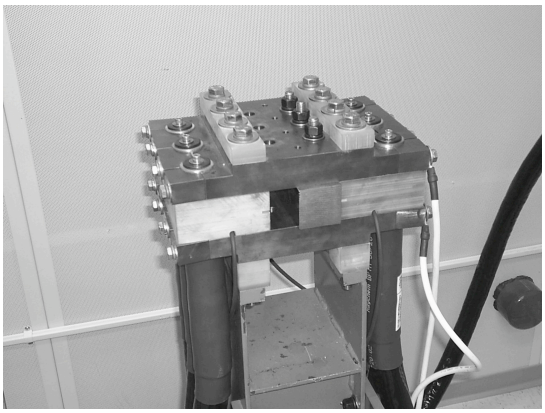

(b) Breech Clamp and Power Cables

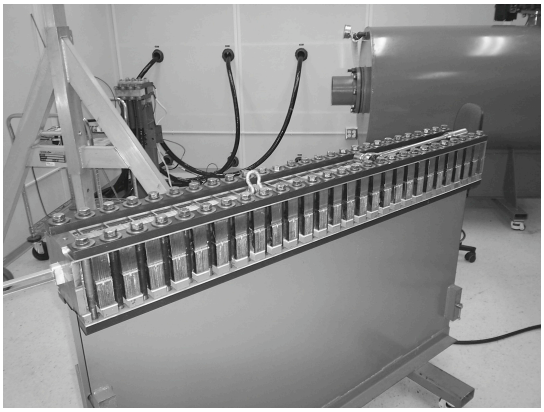

(c) Assembled Launcher Containment

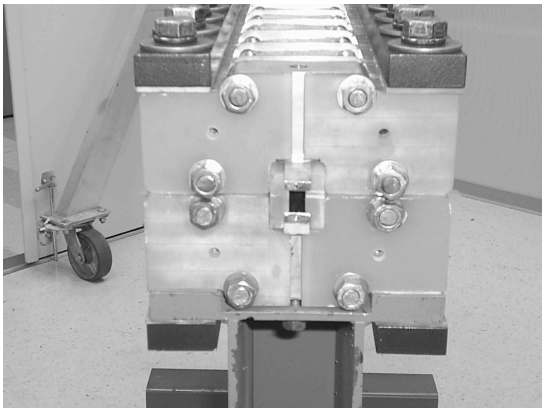

(d) Picture of Cross Section

Figure 3.2: Georgia Institute of Technology Launcher

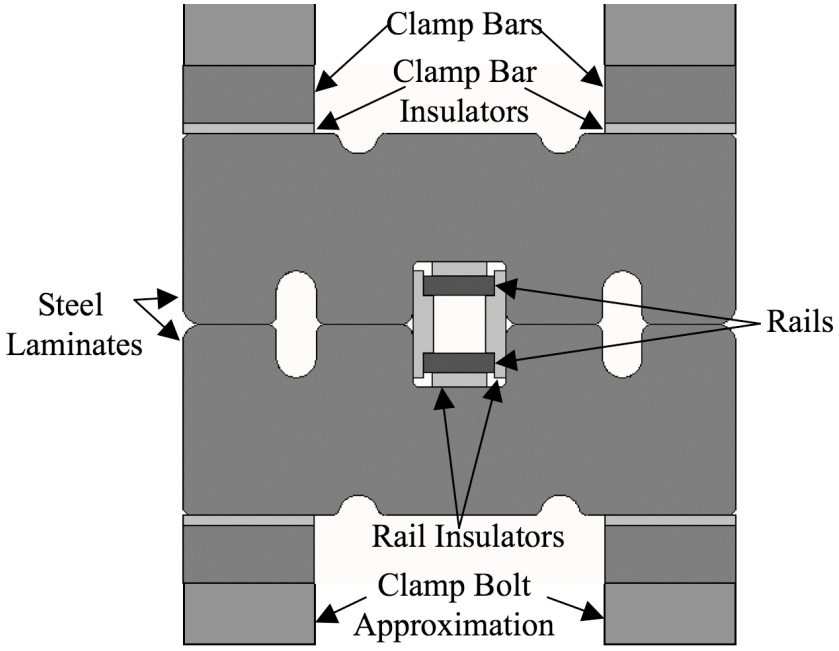


(a) Cross Section Drawing

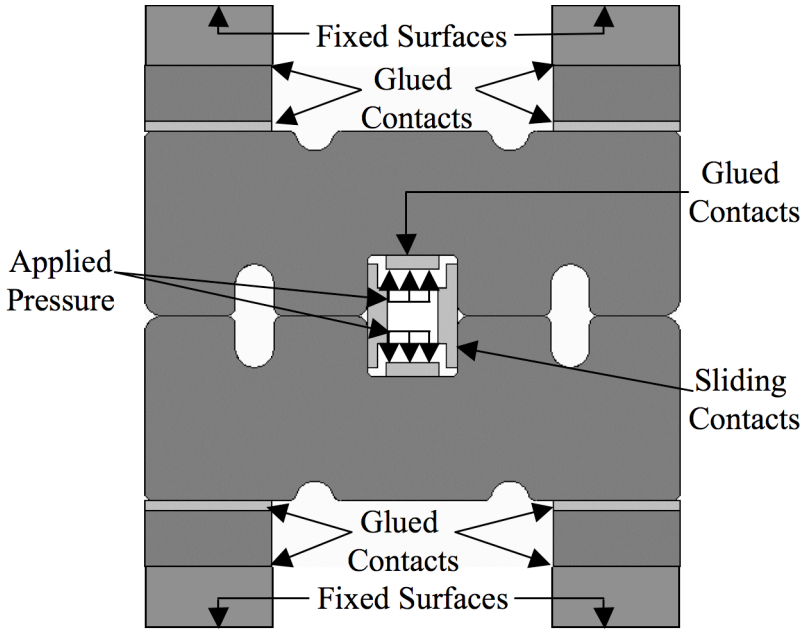


(b) Cross Section Boundary Conditions

Figure 3.3: Cross Section of Georgia Institute of Technology Launcher

together by a series of bolts and in the simulation these bolts are approximated by the blocks shown in Figure 3.3(b). As with the MCL, a pressure was applied to the insulation material behind the rail and the deflection was calculated for various static pressures. The boundary conditions and applied pressures are shown in Figure 3.3. The final result of this calculation is shown in Table 3.2. As before, the stiffness shown in this table is at the point of maximum deflection of the foundation. In addition to the stiffness, a summary of the necessary parameters for modeling this launcher are shown in Table 3.2.

Table 3.2: Georgia Institute of Technology Launcher Parameters

| Symbol | Description | Value |
|---|---|---|
| $E$ | Elastic Modulus for Rail Material | 120 $GPa$ |
| $G$ | Shear Modulus for Rail Material | 47 $GPa$ |
| $\kappa$ | Timoshenko Shear Coefficient | 0.833 |
| $\rho$ | Density of Rail Material | 8320 $kg/m^3$ |
| $J$ | Cross-Sectional Moment of Inertia of Rail | $1.372 \times 10^{-9}$ $m^4$ |
| $A$ | Cross-sectional Area of Rail | $1.815 \times 10^{-4}$ $m^2$ |
| $h$ | Height of Rail | 0.0096 $m$ |
| $B$ | Width of Rail | 0.0189 $m$ |
| $k_0$ | Areal Stiffness of Foundation Material | $5.45 \times 10^{11}$ $N/m^3$ |
| $v_{cr}$ | Bernoulli-Euler Critical Velocity | 1314 $m/s$ |
| $v_{sh}$ | Shear Velocity | 2170 $m/s$ |
| $v_{cr}$ | Bar Velocity | 3797 $m/s$ |

## 3.3 Modeling the Beam on an Elastic Foundation

The basic principle of the finite element method is to discretize the dynamics of the system by representing the components using nodes and interpolation functions. The basic equation being solved in a finite element analysis is as follows.

$$[M]\ddot{\delta} + [C]\dot{\delta} + [K]\delta = F \tag{3.4}$$

Where $\delta$ represents the deflection of the nodes, $[M]$ is called the mass matrix, $[C]$ is the damping matrix, $[K]$ is the stiffness matrix and $F$ represents the forces at the nodes [44], [71]. The mass, stiffness and damping matrices are derived based on the physics that the elements are intended to model. This section will briefly discuss the Timoshenko beam elements used in ANSYS. The purpose of discussing these elements in terms of their stiffness matrices is to point out their limitations, and introduce an alternative method for simulating a beam on an elastic foundation that allows more complexity of the model. Finally, the verification solution for these elements will be shown.

### 3.3.1 Rail Element Formulation

The beam elements used in the simulations in this dissertation are the BEAM54 elements in ANSYS. They are two node elements derived from the Timoshenko beam theory [106], [82]. The interesting thing about the BEAM54 elements is that they include the stiffness of the foundation into the element mass and stiffness matrices. This representation reduces the number of elements necessary to model an elastic foundation but it limits the flexibility of these elements in a number of ways.

First, damping cannot be taken into account in the foundation itself. A damping matrix made of weighted versions of the mass and stiffness matrix can be added into the model in the following manner.

$$[C] = \alpha[M] + \beta[K] \tag{3.5}$$

This is the standard method for adding damping into a system in ANSYS and it is referred to as Rayleigh damping. The problem with this type of damping is that the damping coefficients do not necessarily correspond with a damping coefficient

that one might measure in a laboratory experiment. This complication will not be studied in this dissertation but it is worth mentioning because damping is seen in the experimental data in Chapter 4 and should be taken into account in the design of an actual launcher.

The other major limitation with this type of construction is that only a linear stiffness is available. The devices being modeled in this dissertation have inherently non-linear foundations and so a more adaptable formulation is necessary. This flexibility can be gained back in a surprisingly simple way. This is done by setting the foundation stiffness equal to zero in the beam element formulation and adding spring-damper elements at either end of the beam element. This modification increases the number of nodes necessary, but it widens the number of problems that can be explored. The simulations in this dissertation use both of these formulations so it is necessary to run verification simulations for both of these situations. This is the topic of the next section.

### 3.3.2 Verification of the Elements

The first step in any finite element analysis is verification of the elements. This is done by solving a problem using both the elements and an analytic model. For the problems explored in this dissertation, an appropriate element verification can be made using the problem of a load moving at a constant velocity on and infinitely long beam. This specific case is solved in great detail by Frýba [34] and the analytic solutions of interest for this dissertation are included in Appendix B for convenience.

For these simulations, the beam is made long enough for there to be no wave reflections from the ends of the beam. This is necessary to approximate the infinite beam. This simulation is performed for four different velocities and the results are

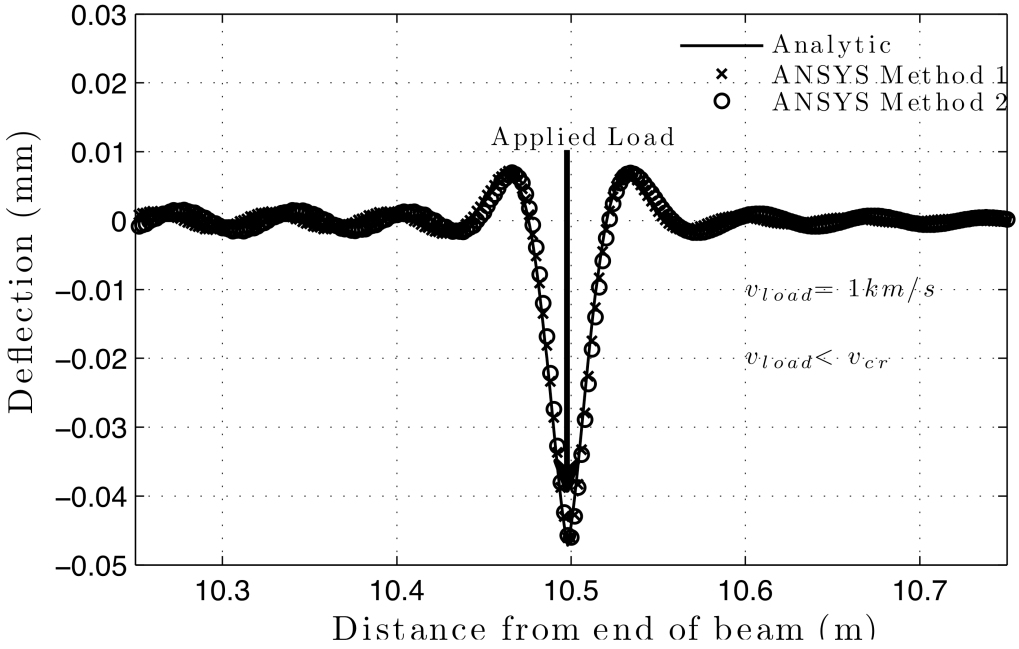


Figure 3.4: Verification for load velocity below the critical velocity

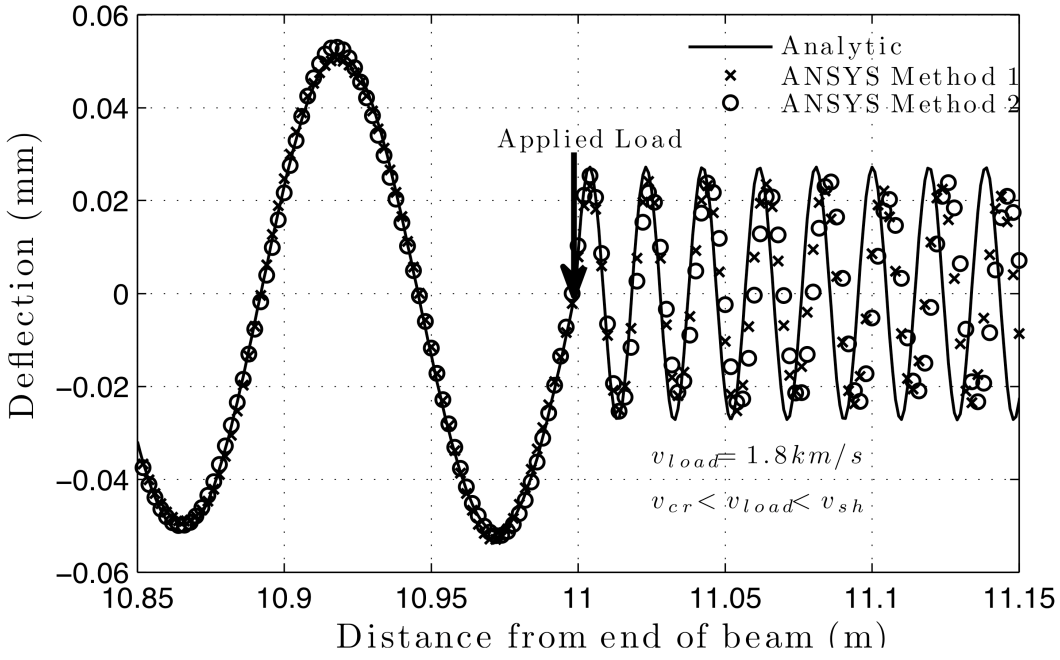


Figure 3.5: Verification for load velocity between the critical and shear velocities

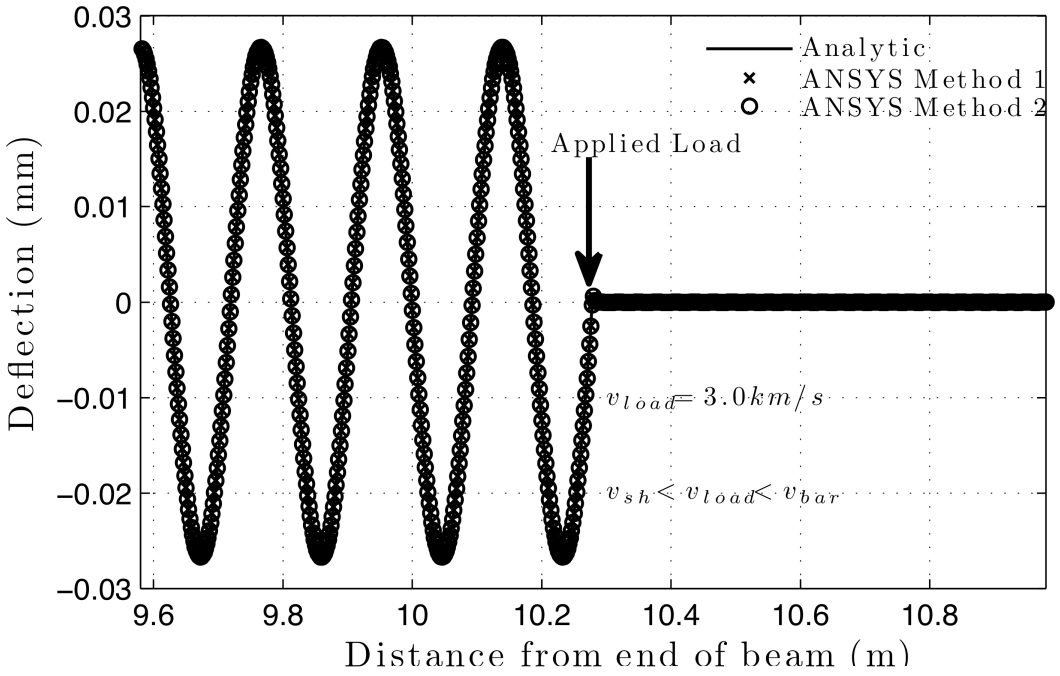


Figure 3.6: Verification for load velocity between the shear and bar velocities

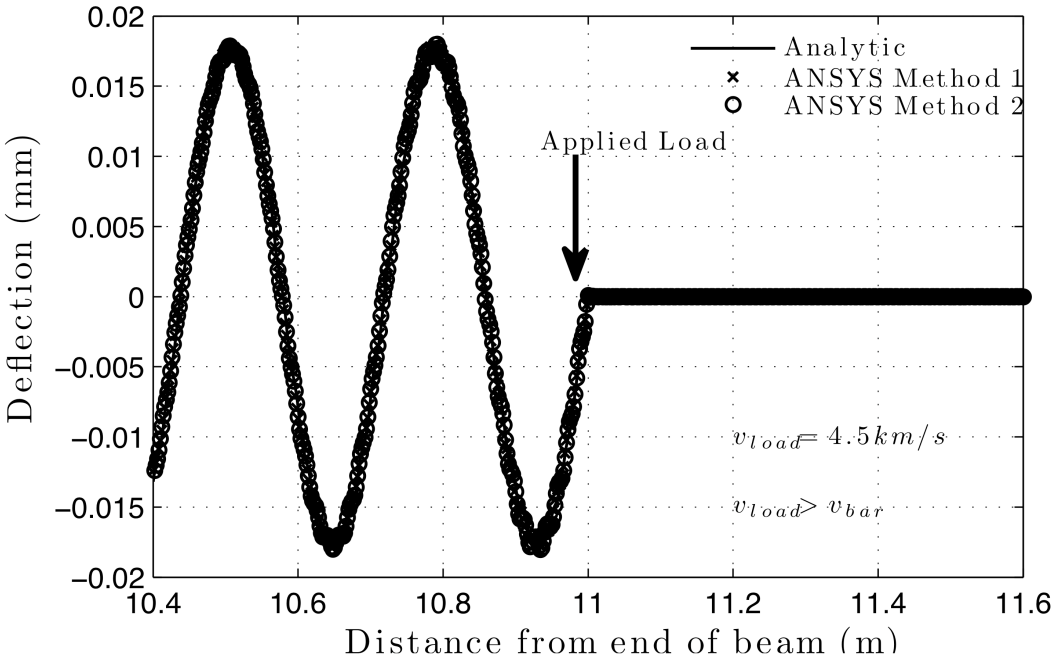


Figure 3.7: Verification for load velocity above the bar velocity

shown in Figures 3.4-3.7. In these figures, Method 1 refers to the formulation in the previous section that includes the foundation stiffness in the mass and stiffness matrix of the BEAM54 element and Method 2 refers to the formulation where spring elements were added to the ends of each beam element.

These results are shown for the beam properties listed in Table 3.1. Both of these finite element models match the analytic results very well over all of the velocity ranges up to and beyond the bar velocity. The plots in Figures 3.4-3.7 were simulations of a $20m$ long beam with 10,000 befam elements where the load traversed the first 10 meters of the beam. The velocity of the load is indicated in each plot along with the velocity range which each solution represents.

Fortunately, in this problem there is also some intuition to be gained by looking at these quasi-static solutions. One interesting thing to be pointed out in Figures 3.4-3.7 is the motion of the load relative to the point of maximum deflection. In the first case, Figure 3.4, the load lies directly at the point of maximum deflection. This is similar to the deflection when the load is stationary. In the second case, Figure 3.5, the load has moved up to the point of zero deflection. At this point, the load is moving fast enough to climb out of the deflection well generated by the load. In the third case, Figure 3.6, the load has moved to the top of the deflection well. The load is moving at a constant velocity in these equations but when the load is accelerating, it can transition between these quasi-static states.

Another interesting thing to point out in these analytic solutions is the fact that the case pictured in Figure 3.5 shows no attenuation on the waves in front of or behind the moving load. In Figure 3.4 there are no waves, and the solutions in Figures 3.6-3.7 show no waves in front of the armature. This means that the velocities between the critical and shear velocities can be thought of as a radiation zone where the load is capable of sending out waves in both directions. This wave

radiation will have dramatic consequences for an electromagnetic launcher [48],[49].

## 3.4 Rectangular Armature

With the stiffness of the launcher calculated and the rail elements verified, it is possible to model the dynamics of the launcher using the finite element model described in section 3.1. This simulation will be presented in this section. The results of this simulation have been previously published [48].

First, a symmetric rectangular armature is modeled to exclude the complexities of a more realistic geometry. This simplification will be removed in later sections. The basic geometry of the finite element mesh is shown in Figure 3.8. In this picture, two rails are shown, this is just for display purposes. In the actual simulation, symmetry was assumed and only one half of the armature and one rail were actually simulated. The launcher was modeled as being 1.5 meters long and the armature was 7 cm long. The material parameters and geometry of this system are based on the Medium Caliber Launcher presented in Section 3.2.1.

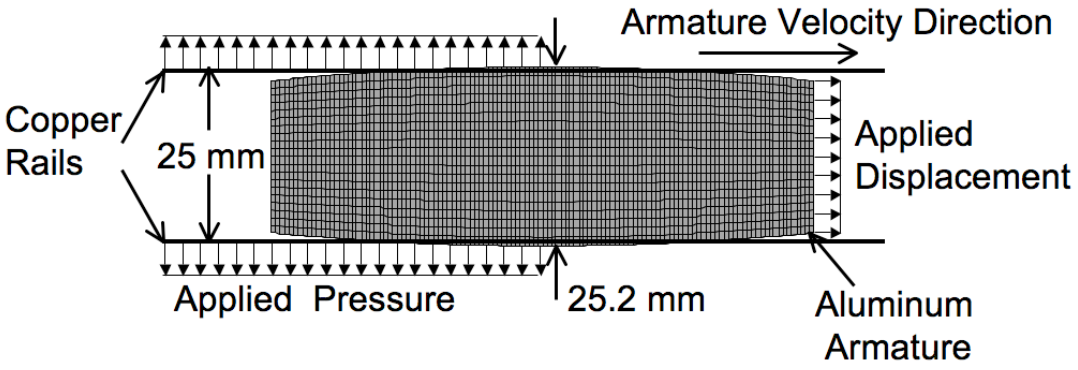


Figure 3.8: Square Armature Finite Element Mesh (©2006, IEEE. Reprinted, with permission from Johnson and Moon, 2006)

The armature shown in Figure 3.8 is slightly wider than the distance between the rails. This extra width is what causes the initial static pre-stress between the

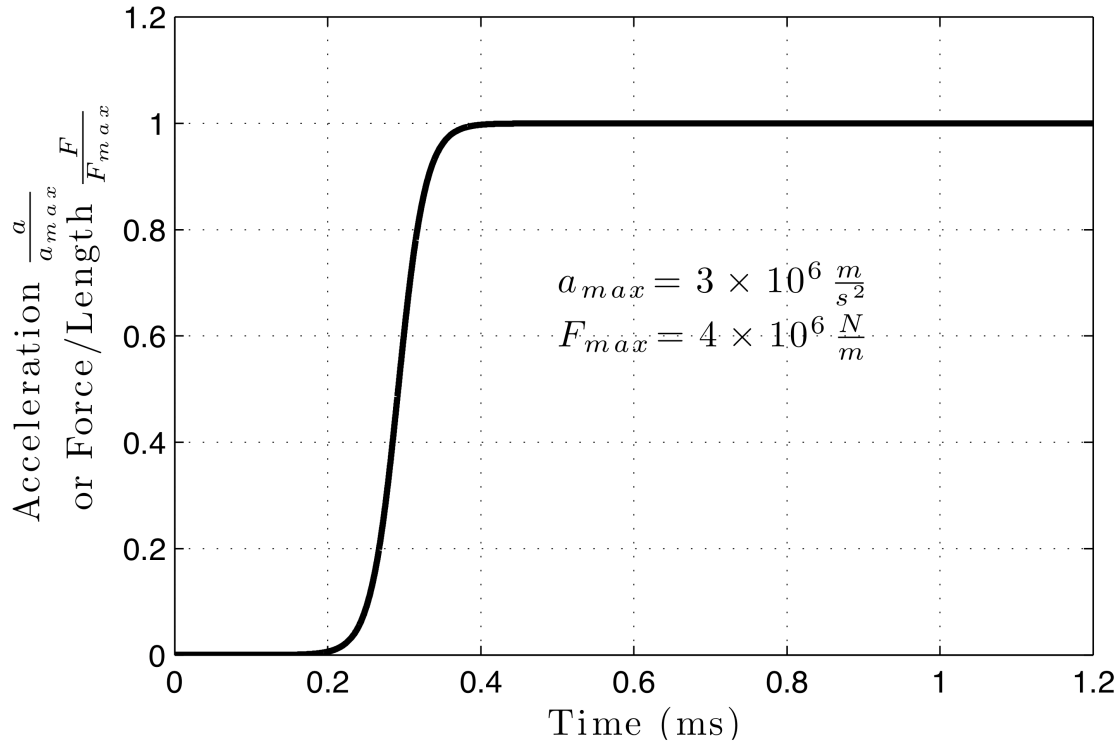


Figure 3.9: Acceleration and Pressure as a Function of Time

rails and armature (pictured later in Figure 3.12). This is done in experimental launchers so that electrical contact is maintained throughout the launch.

The boundary conditions and forces are also pictured in Figure 3.8. The contact between the armature and the rails was modeled using sliding contact elements with no friction that were capable of contact separation. The lack of friction makes it necessary to accelerate the armature by applied displacements. A pressure was applied to the rails behind the center of the armature to approximate the effects of the magnetic field. The pressure and the acceleration are ramped on at the beginning of the launch following the function plotted in Figure 3.9. This function assumes a gradual turn-on of the acceleration and pressure up to a constant value that is then maintained through out the launch. This is essentially the same as assuming an ideal power supply. The gradual turn-on is necessary to get rid of

jerk-effects (i.e. abrupt changes in the acceleration, see Section 3.5). When the acceleration is ramped on too fast, waves are radiated from the armature. The acceleration and applied pressure were scaled so that they are consistent with each other according to Equation 3.2. The final result of all of this is a simulation of an armature accelerating from zero up to approximately $3\,km/s$ as it exits the rail guide way in about 1.2 ms. This is accomplished by solving approximately $13,000$ transient load steps.

As a final note it should be also stated that the materials used in this simulation have been assumed to have a linearly elastic response throughout the launch. Large enough stresses to cause plastic deformations were encountered but studying these higher order effects is not the purpose of this simulation.

### 3.4.1 Railway Dynamics

The first thing to discuss is the dynamics of the rails during this launch. This is done by plotting a few snapshots of the rail deflection at different times. These plots are shown in Figure 3.10 The purpose of this figure is to illustrate the fact that waves propagate out in front of the armature after it passes through the critical velocity. This plot can be made more enlightening by taking many of these 'snapshots' in time and generating a surface plot of the entire time history of the beam. A gradient plot of this surface is shown in Figure 3.11. In this plot, there are two vertical lines that show when the armature passes through the critical velocity and the shear velocity. In addition to this, there are dotted lines showing the position of the front and rear of the armature. When the critical velocity is reached, waves propagate out in front of and behind the armature. In this particular simulation, the armature accelerates past these waves. This phenomenon has serious implications for the contact pressure between the armature

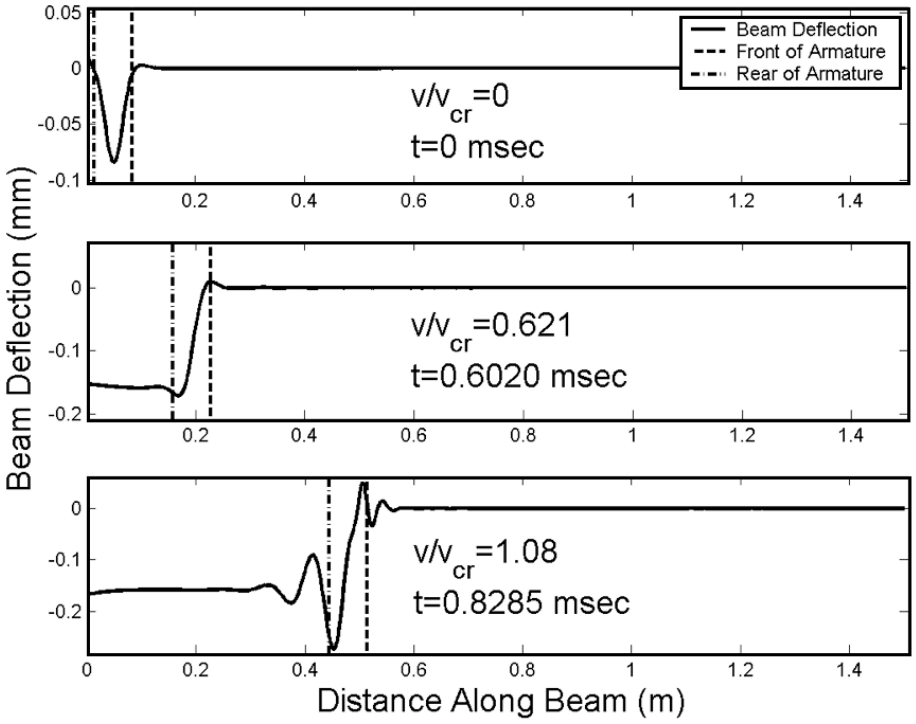


Figure 3.10: Snapshots of Rail Deflections Throughout Launch (©2006, IEEE. Reprinted, with permission from Johnson and Moon, 2006)

and the rails.

After passing through the critical velocity the armature is no longer centered in the minimum of the deflection curve. This is analogous to the constant load situation where the load starts to climb out of the 'deflection well' (see Section 3.3.2). The armature eventually accelerates past the shear velocity. When this occurs, the armature is now traveling faster than the waves it radiated at the critical velocity. This means that it catches up to them and passes over them. This can be seen in the zoomed in plot in Figure 3.11. This causes serious interference effects that drastically change the contact pressure which will be shown in the next section.

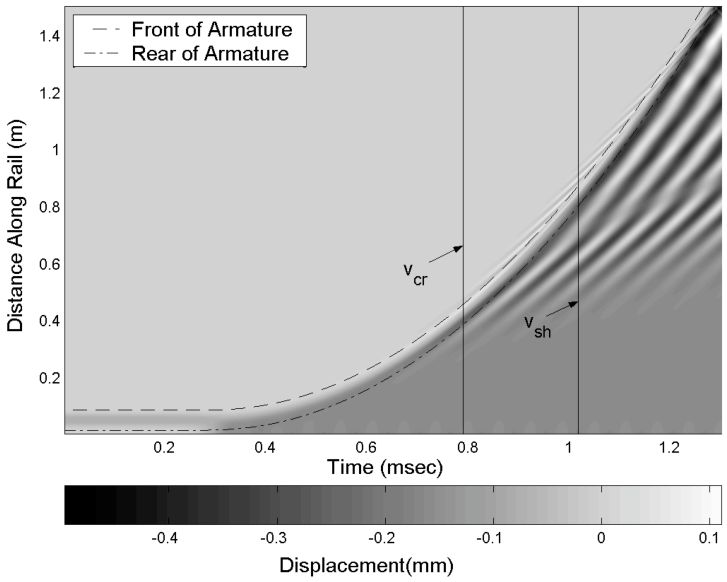


(a) Dynamic Rail Deflection

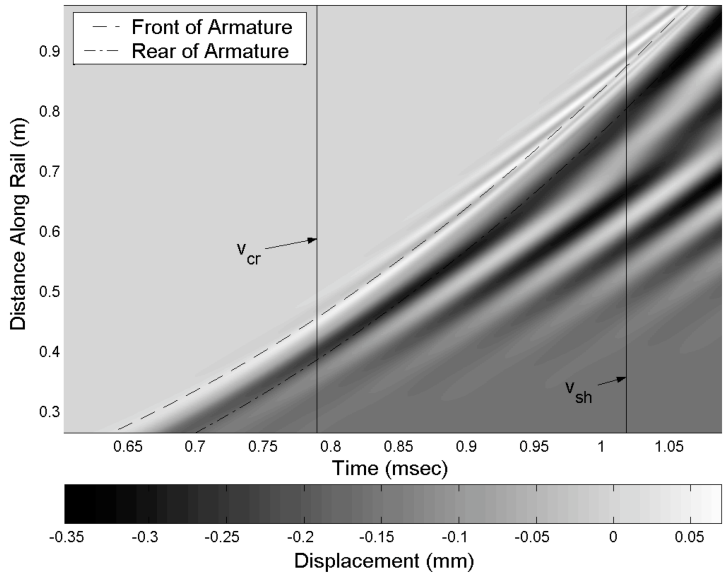


(b) Dynamic Rail Deflection in the Radiation Region

Figure 3.11: Deflection of the Rails as a Function of Time for Square Armature (©2006, IEEE. Reprinted, with permission from Johnson and Moon, 2006)

### 3.4.2 Contact Pressure

The dynamics of the rails illustrated in the previous section strongly influence the contact pressure between the armature and rails. Figure 3.12(a) shows the normal static contact pressure between the rails and armature before the magnetic pressure is applied to the rails. The normal contact pressure can be made into a surface plot in a similar fashion as the rail deflection in the previous section. This plot can be used to visualize the contact pressure dynamically as the armature accelerates down the rails. This surface plot and its corresponding contour gradient plot are shown in Figure 3.12. The time history had to be split into three different plots; this is because it jumps in magnitude twice, making parts of the time history difficult to see on the same scale. These figures also include straight lines showing the critical and shear velocities. The x-axis on these plots represents the distance along the armature; measured from the rear of the armature (i.e. the pressure is being displayed in the frame of reference of the armature). Example snapshots of each region are also shown in Figure 3.12.

Figure 3.12(b) shows the region when the armature passes through the critical velocity. As one can see, the contact pressure shifts towards the front of the armature. This is caused by the fact that the armature is beginning to pass over the wave front that it has been traveling with. This is the same effect seen with the constant load when it climbed up the side of the 'deflection well' at velocities higher than the critical velocity (see Figures 3.4-3.7). This effect causes both the position and magnitude of the contact pressure to change.

Figure 3.12(d) shows the region when the armature passes through the shear velocity. The change in this diagram is not as severe as the critical velocity, but as one can see, the magnitude does start to increase after the shear velocity is reached. This is also consistent with the verification solutions. There exists no

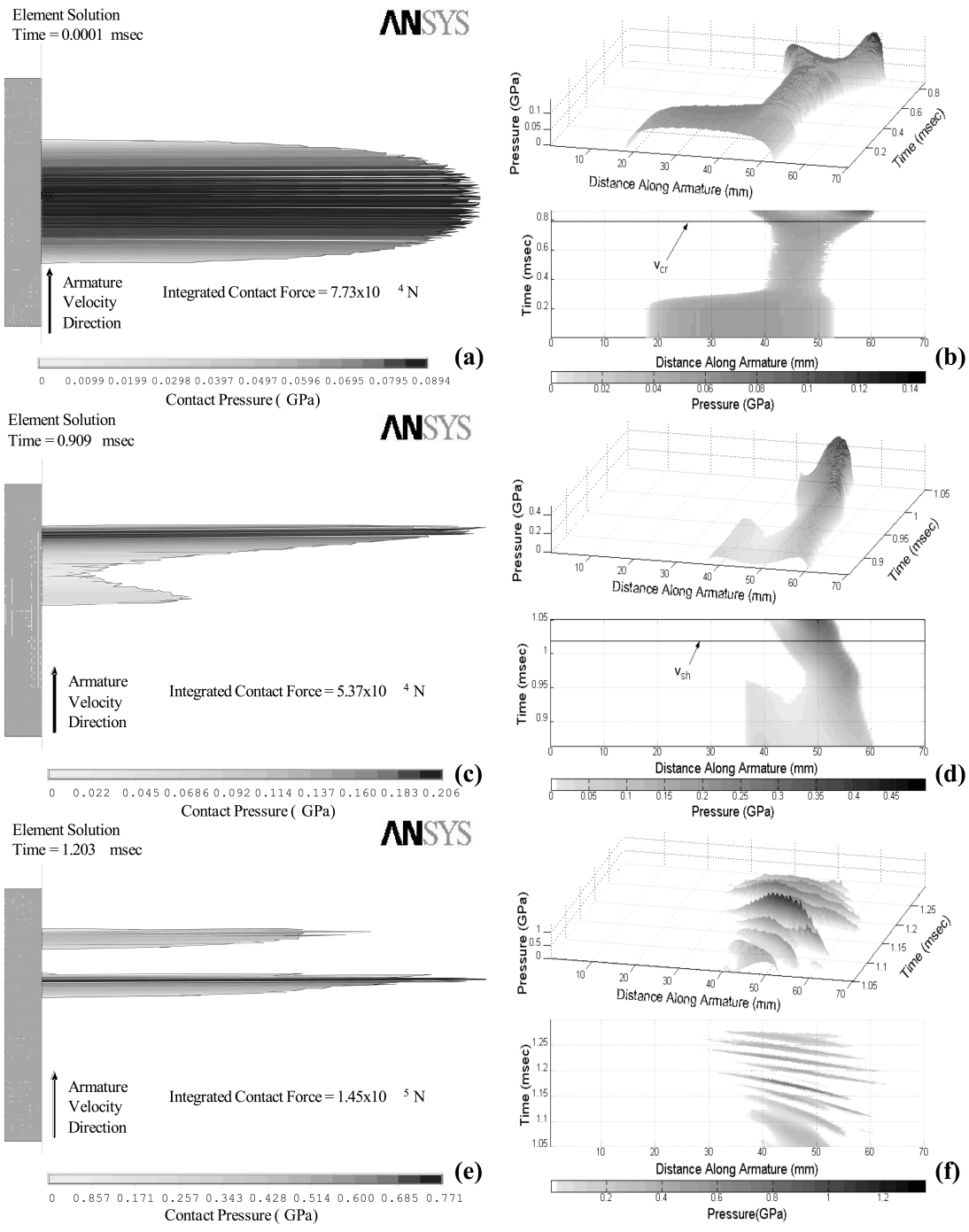


Figure 3.12: Dynamic Contact Pressure for Square Armature (©2006, IEEE. Reprinted, with permission from Johnson and Moon, 2006)

analytic solution for the quasi-static case (see Equation B.1) at the critical velocity, but there is an analytic solution at the shear velocity. It is for this reason that one would expect something more dramatic to occur at the critical velocity than at the shear velocity.

A short time after the shear velocity, the contact area of the armature moves to the rear and disappears, concurrently another contact area develops towards the front of the armature and moves towards the rear. This cycle repeats itself, and corresponds to the armature skipping over the waves on the rails. This effect is seen in Figure 3.12(f). The slash pattern represents points of pressure that are moving backward relative to the armature; this is reflected in the negative slope of these slashes. This shows that the armature is actually skipping over the top of these elastic waves. In a real electromagnetic launcher the current flow would be interrupted at the onset of this skipping phase and an arc could form. The relative velocity between the armature and waves is about 400 m/s and the maximum contact pressure is far beyond the shear strength of the copper rails (approx. 0.2 GPa). The contact pressure is also very sharply peaked. As one can imagine, this could cause the gouges seen in hypervelocity electromagnetic launchers [60]. The model being explored in this dissertation is not sophisticated enough to offer an outright explanation for gouging, but it does show a potential avenue for explaining for the onset of rail gouging. The presently accepted model for gouging is an empirical model that explores the interaction between two sliding interfaces based on collected data [93]. This empirical model assumes that the pressure between the rails and armature increases to a certain threshold where gouging will begin to occur. This gouging threshold is a function of the material properties of the two sliding bodies. What this simulation shows is how the pressure increases. The waves in the rails cause the rails to essentially pinch the armature as it pushes to

higher velocities. This model is not quite sophisticated enough to give an accurate representation of the gouging threshold because the rail is only being modeled in one dimension and the materials are being modeled as linear elastic. It is possible though, that a three-dimensional or even a two-dimensional model of the rail might be able to correlate better with the data collected on rail gouging.

## 3.5 'Jerk Effect' Waves

In the previous section, the simulations were carefully constructed so that the acceleration did not change abruptly (See Figure 3.9). The acceleration was ramped on over a period of time (roughly equal to $200\,\mu s$). This was done because when the acceleration is ramped on more quickly, waves are seen to radiate at the beginning of the launch. When this phenomenon was first seen it was thought to simply be a consequence of a poorly formulated acceleration curve, but these waves have been observed on the Georgia Institute of Technology launcher (See Section 4.2.2). It is for this reason that this section will explore this phenomena computationally. Throughout this dissertation, this phenomena is referred to as 'jerk effect' wave radiation because it occurs when there is a sharp change in the acceleration which is referred to as jerk.

To explore these 'jerk effect' waves, a simulation was constructed that would show them. For the sake of comparison, this simulation used the exact same geometry and material parameters as the simulation in the previous section. The only difference was that the acceleration was ramped on in approximately $20\mu s$. This is shown in the plot in Figure 3.13. This acceleration is still ramped on continuously, but it is ramped on ten times faster. It is important to note that this does make the exit velocity of the armature slightly different than the simulations in the previous section, but the difference is only a few percent.

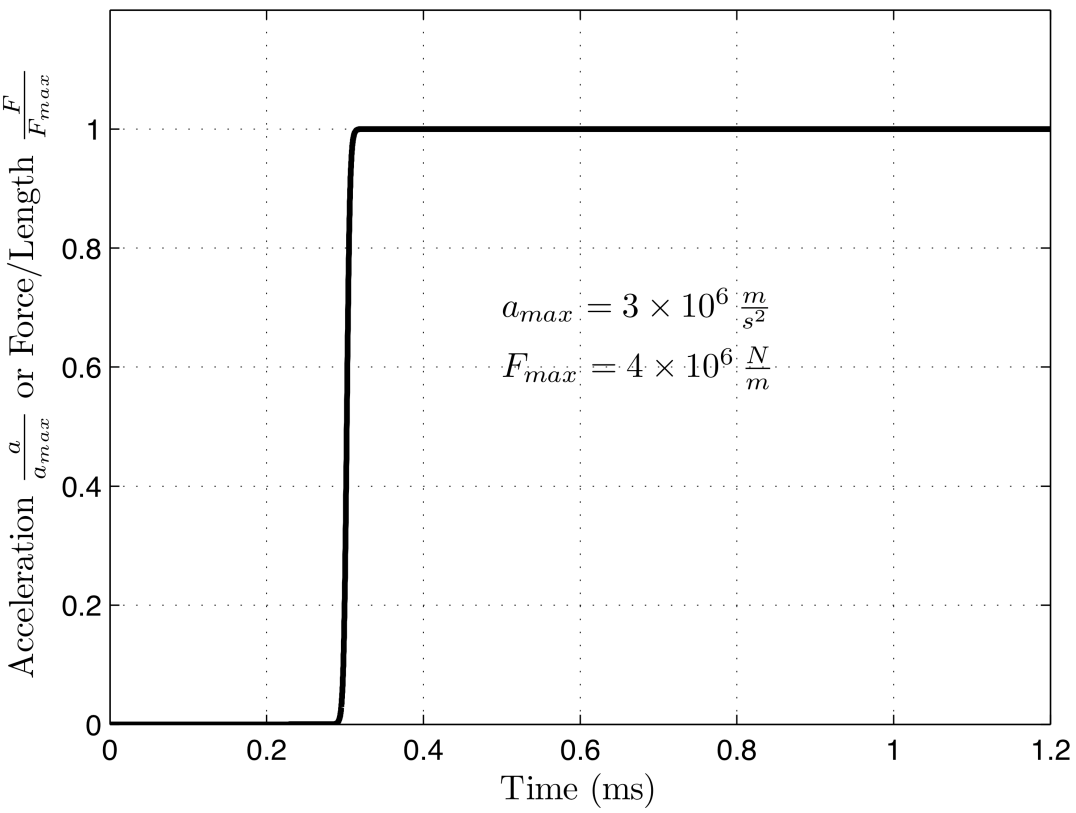


Figure 3.13: Acceleration and Pressure as a Function of Time for Jerk Effect Simulation

### 3.5.1 'Jerk Effect' Railway Dynamics

As before, the first thing to look at is the dynamic deflection of the rails. This is plotted in Figure 3.14. The major difference between this plot and Figure 3.11 is that the wave radiation begins almost as soon as the armature starts to move. The amplitude of these waves will be a function of the amount of jerk that there is but in general they will be smaller in amplitude than the waves seen after the critical velocity. It is important to stress that this wave radiation effect is distinct from the critical velocity wave radiation and should be treated as such.

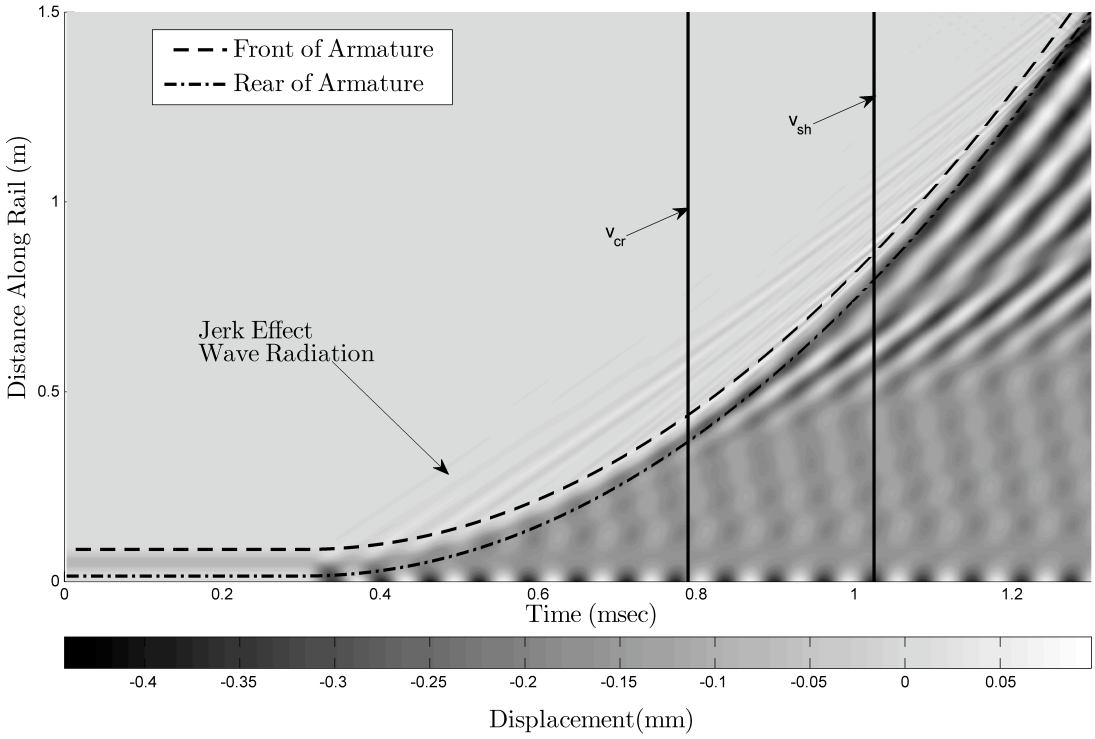


Figure 3.14: Dynamic Rail Deflection With Jerk Effect Waves

### 3.5.2 'Jerk Effect' Contact Pressure

Even though the jerk effect waves are smaller in amplitude than the critical velocity waves, they can still have a dramatic impact on the contact pressure between the armature and the rail. This is shown in Figure 3.15. The first thing to note is that the contact pressure shifts abruptly to the front of the armature when the acceleration is ramped on (near $300\,\mu s$ in Figure 3.15). This is in contrast to the the more continuous change that is seen in Figure 3.12. After the acceleration is ramped on, the contact pressure is seen to oscillate back and forth. This oscillation appears to be caused by vibrations of the armature itself. This is reflected in the constant frequency of these oscillations in the reference frame of the armature (see Figure 3.15(a)). If they were caused by the armature passing over waves in the rail then the frequency would increase dramatically as the armature accelerated. In a

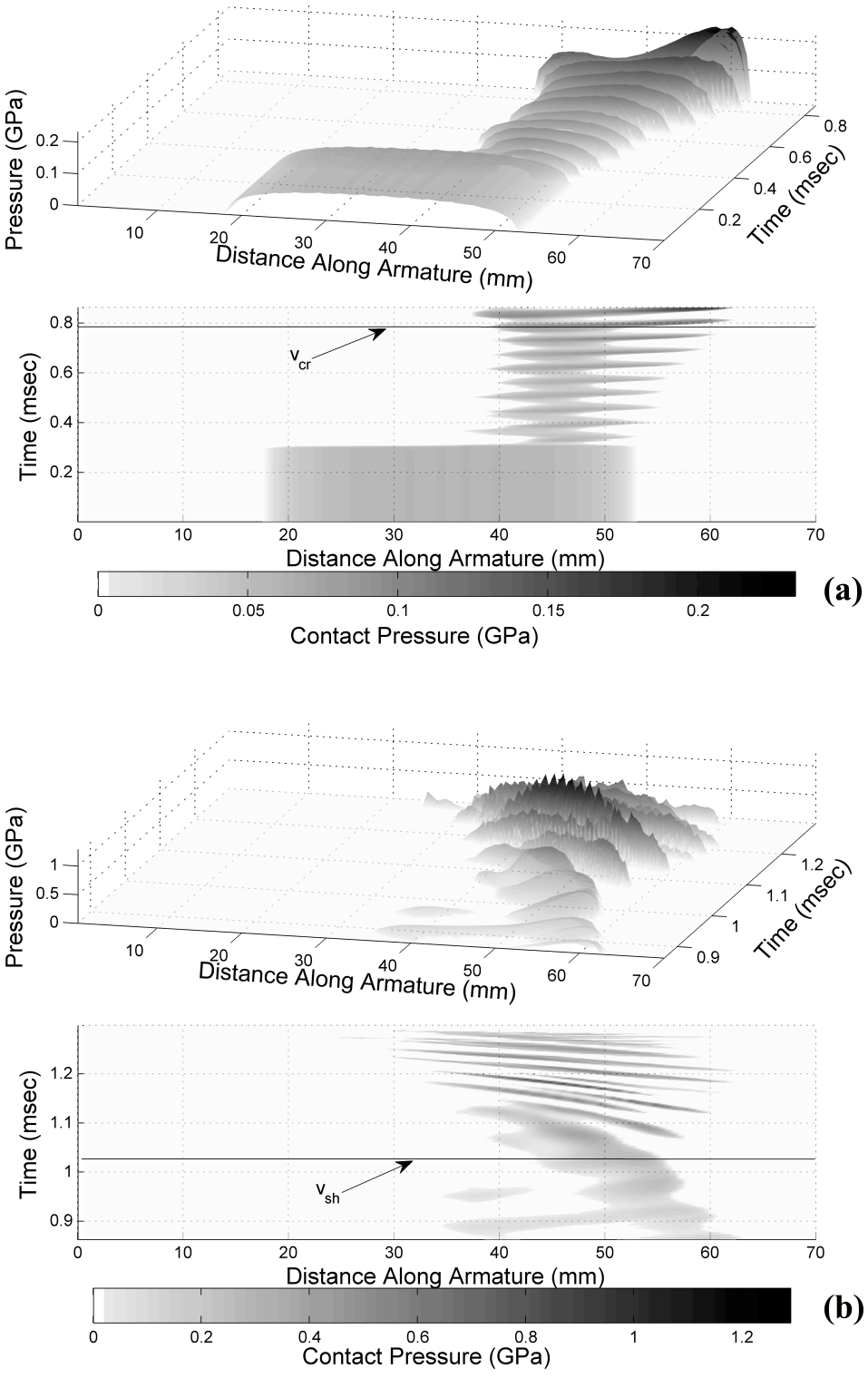


Figure 3.15: Dynamic Contact Pressure With Jerk Effect Waves

real launcher, this jerk is believed to occur when the armature breaks free of the static friction between it and the rail. This oscillation of the contact pressure is an interesting side effect that could be detrimental to the overall performance and integrity of the armature to rail contact. Measurement of these waves could offer a technique for comparing different armature designs and material combinations (see Section 4.2.2).

As before, when the armature passes through the critical velocity, the contact pressure shifts forward and increases in amplitude. This effect is a bit harder to see in this simulation but it is visible in Figure 3.15(a). Finally, in the region above the shear velocity, the armature is skipping over the waves in the rail, just as it did in the simulation in the previous section.

## 3.6 'C' Shaped Armature

The next step in making this simulation less idealized is to model a more realistic armature shape. Typical armatures are shaped with trailing arms as shown in Figure 3.16. This type of armature is referred to as a 'C' shaped armature [40]. The idea behind this armature design is to take advantage of the electromagnetic field to keep the armature in contact with the rails. The trailing arms carry currents traveling in opposite directions, these currents repel each other and push the armature legs against the rails. The removed section in the middle of the armature also reduces the parasitic mass for the launch.

The overall method for simulating the 'C'-shaped armature is very similar to the square armature in the previous section. A pressure is applied to the rails behind the armature and the armature is moved by an applied displacement. The pressure and acceleration are then scaled in the same way indicated in the previous section. The major difference is that a repulsive pressure must also be applied to

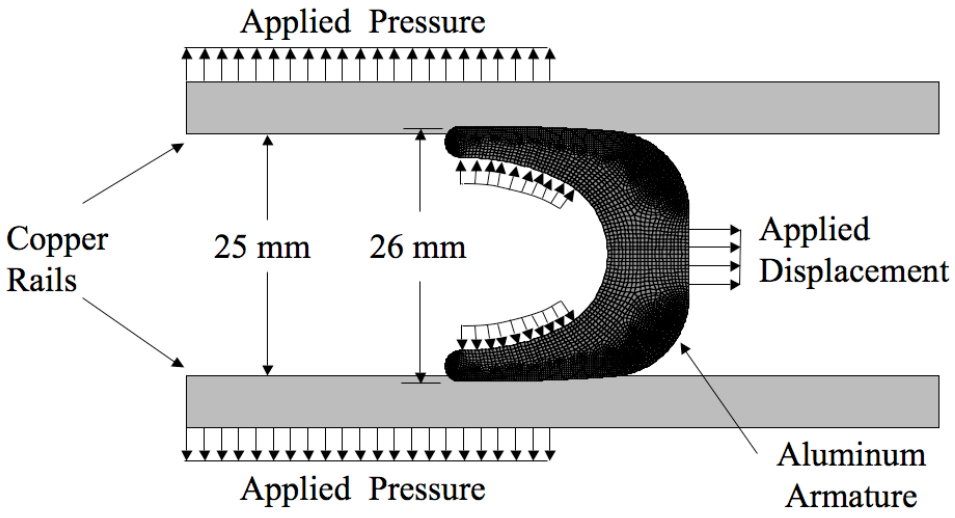


Figure 3.16: 'C'-Shaped Armature Finite Element Mesh (©2007, IEEE. Reprinted, with permission from Johnson and Moon, 2007)

the trailing arms of the armature. This was done, and to keep things simple the pressure was assumed to be 32% larger than the pressure applied to the rails. This increase in pressure is justified because of the increased magnetic field behind the armature. The percentage used corresponds to a 15% increase in the magnetic field directly behind the armature as compared to the field between the rails far behind the armature. This is a conservative number for the increase in the magnetic field, but other values have been simulated and the general observations that will be made about this simulation do not change with this percentage. The magnitudes of the pressures change, but the dynamic effects discussed in this section are still present.

As with the square armature, the final result of this simulation is an armature accelerated from zero to 3 km/s on 1.5 meter long rails in 13,000 load steps. The material parameters and geometry of this system are also based on the Medium Caliber Launcher parameters presented in Section 3.2.1.

### 3.6.1 Railway Dynamics with a 'C' Shaped Armature

As before, the first thing to plot is the dynamics of the rails. Figure 3.17 shows the surface plot of the railway dynamics. The railway dynamics are very similar to those of the square armature. Wave radiation occurs at the critical velocity in the same way it does in Figure 3.11. The only major difference is that the maximum deflections are slightly larger. This is just because of the larger interference fit of the C-Shaped armature versus the square armature pictured in Figure 3.8, and the transverse load applied to the trailing arms.

### 3.6.2 Contact Pressure with a 'C' Shaped Armature

The contact pressure can also be plotted for this simulation. This plot is shown in Figure 3.18. The surface plot had to be split into two different plots because of the large increases in the contact pressure.

In this simulation, the armature begins with a small portion at the front in contact with the rails. The rear of the armature is then brought into contact as the repulsion force between the trailing arms increases. The contact pressure is relatively evenly distributed over the contact interface until the armature reaches the critical velocity. At this point the contact pressure again moves forward and increases in amplitude. In contrast to the square armature, the rear maintains contact through this transition. This is because of the repulsion forces between the trailing arms.

As with the square armature, a short time after the shear velocity the contact pressure moves towards the rear of the armature and disappears. The front of the armature comes back into contact with the rails and moves towards the rear of the armature. This process repeats just as it did with the square armature. This

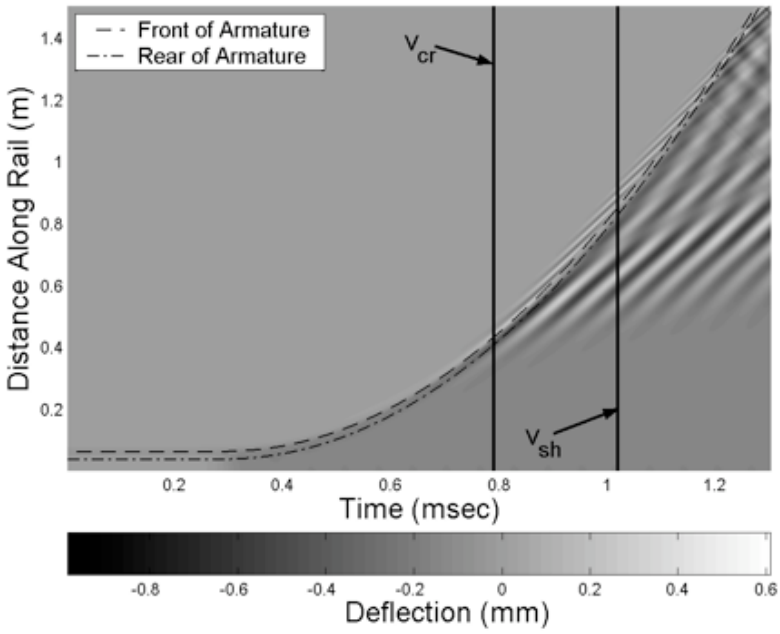


(a) Dynamic Rail Deflection

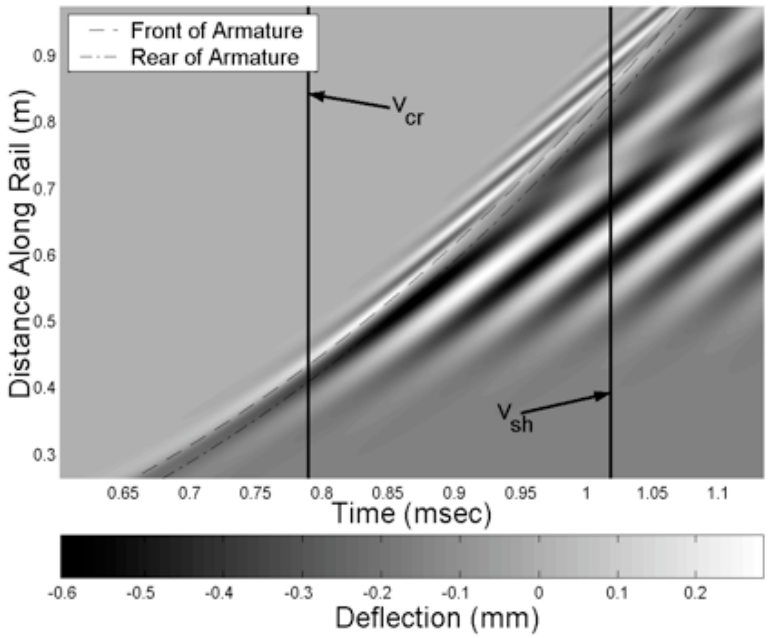


(b) Dynamic Rail Deflection in the Radiation Region

Figure 3.17: Deflection of the Rails as a Function of Time for 'C'-Shaped Armature (©2007, IEEE. Reprinted, with permission from Johnson and Moon, 2007)

indicates that the 'C' shaped armature will skip over the stress waves as well.

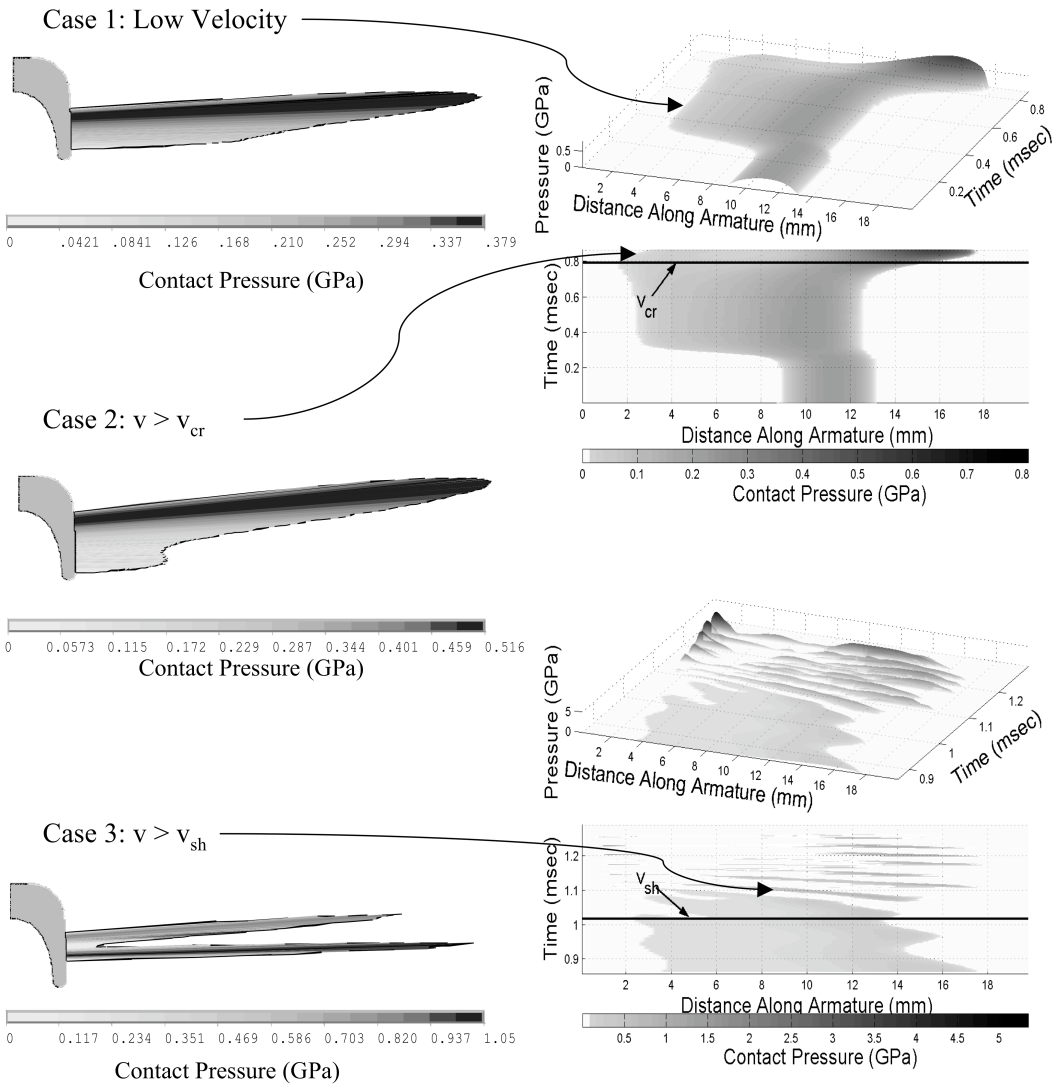


Figure 3.18: Dynamic Contact Pressure for 'C'-Shaped Armature (©2007, IEEE. Reprinted, with permission from Johnson and Moon, 2007)

The major difference between this situation and the square armature is that the repulsion force on the trailing arms keeps the rear of the armature in contact with the rails for a slightly longer period of time. As one can see though, the shift forward at the critical velocity and the skipping phase after the shear velocity still occur with the C-shaped armature.

## 3.7 Nonlinear Foundation

The simulations up to this point have assumed that the foundation is perfectly linear. For a real launcher, this is not the case. The containment is typically soft for small loads and becomes more stiff for larger loads. This results in a nonlinear load-deflection curve. This curve has actually been measured for the Georgia Tech. launcher. A hydraulic device was constructed by Dr. Scott Bair of Georgia Tech. for just this purpose. This device fits inside the bore of the assembled launcher and applies a symmetric load to both rails while measuring the displacement. A typical curve from one of these measurements is shown in Figure 3.19[1]. As one

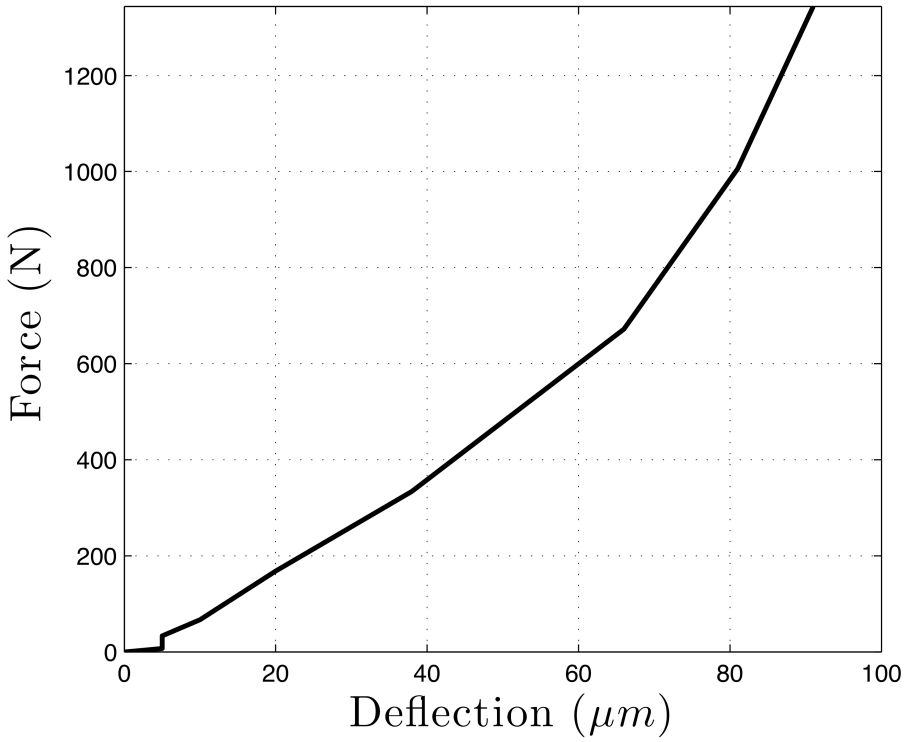


Figure 3.19: Measured Load-Deflection Curve for Georgia Tech. Launcher

can see, the real launcher is very soft at first and then becomes stiffer as the

[1]Data in Figure 3.19 courtesy of Dr. Scott Bair of Georgia Tech.

load increases. This is most likely because of small gaps in the system when the launcher is clamped together. Using the elements of the spring-damper formulation discussed in Section 3.3 it is possible to put together a simulation with a nonlinear foundation.

This simulation was done using data from the Georgia Tech. launcher. A current curve was taken from an experiment on the launcher. The square of this current was integrated to get the acceleration and then the acceleration was scaled to fit the velocity information from the same launch. The experimental current and integrated armature displacement curves are shown in Figure 3.20. These two were used as inputs for the displacement of the armature and the pressure applied to the rails. The boundary conditions for this launch were the same as those shown in Figure 3.16 except that the bore was only assumed to be 12.7 $mm$(the armature was scaled accordingly). The rail parameters were taken from Table 3.2 and the load-deflection curve from Figure 3.19 was used for the nonlinear foundation springs.

A surface plot of the dynamic deflection for this simulation is shown in Figure 3.21. The interesting thing about this plot is that waves are now being generated well before the armature reaches the critical velocity. In this particular simulation, wave radiation begins at roughly 0.7 $ms$. This point in time corresponds to an armature velocity of just under 1100 $m/s$. The expected critical velocity for a linear foundation is 1314 $m/s$ as shown in Table 3.2. This means that a nonlinear foundation will effectively lower the velocity at which waves are generated. This is a reasonable result since the critical velocity depends on the stiffness of the foundation. Having a nonlinear load-deflection curve of the form shown in Figure 3.19 lowers the effective stiffness of the foundation. This reduction of the onset of wave radiation will also be seen in the experimental data presented

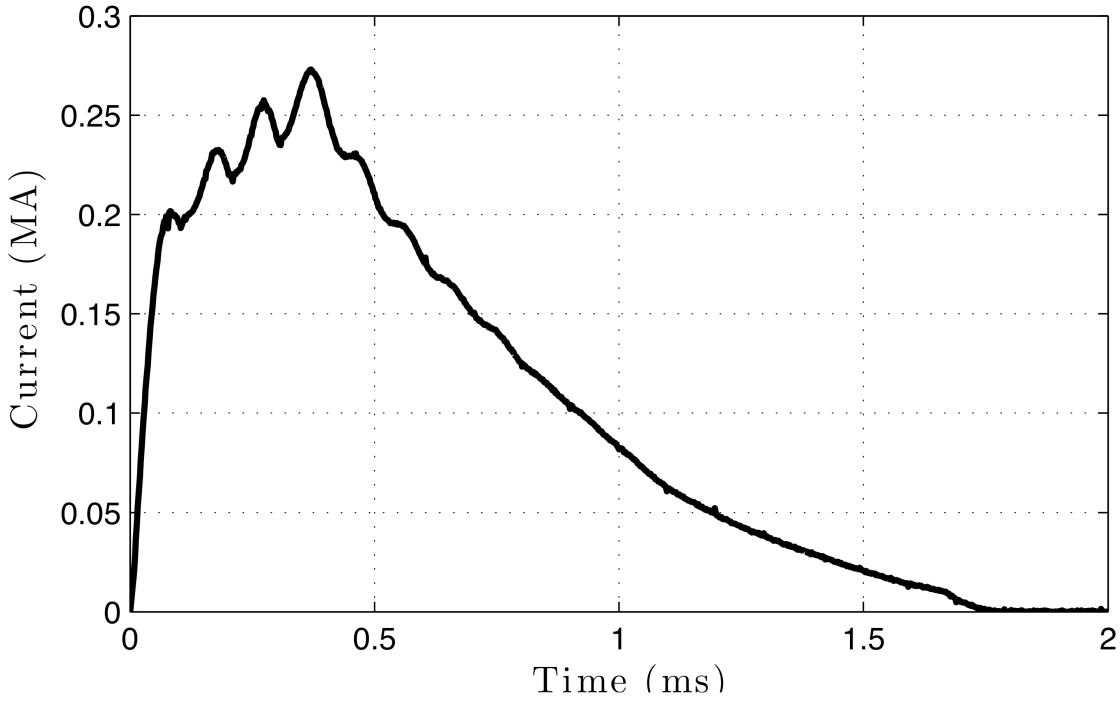


(a) Current Data From Georgia Tech. Launcher

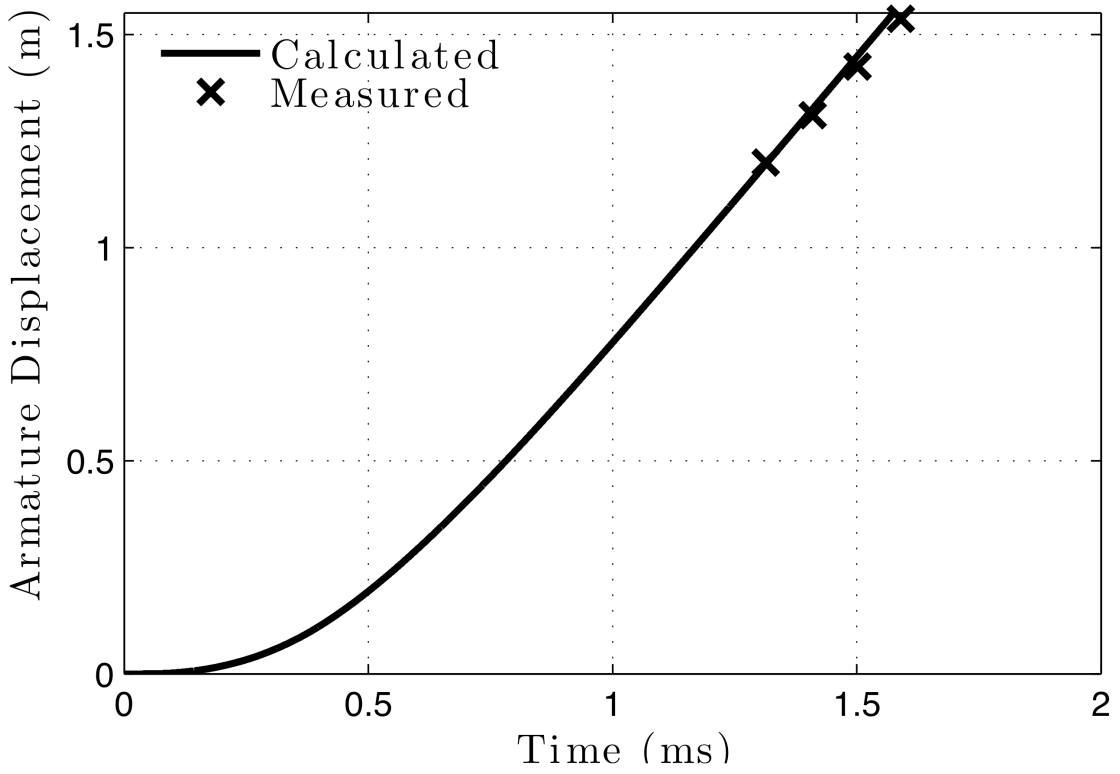


(b) Calculated Displacement Curve for Armature

Figure 3.20: Current and Displacement Input for Simulation

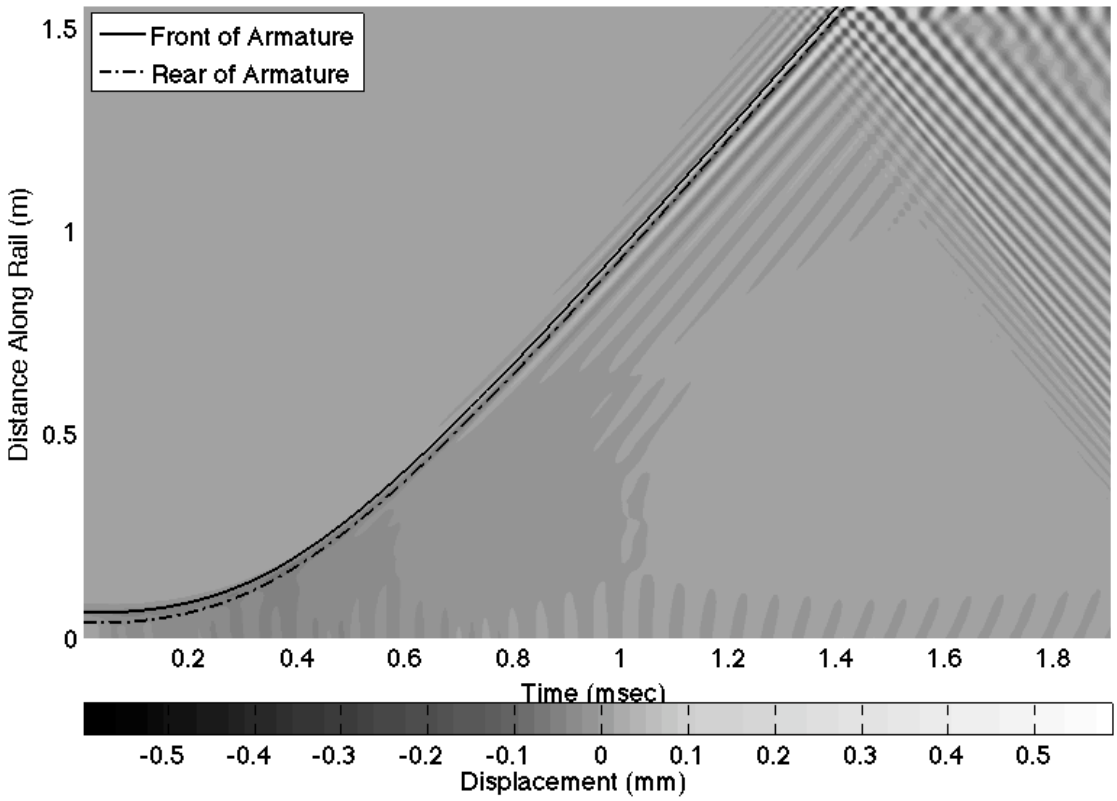


Figure 3.21: Dynamic Deflection of Rails During Launch

later in this dissertation. In fact, this particular simulation is compared directly to experimental data in Section 4.2.1.

In addition to nonlinear foundation effects, this particular launch shows the phenomenon of wave reflection. Waves are reflected from the end of the rail before the armature leaves the bore of the launcher. This effect occurs when the armature is traveling fast enough to radiate waves, but too slowly to pass over those waves. This effect is seen in experimental measurements in Section 4.2.1

# Chapter 4
# Stress Wave Measurements on the Georgia Institute of Technology Launcher

One of the primary purposes of the Georgia Tech. launcher is to help develop diagnostic and sensor techniques to advance the study of wear in electromagnetic launchers. Since the simulations in Chapter 3 indicate that elastic waves may contribute to the damage of the rails, an effort was made to measure the stress waves in the rails of the Georgia Tech. launcher. To conduct these measurements, a device had to be constructed that was capable of measuring high frequency, large magnitude strains in a pulsed electromagnetic field.

The requirements for this device were defined with the help of the wave simulation results in Chapter 3 and a device was constructed by researchers at the Georgia Tech. Research Institiute (GTRI) and Micron Optics. Experiments were then conducted by the author and researchers from the Georgia Institute of Technology and GTRI. The results of these experiments will be presented in the following sections.

## 4.1 Fiber Optic Sensor System

To construct a device for measuring the stress waves in the rails of the Georgia Tech. launcher it was first necessary to define the requirements of the measurement system. This was done using the simulation results in Section 3.7. These results show that the magnitudes of the strain maxima are on the order of $5000 - 10000\,\mu m/m$. The frequencies involved require the strain measurement device to be capable of sampling rates greater than $200\,kHz$. It was decided that the device should be capable of a measurement range of $\pm 5000\,\mu m/m$ and a minimum sampling frequency

of $200\,kHz$. The simulations actually show strains larger than this range, but a trade-off between resolution and maximum range had to be considered. This range turned out to be sufficient because the armature wears during each shot and this causes the strain maxima to be below the predictions of the simulations (which do not model wear).

Before the results are presented a brief explanation of how fiber Bragg grating strain sensors work is necessary. This will be just a simple explanation of how strains are measured using fiber Bragg grating sensors.

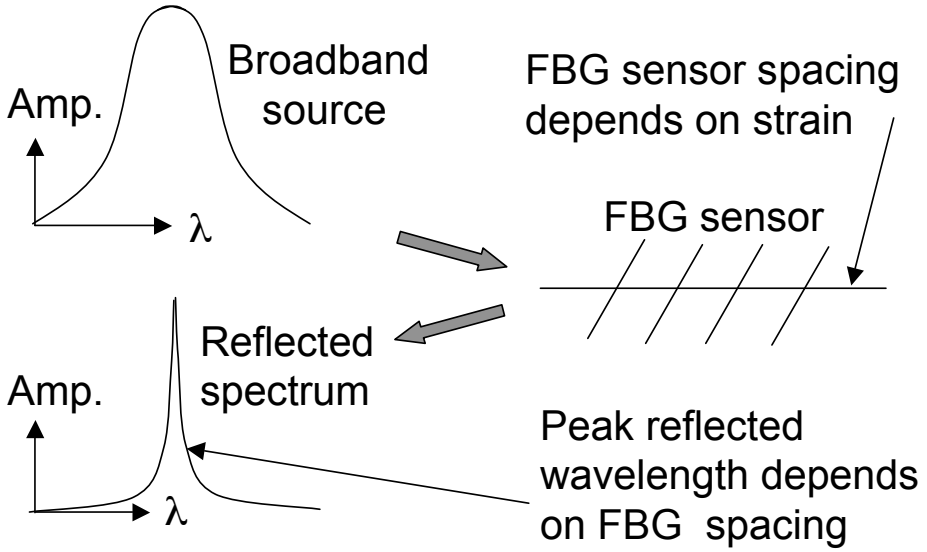


(a) Fiber Bragg Grating Measurement Concept

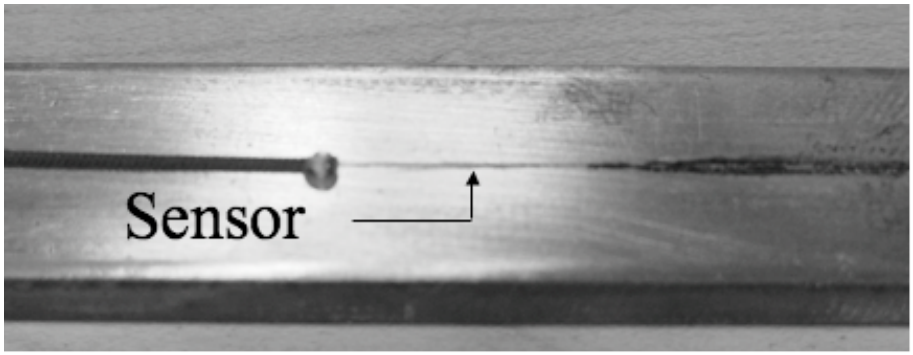


(b) Fiber Bragg Grating Sensor Attached to Rail

Figure 4.1: Fiber Bragg Grating Strain Measurement

The sensor itself is a short Bragg grating near the end of an optical fiber. The Bragg grating portion of the sensor is attached to the specimen using a special adhesive. A picture of one of these sensors attached to a copper rail from the Georgia Tech. launcher is shown in Figure 4.1 along with a sketch of the basic mechanism by which they operate.

The basic principle of operation of one of these sensors is relatively simple. First a broadband light source is transmitted down the fiber. When the light reaches the sensor the majority of light passes through unimpeded, but a small band of light is reflected back down the fiber and back to the measurement device. This process is pictured in Figure 4.1. The wavelength $\lambda$ of this reflected signal depends on the spacing of the grating in the following way [19].

$$\lambda = 2nD \tag{4.1}$$

Where $D$ is the period of the grating and $n$ is the refractive index of the fiber material. For the case of a fiber Bragg grating attached to a specimen, when the specimen is strained, so is the fiber. This translates to a change in the reflected wavelength. The wavelength of the reflected signal is measured and this gives a measure of the strain according to the following equation.

$$\epsilon = \eta \Delta\lambda \tag{4.2}$$

Where $\epsilon$ is the strain, $\Delta\lambda$ is the change in the peak reflected wavelength and $\eta$ is a calibration constant. For the sensors used in the experiments in this chapter the typical change in wavelength was $1.2\,pm$ per microstrain. The difficult part of this type of measurement is to detect these very small changes in the peak reflected wavelength. This is typically accomplished using a wavelength tunable filter. These systems are typically limited to frequencies below 2 kHz so they would not work for our application. To solve this problem, Micron Optics developed a Fabry-Perot tunable filter based system that meets our high frequency requirements.

The details of this specific device are proprietary, but a description of Fabry-Perot tunable filters in general can be found in a book by M. Vaughan [102]. Essentially, a Fabry-Perot filter uses interference of light between two parallel planes that only allows transmission of a small bandwidth of light. A tunable Fabry-Perot filter changes the spacing of the parallel planes to change the peak transmission wavelength. This is used to scan over the output of the fiber Bragg grating to give a measure of the peak wavelength reflected from the sensor (which leads to the measurement of strain).

## 4.2 Measurements

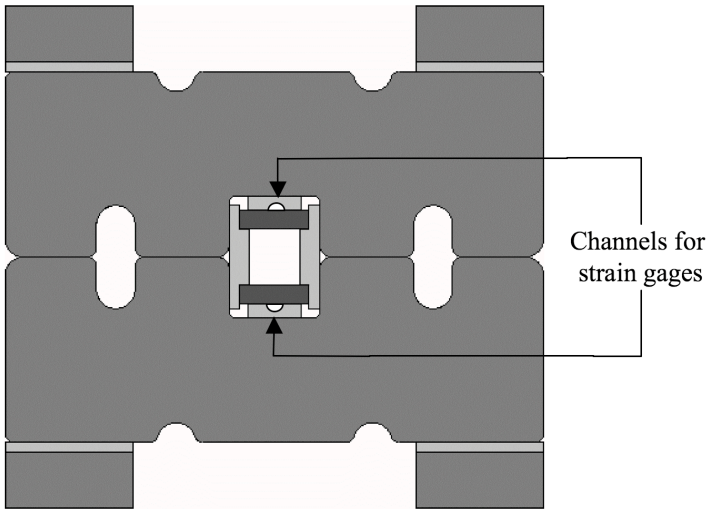


Figure 4.2: Modified Georgia Tech. Launcher Cross-Section

Various strain measurements were made during the launch of the projectile. The intention of these measurements was to test the validity of the finite element simulations of Chapter 3. This was done by measuring the strain at various positions along the length of the launcher for various different launch energies. To accommodate the strain gages, a minor modification to the insulators behind the

rails had to be made. A 0.1875" diameter ball end mill was used to cut a small channel down the length of these insulators to accommodate the strain gages (approximate depth = .07"). A drawing of the modified containment is pictured in Figure 4.2.

### 4.2.1 Single Rail Experiment

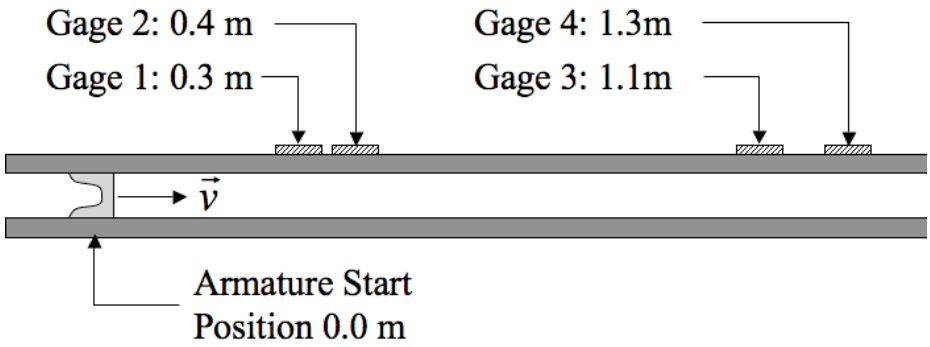


Figure 4.3: Gage Positions for Single Rail Experiments

The first set of tests conducted involved instrumenting just one of the rails. For this test, strain gages were placed at 0.3 m, 0.4 m, 1.1 m and 1.3 m from the start position of the armature as pictured in Figure 4.3. The launcher was then fired at launch velocities ranging from 0.9 km/s to 1.9 km/s and the dynamic strain was recorded on all four channels. The data for these launches is shown in Figures 4.4-4.7 along with the current pulses. The data from these launches shows that the strain can reach values of 5000 $\mu m/m$ as the armature passes by. This observation is well in line with the predictions of the simulation. It should be noted that a large dip in the strain was seen in Figure 4.7 on the fourth sensor. This anomaly is believed to be a problem with the data acquisition card used in the strain measurement device.

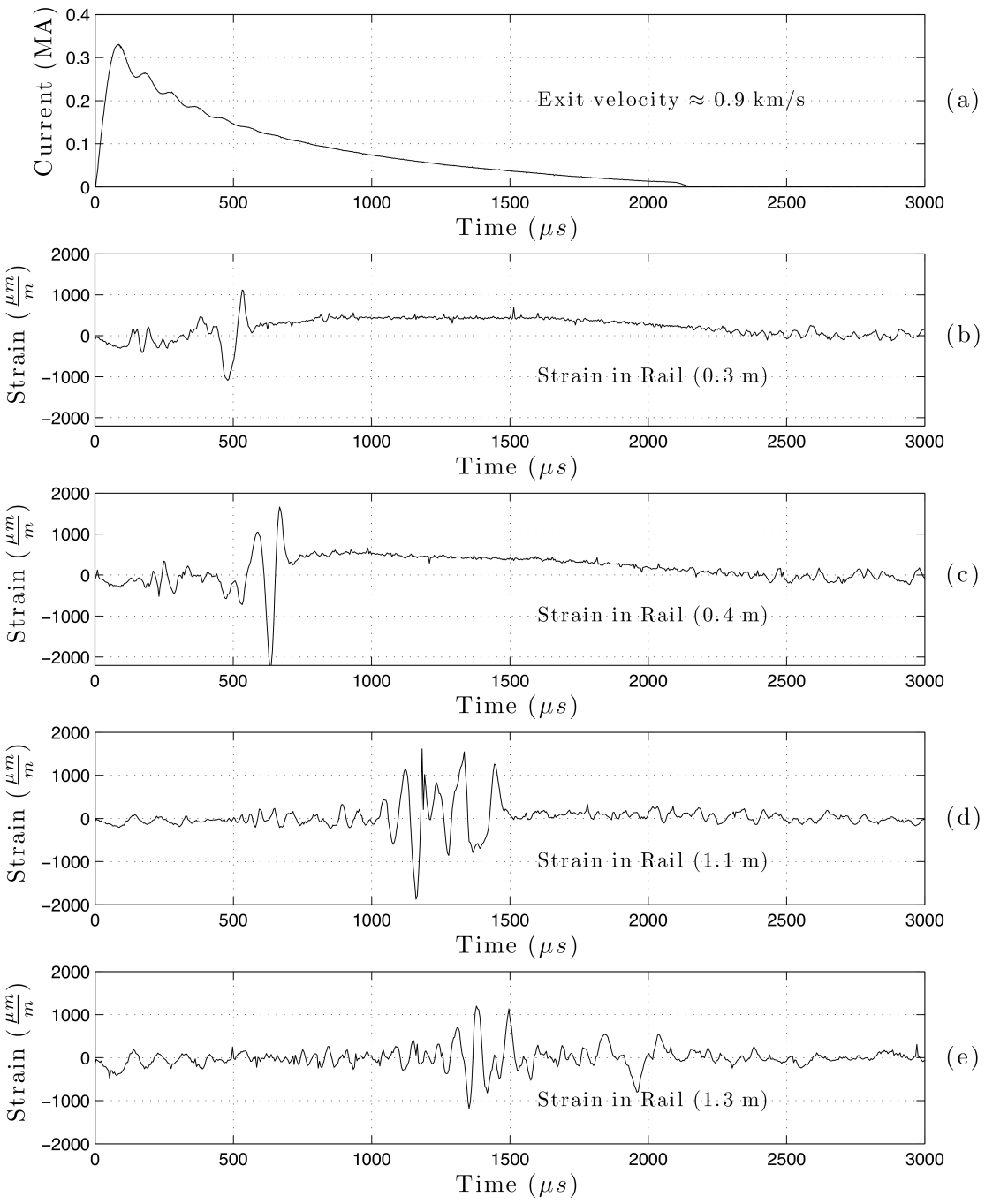


Figure 4.4: 900 m/s launch velocity single rail strain test. (a) Drive Current, (b) Strain at 0.3 m, (c) Strain at 0.4 m, (d) Strain at 1.1 m, (e) Strain at 1.3 m

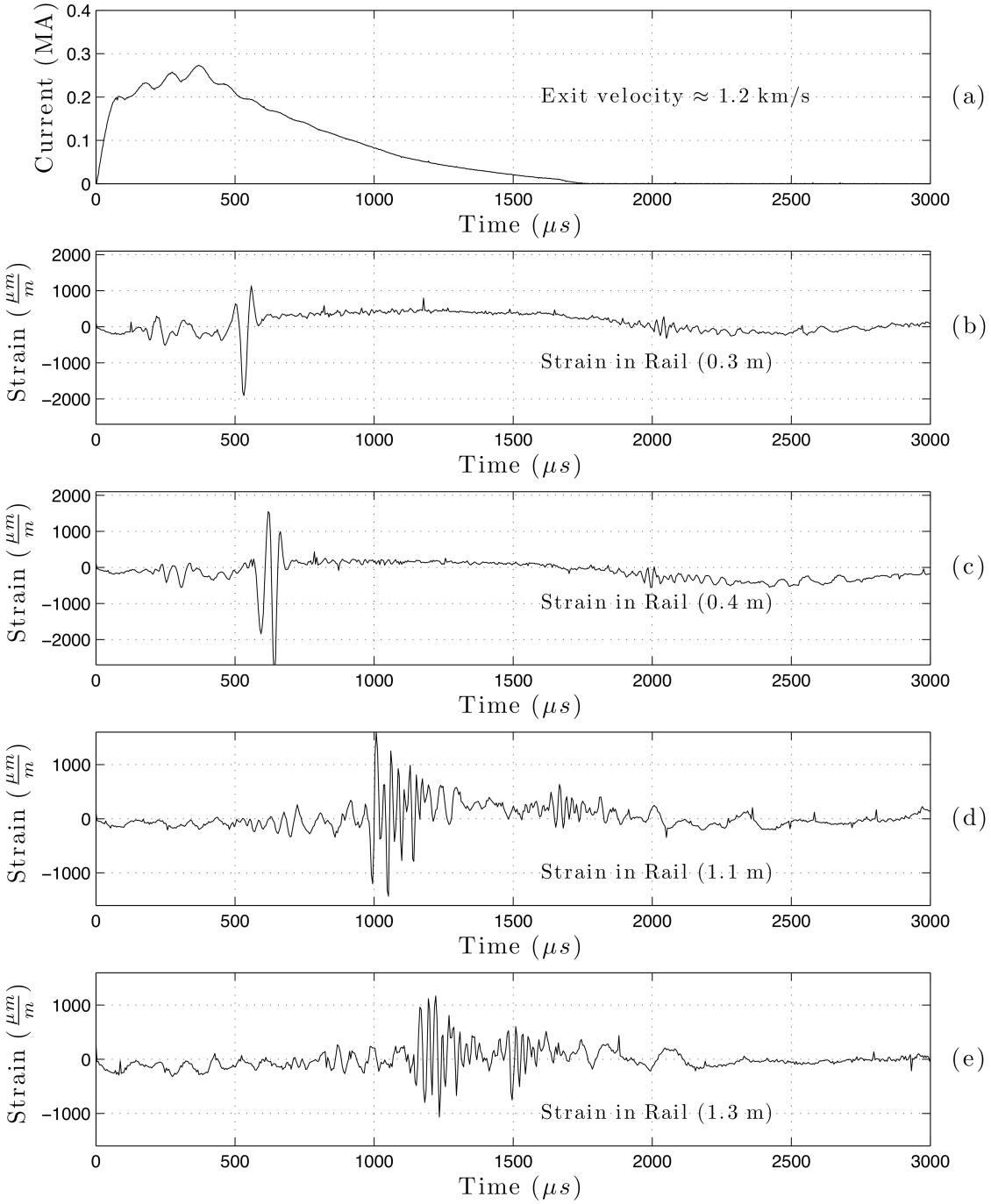


Figure 4.5: 1200 m/s launch velocity single rail strain test. (a) Drive Current, (b) Strain at 0.3 m, (c) Strain at 0.4 m, (d) Strain at 1.1 m, (e) Strain at 1.3 m

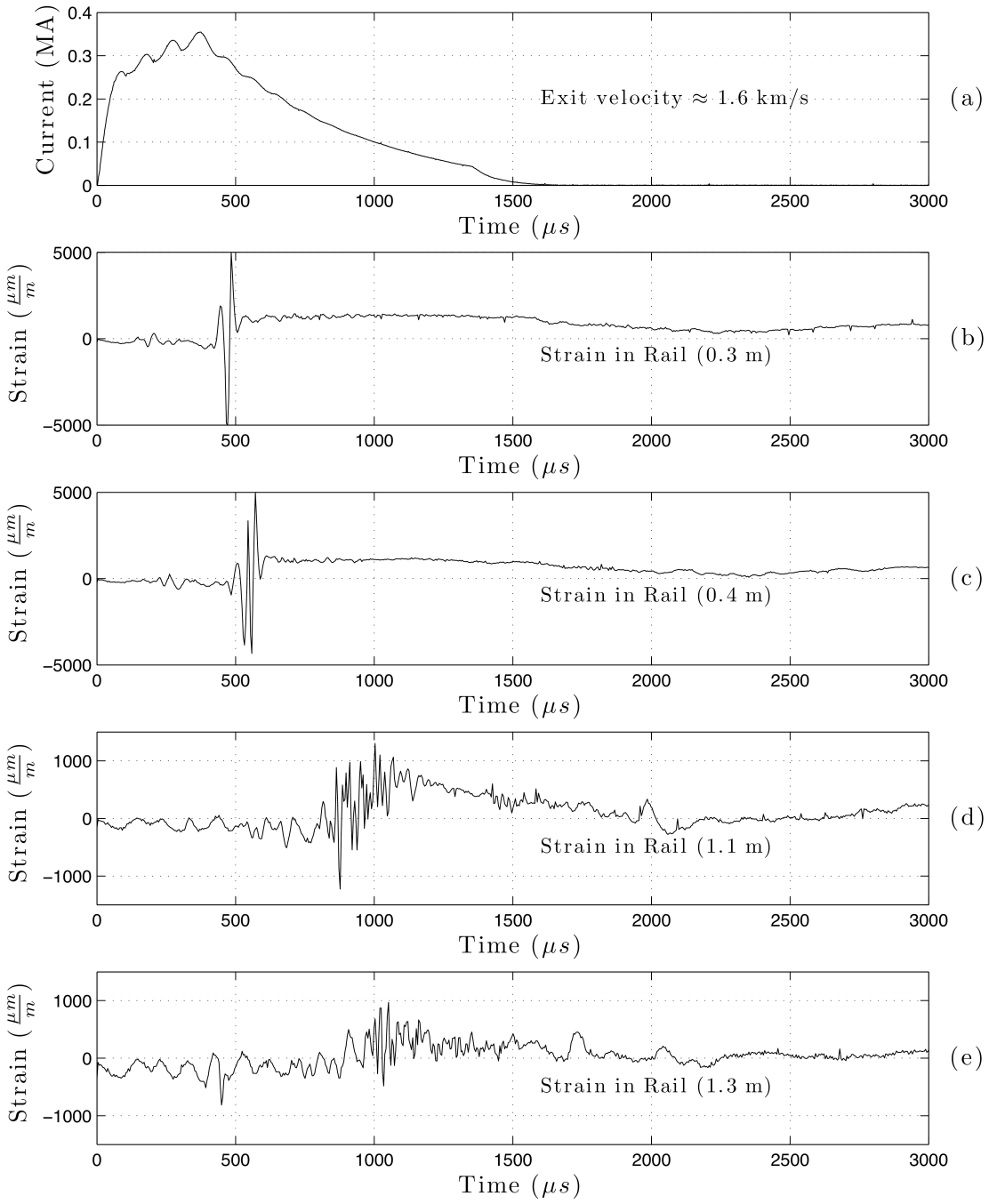


Figure 4.6: 1600 m/s launch velocity single rail strain test. (a) Drive Current, (b) Strain at 0.3 m, (c) Strain at 0.4 m, (d) Strain at 1.1 m, (e) Strain at 1.3 m.

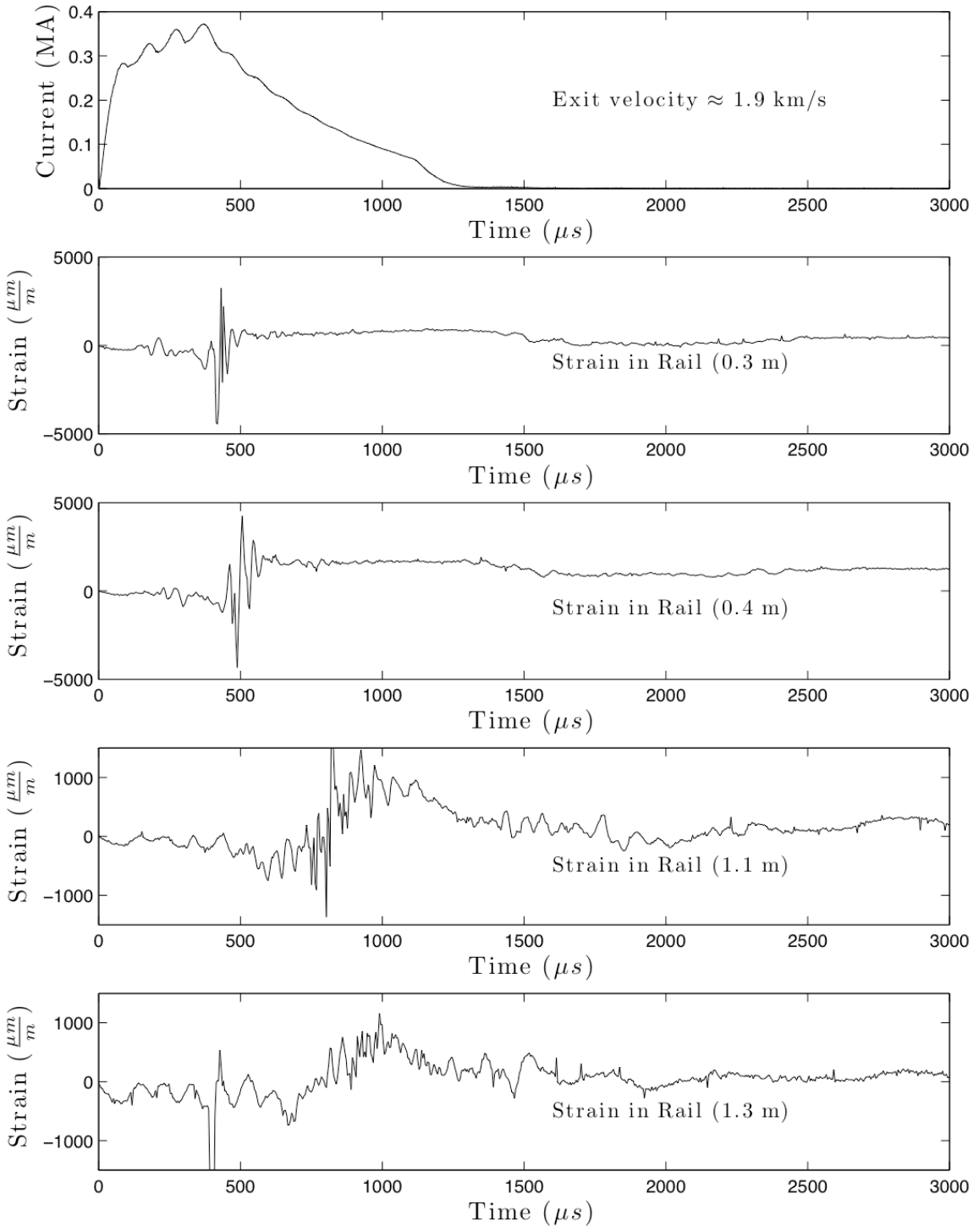


Figure 4.7: 1900 m/s launch velocity single rail strain test. (a) Drive Current, (b) Strain at 0.3 m, (c) Strain at 0.4 m, (d) Strain at 1.1 m, (e) Strain at 1.3 m

A definite transition from no wave radiation to wave radiation is visible. This transition is indicative of passing through a critical velocity. This is seen in all of the launches in Figures 4.4-4.7. Interestingly enough, wave radiation is visible even in the 800m/s launch. This is well below the predicted value for a linear foundation and shows that either the nonlinearity in the load deflection curve of the foundation (see Section 3.7) and/or the inertia effects of the foundation (see Section 2.4.1) cause wave radiation to occur below the critical velocity predicted by the simple linear theory (Section 2.4). At this point it is difficult to say which of these effects is the most prominent.

Another phenomenon that is seen in these plots is wave reflection. This is most visible in Figure 4.5 where the first wave reflection is seen at approximately 1500 $\mu s$ on the fourth sensor. The wave can then be followed all the way back to the first sensor where it has decreased in amplitude. In this particular shot, the armature left the end of the launcher at approximately the same time that this wave reflection is seen($\approx$ 1600 $\mu s$). This means that the wave had to have reflected from the end of the beam before the armature left the launcher. The end result of this is that the armature had to have passed over this wave. This sort of interaction is also seen in the simulations of Chapter 3.

One phenomena visible in these tests that is not in the simulations is the reduction of strain along the length of the rails. For example, in Figure 4.6 the maximum strain on the first and second gages is nearly 5000 $\mu m/m$, while on the third and fourth gages it has dropped by nearly a factor of five. The simulations in Chapter 3 predict that this strain should increase farther down the rails. This discrepancy can be explained by the fact that the simulation does not take into account the wear of the armature during launch. For these high velocity launches, the contact surface of the armature is melted during the launch. This decreases the

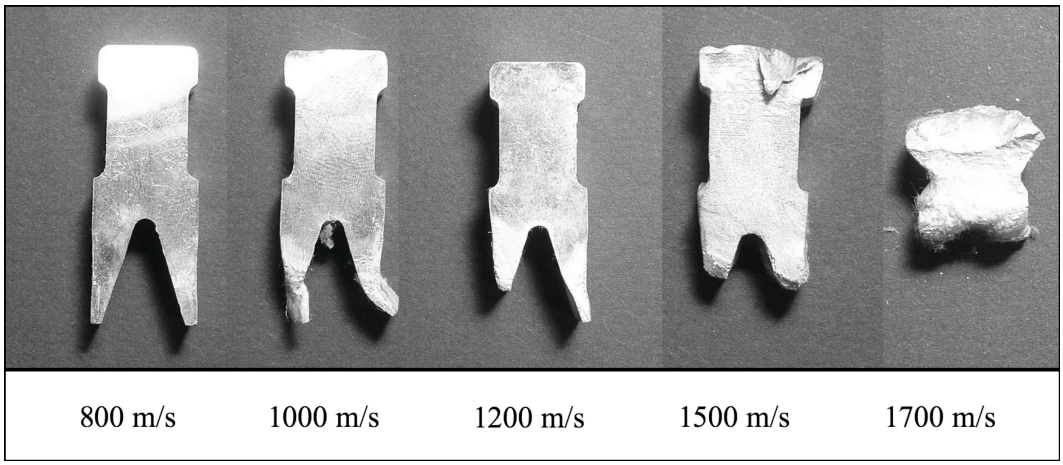


Figure 4.8: Armatures Fired at Various Velocities

interference fit and would cause a decrease in the strain seen at the muzzle end of the launcher. A picture of some armatures fired on the Georgia Tech. launcher at velocities similar to those in these launches is shown in Figure 4.8. These are not the actual armatures fired on the shots in Figures 4.4-4.7, but they do illustrate the typical wear patterns seen during launch. In low velocity shots, the surfaces of the armature melt and wear down and the trailing arms melt off in very high velocity shots. The damage to the front of the armatures in Figure 4.8 is due to them hitting the end of the catch chamber.

Another interesting plot to make is the maxima of the strain signals as a function of the instantaneous velocity for each of the sensors. The instantaneous velocity can be calculated by integrating the square of the current and then using a least squares program to scale it to the information from the b-dots. This instantaneous velocity can then be interpolated at the position of the armature. This plot is shown in Figure 4.9. Both the maximum tensile and compressive strains are shown for each of the sensors for all of the shots in Figures 4.4-4.7. In this plot it is seen that the strain increases dramatically after approximately 1 km/s. This is expected when the armature passes into a wave radiation state. This transition

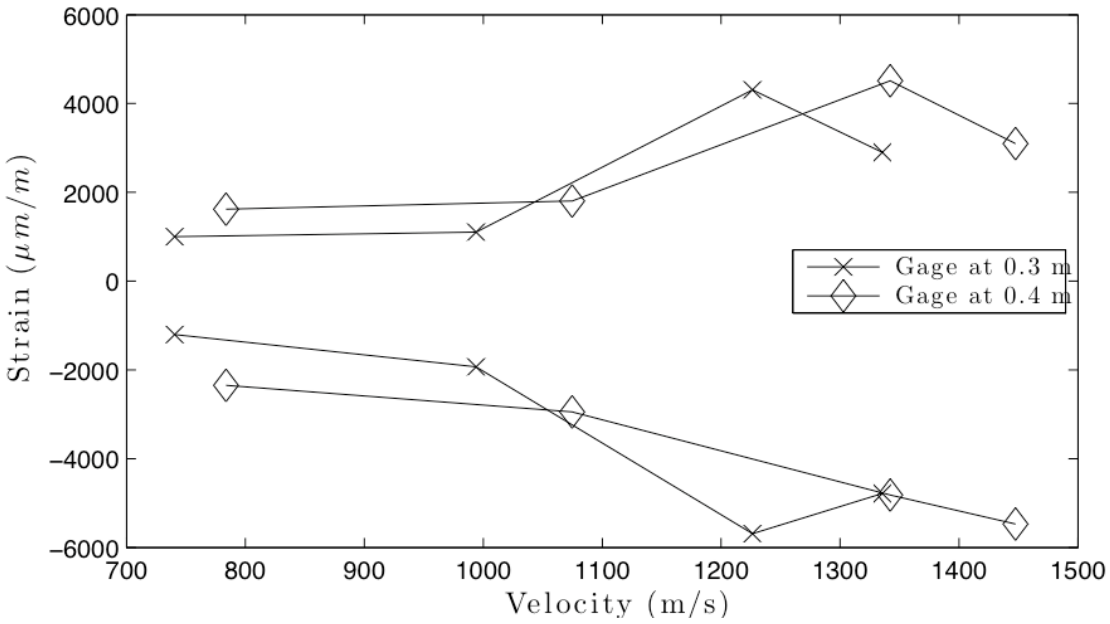


(a) Strain Maxima Near Breech

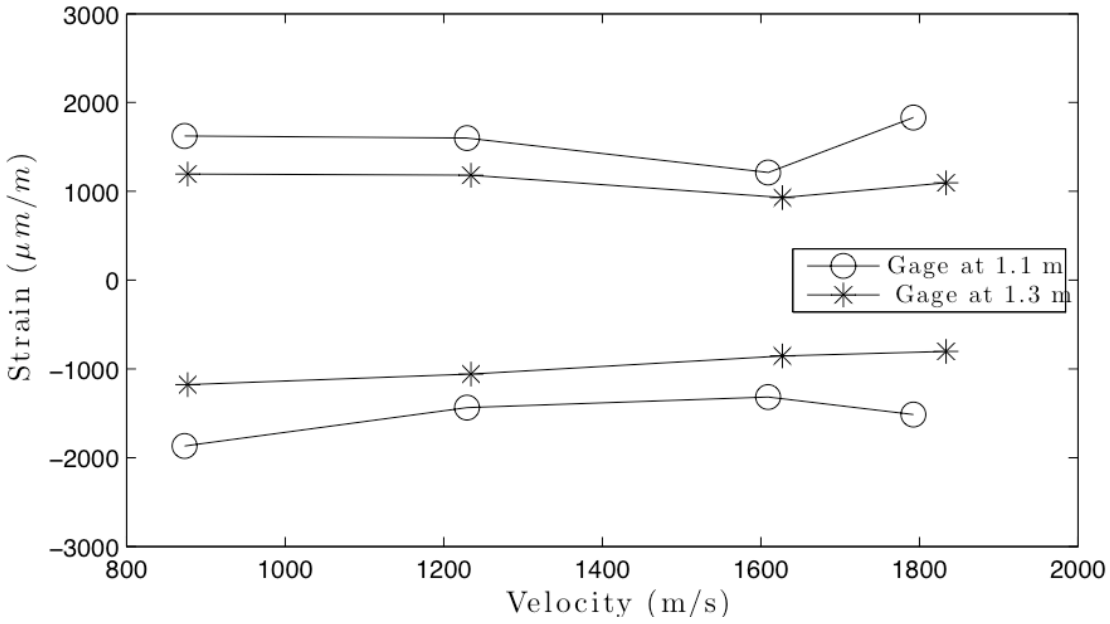


(b) Strain Maxima Near Muzzle

Figure 4.9: Strain maxima as a function of instantaneous armature velocity in sensors near muzzle and breech.

can also be seen in the actual strain data in Figures 4.4-4.7. It is interesting that the gages at the muzzle end of the launcher are essentially flat until approximately 1600 $m/s$, where a small increase is visible. This increase in the strain in this shot could be due to the fact that the armature is approaching the shear speed of the beam. This statement is only a conjecture of course, but this launch reached the highest velocity that has been attained on the Georgia Institute of Technology launcher and so no data is available beyond this point. This is definitely a question for future research.

### 4.2.2 'Jerk Effect' Wave Analysis

For the plots shown in Figures 4.4-4.7, there is consistently a small wave that is traveling in front of the armature. This wave is believed to be generated when the armature breaks free from the static friction between the armature and guide rails. When this occurs, there is a discontinuity in the acceleration of the armature. This wave radiation can be called 'jerk effect' wave radiation. This effect has been seen computationally (see Section 3.5) and this section will look at it a little more closely for the experimental data from the launches in the previous section.

Table 4.1: Jerk Effect Analysis Parameters

| Shot Velocity | Wave Offset Time | Wave Velocity | Armature Release Current |
|---|---|---|---|
| $900m/s$ | $58\,\mu s$ | $1720m/s$ | $0.095MA$ |
| $1200m/s$ | $58\,\mu s$ | $1720m/s$ | $0.180MA$ |
| $1600m/s$ | $57\,\mu s$ | $1750m/s$ | $0.153MA$ |
| $1900m/s$ | $60\,\mu s$ | $1670m/s$ | $0.138MA$ |

This analysis will focus on first two gages from the low velocity shot. Figure 4.10 shows zoomed in versions of these waves. If the second signal is offset then these two signals can be plotted on top of each other. This is also shown in Figure 4.10. The offset necessary to make this work for this particular launch

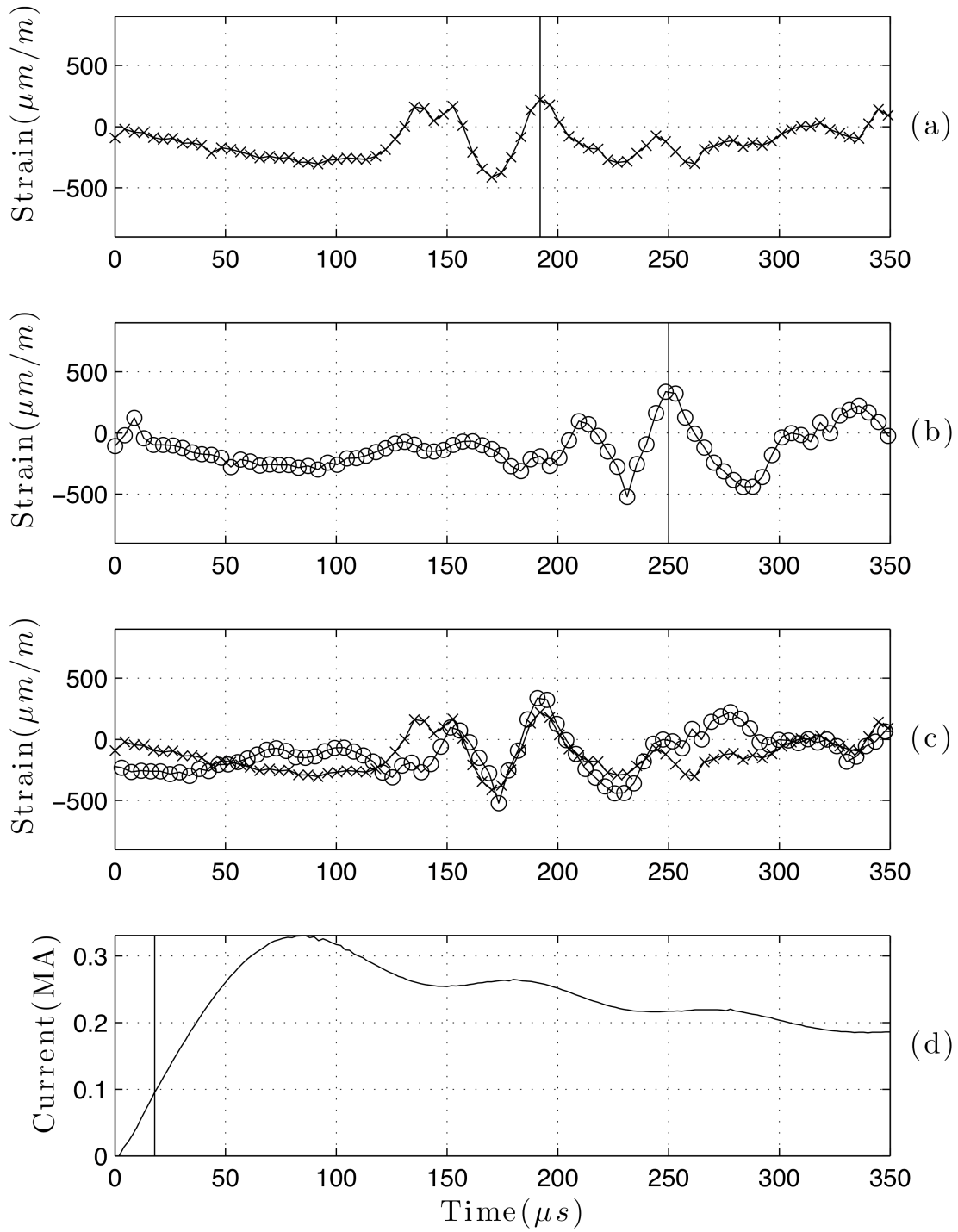


Figure 4.10: Jerk Effect Analysis Plot for $900\,m/s$ shot. (a) Strain at 0.3 m, (b) Strain at 0.4 m, (c) Strains offset in time so that the peaks overlap, (d) Drive current during shot

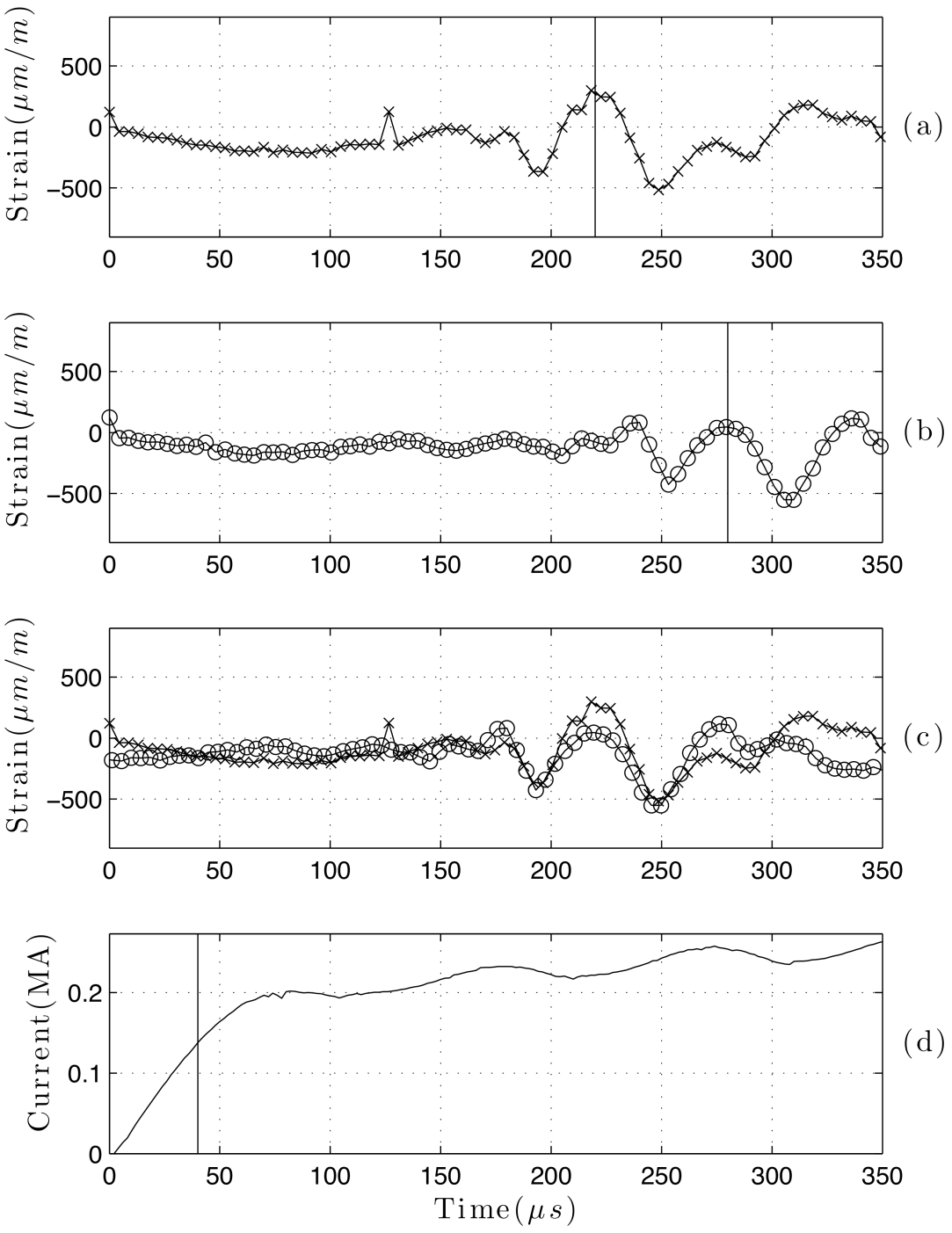


Figure 4.11: Jerk Effect Analysis Plot for $1200\,m/s$ shot. (a) Strain at 0.3 m, (b) Strain at 0.4 m, (c) Strains offset in time so that the peaks overlap, (d) Drive current during shot

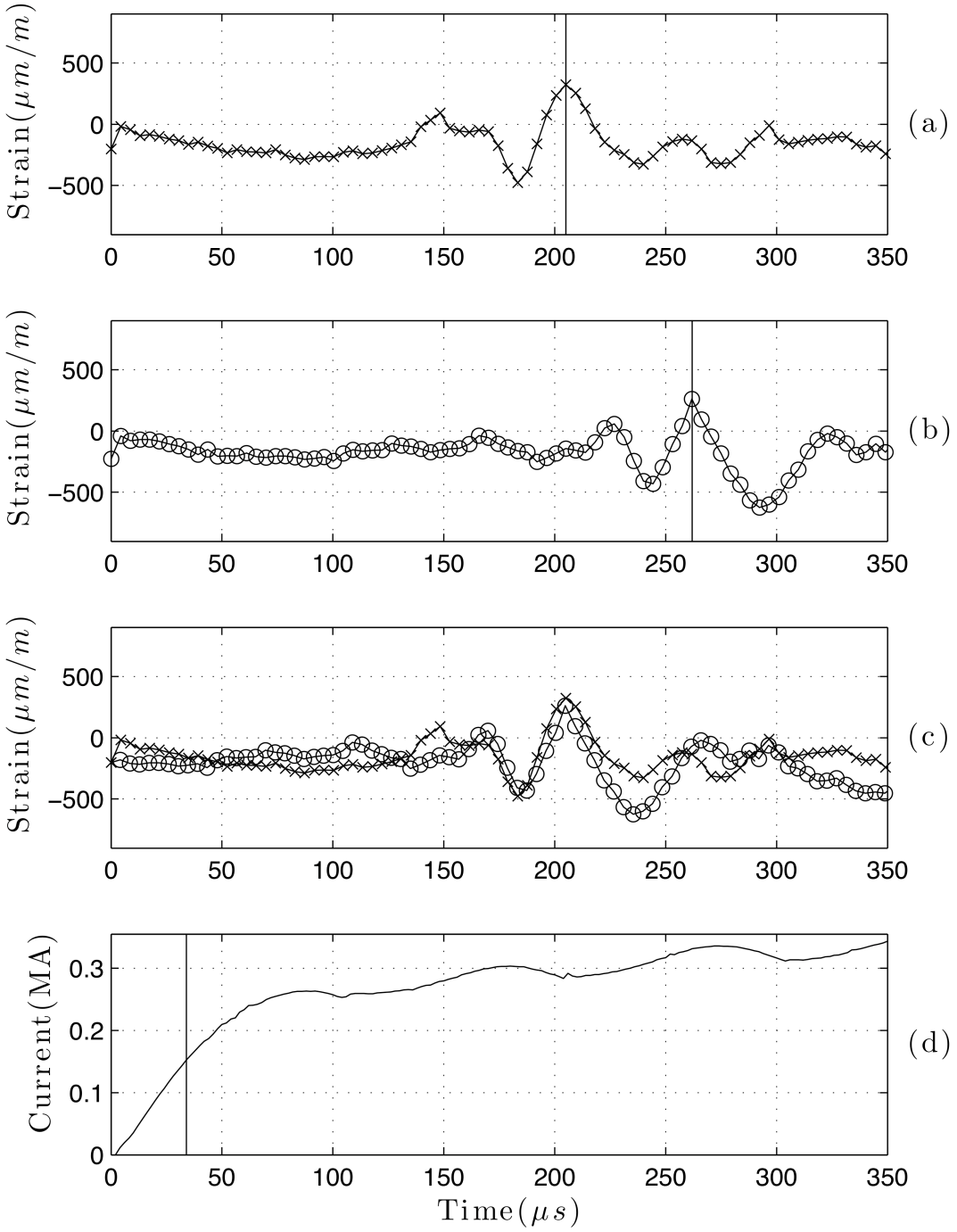


Figure 4.12: Jerk Effect Analysis Plot for 1600 $m/s$ shot. (a) Strain at 0.3 m, (b) Strain at 0.4 m, (c) Strains offset in time so that the peaks overlap, (d) Drive current during shot

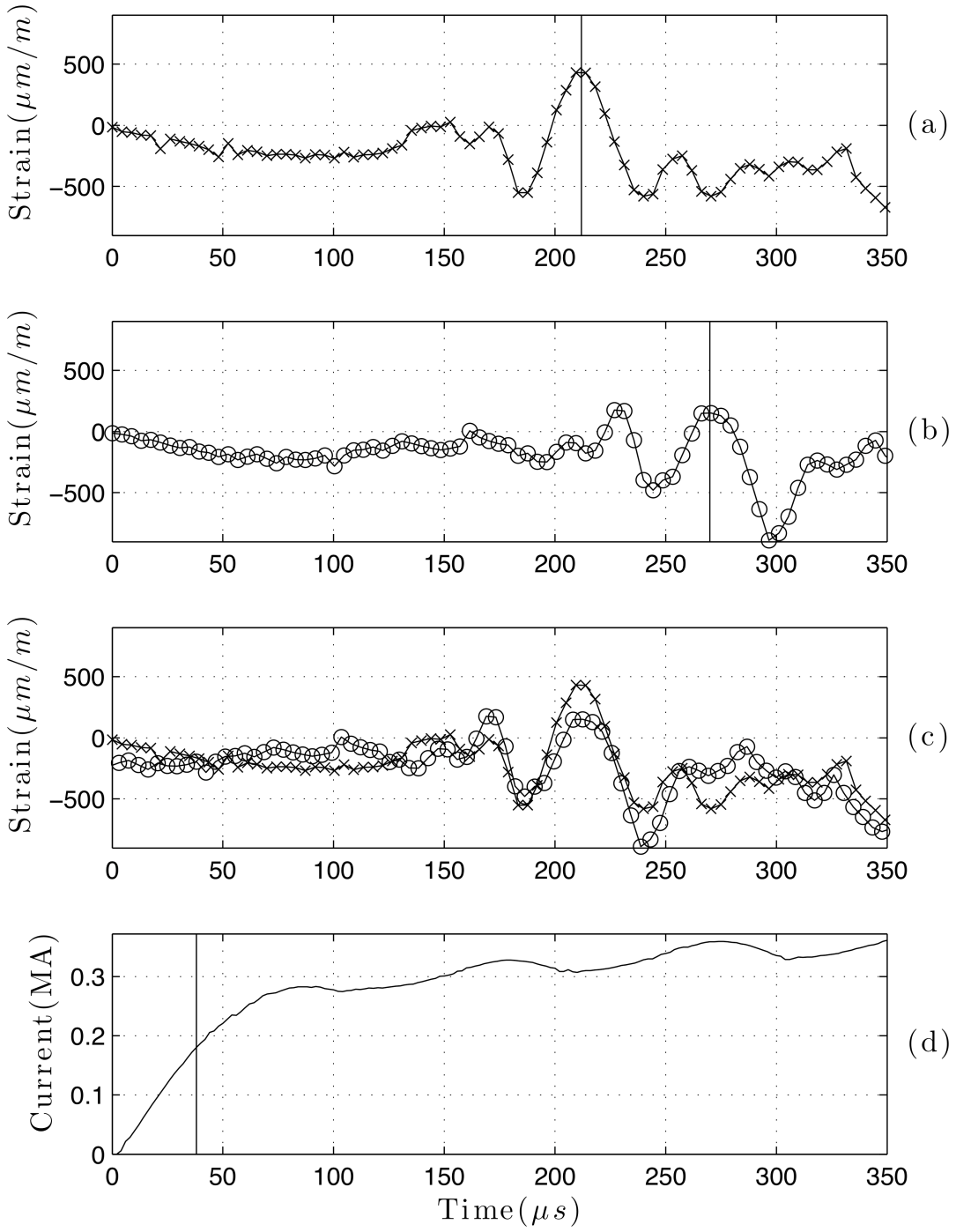


Figure 4.13: Jerk Effect Analysis Plot for 1900 $m/s$ shot. (a) Strain at 0.3 m, (b) Strain at 0.4 m, (c) Strains offset in time so that the peaks overlap, (d) Drive current during shot

is $58\,\mu s$. Since the gages were offset from one another by $0.1\,m$ then this wave is traveling at approximately $1720\,m/s$. If this velocity is propagated back to the start position of the armature then one finds that the wave was radiated $18\,\mu s$ after the capacitor banks were fired. This point is indicated in the fourth plot of Figure 4.10 with a vertical line. This indicates that the armature broke free at approximately $0.095\,MA$ of current. Since the force on the armature can be related to the current, through Equation 1.7, this is essentially a measure of the frictional force between the armature and the rails. The corresponding values from this analysis for all four shots are shown in Table 4.1.

This analysis could be used as a comparative test for different armature designs and material parameters. For example, two similarly shaped armatures could be coated with different materials to see how coatings effect the initial contact friction. Tests of this sort have not been conducted yet, but with this jerk effect measurement a quantitative comparison could be made. It should be noted that these shots were fired on the same set of rails and that each shot lays down a layer of material on the rails so if frictional tests are conducted then new rails should be used. Of course all of this is heavily dependent on whether the jerk effect waves are visible. In the tests in the next section, they are not. These tests were performed after the launcher containment was modified. Between these two test series, the laminates of the launcher containment were found to slip apart. The containment was fixed, and a large aluminum plate was added to the top. With the addition of this plate the jerk effect waves are no longer visible. The exact mechanism that caused this is unknown, but is probably because of the extra bending rigidity that the aluminum plate offers over the laminated structure. This would be another interesting phenomenon to study in future tests.

### 4.2.3 Computational Comparison

The data in Figure 4.5 shows some of the same phenomena seen in Chapter 3 such as wave reflection and 'jerk effect' waves (see Sections 3.4 and 3.5). It is for this reason that this launch was simulated for a comparison. The results of this comparison will be shown in this section. The launch simulated in Section 3.7 was actually based on the experimental data from the launch in Figure 4.5. The final results of this simulation are plotted in Figure 4.14. The computational results have been offset just so that the results can be more easily compared. This simulation illustrates both the strengths and weaknesses of this simulation technique.

First of all, the signals do not correspond exactly in time because of the lack of experimental information about the armature position during launch. The strain at the breech end of the launcher is similar in shape between the two. The magnitude is off because the armature simulated in this launch is different than the armatures actually used in the launcher (compare Figures 4.8 and 3.16). The armature appears to radiate waves before the simulation. This is reflected in the width of the wave group at the muzzle end and the wave generation seen in the second sensor (Figure 4.14(b)). The experimental data shows more wave peaks than the simulated data. This early wave radiation could be caused by extra slack in the foundation or inertial effects from the mass of the foundation. The simplified model being explored here is capable of exploring the extra slack, but the inertial effects would have to be taken into account using mass elements attached to the foundation springs.

Another difference is that the strain in the simulation is higher at the muzzle end of the launch. This discrepancy is primarily because the simulation does not model the wear of the armature during launch. To get a better representation of the magnitude of the strain, the wear of the armature must be modeled in a future

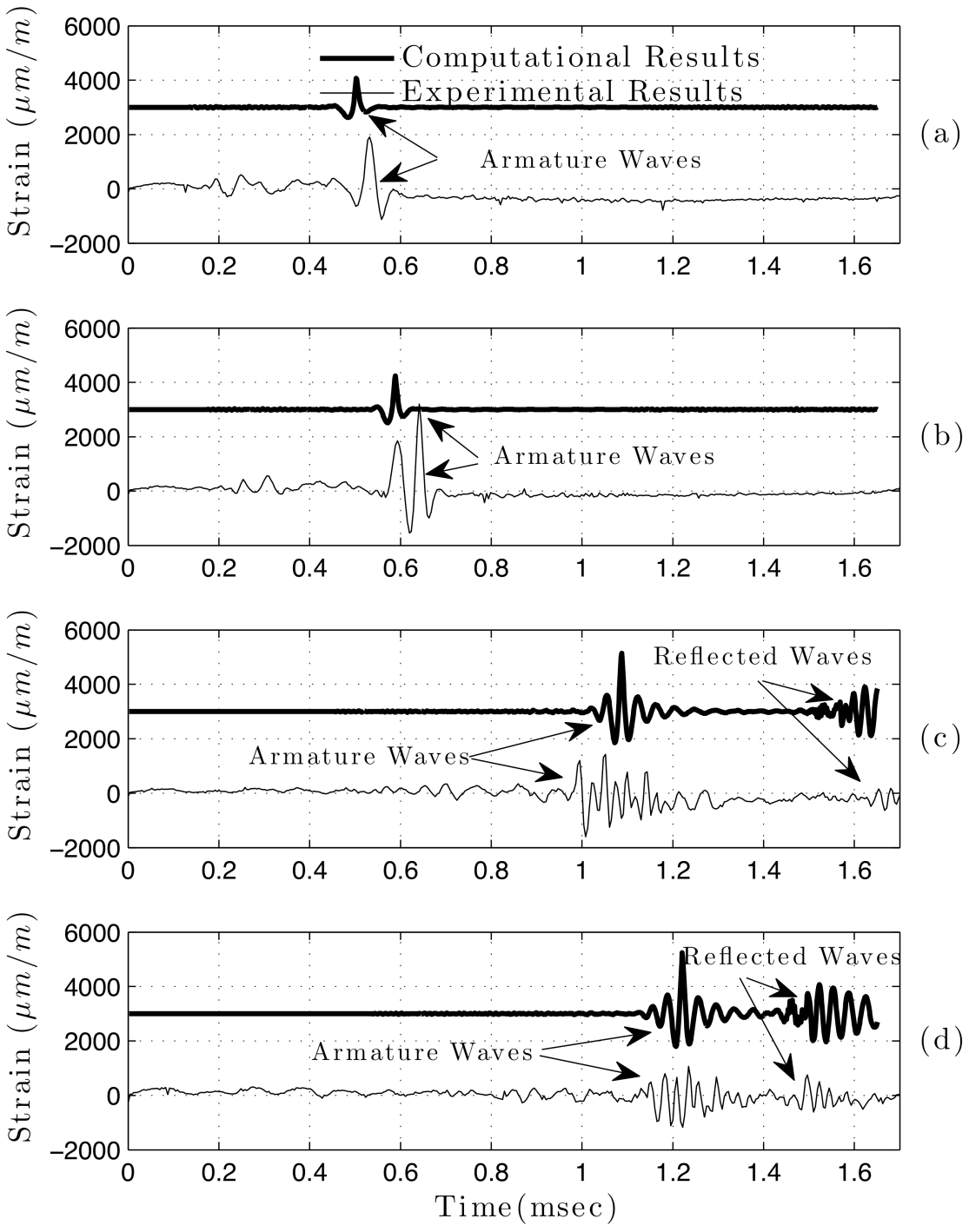


Figure 4.14: Comparison of Simulated System and Experimental Measurements. (a) Strain at 0.3 m, (b) Strain at 0.4 m, (c) Strain at 1.1 m, (d) Strain at 1.3 m

version of this simulation.

Finally, wave reflection is seen in both the simulation and experiment. This reflected signal occurs in this shot because the armature was traveling just fast enough to radiate waves, but not fast enough to pass over them. The magnitude and temporal width of these reflected waves are similar in the experiment and simulation (See Figures 4.14(c) and (d))

### 4.2.4 Two-Rail Experiments

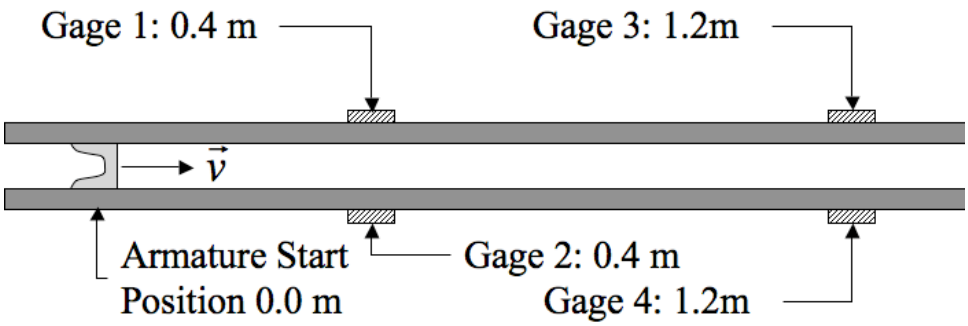


Figure 4.15: Gage Positions for Two Rail Experiments

The next set of tests on the Georgia Tech. launcher consisted of instrumenting both of the rails during the launch. This was done according to the diagram in Figure 4.15. This time the launcher was fired at five different velocities and the results are shown in Figures 4.16-4.20. This data shows some interesting characteristics. First of all, the signals from the breech sensors are roughly equivalent for each launch (in most cases), while the signals from the muzzle sensors are very different. The muzzle data shows a bias towards more strain in the top rail. This indicates that the armature has worn down to a loose fit between the rails and has probably lost stability. The reason for the bias towards the top is unknown, but

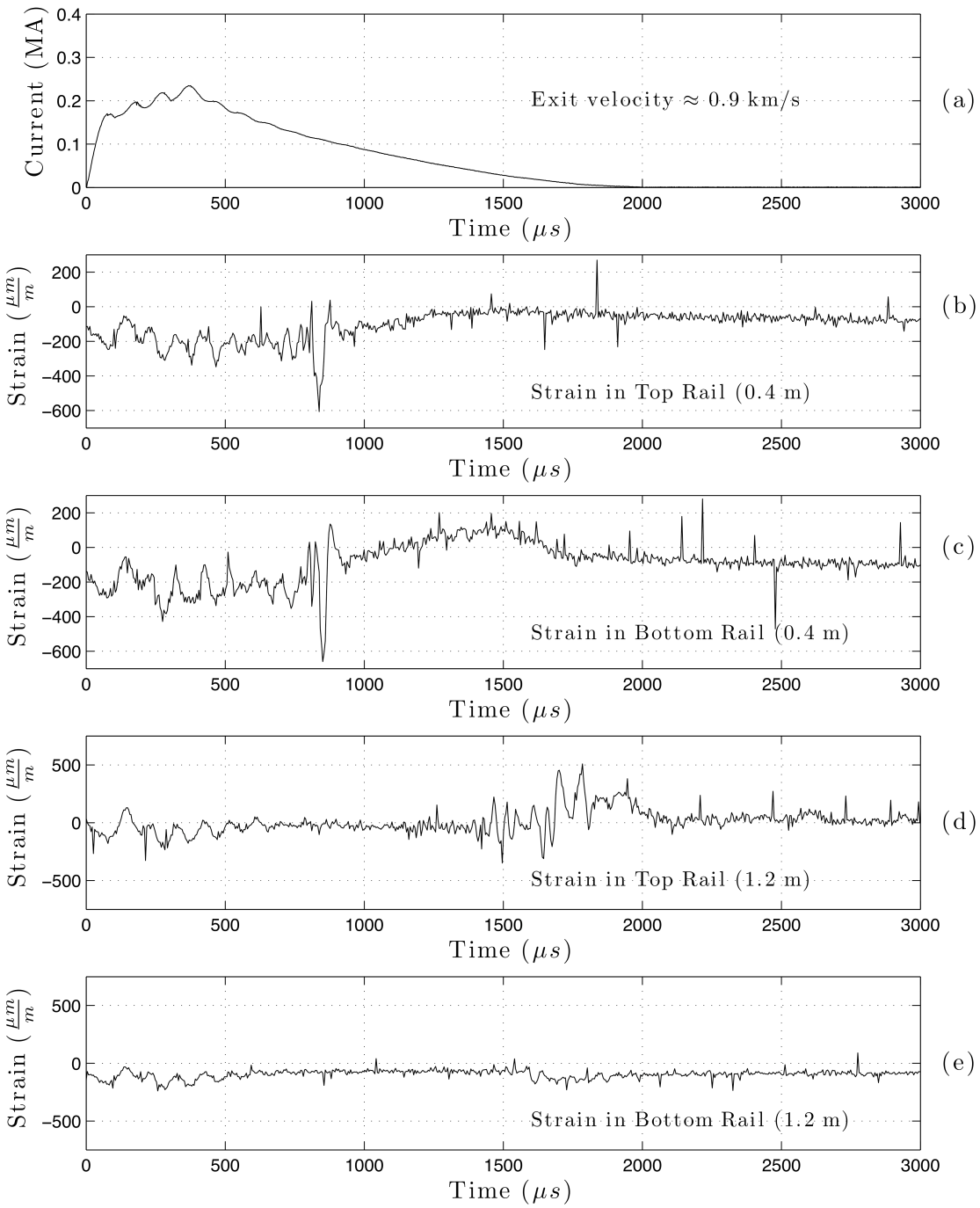


Figure 4.16: 900 m/s launch velocity two rail strain test. (a) Drive current, (b) Strain at 0.4 m in top rail, (c) Strain at 0.4 m in bottom rail, (d) Strain at 1.2 m in top rail, (e) Strain at 1.2 m in bottom rail

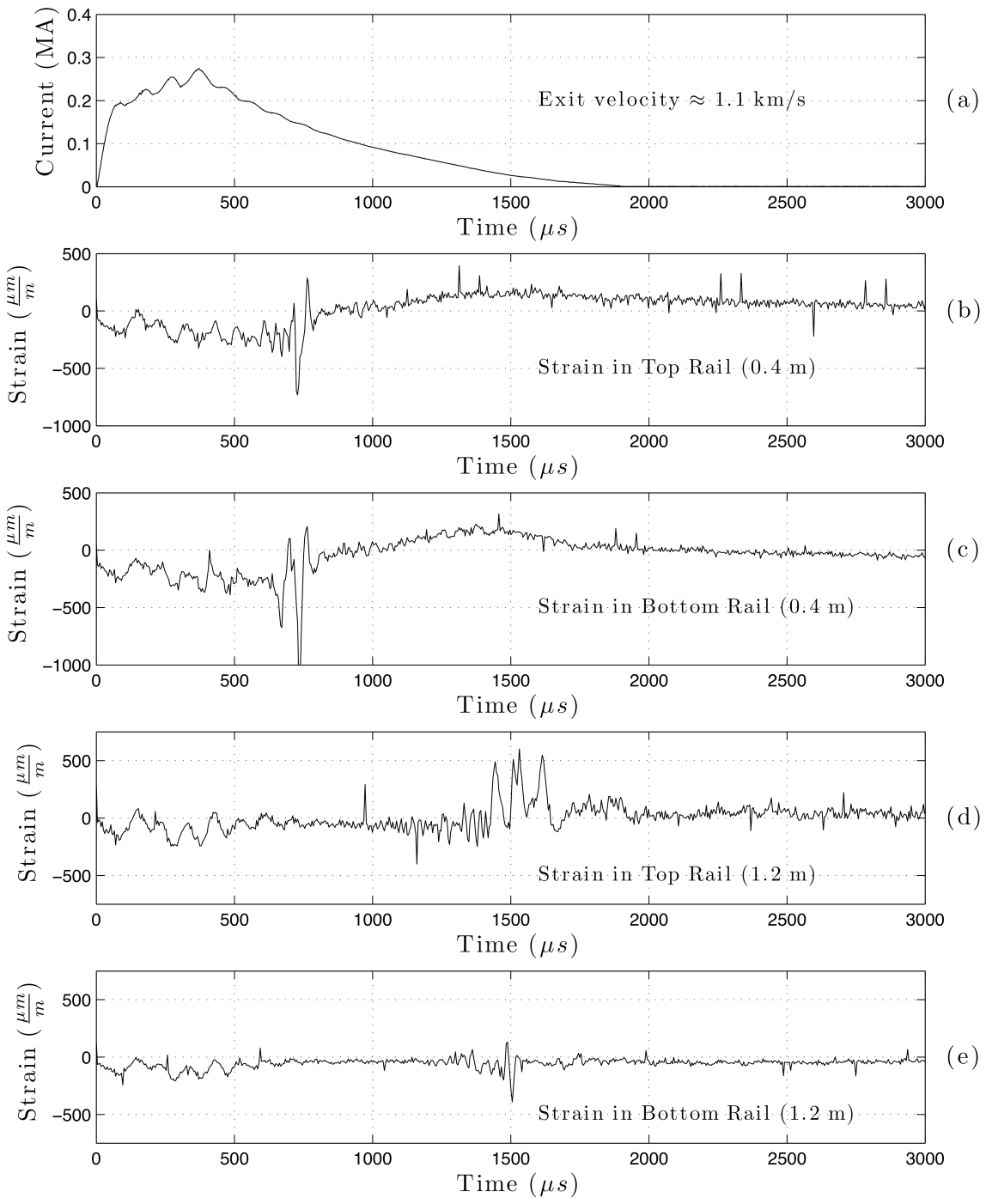


Figure 4.17: 1100 m/s launch velocity two rail strain test. (a) Drive current, (b) Strain at 0.4 m in top rail, (c) Strain at 0.4 m in bottom rail, (d) Strain at 1.2 m in top rail, (e) Strain at 1.2 m in bottom rail

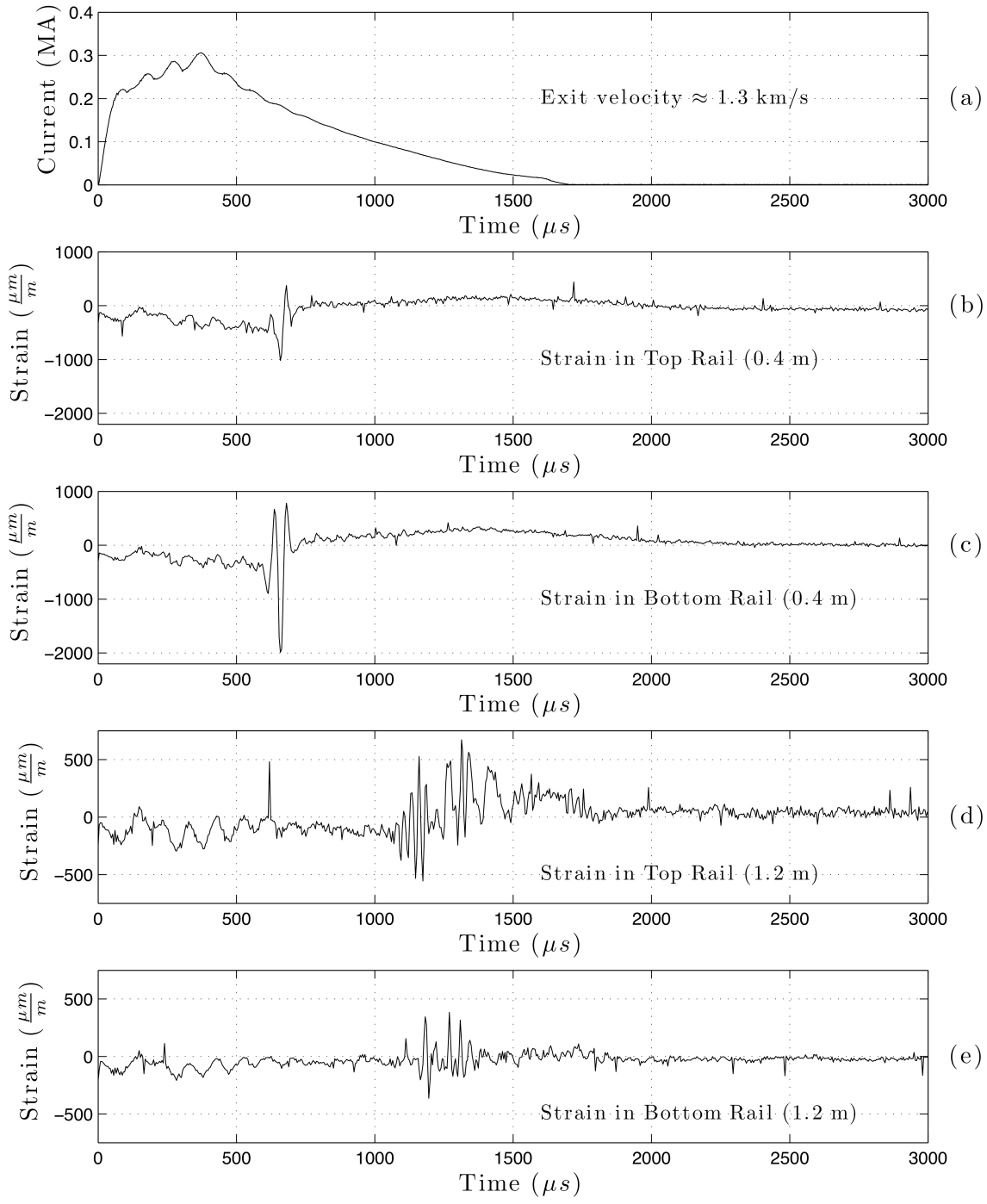


Figure 4.18: 1300 m/s launch velocity two rail strain test. (a) Drive current, (b) Strain at 0.4 m in top rail, (c) Strain at 0.4 m in bottom rail, (d) Strain at 1.2 m in top rail, (e) Strain at 1.2 m in bottom rail

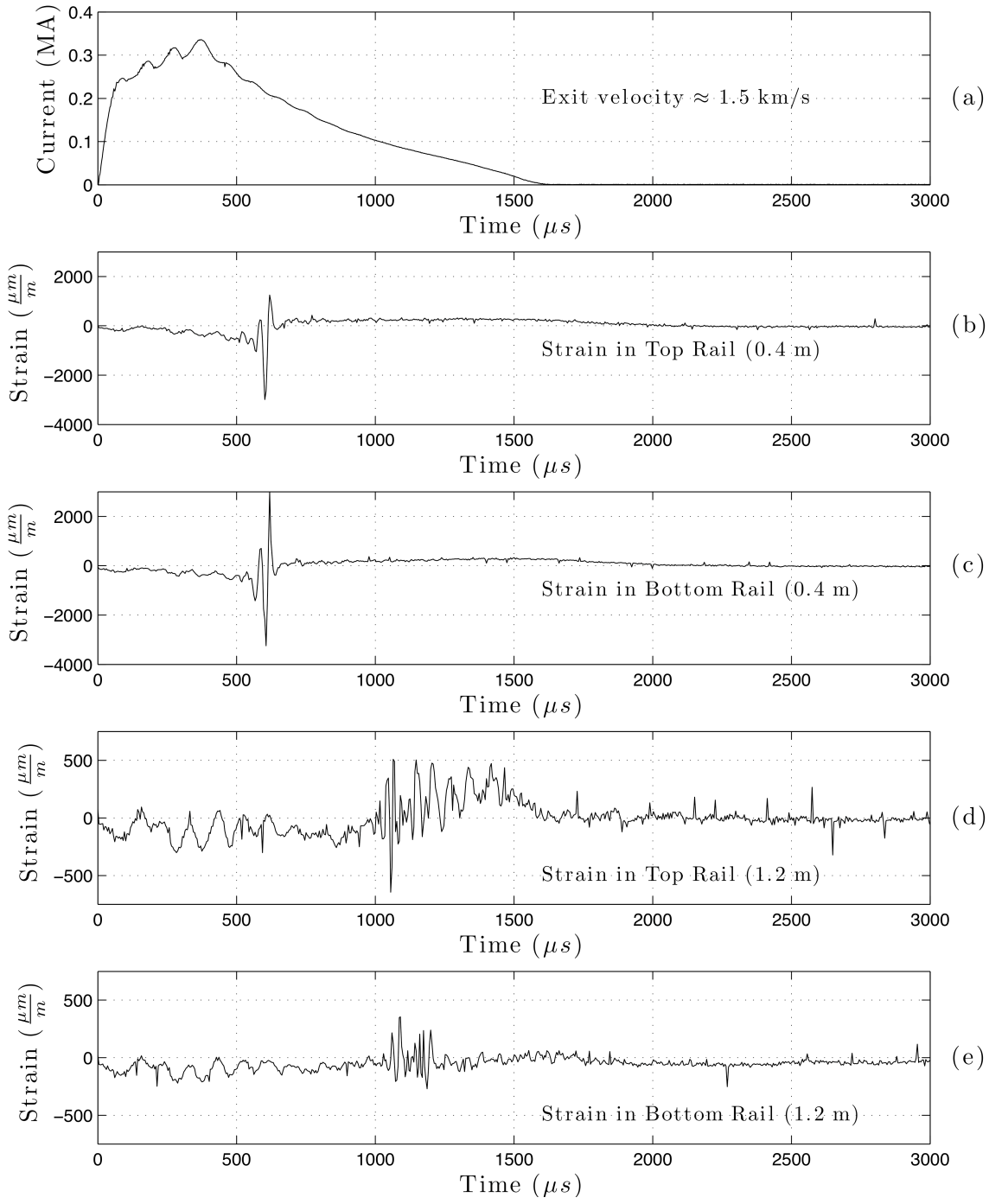


Figure 4.19: 1500 m/s launch velocity two rail strain test. (a) Drive current, (b) Strain at 0.4 m in top rail, (c) Strain at 0.4 m in bottom rail, (d) Strain at 1.2 m in top rail, (e) Strain at 1.2 m in bottom rail

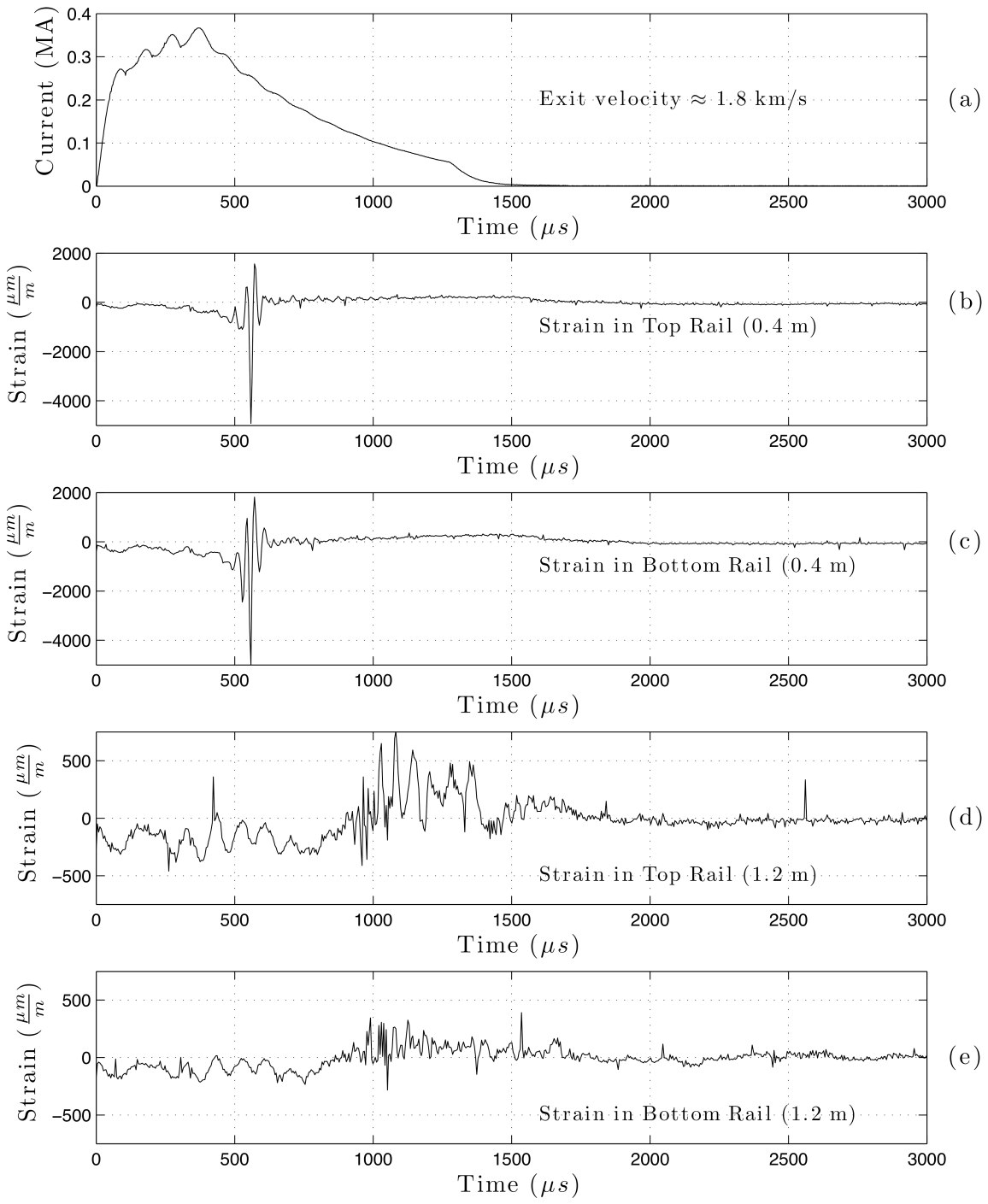


Figure 4.20: 1800 m/s launch velocity two rail strain test. (a) Drive current, (b) Strain at 0.4 m in top rail, (c) Strain at 0.4 m in bottom rail, (d) Strain at 1.2 m in top rail, (e) Strain at 1.2 m in bottom rail

it could be that the armature has moved into a divergent state of stability (see Chapter 5).

The next observation can be made by comparing data from subsequent shots from the breech end sensors. For example, if one compares the strain in the breech sensors between Figures 4.18, 4.19 and 4.20 it is easy to see that the number of oscillations of the strain increases. In lower velocity shots, the strain looks essentially the same as it does in Figure 4.19 (in shape, not magnitude). What this shows is that as the armature velocity increases, the magnitude of the waves increases and the number of waves also increases. This is representative of a transition to a wave radiation state as seen in the simulations in Chapter 3.

Another way to demonstrate this transition is to plot the maximum strain in each rail as a function of the instantaneous velocity of the armature. This plot is shown in Figure 4.21. As in Section 4.2.1, the velocity in this plot is an approximate value for the instantaneous velocity as the armature passes the strain gage. The strain is seen to increase at about 800 m/s in this case. This data set also shows roughly flat strain at the muzzle end of the launcher. Again, this is most likely due to the wear of the armature.

It should also be noted that an attempt was made to compare data between the tests in this section, Section 4.2.1 and other tests that were performed (See Appendix E for the data from these tests). It was found that large discrepancies exist between tests on different builds of the launcher. In other words, if tests are performed and then the launcher is taken apart, put back together then the strain maxima will be different. This indicates that there is some repeatability issues associated with the assembly of the launcher. The source of this uncertainty is unknown, but it does need to be studied because it will probably affect non-mechanical measurements as well.

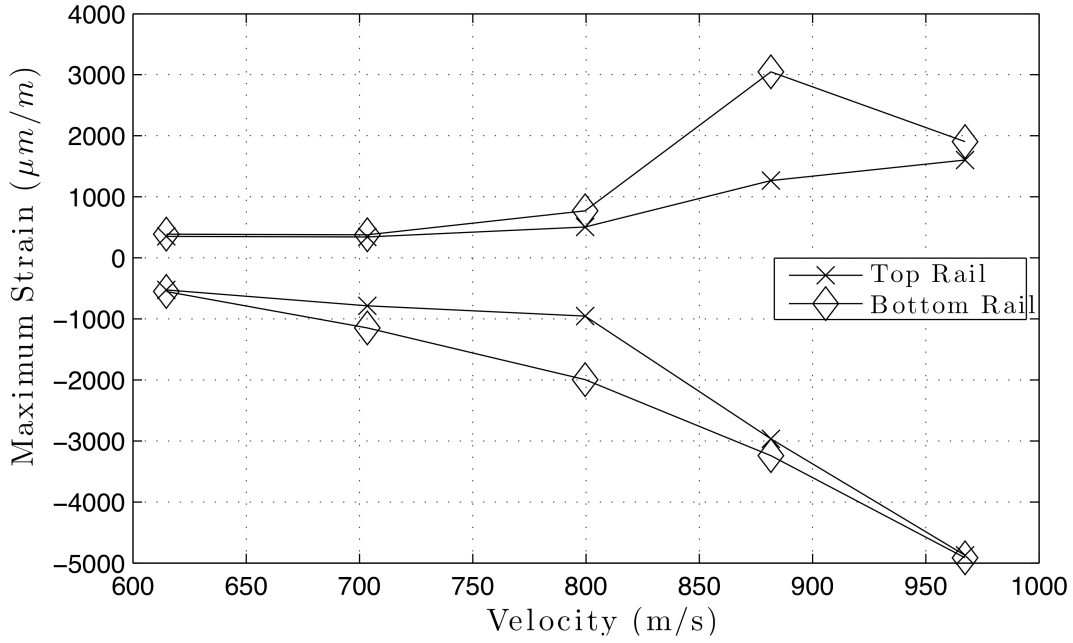


(a) Strain Near Breech

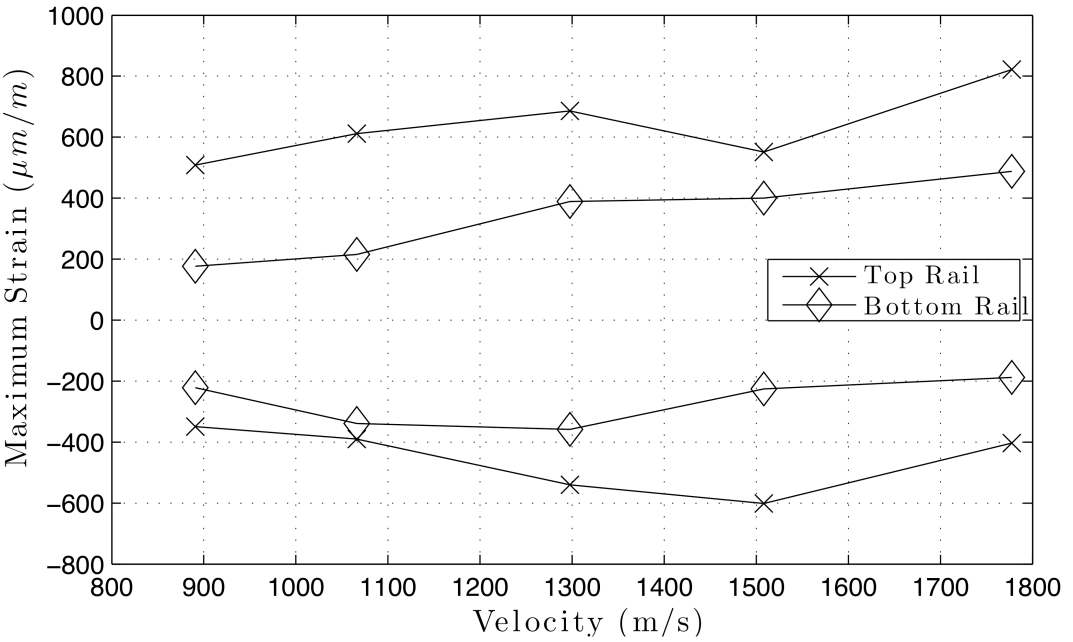


(b) Strain Near Muzzle

Figure 4.21: Strain maxima as a function of instantaneous armature velocity near muzzle and breech.

# Chapter 5
# Armature Stability

The stability of the armature in the bore of the launcher is an important phenomena to understand for all of the possible applications of an electromagnetic launcher. In the design of any launching system it is vital to understand the angular motion of the projectile as it is being accelerated and after it exits the launcher. In classical weapons design, in-bore angular motion of the projectile relative to the axis of the bore is referred to as balloting [17]. Balloting can cause damage and wear to the bore and the payload of the projectile. As the projectile exits the bore it will rotate, this is referred to as tip-off. These phenomena directly effect the accuracy of the launcher. In the case of a Naval rail launcher with a range of 300 km, even a small tip-off could be problematic. It should be noted that the present vision of a Naval launcher includes guided projectiles, but any tip-off will directly effect the amount of payload mass that is dedicated to the guidance system, reducing the overall efficiency/effectiveness of the system.

Much of the literature associated with balloting is directed towards conventional weapons(e.g. see [80] and [88]). The issue of balloting in electromagnetic launchers specifically has been explored in the literature to some extent as well. Balloting has been looked at as a function of the stiffness of the armature and bore rider [17] and the straightness of the rails [14]. The work in this dissertation also looks at the effect of the stiffness of the armature and bore-rider, but explores the problem from the perspective of stability. In the previous chapters of this dissertation, the armature was constrained to follow the axis of the launcher during launch. This constraint prohibits balloting and tip-off effects. In the simulations in this chapter this constraint was removed so that the dynamics of the armature could be explored. Removing this constraint requires that both of the rails be sim-

ulated. The first finite element simulation in this section does this for a geometry similar to the Georgia Tech. launcher. Next, a mathematical model of a projectile accelerated down the bore of a launcher is considered. This model is explored from the perspective of the stability of the armature. It is found that the stability of the armature could be compromised if the armature and payload are not designed properly. The armature could go into an unstable state of divergence or flutter depending on the relative positions of the center of pressure and center of mass.

## 5.1 Two Rail Simulation

To explore the stability of the armature, a simulation of the Georgia Tech. launcher including both rails was developed. For the lateral dynamics of the armature to be visible, it is necessary for the armature to have more than just one degree of freedom. This means that the armature must be pushed by an external pressure instead of an applied displacement. This complication is considerably more difficult than it appears. The main problem is associated with the friction between the armature and the rails. This has to be included for the armature to be constrained in the simulation. Since no experimental friction models exist for a rail launcher, an approximate friction had to be used. For the simulations in this section, the friction was assumed to drop exponentially with the velocity of the armature. A plot of this friction coefficient is shown in Figure 5.1. The static friction was assumed to be approximately 0.25 and this dropped to one fifth of its original value at high velocities. Since no experimental model of friction exists for these systems, this friction model is essentially a guess.

The boundary conditions for this simulation are pictured in Figure 5.2. In this case, both rails were actually simulated and the foundation was assumed to be nonlinear as pictured in Figure 3.19 in Section 3.7. The armature was shaped

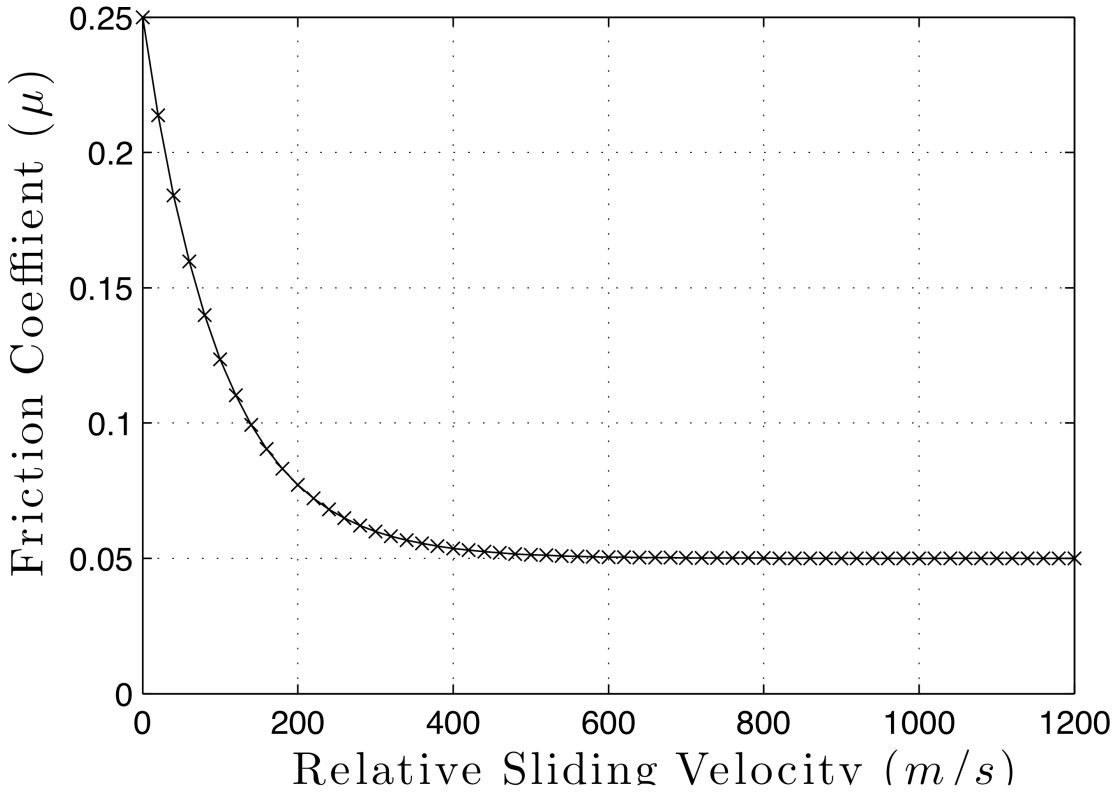


Figure 5.1: Assumed Friction Model

.

like the Georgia Tech. launcher armature and an offset in the center of mass was introduced. This offset was introduced by offsetting the middle region of the armature as shown in Figure 5.2. This offset was introduced to break the symmetry in order to test whether any instabilities might be present. The front of the armature in Figure 5.2 has what is referred to as a bore rider. In the simulation in this section this bore rider is assumed to be more narrow than the space between the rails by approximately $0.25\,mm$ on each side. In experiments, this space is filled by wrapping non-conductive tape around the end of the armature. It is possible for this tape to be pushed off of the tip of the armature during loading or launch and it will be ignored in this simulation to look at a worst case scenario for the stability of the armature. For this simulation, the applied pressure was scaled according

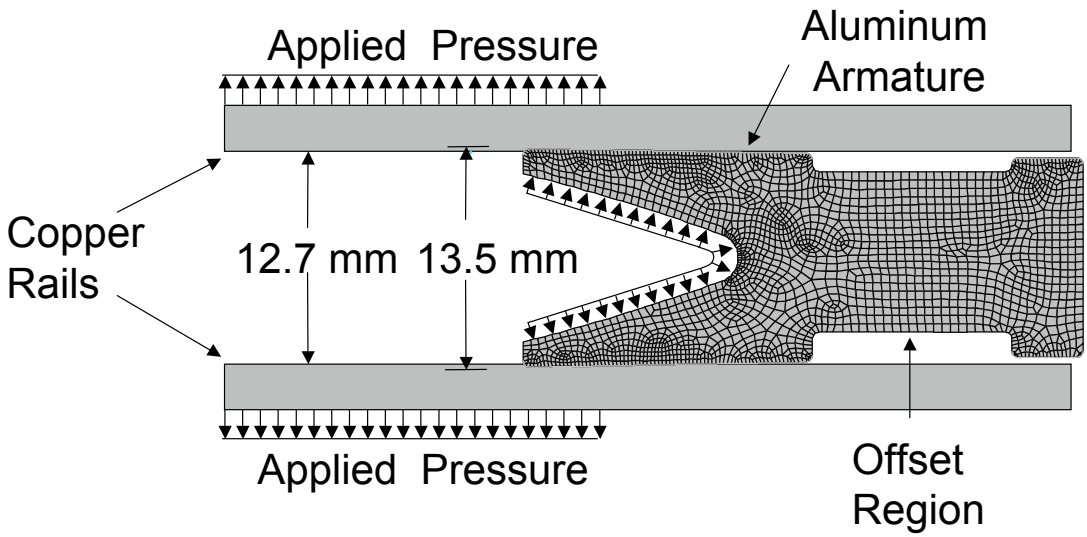


Figure 5.2: Boundary Conditions for Two Rail Simulations

.

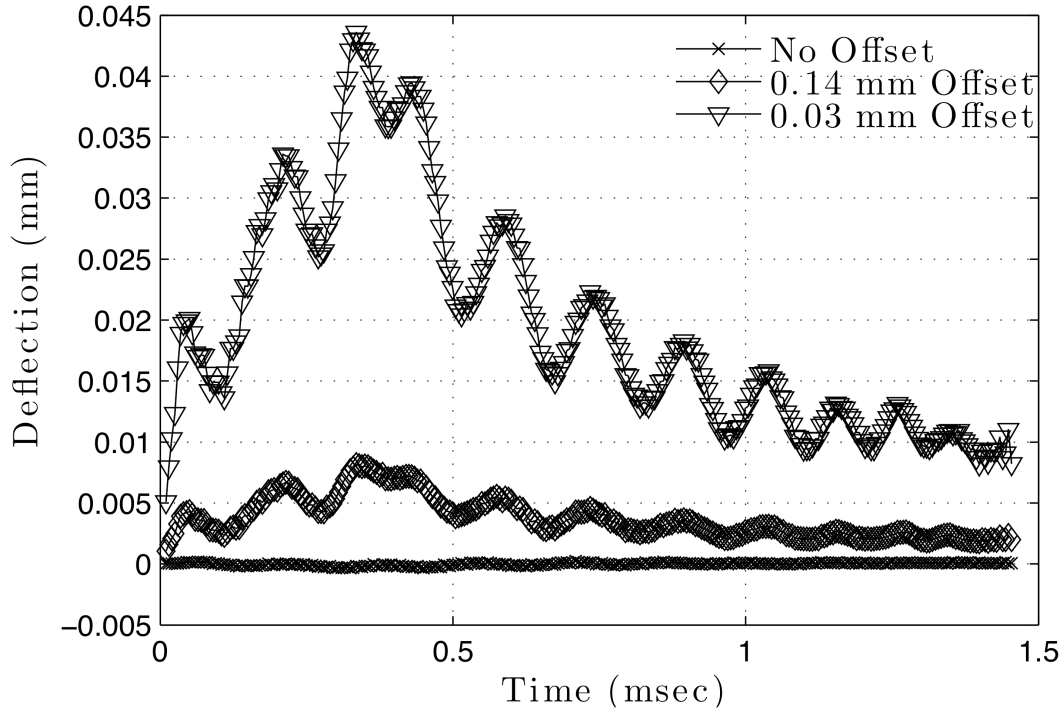


Figure 5.3: Off-Axis Tip Deflection of Armature

.

to the current in Figure 3.20. The pressure in the throat of the armature was multiplied by 50% to attain a higher launch velocity. In these simulations, this gave the armature a final velocity of approximately $1400\,m/s$.

This simulation was run for various offsets of the center of mass, and the results are shown in Figure 5.3. This plot shows the off-axis deflection of the tip of the armature as a function of time. As one can see, the front of the armature tips to one side and oscillates for the entire launch. This is very similar to the results in the literature [17],[18]. From the perspective of stability analysis, this pitching of the armature to one side is indicative of an unstable system that is in a state of divergence. This interpretation will be discussed in detail using a mathematical model in the next section.

## 5.2 Mathematical Model

A relatively simple model can be constructed to study the basic lateral dynamics of the launcher during launch. The basic geometry and a free-body diagram of the armature for this model are shown in Figures 5.4 and 5.5. This is a model of a projectile with spring-loaded sliding contacts and two degrees of freedom $x$ and $\theta$ which represent the deflection of the center of mass and rotation about the center of mass away from the centerline of the guide way. The sliders are constrained to slide in between two guides which are analogous to the rails of an electromagnetic launcher. The only difference is that in this section, the rails are assumed to be stationary. A model very similar to this was explored by Chu and Moon [16] for the dynamics of magnetically levitated vehicles. For the electromagnetic launcher, a modified version of their model is necessary. The major modification to the Chu and Moon model is that the longitudinal forces are assumed to be proportional to the lateral forces via a friction coefficient $\mu$ as shown in Figure 5.5. The derivation

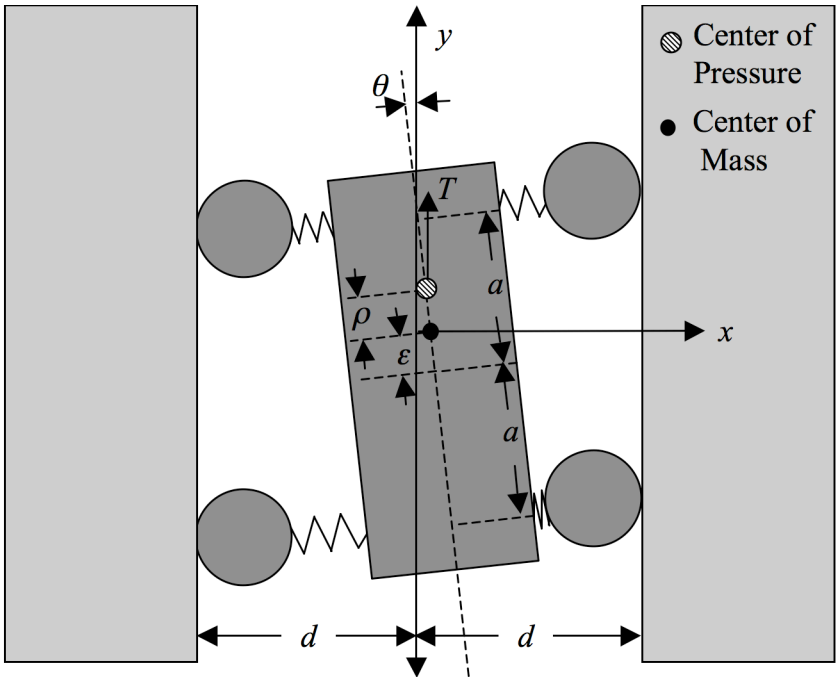


Figure 5.4: Armature Stability Model Geometry

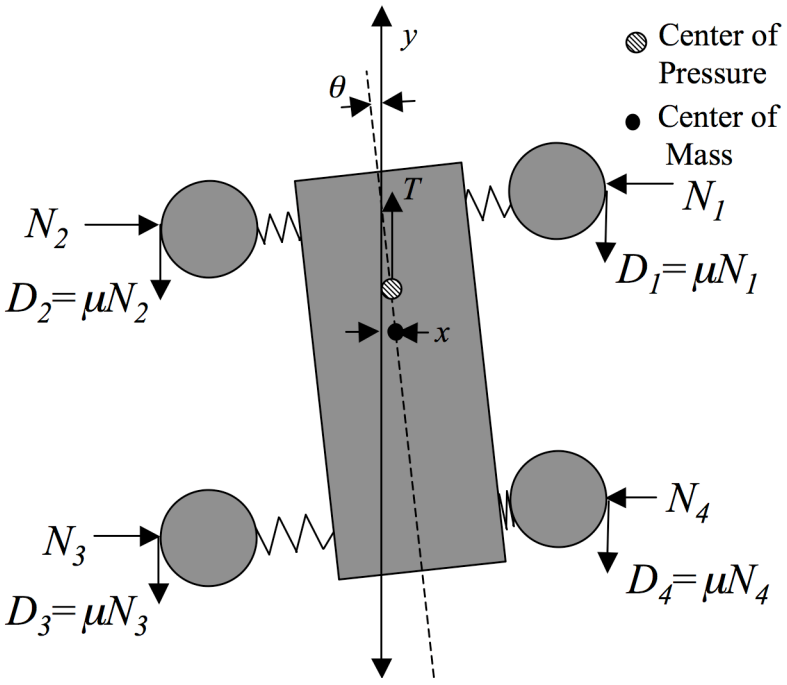


Figure 5.5: Armature Free-Body Diagram

of the equation of motion for this system can be found in Appendix D The equation of motion for this system is as follows.

$$\begin{bmatrix} m & 0 \\ 0 & I_m \end{bmatrix} \begin{bmatrix} \ddot{x} \\ \ddot{\theta} \end{bmatrix} + \begin{bmatrix} 4k & 4k\epsilon \\ 4k(\epsilon + \mu d) & 4k(a^2 + \epsilon^2 + \mu\epsilon(d + \Delta) + \Delta\mu\rho) + a_y m\rho \end{bmatrix} \begin{bmatrix} x \\ \theta \end{bmatrix} = 0 \tag{5.1}$$

For the sake of brevity, the derivation of this equation of motion is presented in Appendix D. The distances $2a$ and $2d$ represent the length of the armature and the width of the guide way. The distance from the geometric center of the armature to the center of mass is represented by $\epsilon$ and the propulsion force $T$ is applied at a distance $\rho$ from the center of mass as shown in Figure 5.4. The propulsion force has been assumed to give a constant acceleration $a_y$ along the $y$ direction. This assumption is covered in detail in Appendix D. The mass and moment of inertia about the center of mass are represented by $m$ and $I_m$. The stiffness of the springs is represented by $k$ and the interference fit in between armature and the guide way is $\Delta$. This is a very simplified model of an armature, but the intention here is just to get a rough idea of the requirements on stability for an armature in a rail launcher. A key property of these equations is that the stiffness matrix is not symmetric. This means that it is possible to have complex eigenvalues that can lead to flutter instabilities. Similar properties are found in the Chu-Moon model for magnetic levitation stability [16].

## 5.3 Stability Analysis

Stability information can be extracted from Equation 5.1 by solving this system as a generalized eigenvalue problem. This can be accomplished by first writing

Equation 5.1 in a shorter form.

$$[M]\ddot{q} + [K]q = 0 \tag{5.2}$$

Where $q$ is the vector containing $x$ and $\theta$ and $[M]$ and $[K]$ are the mass and stiffness matrices as shown in Equation 5.1. If one assumes a solution of the form $q = \hat{q}e^{i\omega t}$ where $\hat{q}$ is a constant, then Equation 5.2 becomes the following

$$[M]^{-1}[K]\hat{q} = \omega^2\hat{q} \tag{5.3}$$

Which is just an eigenvalue problem for the eigenvalue $\omega^2$. The characteristic equation for this problem is as follows.

$$det([M]^{-1}[K] - \omega^2[I]) = 0 \tag{5.4}$$

Where $[I]$ is the identity matrix. Carrying out the determinant gives the following equation for $\omega$.

$$\omega^4 - \alpha\omega^2 + \beta = 0 \tag{5.5}$$

Where $\alpha$ and $\beta$ are given by the following expressions.

$$\alpha = \frac{4k}{mI_g}(a_y m\rho + 4k(a^2 + \Delta\mu(\epsilon + \rho))) \tag{5.6}$$
$$\beta = \frac{1}{mI_g}(4k(I_g + m\Delta\mu\rho + m(a^2 + \epsilon(\epsilon + \mu(d + \Delta)))) + m^2 a_y)$$

The stability of the system is defined by the value of $\omega$. This can be understood by looking at the assumed form of the solution and re-writing $\omega$ in terms of its real and imaginary parts $\omega_r$ and $\omega_i$.

$$q \propto e^{i\omega t} = e^{(i\omega_r - \omega_i)t} \tag{5.7}$$

When the imaginary part of $\omega$ is negative and the real part is zero the solution will grow exponentially. This is referred to as *divergence*. When the imaginary part of $\omega$ is negative and the real part is non-zero the solution will oscillate with an envelope

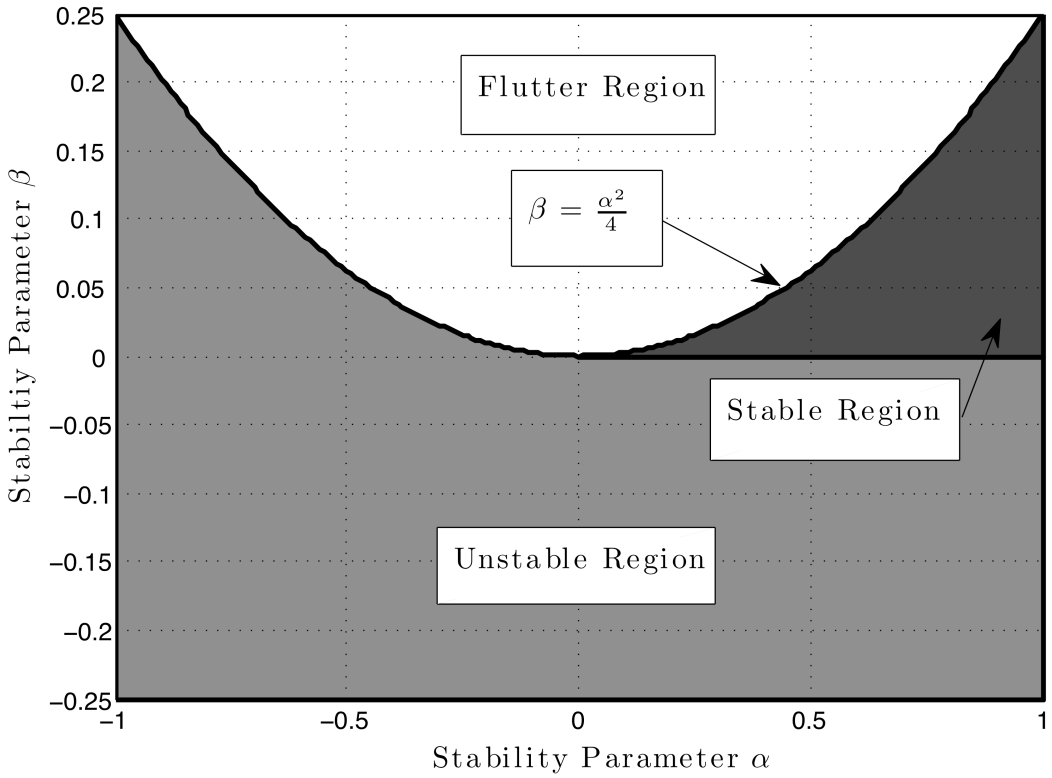


Figure 5.6: Stability Diagram

that diverges to infinity. This type of solution is referred to as *flutter*. When the imaginary part is equal to zero, the solution will oscillate. When damping is included, these oscillations will die down. Either way, this represents a stable solution to the differential equation.

In addition to looking at the frequency of the solution it is possible to describe the stability of the system using the parameters $\alpha$ and $\beta$. These quantities give the stability of the system according to the plot in Figure 5.6. See [16] or [94] for an in-depth explanation of this plot. Because of the large number of parameters in this problem it is helpful to generate a specific example to explore the stability of the system. This is the purpose of the next section.

### 5.3.1 Stability Parameters

Now that the stability requirements have been obtained graphically, it is useful to develop approximate values for all of the parameters in Equation 5.1. Of course, the actual values depend heavily on the launcher and armature being used but it is possible to put together a reasonable set of estimates for a typical launcher. The values for this section are shown in Table 5.1.

Table 5.1: Armature Stability Parameters Estimates

| Symbol | Representative Value |
|---|---|
| $m$ | $0.01\ kg$ |
| $I_m$ | $1.6 \times 10^{-7}\ kgm^2$ |
| $a$ | $5\ mm$ |
| $d$ | $5\ mm$ |
| $\Delta$ | $0.5\ mm$ |
| $\mu$ | 0.25 |
| $k_f$ | $2.3 \times 10^8\ N/m$ |
| $k_r$ | $2.3 \times 10^7\ N/m$ |
| $k_{rail}$ | $1.25 \times 10^9\ N/m$ |
| $k_{cont}$ | $5.5 \times 10^7\ N/m$ |
| $a_y$ | $0.25 \times 10^6\ m/s^2$ |

The parameters in Table 5.1 are roughly comparable to the Georgia Tech. launcher armature pictured in Figure 5.2. The coefficient of friction is from the work of Richard Marshall and Chadee Persad [60]. This is a rough guess at the average friction coefficient since a dynamic value has not been measured in an electromagnetic launcher. The mass is the actual value for the Georgia Tech. armature and the moment of inertia is calculated from the value for a rectangular plane of length 2a and width 2d (i.e. $I_m = \frac{m}{12}((2a)^2 + (2d)^2)$). The acceleration $a_y$ is assumed to be $0.25 \times 10^6\, m/s^2$ which is a reasonable value for an electromagnetic launcher. The geometric parameters $a$ and $d$ are also loosely based on the armature pictured in Figure 5.2. The interference fit is assumed to be approximately $0.5\, mm$.

The difficult parameter to estimate is the stiffness of the springs pictured in Figure 5.4. These springs can be used to describe the stiffness of the armature or they can also be used to include the stiffness of the rail and containment. To get the total stiffness of the springs the stiffnesses of the different components must be added together. Springs in series add reciprocally so the total stiffness can be calculated in the following way.

$$\frac{1}{k_{tot}} = \frac{1}{k_{armature}} + \frac{1}{k_{rail}} + \frac{1}{k_{cont}} \tag{5.8}$$

Estimates of all of these will be presented here so that their relative values can be compared. Some of these components are under compressive loads so their stiffnesses can be approximated by using the following equation [71].

$$k \approx \frac{EA}{L} \tag{5.9}$$

Where $E$ is the elastic modulus of the material, $A$ is the cross-sectional area perpendicular to the load and $L$ is the length of the component along the direction of compression.

The armature actually has two different stiffnesses. It is very stiff in the front and relatively soft in the rear. This is because the rear of the armature is primarily under bending stresses while the front is primarily under compressive stresses. The mathematical model presented in the previous section does not consider the two different stiffnesses so estimates for both of the front and rear of the armature will be presented here. These estimates are labeled $k_f$ and $k_r$ in Table 5.1 . It should be noted that for the following discussion, the armature will be assumed to be in a square bore launcher. This means that its width and height are both equal to $2d$. The estimate of $k_f$ in Table 5.1 was calculated by assuming that the cross-sectional area of the part of the armature under compression is equal to $(2a/3)(2d)$ (i.e. length of $2a/3$ and width of $2d$)and the length under compression is equal to

$2d$.

$$k_f \approx \frac{2Ea}{3} \tag{5.10}$$

Where $E$ is the elastic modulus of the armature material (assumed to be aluminum, $E = 70\ GPa$). Because the rear of the armature is under bending stresses, $k_r$ will be roughly one tenth of this value. This value is also listed in Table 5.1.

The stiffness of the rail can be also be approximated by assuming it is under compression. The rails are typically made of copper so the elastic modulus is approximately $120\,GPa$. The length of the armature is equal to $2a$ and the width of the armature is $2d$ so the effective area of the rail under compression is $4ad$. The effective length is equal to the height of the rail which is approximately $9.6\,mm$ for the Georgia Tech. Launcher. Plugging these numbers into Equation 5.9 give the effective stiffness $k_{rail}$ in Table 5.1.

Finally, the stiffness of the containment $k_{cont}$ can be approximated using the stiffness per unit area $k_0$ that was calculated in Table 3.2. multiplying this by the effective cross-sectional area under compression ($4ad$ as with the rail) gives the value in Table 3.2.

When the stiffnesses are added together reciprocally, the smallest one dominates. The smallest stiffnesses in Table 5.1 are $k_r$ and $k_{found}$ and they are both on the order of $10^7\ N/m$. This means that, depending on which components are considered, the effective stiffness of the springs will be between $10^7\ N/m$ and $10^8\ N/m$. In the following plots both of these values will be used.

In Figure 5.7, the stability is plotted as a function of the distance to the center of mass $\rho$ and the distance to the center of pressure $\epsilon$. This plot is shown for two different stiffnesses. As one can see, with these particular parameters the armature could be divergent, flutter or stable during launch. For flutter to occur, $\epsilon$ would have to be negative. If the center of pressure is to far behind the center of mass

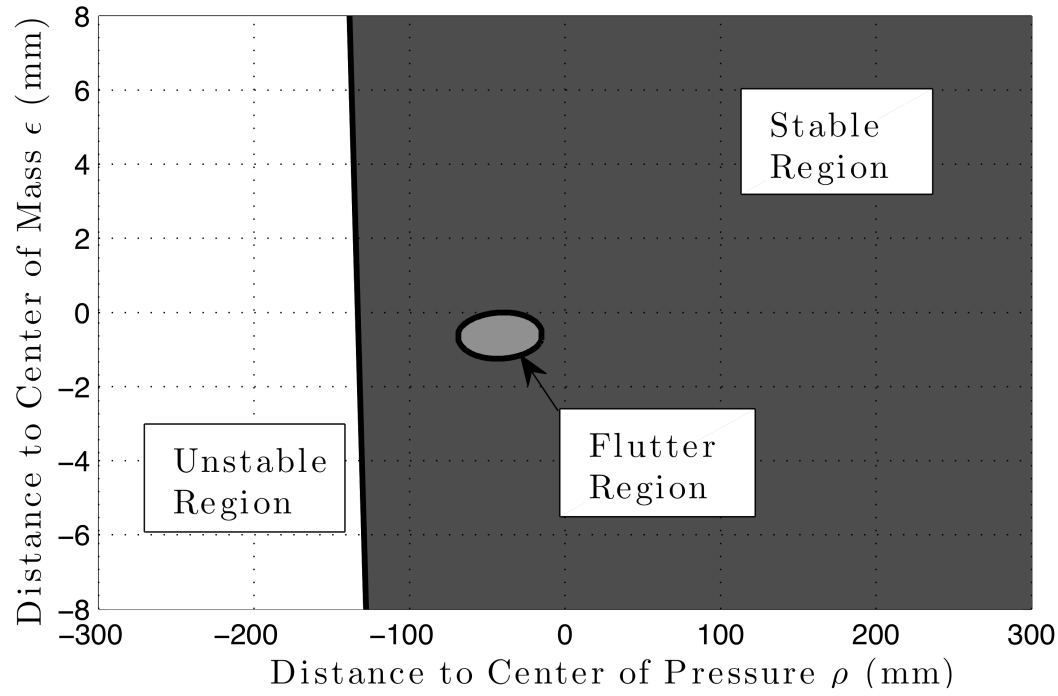


(a) Stability Diagram for $k = 1 \times 10^7$

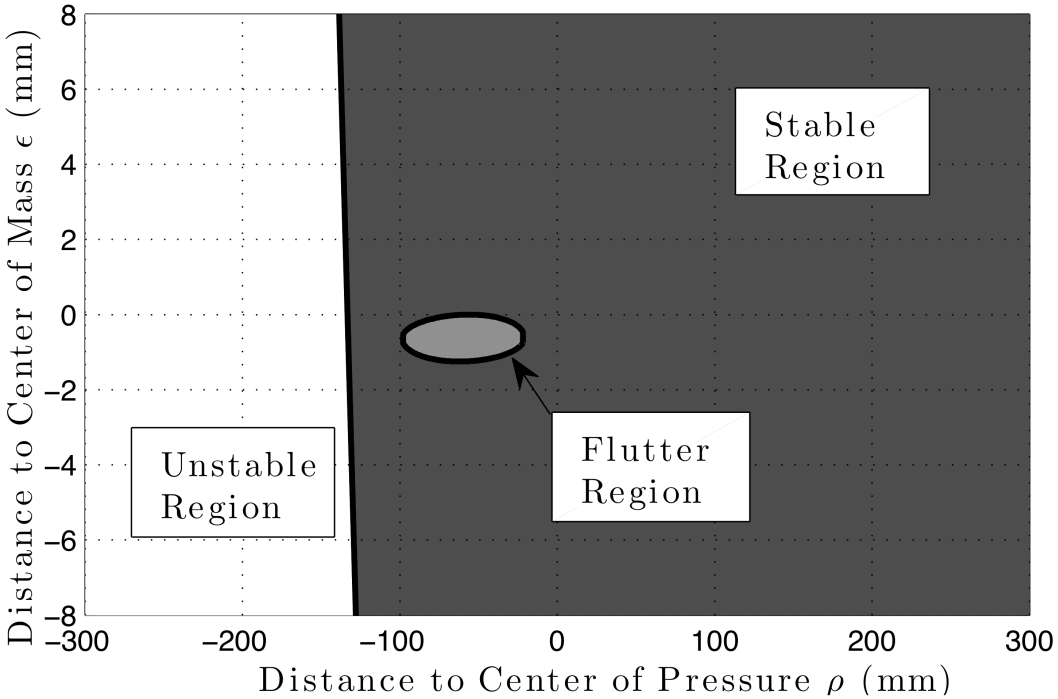


(b) Stability Diagram for $k = 1 \times 10^8$

Figure 5.7: Stability Diagrams for $\rho$ and $\epsilon$

then the armature will be in a state of divergence. This is essentially what occurred in the simulation in Section 5.1. The center of pressure of the applied load was well behind the center of mass of the armature. The magnitude of the stiffness will also affect the position of the lines dividing the stable and unstable regions. This is important to take into consideration not only in the structural design of armatures but also in the thermal design. As the armature heats up during launch, it's effective stiffness will change and this could potentially push it into an unstable region.

Most projectile designs in the literature show the armature as pushing the payload from behind while using a bore-rider at the front of the payload (e.g. see [56]). In principle, these designs could have a negative value for $\epsilon$ so stability calculations should be taken into account in their design to avoid flutter. In addition to this, since the armature is pushing the payload in most of these designs, the value of $\rho$ will most likely be negative. This could lead to divergent solutions. Either of these problems will severely influence the overall effectiveness of any electromagnetic launching system.

### 5.3.2 Simulations of Armature Stability Regions

In the interest of exploring the different regions in Figure 5.7 a MATLAB program was written to simulate Equation 5.1. This program solves the differential equation using a fourth order Runge-Kutta solver and the results will be presented in this section for the three different regions. For the following simulations, the initial displacement of the center of mass and the initial rotation of the armature were assumed to be non-zero. The initial displacement was equal to $10^{-4}\,m$ and the initial angle was set to $10^{-4}$ radians. This was done so that the instabilities would be brought out. The initial velocities and accelerations were assumed to be zero.

All of the simulations in this section are of the system described in Figure 5.7 with a spring stiffness of $1 \times 10^7 N/m$.

An example of the stable region is shown in Figures 5.8 and 5.9. Both the time history are shown as well as the phase plane plot of each coordinate versus its velocity. These plots are for the case when $\rho = 0.1$ and $\epsilon = 0.004$. For this case, the armature is stable. This stability is reflected in the oscillatory nature of the solution. For this case the eigen-frequencies are pure real and since there is no damping the oscillations do not die down. The vibrations in $x$ and $\theta$ are coupled so if vibrations are generated in one of the degrees of freedom, they will generate vibrations in the other.

Next, an example of the divergence region is shown in Figures 5.10 and 5.11. As before, both the time history and the phase plane are plotted. These plots are for the case when $\rho = -0.2$ and $\epsilon = 0.004$. For this case, the armature is in a state of divergence. This is reflected in the fact that $\theta$ and $x$ blow up to large values. As with the vibrations, the coupled nature of the problem causes both of the degrees of freedom to diverge. It is important to note that the large deflections and rotations seen in Figures 5.10 and 5.11 are so large because of the absence of any nonlinear restoring terms in the Equation 5.1. In the physical system, nonlinearities would take over well before the deflections/rotations would get this large.

Finally, an example of the flutter region is shown in Figures 5.12 and 5.13. Again, both the time history and the phase plane are plotted. This plots are for the case when $\rho = -0.05$ and $\epsilon = -0.001$. For this case, the armature is in a state of flutter. This is reflected in the fact that $\theta$ and $\rho$ both blow up to large values while oscillating. Again, the coupling between the degrees of freedom causes flutter to be seen in both $x$ and $\theta$. As with the divergent solution, the deflection and rotation shown in Figures 5.12 and 5.13 will grow without bound for this

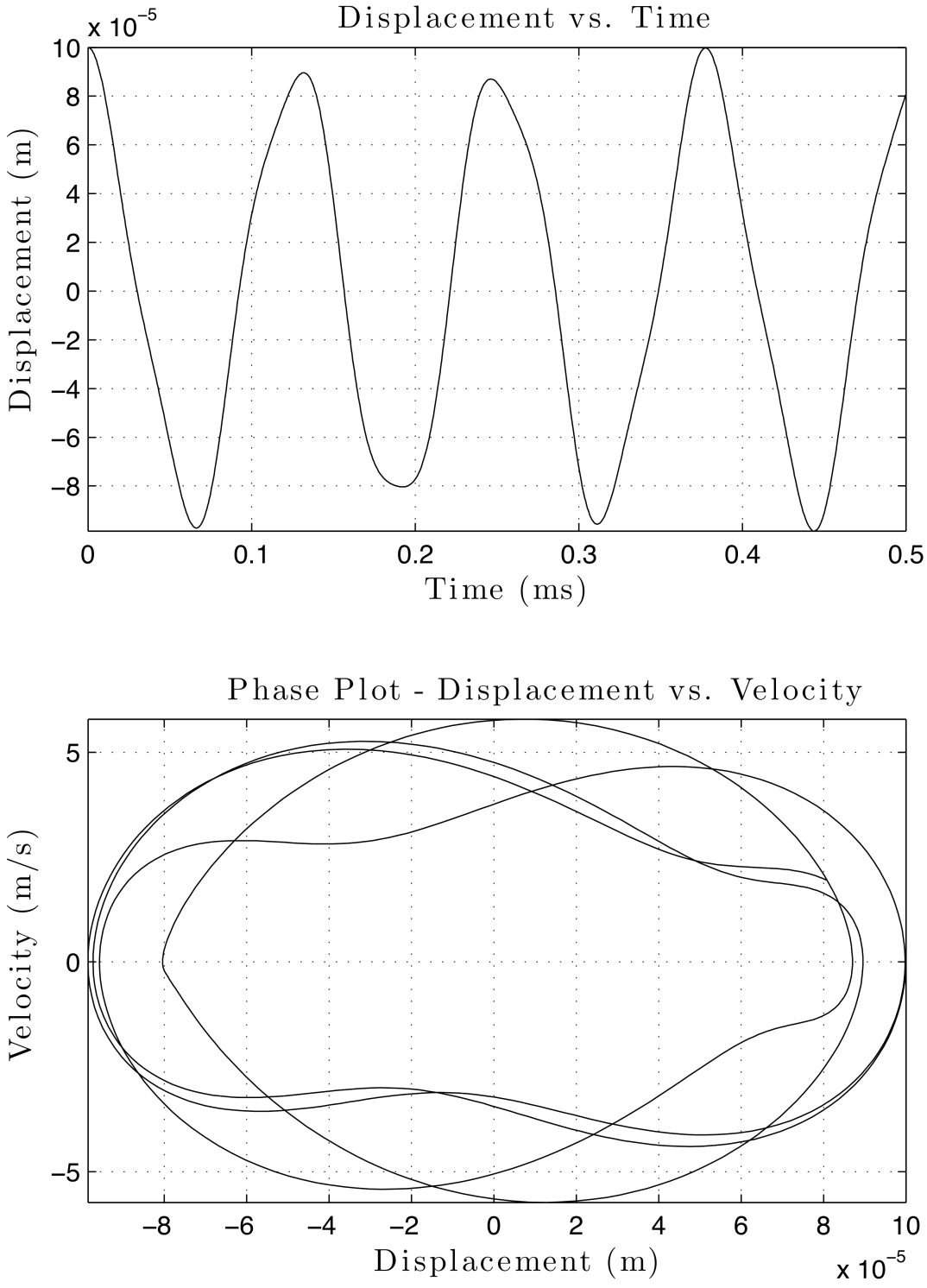


Figure 5.8: Stable Solution: Top - Displacement of Center of Mass vs. Time. Bottom - Velocity vs. Displacement

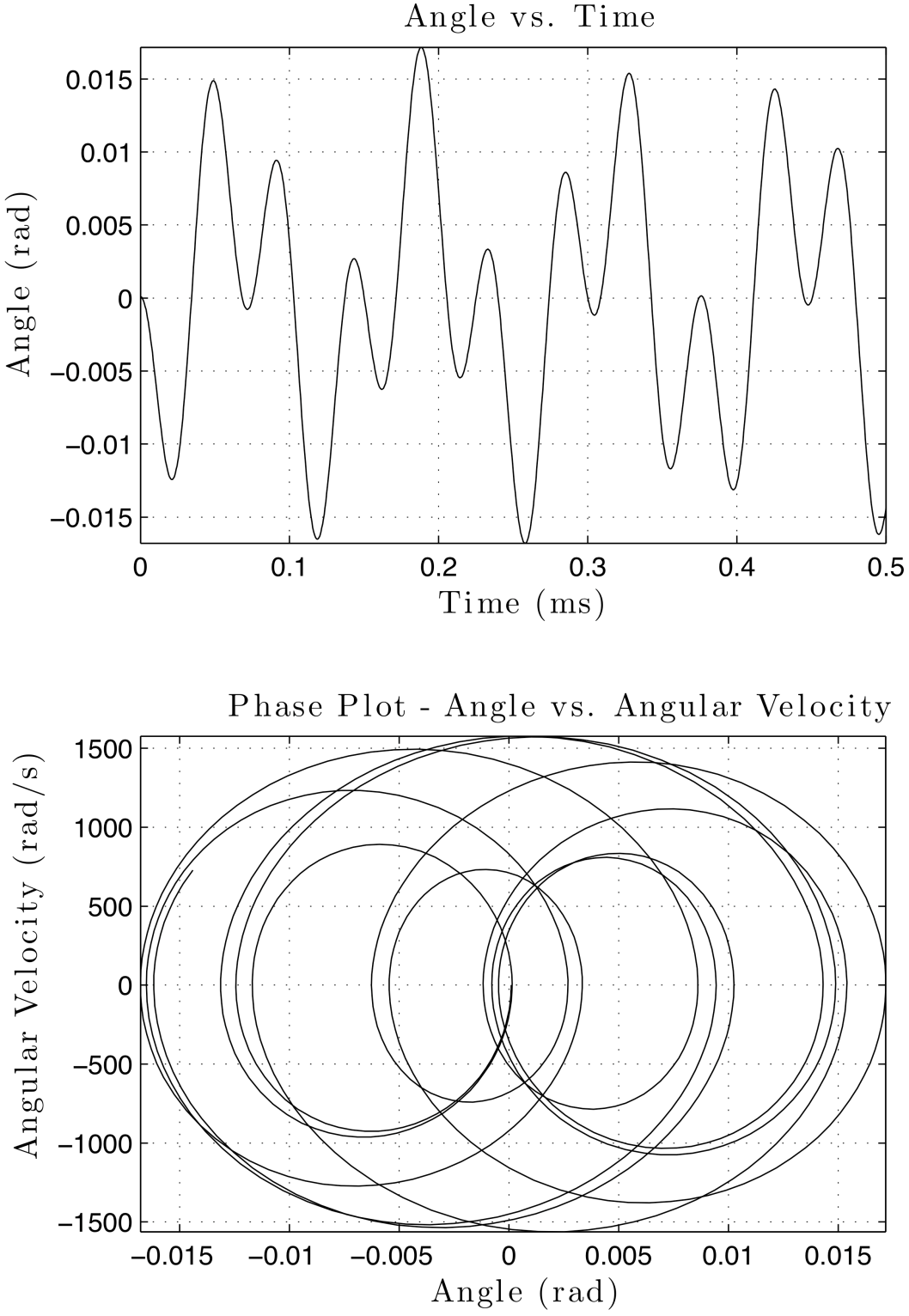


Figure 5.9: Stable Solution: Top - Rotation about Center of Mass vs. Time. Bottom - Angular Velocity vs. Angle

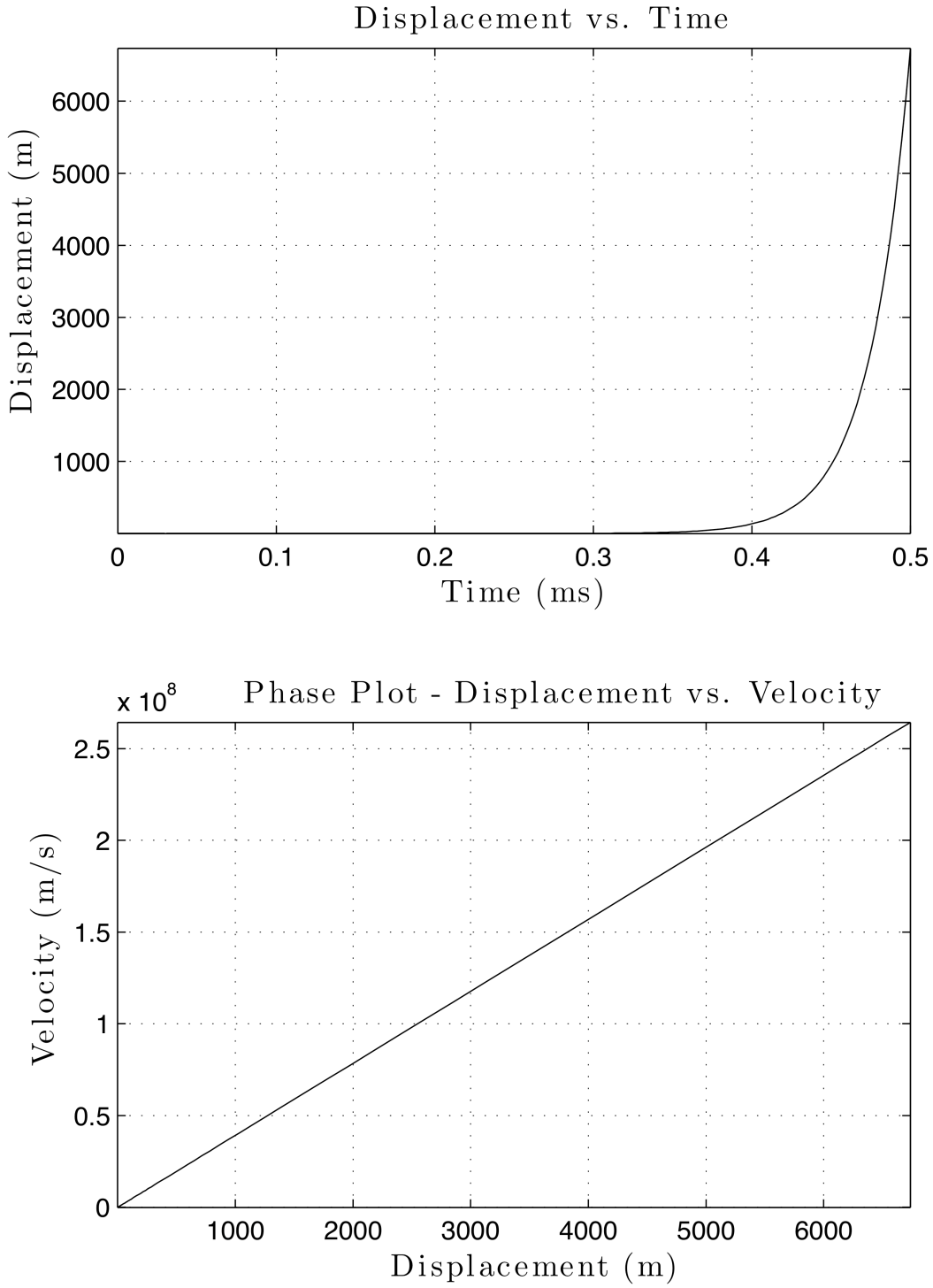


Figure 5.10: Divergent Solution: Top - Displacement of Center of Mass vs. Time. Bottom - Velocity vs. Displacement

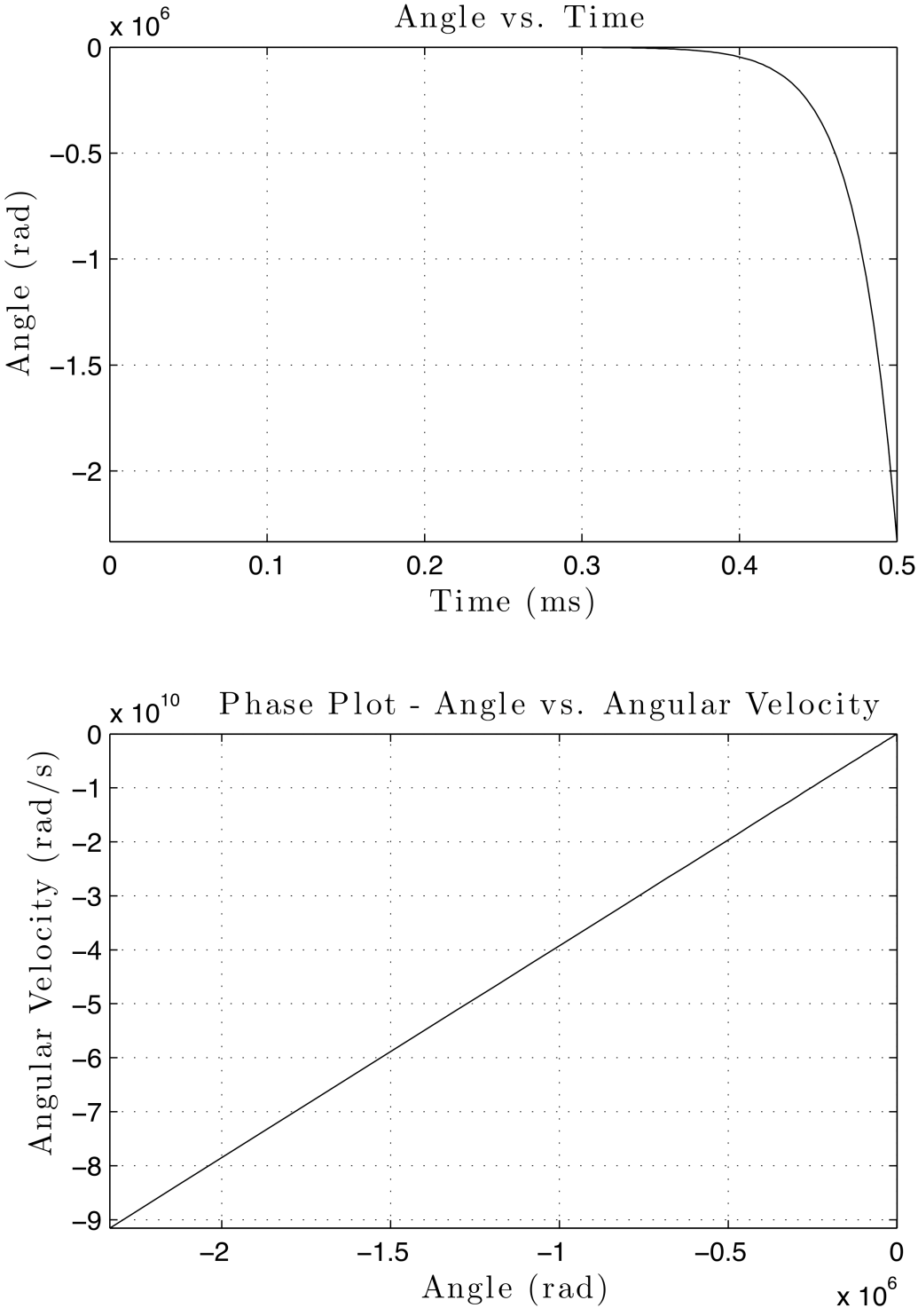


Figure 5.11: Divergent Solution: Top - Rotation about Center of Mass vs. Time. Bottom - Angular Velocity vs. Angle

simple linear model. This can be corrected by considering nonlinearities in the model. This complication will be considered in the next section.

### 5.3.3 The Effect of Nonlinearities

As shown in the previous section the deflection and rotation of the armature can grow without bound for the simple linear model when the armature is in a divergent or flutter state. In a physical system, these values would be bounded by nonlinear terms that would dominate the dynamics for large deflections. A simple model to consider nonlinearities is the Duffing equation [74].

$$\ddot{x} + \alpha x + \beta x^3 = f(t) \tag{5.11}$$

This equation describes the dynamics of an oscillator with a nonlinear load deflection curve given by $\alpha x + \beta x^3$ that is driven by a forcing function $f(t)$. This version of the Duffing equation ignores damping. An in-depth discussion of the properties of this system including damping can be found in text books on chaos [74]. The $x^3$ term serves to give a first order impression of the effect of nonlinearities. For the armature model being considered in this chapter, the nonlinearity would have to be taken into account in both degrees of freedom. This can be done in the following way.

$$\begin{bmatrix} m & 0 \\ 0 & I_m \end{bmatrix} \begin{bmatrix} \ddot{x} \\ \ddot{\theta} \end{bmatrix} + \begin{bmatrix} \beta_{1,1} & \beta_{1,2} \\ \beta_{2,1} & \beta_{2,2} \end{bmatrix} \begin{bmatrix} x^3 \\ \theta^3 \end{bmatrix} + \begin{bmatrix} 4k & 4k\epsilon \\ 4k(\epsilon + \mu d) & 4k(a^2 + \epsilon^2 + \mu\epsilon(d + \Delta) + \Delta\mu\rho) + a_y m\rho \end{bmatrix} \begin{bmatrix} x \\ \theta \end{bmatrix} = 0 \tag{5.12}$$

Where the coefficients $\beta_{1,1}$ and $\beta_{2,2}$ define the magnitude of the nonlinear terms. The of diagonal terms would take into account nonlinear coupling between the two

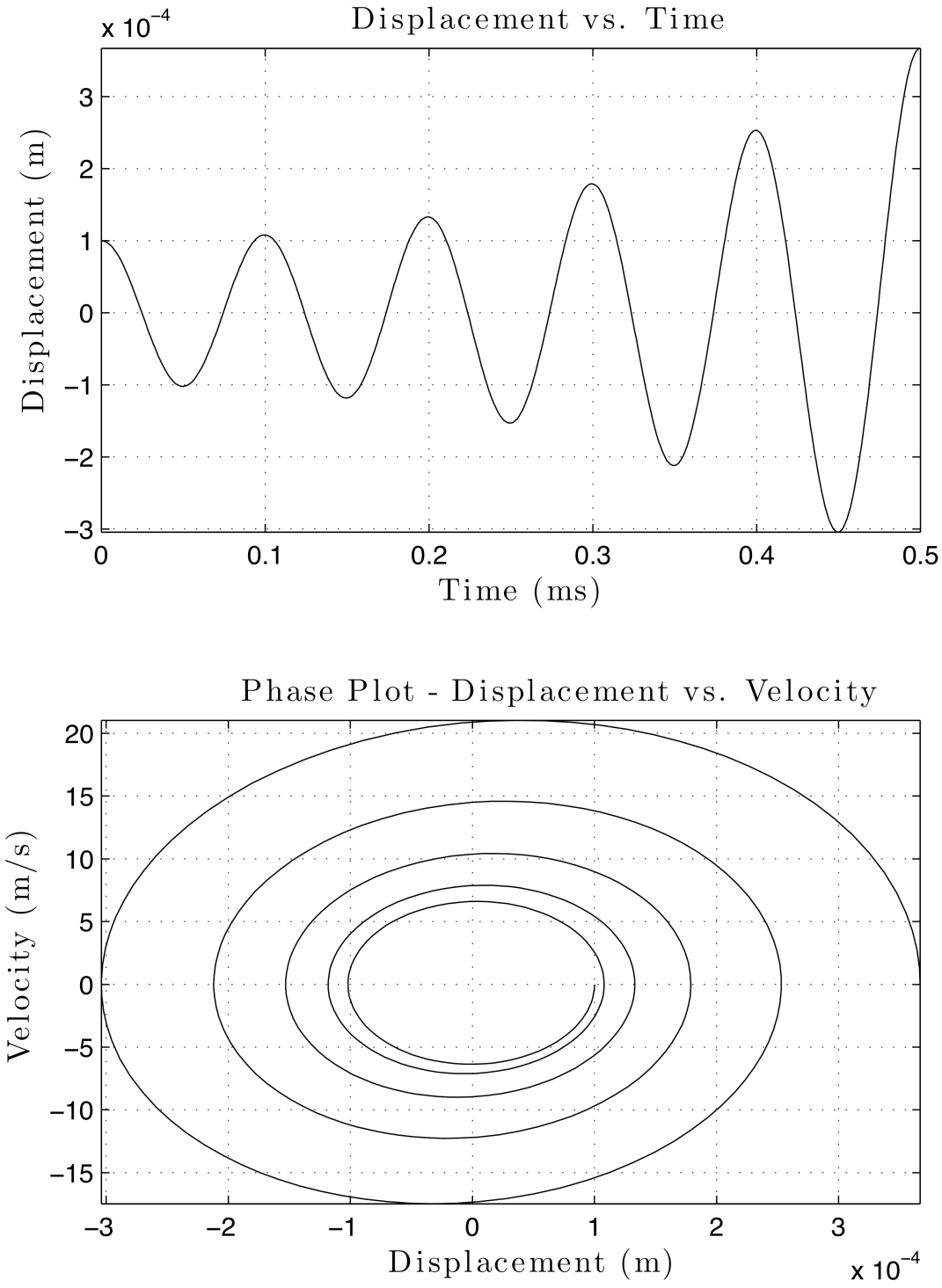


Figure 5.12: Flutter Solution: Top - Displacement of Center of Mass vs. Time. Bottom - Velocity vs. Displacement

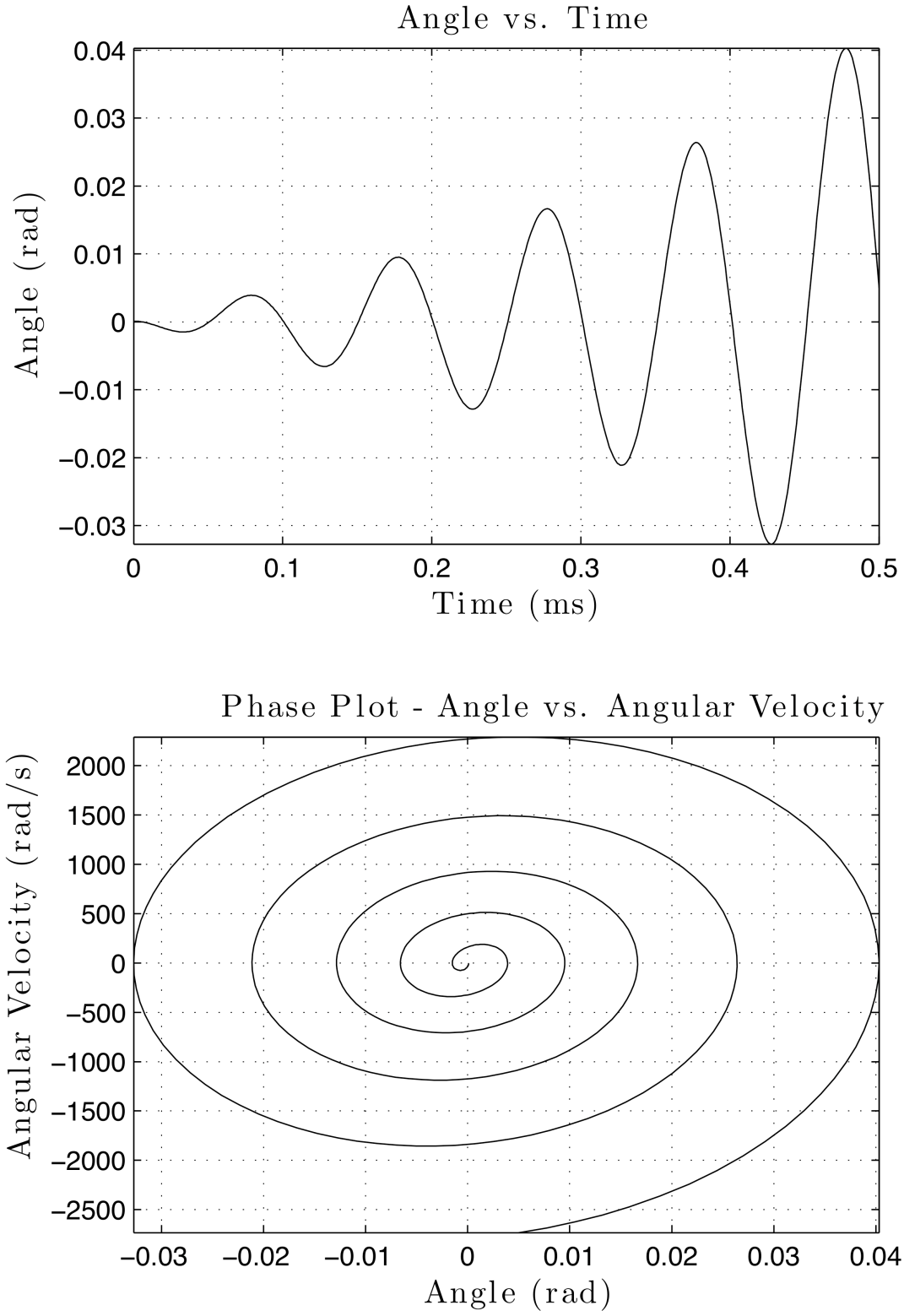


Figure 5.13: Flutter Solution: Top - Rotation about Center of Mass vs. Time. Bottom - Angular Velocity vs. Angle

degrees of freedom. For the sake of simplicity these two terms will be set equal to zero for the following discussion.

Now that nonlinearities have been considered, it is possible to re-run the divergent and flutter solutions shown in the previous section. At the present, values for the $\beta$ parameters are unknown and would be best determined experimentally. For the sake of this discussion, values were chosen so that the maximum displacement of the armature was limited to $0.5\,mm$ and the maximum rotation was limited to 0.1 radians ($\approx 5.7°$). Different values of $\beta_{1,1}$ and $\beta_{2,2}$ were tried until these requirements were met. There is a wide range of values that will meet the criteria, but the simulation results are all comparable so a representative set was chosen. For the following simulations, $\beta_{1,1}$ and $\beta_{2,2}$ were both set equal to $10^5$. Again, these values are essentially arbitrary and are just being used for the sake of discussion. These values were used to repeat the unstable analyses given in the previous section. All of the parameters were the same except for the addition of the $\beta$ matrix.

The result of the divergent simulation is shown in Figures 5.14 and 5.15. These simulations show some interesting behavior in both degrees of freedom. Instead of the deflection and rotation blowing up to infinity they appear to oscillate between two maxima in a chaotic fashion. There are a few places where the armature leans towards one side for multiple cycles as well (e.g. at approximately $2\,ms$). This indicates that it is possible for the armature to lean towards one side of the bore or to oscillate between the different sides of the bore (balloting).

It is important to end this chapter by stating that the model used here is highly simplified and that the parameters used in the Duffing model are unknown. Whether these effects actually occur in the bore of an experimental launcher remains to be seen. Strain measurements were conducted in the Georgia Tech. launcher that show an asymmetry in the strain in the rails (see Chapter 4). This

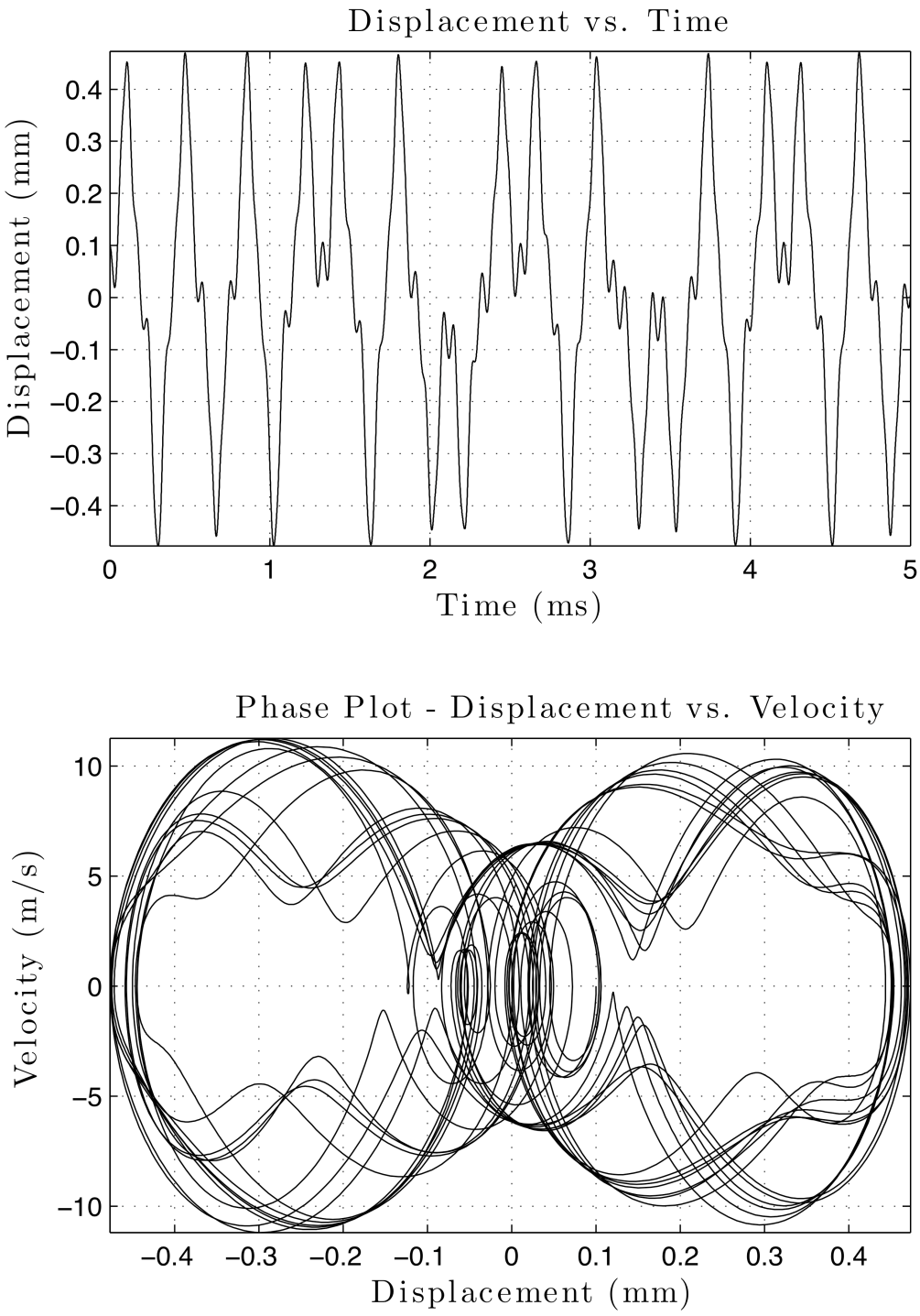


Figure 5.14: Divergent Solution for Duffing Model: Top - Displacement of Center of Mass vs. Time. Bottom - Velocity vs. Displacement

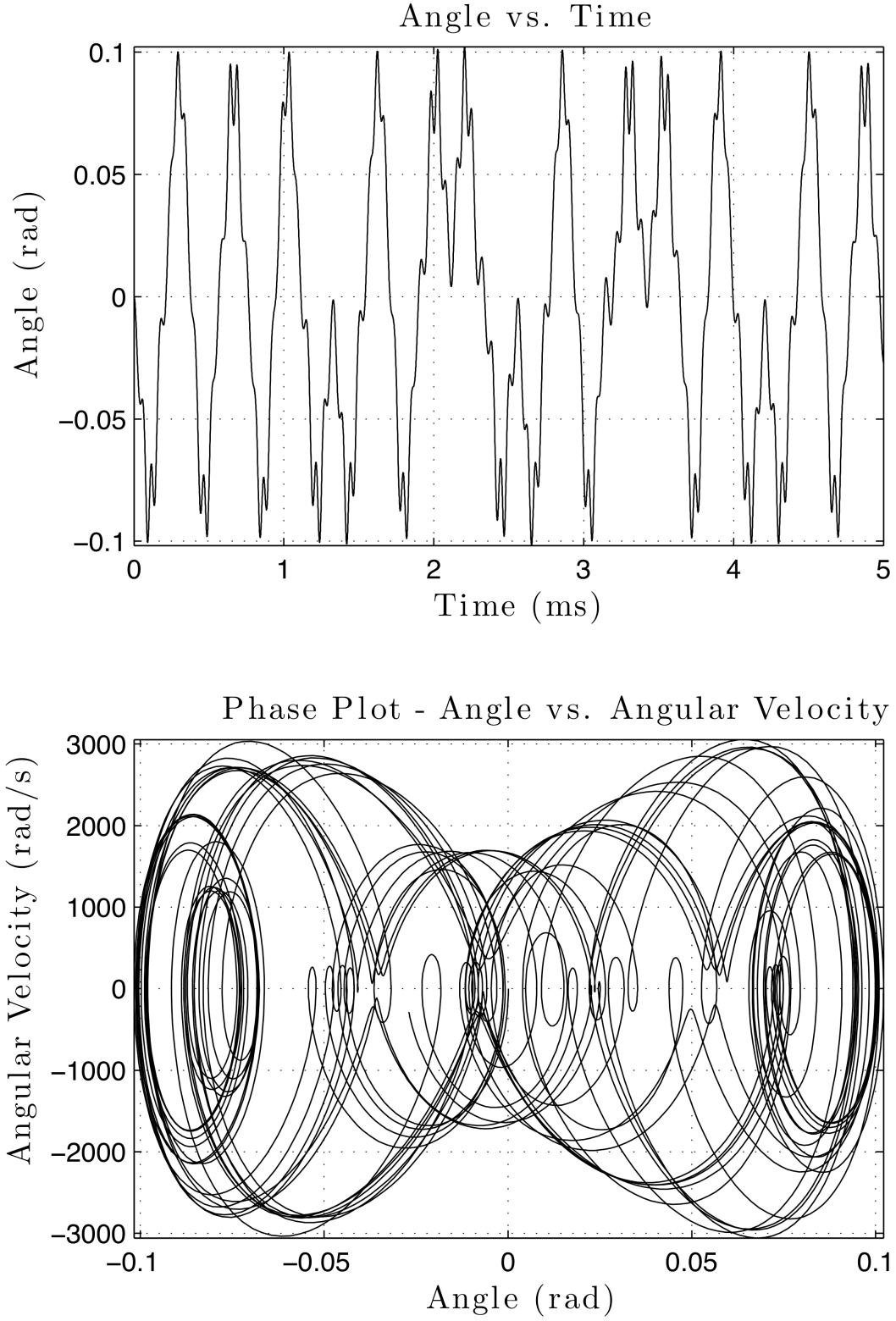


Figure 5.15: Divergent Solution for Duffing Model: Top - Rotation about Center of Mass vs. Time. Bottom - Angular Velocity vs. Angle

asymmetry could have been caused by the armature leaning to one side, but the results do not conclusively show this. Another set of experiments dedicated to detecting this phenomena using these strain gages might be able to confirm this, but the experimental evidence as it stands is somewhat inconclusive.

# Chapter 6
# Cornell Launcher Experiments and Calculations

Electromagnetic launchers have been studied extensively since the early 1970's. Even with this long history of experimental work, there is a surprisingly small number of sensors available for measurements during launch. This is primarily because of the electromagnetic fields generated during launch. To help understand and rectify this problem, a small-scale electromagnetic launcher was constructed at Cornell. This small-scale system allows for testing of different sensors and sensor systems in a short amount of time. This section will discuss this launcher and the sensor tests that were conducted.

## 6.1 Description of Launcher

First it is necessary to give a basic description of the launcher. The basic electrical components, mechanical components, and operation of the launcher will be covered in this section.

### 6.1.1 Power Supply and Electrical Characteristics

The power supply for the small-scale electromagnetic launch is capacitor based. A picture and a circuit diagram of the power supply is shown in Figure 6.1. It consists of twelve $6700\,\mu F$ electrolytic capacitors (donated by Cornell-Dubiler) hooked up in parallel giving a total capacitance of $0.0804F$. An inductor is added to the power supply to stretch out the length of the current pulse ($L = 11.7\ \mu H$). The firing switch is a high power silicon-controlled rectifier (SCR) with a pulse current rating of $14.4\,kA$ for $10\,ms$. The capacitors are electrolytic so a crowbar diode

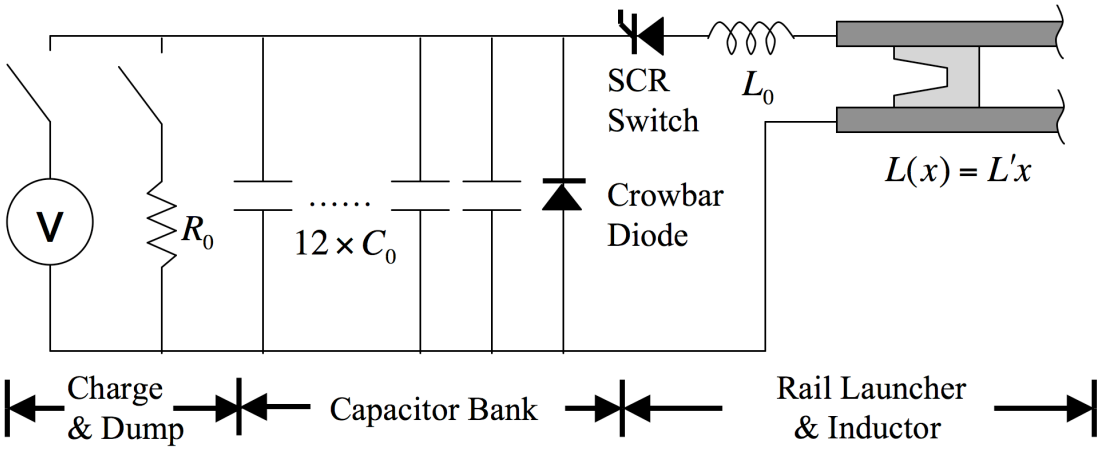


(a) Capacitor bank diagram

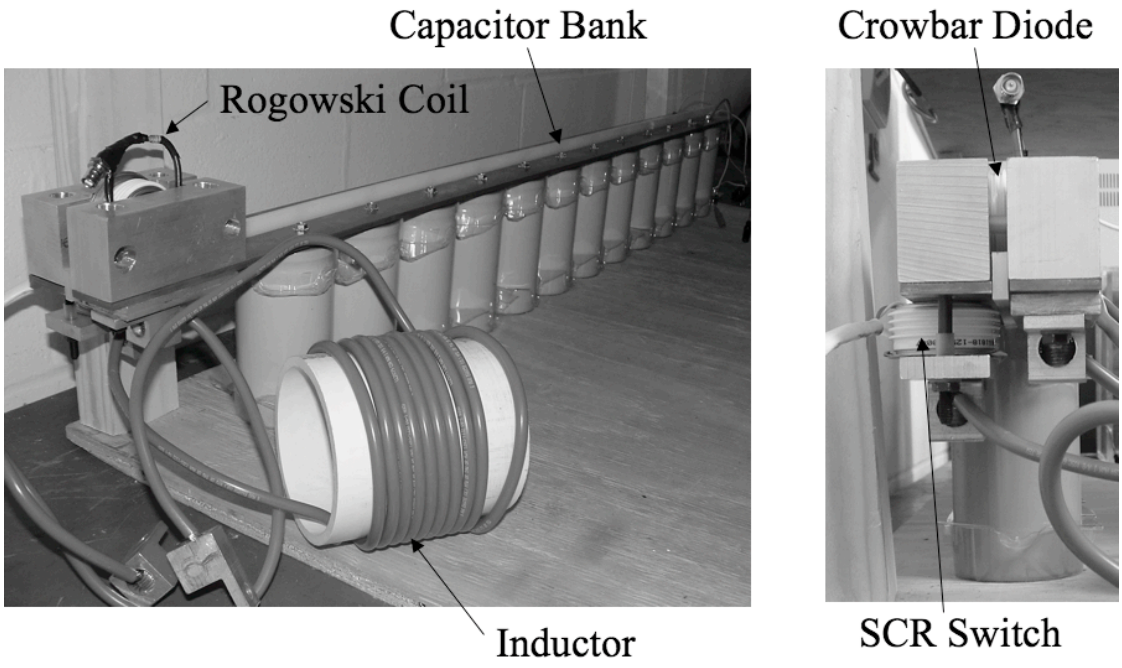


(b) Picture of capacitor bank components

Figure 6.1: Capacitor Bank for Millimeter Scale Electromagnetic Launcher

is also located across the poles of the capacitor bank to keep the voltage from reversing during a shot. The capacitors can be charged to a maximum of $400\,V$. This gives a potential energy storage level of $6.4\,kJ$, but due to the limitations of the switch, the bank has never been charged above $222\,V$ (about $2\,kJ$). Also shown in Figure 6.1(a) is the dump resistor. This is used to clear any excess energy in the bank after firing a shot or in the event that a test shot must be aborted.

In addition to the electrical characteristics of the power supply it is important to mention the characteristics of the launcher itself. The important parameter to understand is the inductance gradient (see Equation 1.7). An approximate value of this quantity can be calculated or measured. For this launcher, both of these have been done. The calculation is based on equations given in a book by Frederick Grover [37]. Grover calculates the inductance of an infinite pair of rectangular conductors running parallel to one another The equation for this geometry is as follows.

$$L' = \frac{\mu_0}{\pi}(Log\left(\frac{d}{B+C}\right) + 1.5 + \Delta_k - \Delta_e)) \tag{6.1}$$

Where d is the distance between the centers of the rails, B and C represent their cross-sectional dimensions (C being the smaller of the two) and the $\Delta$'s are tabulated in Grover's book. For the Cornell launcher $\Delta_k = 0.389$ and $\Delta_e = .00249$. This gives a value of $L' = 0.273\ \mu H/m$. Grover's equation assumes that the length of the rails is infinite and that the current is evenly distributed throughout so this number is only a rough approximation of the inductance gradient of this launcher.

A value for the inductance gradient was also measured using a precision LCR meter. The launcher was loaded and assembled and the inductance was measured at a frequency of 1 kHz. The launcher was then taken apart, the armature was moved down the length of the launcher and the inductance was measured again. This process was repeated to give the data plotted in Figure 6.2. The final exper-

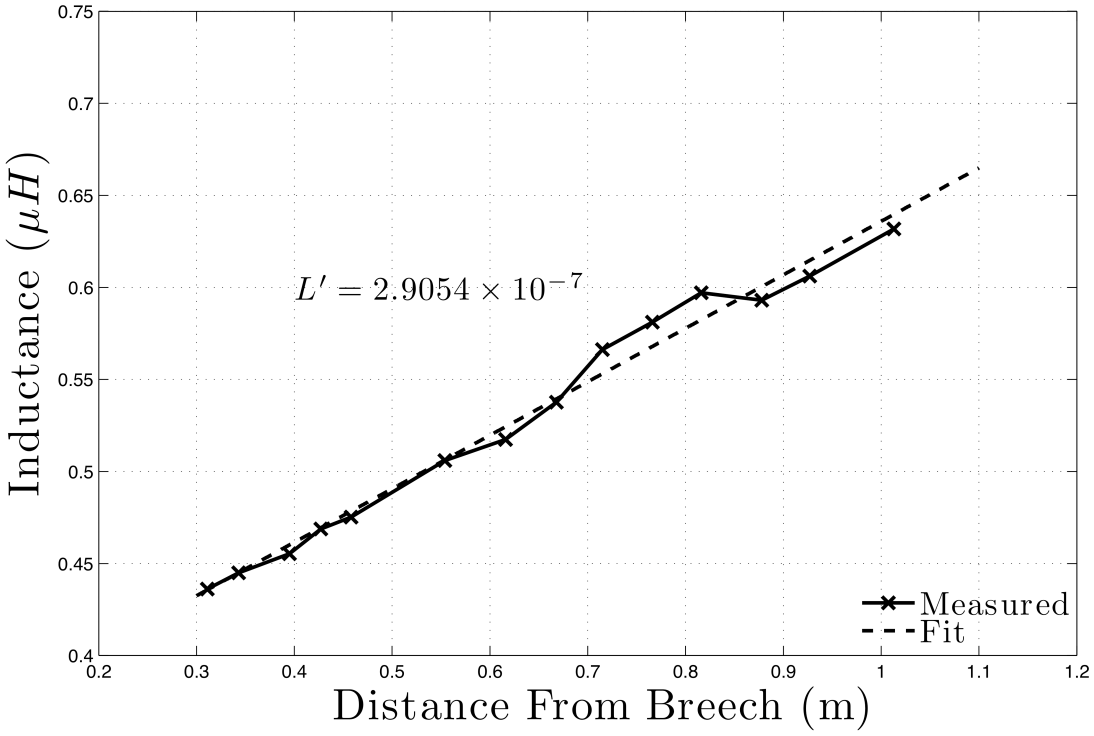


Figure 6.2: Inductance Gradient Measurement

imental value of the inductance gradient is $L' = 0.291\ \mu H/m$. The experimental number is about 6% higher than the calculated number from Equation 6.1.

It is important to note the values of $L'$ presented in this section are only approximate. While they are good enough to use in an approximate model, in an actual launch, the value of this parameter will vary as the current diffuses from the outside of the rails into the interior [35].

### 6.1.2 Mechanical Components

The main mechanical component of the electromagnetic launcher is the containment. A drawing of this containment is shown in Figure 6.3 along with a picture. The containment was made of $1/2'' \times 2''$ polycarbonate. This material was chosen because of its resistance to impact, transparency, machinability and its resistive

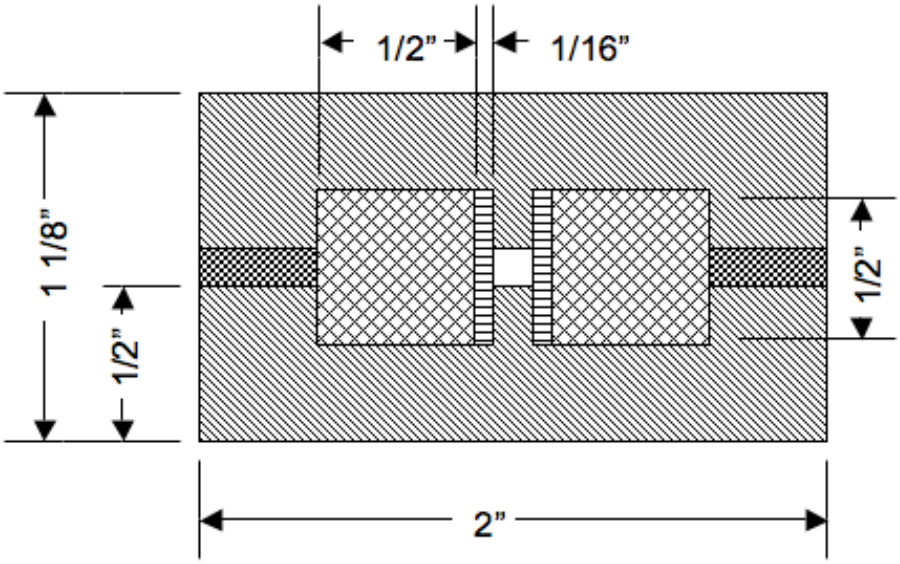


(a) Drawing of containment

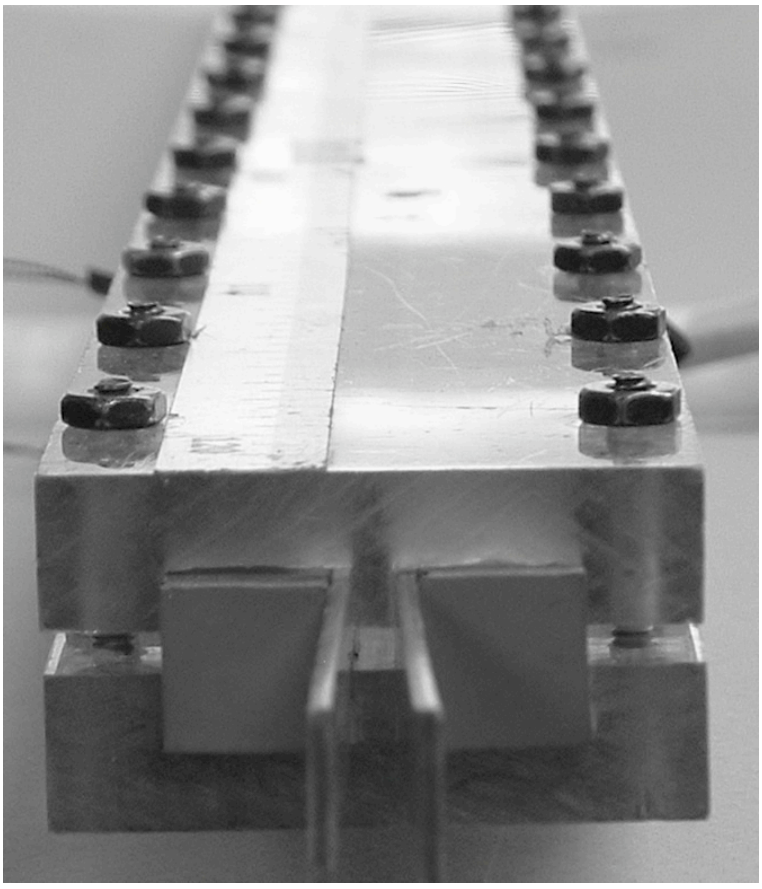

(b) Picture of containment

Figure 6.3: Millimeter Scale Launcher Containment

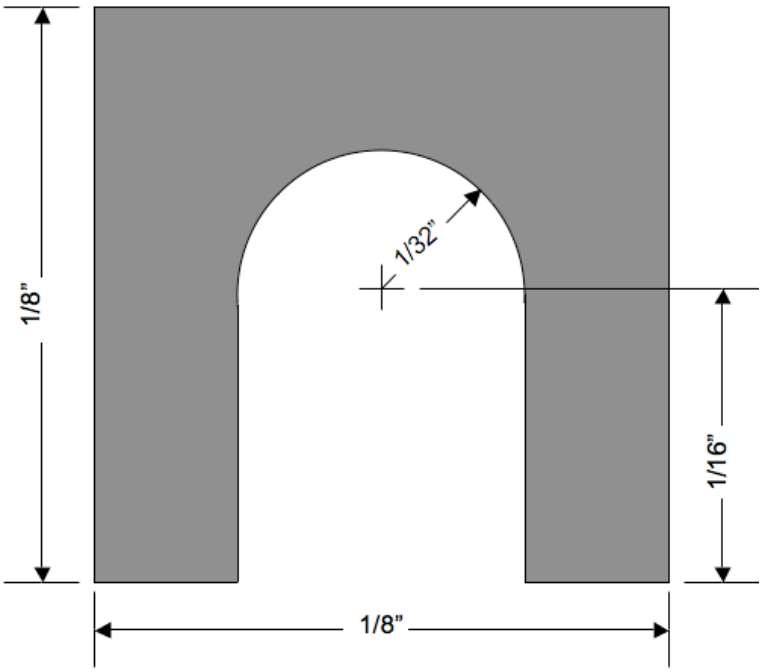


(a) Armature sketch

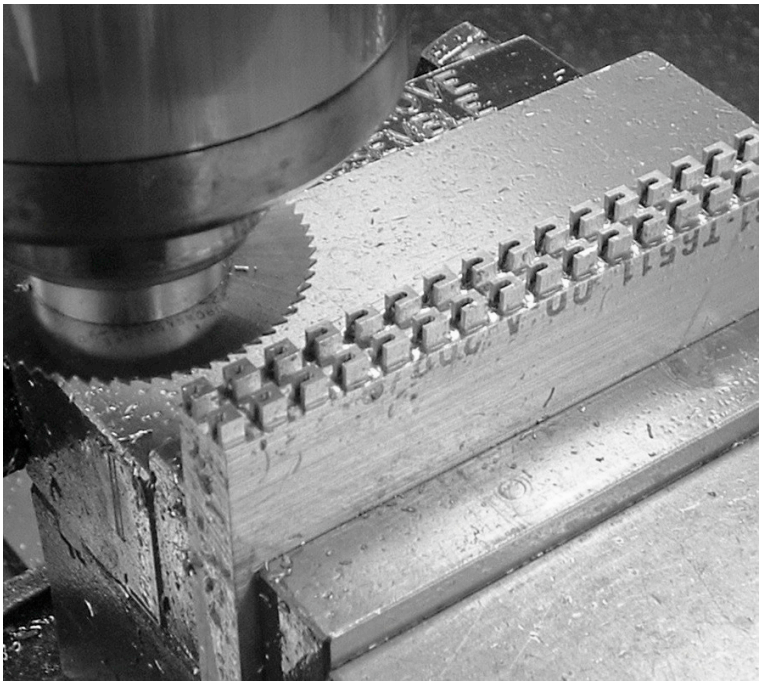

(b) Armatures being machined

Figure 6.4: Millimeter Scale Armature

properties. The rails of the launcher are made from $1/16'' \times 1/2''$ copper bars.The design of the containment also includes a $1/2'' \times 1/2''$ space behind the rails. This space was left so that the foundation stiffness could be modified by filling it with different materials. It is also intended as space for sensors on the back surface of the rails. This space is filled with rubber in the picture in Figure 6.3.

Figure 6.4 shows a picture of the armatures being machined along with a dimensioned sketch of the armature. The sharp corners shown in Figure 6.4 are rounded off with a file before the armature is loaded into the launcher. The launch mass of one of these armatures is approximately 0.08 $g$.

## 6.2 Rail Launcher Diagnostics

Since the purpose of the Cornell launcher is to test sensor systems, this section will cover the diagnostics built for this launcher. Typical measurements made on a rail launcher include current, velocity and muzzle/breech voltage. The techniques involved in the first two of these will be covered in this section. The current is measured using rogowski coils, which is the classic method, but the velocity measurement was done using a new technique that was developed on this launcher. This new technique allows for a higher resolution velocity measurement while using less data acquisition resources.

### 6.2.1 Current Measurement

The primary technique for measuring the current involves the use of Rogowski coils. This device is a coil of wire that is wrapped around the component that is carrying current. A picture of one of the Rogowski coils built for the Cornell launcher is pictured in Figure 6.5 along with a sketch of how it works. A Rogowski

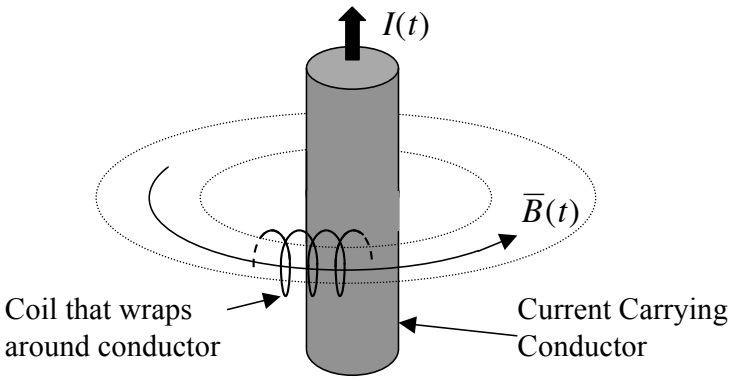


(a) Rogowski Coil sketch

(b) Rogowski Coil Picture

Figure 6.5: Rogowski coil for current measurements

coil measures the change in the magnetic field along its length. The integral of the output of the gives the current flowing through the conductor according to the following equation.

$$I(t) = \gamma \int_0^t V_{coil}(\tau) d\tau \tag{6.2}$$

Where $\gamma$ is a calibration constant. For the Rogowski coils on the Cornell launcher, the calibration constant was measured by pulsing a current through a calibrated shunt with a known resistance. The constant for these coils was found to be equal to $10.63 \times 10^6\, A/Vs$. For the experiments in this section, the voltage is measured using a computer data acquisition card and the integration is carried out using

software. A typical voltage trace from a launch is shown in Figure 6.6. In this plot the current flowing through the rails and the current flowing through the crowbar diode are measured. For this launcher, it is necessary to monitor both of these currents because the SCR switch and crowbar diode are operating near their design limits.

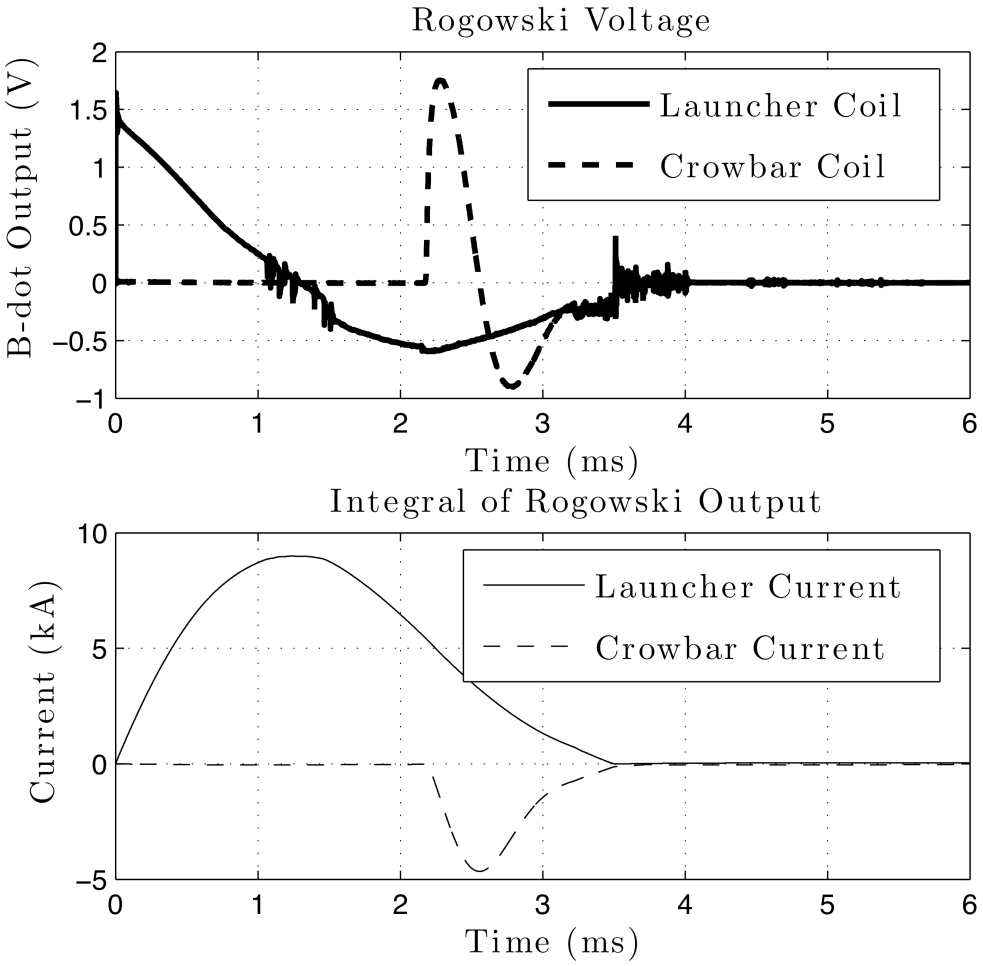


Figure 6.6: Example Rogowski Coil Measurement

### 6.2.2 Velocity Measurements

One of the primary measurements made in any electromagnetic launcher is the velocity of the projectile. In this harsh environment, even this measurement can be surprisingly difficult. Typically it is conducted by using a series of inductive coils placed at intervals along the length of the launcher. When the armature passes by these coils, a small voltage pulse is generated. This is process is pictured in Figure 6.7. The voltage trace seen in Figure 6.7 is typical for rail launchers. The signal consists of a high frequency, high amplitude pulse followed by a low frequency pulse of opposite polarity. The high frequency component is generated by the electromagnetic field in front of the armature and the low frequency component is generated by the relatively slowly changing magnetic field behind the armature. This type of sensor is referred to as a B-dot [69]. By using multiple B-dots and comparing the time between the pulses, a measure of the velocity of the projectile can be obtained.

While the B-dot is quite robust, it does have shortcomings. The primary lim-

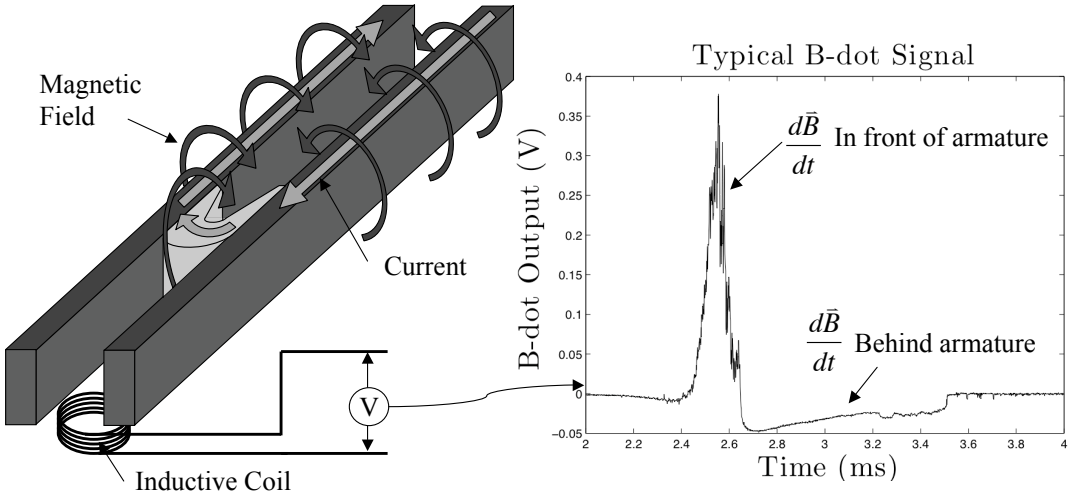


Figure 6.7: B-dot Signal for Measuring Armature Velocity

itation of this technique is its resolution. The spatial resolution is limited by the number of B-dots available. In addition to this, conventional techniques require one data acquisition channel per B-dot. This can cause the cost of measuring the velocity to become large very quickly. The combination of these two limitations typically limits the number of velocity data points during launch to below 20 points. This low resolution makes it very difficult to verify the basic dynamics of the armature during launch. A higher resolution system could allow for a better model of the launch dynamics to be developed (e.g. dynamic friction and wear). Other techniques such as Doppler-radar [83] and laser-Doppler [5] have been tried, but the standard technique is still to use a series of B-dots.

The velocity measurement technique presented in this section is a modified version of the conventional technique. To illustrate the difference between the two, an experiment was performed on the Cornell launcher where both techniques were applied at the same time. The results of that experiment will be presented next.

One technique to reduce the number of channels is to add up the signals from different B-dots to get one signal with a number of peaks. This idea can work under some circumstances, but typically the combination of positive and negative voltages gives a distorted signal that is difficult to interpret. One way to get around this problem is to insert a precision half-wave rectifier before adding the signals together. A diagram of the circuit used is shown in Figure 6.8. This gets rid of the distortion introduced by the low frequency negative troughs in the individual B-dot signals.

One other type of distortion must be considered before the system will work and that is interference between adjacent peaks. If two positive peaks are too close together in time then the peaks will be distorted when the two signals are added together. Fortunately, there is a simple solution to this problem as well; adding

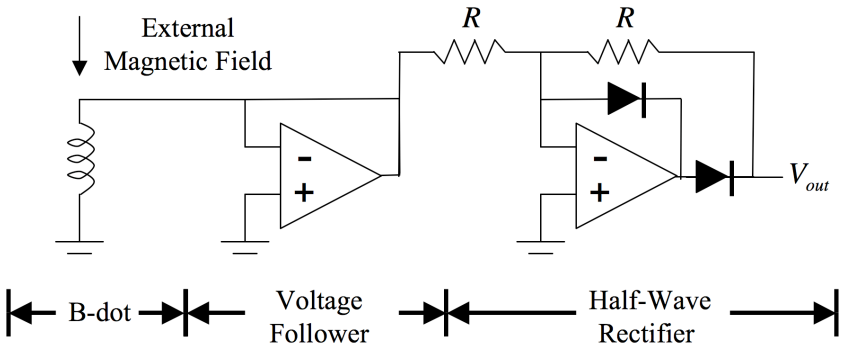


Figure 6.8: Precision Half-Wave Rectifier

together alternating B-dots separates the signals. A diagram of this technique is shown in Figure 6.9. This diagram illustrates how the resolution can always be increased by simply sampling on more channels. The nice thing about this technique is that it is possible to calculate the spatial resolution. It is dependent on the frequency of the pulse in front of the armature which can be calculated very roughly in the following way.

$$f_{pulse} \approx \frac{v_{arm}}{\beta L_{arm}} \tag{6.3}$$

Where $v_{arm}$ is the velocity of the armature as it passes the B-dot, $L_{arm}$ is the length of the armature. The quantity $\beta$ requires a bit more explanation. As stated before, the high frequency pulse in the B-dot signal represents the change in the magnetic field in front of the armature. The quantity $\beta L_{arm}$ represents how far this field extends in front of the armature. This means that $\beta$ represents the number of armature lengths that the magnetic field occupies in front of the armature. This means that it would have to be measured/simulated for any launcher which uses this technique. For the case of the Cornell launcher, a rough value for $\beta L_{arm}$ is $8\,cm$. This value was found experimentally through the tests outlined in this section by measuring the frequency of the pulse and the velocity of the armature.

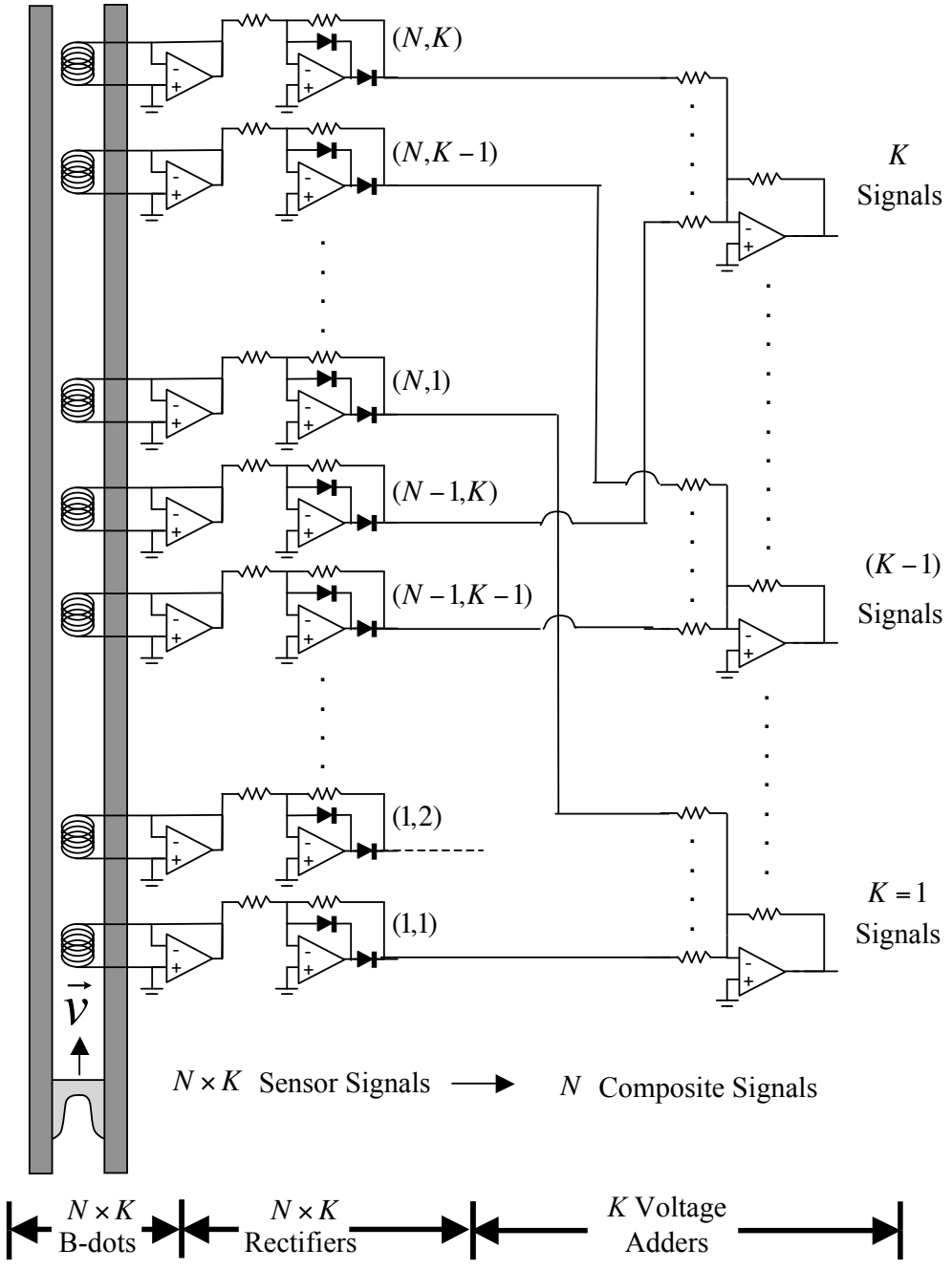


Figure 6.9: Composite B-dot System for Measuring Armature Velocity

With the frequency of the pulse calculated it is possible to write down the equation for the maximum spatial resolution for one channel.

$$w_{min} \approx \frac{v_{arm}}{2f_{pulse}} = \frac{\beta L_{arm}}{2} \tag{6.4}$$

The extra factor of two comes from the fact that only half of the pulse is seen. The interesting thing about this technique is that Equation 6.4 represents the maximum spatial resolution for one channel. The resolution can always be increased by adding more channels. For an evenly spaced array of B-dots separated into $N$ channels, the maximum resolution for this technique is given by the following equation:

$$w_{min} \approx \frac{\beta L_{arm}}{2N} \tag{6.5}$$

This assumes of course that the peaks between channels are actually distinguishable. In a real system, the practical limitation of this technique would be space for the sensors and cables.

Next, an experiment was put together to test this technique. This involved a series of ten B-dots added together over two different channels. A picture of these B-dots is shown in Figure 6.10. The spacing between adjacent B-dots is 4 $cm$, this is equal to the resolution as calculated from Equation 6.4. The b-dots pictured are just simple coils of 32 gage magnet wire with 75 turns each. They are embedded in a piece of polyethelene on top of which the launcher sits. For this test, the capacitor bank was charged to $222\,V$. As shown in Figure 6.8, the output of each sensor is sent through a voltage buffer and a precision rectifier. Alternating B-dot signals are then added together to give the final signal shown in Figure 6.11. This test used two channels, but probably would have also worked on a single channel. Also included are the signals from four of the individual B-dots for comparison. This is done to show that the rectifier circuit doesn't introduce a noticeable amount of distortion into the positive portion of the b-dot signal (phase shift or amplitude

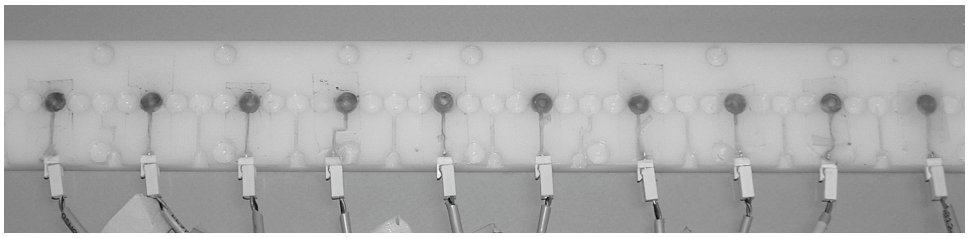

Figure 6.10: Picture of B-dot array used on Cornell launcher

variation). The precision rectifiers built for this experiment were found to operate without noticable distortion up to about 100kHz. The operational amplifiers used in this circuit have a gain bandwidth product of 100 MHz. Amplifiers with a gain bandwidth product of 4 Mhz were found to give about 4 kHz of bandwidth. This indicates that the nonlinear nature of the circuit pictured in Figure 6.8 tends to reduce the bandwidth by roughly a factor of 1000. Taking this into account, this set-up on the Cornell launcher should be capable of measuring velocities up to about 8 $km/s$. Unfortunately, this launcher is not capable of launch velocities this high so this cannot be tested.

Now that the B-dot signal has been obtained, it is possible to plot the velocity as a function of time. This is done by taking the spacing $\Delta x$ between the different B-dots and dividing it by the time $\Delta t$ between the signal peaks. For this test, $\Delta x$ was $4\,cm$ and the armature was started $1.8\,cm$ from the first B-dot. This gives the velocities plotted in Figure 6.12. The time for each data point is assumed to occur half way between the two peaks (i.e. plotted time is first peak time plus $\Delta t/2$).

The curves plotted with the experimental data in Figure 6.12 are calculated by integrating the acceleration of the armature throughout the launch. Neglecting friction and mass loss effects, the acceleration is given by the following relationship.

$$F_{prop} = \frac{L'I^2}{2} \quad \longrightarrow \quad a = \frac{L'I^2}{2m} \tag{6.6}$$

Since the current was measured for the launch, it can be squared and integrated

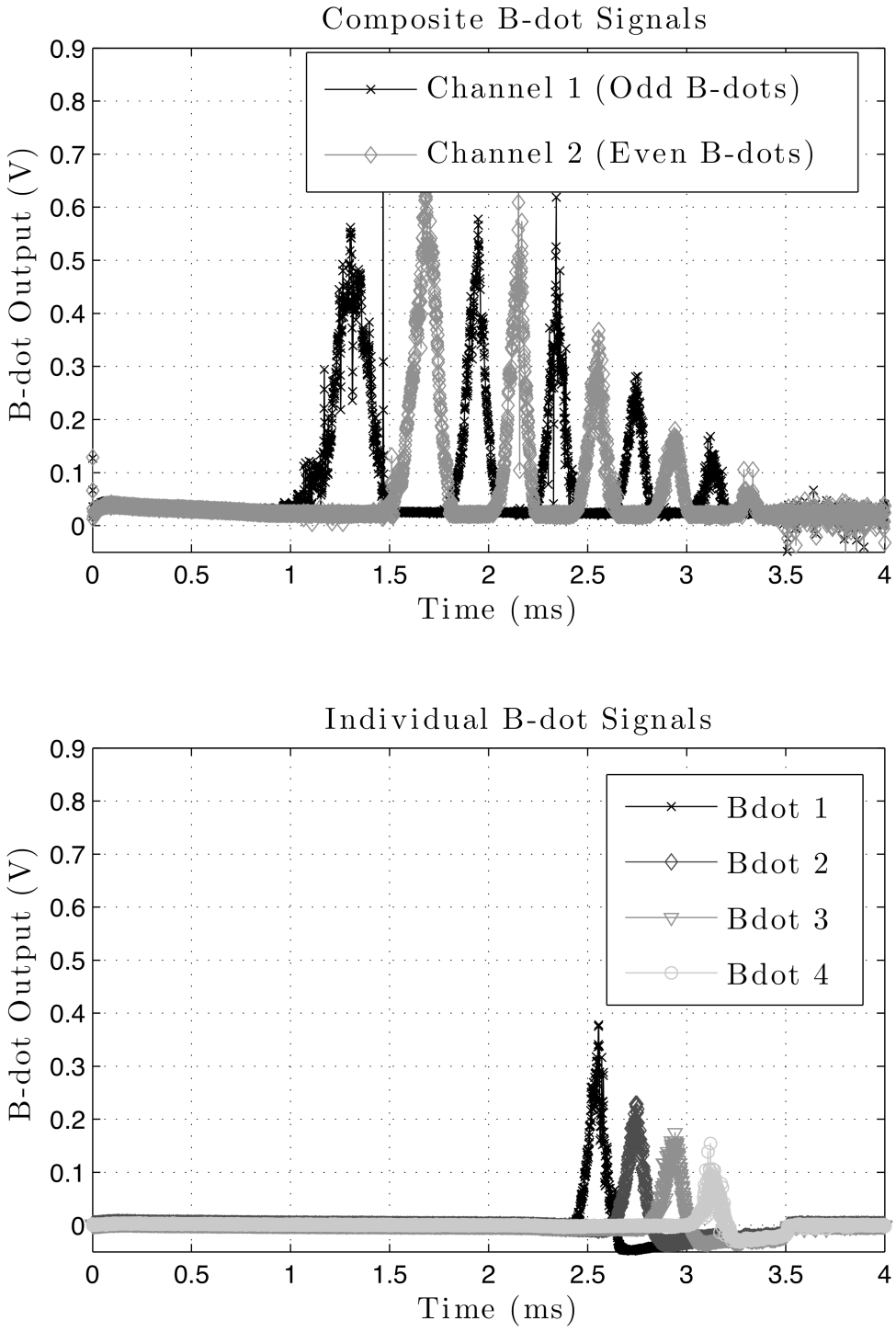


Figure 6.11: B-dot signals from composite circuit with ten B-dots(top) and signals from four of the individual B-dots (bottom).

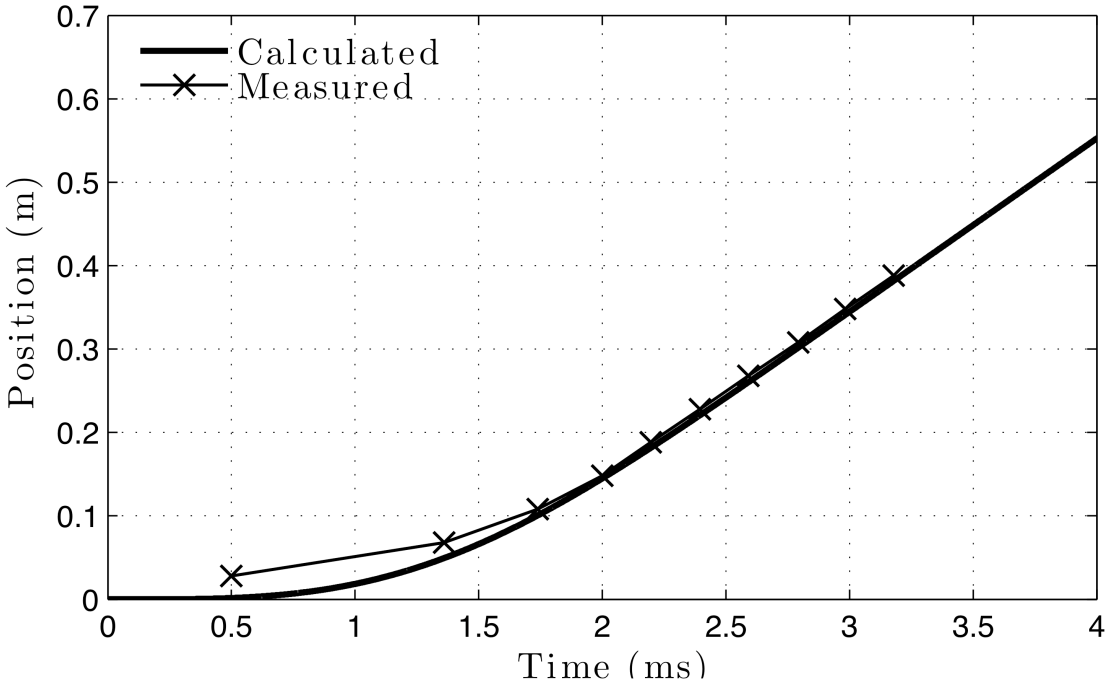


(a) Armature Position

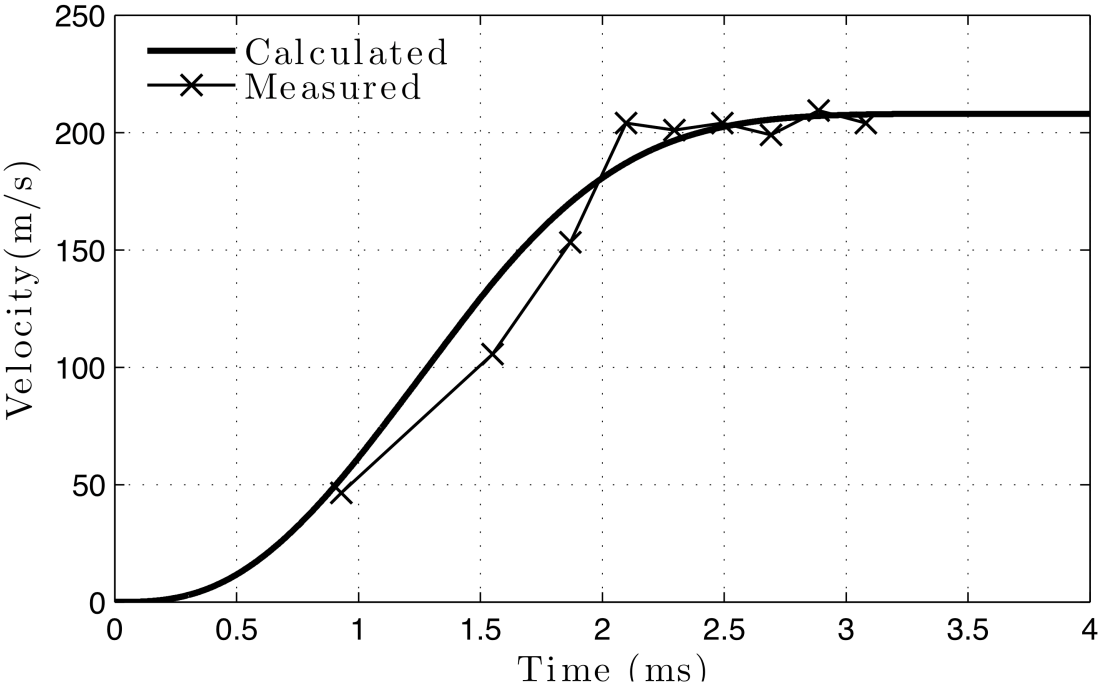


(b) Armature Velocity

Figure 6.12: Armature Velocity Measurement

to give an idea of the velocity of the launch. For the curve in Figure 6.12 the scaling constants of this curve, $L'$ and $m$, were set equal to $0.273\,\mu H/m$ and $0.08\,g$ (from Section 6.1). As one can see, the model fits the data pretty well using these parameters. This is actually somewhat surprising because approximately 2/3 of the armature melted during this launch. This means that the mass-loss term should not have been neglected. This highlights the need for a high resolution measurement system. If higher resolution techniques were available then it might be possible to measure quantities such as dynamic friction and wear (i.e. mass-loss). Unfortunately, this is not possible with the system described here, but a Doppler sensor may be capable of making these measurements. The next section will address the requirements for this type of system.

## 6.3 Parameter Estimation Techniques for Friction and Wear Measurements

High resolution measurement techniques using the Doppler effect do exist for in-bore measurement of armature velocity (See [5] and [83]). Unfortunately these techniques are not used widely in experiments. This section will illustrate how parameter estimation techniques could be used with these systems to measure more than just the velocity of the armature. Specifically this section will cover the use of parameter estimation for the measurement of in bore armature wear and friction. As stated in the previous section, the B-dot system used in most launchers is not capable of making these measurements. Therefore, one of the goals of this section will be to outline the basic requirements for a system to make these measurements. This will be accomplished by modeling a rail launcher with an assumed physical model and then attempting to calculate various parameters

of that model using parameter estimation. The specific parameters that will be used in this section will be similar to the Cornell launcher, but the basic model is general enough to be applied to other launchers.

### 6.3.1 Basics of Parameter Estimation

This section will outline the basic principles of parameter estimation. Only the basic equations necessary for the calculations in this dissertation will be presented. A more complete explanation can be found in a number of books (e.g. see [107], [89] or [75]).

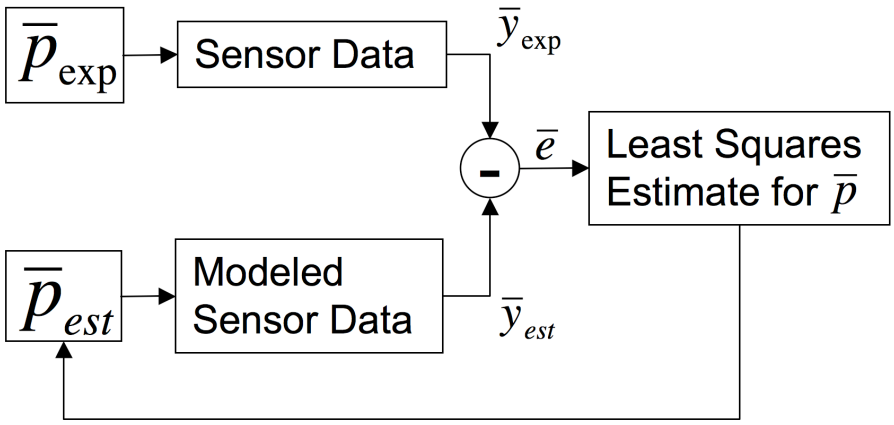


Figure 6.13: Flow Diagram for Basic Parameter Estimation Routine

In essence, parameter estimation uses fitting routines to fit a system, usually defined by a differential equation, to a set of data. The basic principle behind this is shown in Figure 6.13. An estimate of the parameters $\bar{p}_{est}$ is given and then a simulation of the system using $\bar{p}_{est}$ is generated. The output of that simulation is compared to experimental data and a new value of $\bar{p}_{est}$ is generated. The whole process is repeated and when this is done in a systematic way it is possible to

converge on a set of parameters $\bar{p}_{est}$ that are close to the real system $\bar{p}_{exp}$.

The first step in putting together a parameter estimation scheme is to develop a model for the physical system. This step is specific to the system being looked at and will be covered in detail in the next section. Once the model is developed, an estimation scheme must be chosen. As indicated in Figure 6.13 the calculations in this thesis will use the least squares method. This method starts by calculating the error $\bar{e}$ (also called the residual) in the solution generated by the computational model as shown in Figure 6.13.

$$\bar{e} = \bar{y}_{exp} - \bar{y}_{est} \tag{6.7}$$

The residual is then formed into the loss function $\Phi(\bar{p})$ which can be written as follows.

$$\Phi(\bar{p}) = \frac{1}{N}\bar{e}^T\bar{e} \tag{6.8}$$

Where $N$ is the number of data samples. The loss function gives a measure of how close the model is to the experimental system. The next step is to minimize the loss function with respect to the parameters. This minimization can be accomplished using many different techniques. For the problems in this dissertation, Newton's method is used (see [75] for an in-depth discussion of this method). Newton's method involves modifying $\bar{p}$ by an amount $\Delta\bar{p}$ given by the following relationship.

$$\Delta\bar{p} = H^{-1}\frac{\partial\Phi(\bar{p})}{\partial\bar{p}} \tag{6.9}$$

Where $H$ is the Hessian matrix given by the following relationship.

$$H_{ij} = \frac{\partial^2\Phi(\bar{p})}{\partial\bar{p}_i\partial\bar{p}_j} \tag{6.10}$$

The parameter estimate is changed to $\bar{p}_{est} - \Delta\bar{p}$ and the whole process is repeated until $\bar{p}_{est}$ approaches $\bar{p}_{exp}$. For this to occur, the model must be a reasonable approximation to the physical system and the initial value of $\bar{p}_{est}$ must be close to the experimental value.

In addition to calculating the parameters, the theory offers a structure for calculating the uncertainty in those parameters. This is done by looking at the diagonal elements of the covariance matrix.

$$cov\{\bar{p}\} = \sigma^2 H^{-1} \tag{6.11}$$

Where $\sigma$ is the noise variance in the signal (assumed to be gaussian). If $\sigma$ is unknown then it can be approximated by the following relationship.

$$\sigma^2 = \frac{\bar{e}^T \bar{e}}{N - n} \tag{6.12}$$

Where $N$ represents the number of data points and $n$ represents the number of parameters. Using these relationships it is possible to write the value of the parameter vector including uncertainty.

$$\bar{p} \pm \sigma \sqrt{Diagonal\{H^{-1}\}} \tag{6.13}$$

This gives a measure of the accuracy of the model and the parameter estimates. It is important to note that these uncertainty calculations assume a random noise and a correct model structure. Both of these assumptions are valid for the calculations that will be presented in this chapter. In general, however, they will not be valid. This means that these uncertainties should be treated carefully.

This gives the basic foundation to carry out some parameter estimation calculations. This section was only intended to give a very basic introduction to the concept of parameter estimation. The reader is referred to the literature for a more in depth discussion of the subtleties of this process (See [107], [89] or [75].

### 6.3.2 Static Friction Model

This section will outline the basics of measuring a constant friction force. The first step in this process will be to model an ideal electromagnetic launcher with a

known friction force. The armature velocity will be extracted from this model and noise will be added to simulate the noise of a sensor. The computational model will then be run again using a value for the friction force that differs by 40%. This represents the initial guess of the parameter $\bar{p}_{est}$ in Figure 6.13. The velocity of the armature will then be compared to the noisy data and the friction parameter will be modified using the least-squares technique described in the previous section. This process is then repeated multiple times to give the final estimate of the parameter. This will be done for different levels of sensor noise to give an idea of what the requirements on the sensor system for measuring this parameter would be.

The launcher will be simulated using the electromechanical rail launcher model described in Section 1.1.3. For the case of a constant friction force $F_\mu$, the equation of motion is as follows.

$$m\ddot{x} = \frac{1}{2}\dot{Q}^2 L' - sign(\dot{x})F_\mu \tag{6.14}$$

$$(L_0 + L'x)\ddot{Q} + (R_0 + L'\dot{x})\dot{Q} + \frac{Q}{C_0} = 0 \tag{6.15}$$

Where $Q$ is the charge on the capacitor bank and $x$ is the position of the armature. A description and value for the other parameters is outlined in Table 6.1. It is interesting to note that the resistance in this model is assumed to be constant. In reality, the resistance of the contact between the armature and the rail will change during the launch. Parameter estimation could be used to quantify this change if it were coupled with the proper model. The values given in this table are the assumed values for the known model. In this section, all of them will be assumed to be known except the friction force $F_\mu$. This is done for the sake of simplicity but multiple parameters can be included in the estimation without too much difficulty. It should be also noted that the resistance value in Table 6.1 was chosen so that the current would be of the same order of magnitude as the experiments in the previous sections. Also listed in Table 6.1 is the assumed value for the initial

voltage on the capacitor bank $V_0$. This is needed as an initial condition for solving the system.

Table 6.1: Assumed Model Parameters

| Symbol | Description | Assumed Value |
|---|---|---|
| $L'$ | Inductance Gradient of Launcher | $0.273\,\mu H/m$ |
| $L_0$ | Added Inductance of Launcher | $11.7\,\mu H$ |
| $C_0$ | Capacitance of Power Supply | $0.0804\,F$ |
| $R_0$ | Resistance of Launcher | $0.015\,\Omega$ |
| $m$ | Mass of Armature | $0.08\,g$ |
| $F_\mu$ | Constant Friction Force | $1\,N$ |
| $V_0$ | Constant Friction Force | $220\,V$ |

To give an example, the parameters in Table 6.1 were modeled and the velocity of the armature was calculated. For this example the velocity was sampled at a rate of $100\,kHz$ and random noise with a magnitude of $20\,m/s$ was added to the velocity signal. This signal is plotted in Figure 6.14 labeled simulated experiment. The simulation was run again using $F_\mu = 0.6$ as a guess for the friction force; this is also plotted in Figure 6.14 labeled guess. This guess was put through the least squares fit and iterated 20 times and the final result of this iteration process is also plotted in Figure 6.14 labeled fit. The calculated fit value of the friction force was found to be $F_\mu = 0.99 \pm 0.04$($F_\mu = .9867$ without rounding). This means that if this were a real experiment and the model presented here was a good approximation for that experiment it would be possible to measure the friction force to within about 4% with this sensor. Since the 'experimental' data was simulated, the actual accuracy is also known and it is roughly 1.3%. For this type of calculation the actual accuracy and the calculated uncertainty will depend on the noise level of the signal, and the sampling rate of the velocity sensor. In a real experiment, only the calculated uncertainty will be known and it will also depend on the accuracy of the model being used in the fitting program.

Requirements for sensing can be looked at by doing this calculation many times

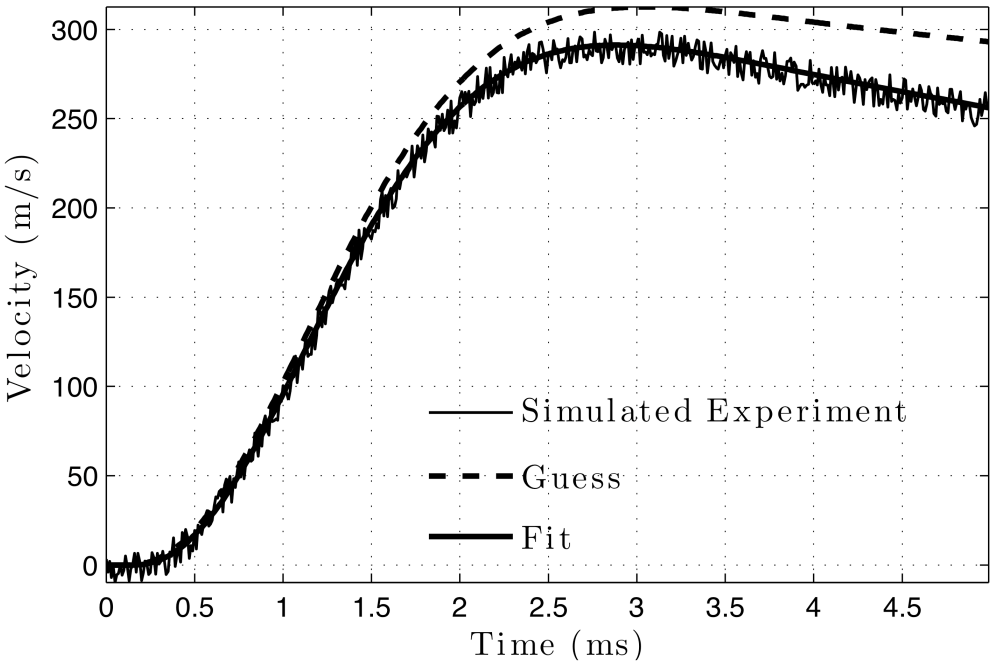


Figure 6.14: Example Friction Calculation

for different values of sampling rate or noise level. This was done for the case of different sensor noise levels. This case is pictured in Figure 6.15, the sampling rate was fixed at $100\,kHz$ and the noise level was varied between $5\,m/s$ and $75\,m/s$. In this plot, the actual percent error is plotted along with the calculated uncertainty from the least squares fit. Each data point in this plot was calculated 30 different times using a different random noise each time. This was done because each solution uses different random noise and gives a slightly different value for the uncertainty. These 30 different values are where the error bars in Figure 6.15 came from. They illustrate the spread in the accuracy that one might expect when attempting this type of measurement. Figure 6.15 was generated by running the parameter estimation program 450 times. Because there are 20 iterations, each time this routine is executed this amounts to numerically solving Equation 6.14 approximately 9000 times.

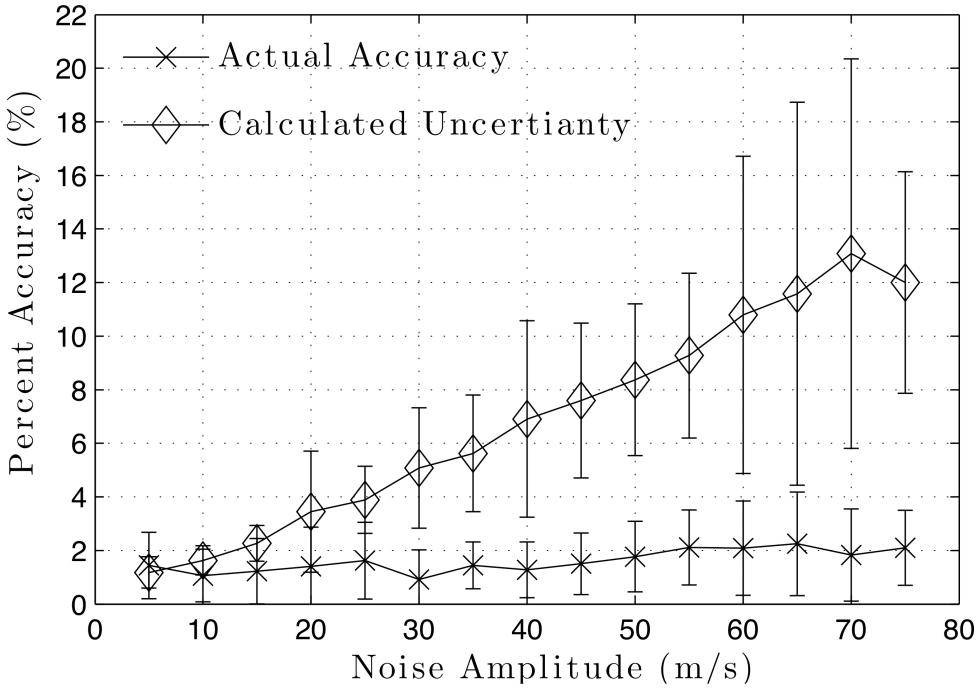


Figure 6.15: Friction Uncertainty for Varying Noise Level

For the plot pictured in Figure 6.15 the calculated uncertainty shows a strong dependence on the noise amplitude while the actual accuracy does not. This is probably an artifact of the fact that the model being used here is exactly correct. If the noise level is pushed close to the total signal level then this actual accuracy will grow substantially. It will also grow if the sampling rate is reduced. It is important to remember that this number will be unknown in a real experiment and is of very little practical use. It is only shown in Figure 6.15 for the sake of reference. The calculated uncertainty on the other hand will be known. Figure 6.15 indicates that if one wanted to make a measurement of the friction with an uncertainty of 10% the noise level of the sensor would have to be smaller than approximately $40\,m/s$ if the sampling rate were $100\,kHz$. This requirement is well beyond the capabilities of a reasonable B-dot based system. This highlights the need for better velocity measurement techniques in electromagnetic launcher experiments.

# Part III

# Superconducting Homopolar Motor Brushes

# Chapter 7
# Homopolar Motor Brush Calculations

As described in Section 1.2, the homopolar motor associated with the research in this dissertation uses metal fiber brushes for current transfer (see Figure 1.4). These brushes operate under different conditions than conventional brushes (see Figure 1.1). Specifically, they they operate under considerably smaller contact pressures for a given current. This chapter introduces the properties of these homopolar motor brushes. Then an introduction to the basics of electrical contact theory is given and this is used to develop a statistical model for the compliance of straight fiber brushes. The intent of this model is to predict the load-deflection and resistance deflection curves of the brush fiber. An attempt is also made to develop an idealized model for the interaction of the fibers under compression.

## 7.1 Homopolar Motor Brushes

Before getting into the calculations it is necessary to discuss the characteristics of these brushes in a qualitative sense. There have been many iterations of the brushes in this motor and so it is necessary to discuss the qualitative differences between the different brushes. Pictures of some of the brushes are shown in Figure 7.1. These brushes were manufactured by SSI and Hipercon and they have very different constructions. The Hipercon brush is made of a tangled mesh of irregular copper fibers and the SSI brush is constructed from straight round fibers. Each of the brushes is wrapped with copper wire. The SSI brush uses a mesh and the Hipercon brush is wrapped with individial wires. The differences in the construction of these brushes gives them very different mechanical properties.

The fibers in the Hipercon brushes are irregular in nature. To illustrate, SEM

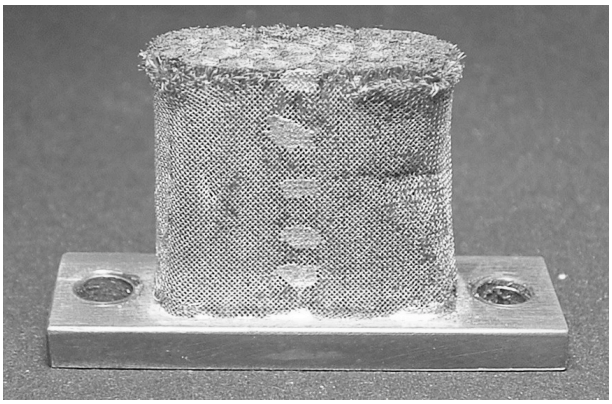

(a) SSI Brush

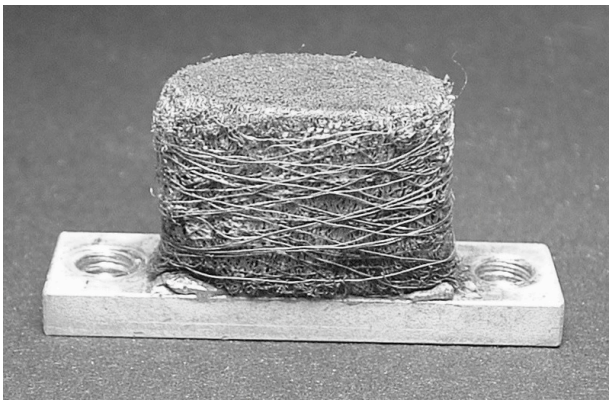

(b) Hipercon Brush

Figure 7.1: Different Copper Fiber Brushes

pictures were taken of some of these fibers. These pictures are shown in Figures 7.2-7.3[1]. These pictures clearly show that the fibers are very irregular in cross section and that the diameters of these fibers appear to vary from 20 $\mu m$ to 200 $\mu m$, but typical fibers are between 50 and 70 $\mu m$. The irregularity of the shape of these fibers means the brush is more of a tangled mesh of fibers than a series of parallel fibers. This irregular construction is not seen in the later versions of the SSI brush pictured in Figure 7.1; where round, straight fibers were used ($\approx$ 60 $\mu m$ in diameter). It is not clear from the analysis done here whether one of these constructions is better than the other.

[1]Pictures courtesy of Alex Holiat of the Cornell Materials Science Department

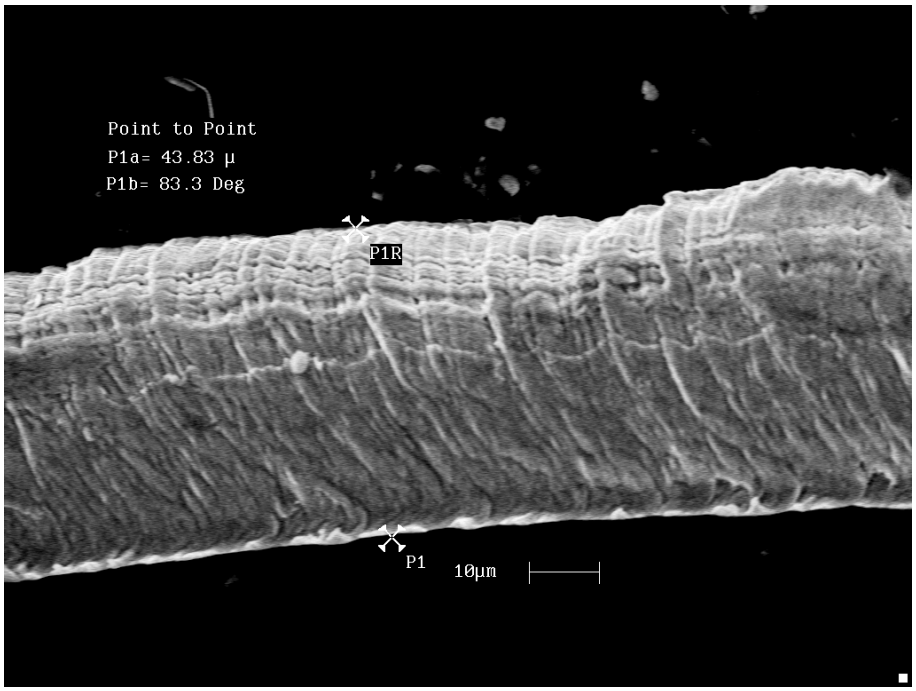


(a) Typical Fiber

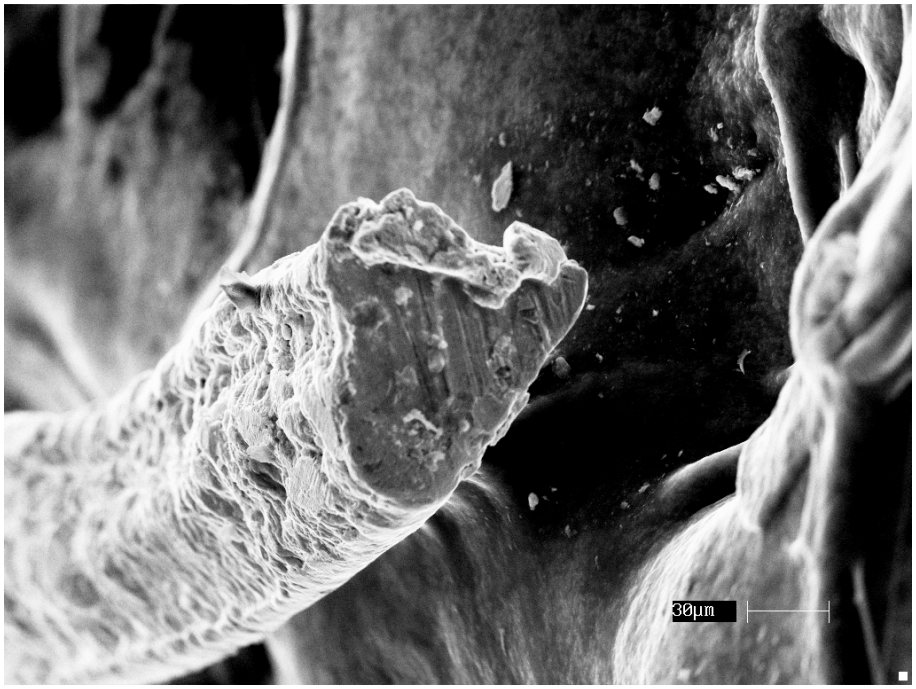


(b) Typical Fiber Cross-Section

Figure 7.2: Typical Homopolar Motor Brush Fiber SEM Pictures

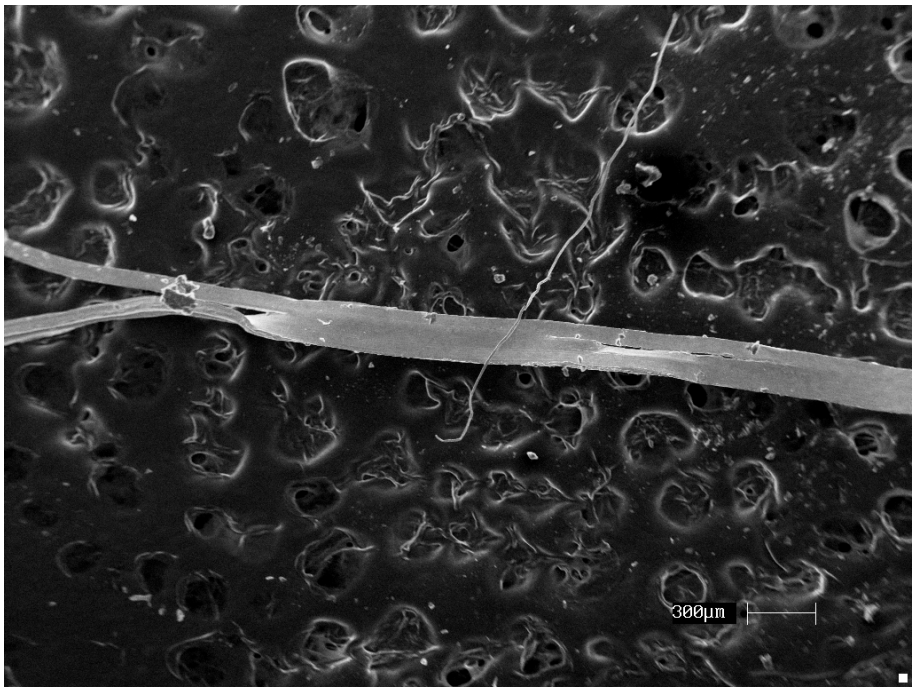


(a) Atypical Split Fiber

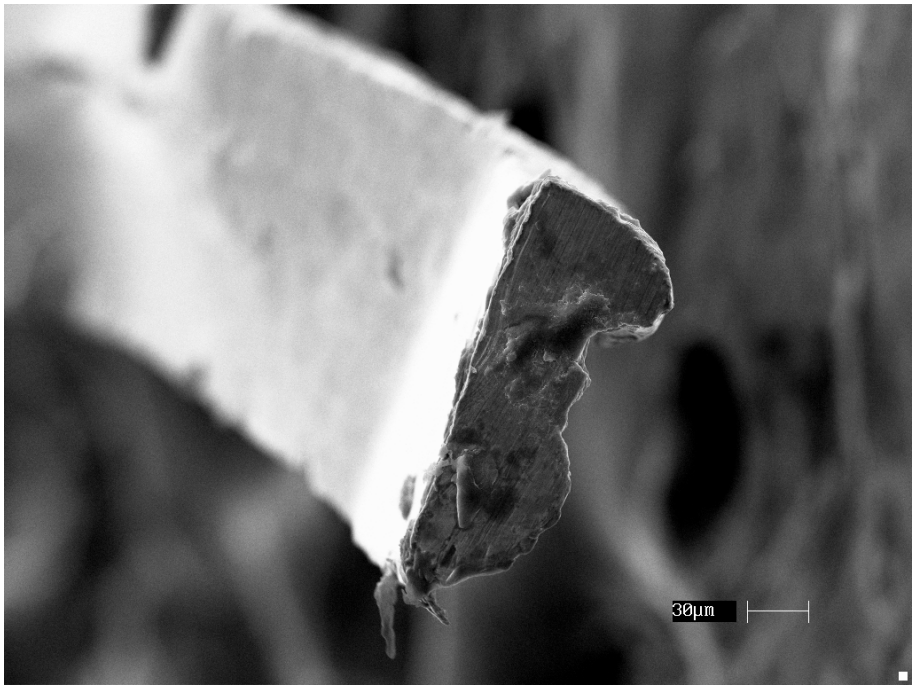


(b) Atypical Fiber Cross-Section

Figure 7.3: Atypical Homopolar Motor Brush Fiber SEM Pictures

## 7.2 Statistical Treatment of Electrical Contacts

On the micro scale, all electrical contacts are rough, as shown in Figure 7.4. The classic method for the treatment of electrical contacts is to use some form of statistical analysis to model the surface roughness. The basic principle of this method is outlined in most tribology texts [10]. Basically, rough surfaces are modeled as a series of bumps whose heights are defined by a distribution fucntion $\phi(z)$ which is usually taken to be a Gaussian. The points of contact are typically treated as spherical bumps and in this section, one of the surfaces will be treated as being nominally flat. For this case, it is possible to characterize both the mechanical and electrical behavior of the contact interface.

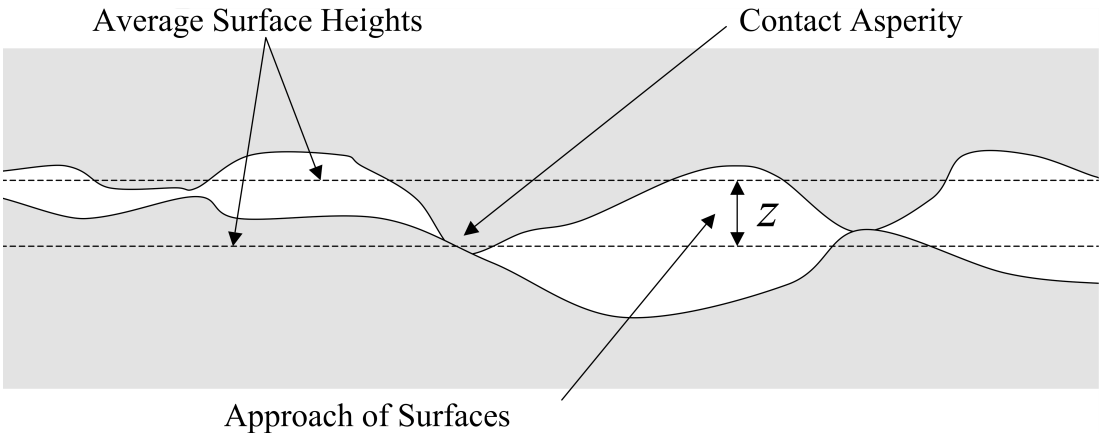


Figure 7.4: Rough Contact Surfaces

For the mechanical characterization, all that is needed is a force deflection curve for the individual contact points. Then it is possible to calculate the total force statistically. When the problem is treated with a continuous distribution of heights this calculation is carried out as follows.

$$F(z) = \int_z^\infty F_s(s-z)\phi(s)ds \tag{7.1}$$

Where $F_s(s-z)$ is the load deflection curve for a single contact asperity and z is

the approach of the average of the two surfaces as shown in Figure 7.4. To treat this case discretely, the force deflection curve is a sum over the individual forces $F_s(z - z_i)$.

$$F(z) = \sum_{i}^{z>z_i} F_s(z - z_i) \tag{7.2}$$

Where the summation is only taken over the contacts with heights greater than the distance between the mean of the two surfaces (i.e. $z > z_i$). Electrical characterization consists of defining the resistance of each individual contact. This can be accomplished with a load-resistance curve or resistance-deflection curve. Since the resistances of each contact will add in parallel, the total resistance for a continuous model can be integrated as follows.

$$R(z) = \frac{1}{\int_z^\infty \frac{1}{R_s(z-s)}\phi(s)ds} \tag{7.3}$$

The discrete version is as follows.

$$R(z) = \frac{1}{\sum_i^{z>z_i} \frac{1}{R_z(z-z_i)}} \tag{7.4}$$

These equations outline the essential calculations that can be carried out in a multi-point electrical contact problem where the asperity heights are statistically distributed.

### 7.2.1 Mechanical and Electrical Characterization of the Contact

Typically, the individual bumps on a surface are treated as small hemispheres as shown in Figure 7.5. Mechanically, the contact between a spherical bump and a nominally flat surface can be described using the Hertz contact model [10]. The load-deflection curve of a Hertz contact is given by the following relationship.

$$F(\omega) = \frac{4E^*\sqrt{R}}{3}\omega^{3/2} \tag{7.5}$$

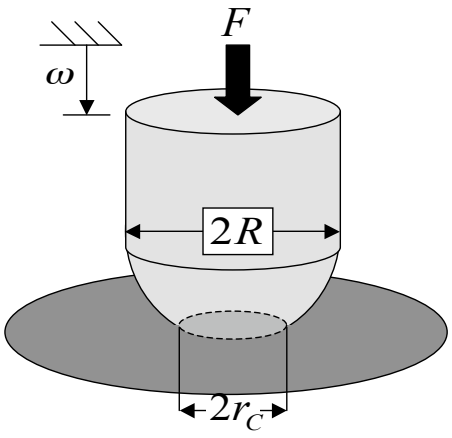


Figure 7.5: The Hertz Contact

Where the quantities R and $\omega$ are the radius and deflection of the spherical bump as shown in Figure 7.5. The parameter $E^*$ is the composite modulus of the two materials[2]. For the case of similar materials, which is what will be considered in this thesis, $E^* = E$. The contact radius for a particular load is given by the following relationship.

$$r_c(F_c) = \left(\frac{3F_cR}{4E^*}\right)^{1/3} \tag{7.6}$$

Combining this equation with the force-displacement relationship gives a radius-deflection relationship [72].

$$r_c(\omega) = \sqrt{R\omega} \tag{7.7}$$

These equations give the basic mechanical relationships of individual electrical contacts under small loads. For larger loads, the individual contacts deform plastically and the load deflection curve must be modified [47]. The small load situations seen in the homopolar motor only require the elastic model. The intent of using fiber brushes is specifically to stay below the plastic limit. This is because when one goes above this limit, increased wear can occur.

It is important to note that the Hertz contact model does not take into account

[2]See Bhushan [10] Table 4.2.1

the fiber structural stiffness. This is because this theory is typically applied to solid bodies which will not buckle under the applied loads The fibers in the homopolar motor brushes are very thin and will buckle under the applied loads and so the structural stiffness must be taken into account in the load-deflection model.

The operating load of the brushes in the homopolar motor is in the range of 2 Newtons. This is very roughly equivalent to the combined critical buckling load of about 1000 of the individual fibers. This highlights the fact that the load deflection curve must be modified to take this buckling into account. In general, the load-deflection curve of a post-buckled fiber is non-linear but for small deflections it can be approximated by a line. The equation for this line is as follows.

$$F_s(z) = k_b z + F_{cr} \tag{7.8}$$

Where $k_b$ is the approximate buckled stiffness and $F_{cr}$ is the critical load which is given by the following relationship.

$$F_c = \frac{\pi^2 E J}{L^2} \tag{7.9}$$

Where $E$ is the elastic modulus of the fiber, $J$ is the cross-sectional moment of inertia and $L$ is the length. Equation 7.8 assumes that the pre-buckled fiber stiffness is much greater than the post buckled stiffness. For the fibers in the hompolar motor, the difference between these stiffnesses is on the order of $10^5$ so this is a reasonable assumption. Another way to state this assumption is that as soon as a fiber comes into contact, it is buckled.

Since the structural stiffness of the fibers is significantly smaller than the effective stiffness of a Hertz contact then the contact equations will be dominated by the buckled fiber load deflection curve (Equation 7.8). This will affect how the contact radius is calculated. For this case, the contact radius is calculated as

follows.

$$r_c(z) = \left(\frac{3R(k_b z + F_{cr})}{4E^*}\right)^{1/3} \tag{7.10}$$

Where the deflection of the Hertz contact has been neglected. The relationships for the contact resistance are dependent on this radius so it is important to calculate it as a function of the dominate load-deflection curve. This equation allows for the full statistical load-deflection relationship to be written. This relationship for the full brush is calculated as follows.

$$F(z) = \sum_{i}^{z>z_i} (k_b(z - z_i) + F_{cr}) \tag{7.11}$$

Where, again, the structural stiffness of the fiber $k_b$ has been assumed to be considerably smaller than the effective stiffness of a Hertz contact (see Equation 7.5).

In addition to the mechanical characterization, it is necessary to present the electrical model. The basic quantity to model is the resistance of the contact. In electrical contact theory, each of these contacts is referred to as an a-spot [42]. The total resistance across an a-spot is given by three main components.

$$R_{tot} = R_b + R_c + R_f \tag{7.12}$$

The first qantuty, $R_b$, represents the bulk resistance of the material away from the contact. In the case of brush fibers, if there is one contact per fiber, this resistance is given by the following.

$$R_b = \frac{\rho A}{L} \tag{7.13}$$

Where $\rho$ is the resistivity of the fiber material, $A$ is the cross-sectional area of the fiber and $L$ is its length.

The second component, $R_f$, represents the film resistance. It is the resistance of any material layers between the two contact surfaces (oxides, contaminants, etc.). A basic relationship that can be used to approximate this resistance is as

follows [42].

$$R_f = \frac{\rho_f t}{A_c} \tag{7.14}$$

Where $\rho_f$ is the resistivity of the film, $t$ is the thickness and $A_c = \pi r_c^2$ is the area of the contact. This component of the resistance is very difficult to approximate in most situations because the composition of the film is typically unknown. In addition to this, the method of current transport can be either ordinary conduction or tunneling. This means that $\rho_f$ can be highly dependent on the film thickness [85]. For copper contacts, an approximate value of $\rho_f t$ is $1.5 \times 10^{-}12\,\Omega m^2$ [3]. The actual value will depend heavily on the atmosphere that the copper is kept in so this is only a rough scale parameter.

The final component represents the constriction resistance. As the name implies, this term comes from the fact that the current is constricted as it passes through the small contact points. For the case of circular contact points, this component of the resistance is given by the Holm constriction resistance [42].

$$R_c = \frac{\rho}{2r_c} \tag{7.15}$$

These equations can be combined statistically as indicated in the previous section to give the overall resistance of the brush. This resistance is calculated as follows.

$$\begin{aligned} \frac{1}{R(z)} &= \sum_i^{z>z_i} \frac{1}{R_b(z-z_i) + R_c(z-z_i) + R_f(z-z_i)} \\ &= \sum_i^{z>z_i} \frac{1}{\frac{\rho\pi(r_c(z-z_i))^2}{L} + \frac{\rho}{2r_c(z-z_i)} + \frac{\rho_f t}{\pi(r_c(z-z_i))^2}} \end{aligned} \tag{7.16}$$

Where $r_c(z - z_i)$ is given by Equation 7.10. Using these relationships it is possible to estimate the load-deflection and resistance-deflection curves for a metal fiber brush. This will be done in Chapter 8.

## 7.3 Fiber Interaction Effects

The fibers in the brush are not completely independent of each other. They are close enough to one another to interact. One way to consider this interaction is to look at buckling of the fibers. The idea behind this is that if two fibers are in contact with one another, they will tend to buckle differently than if they were isolated. The contact between fibers act like discrete supports transverse to the fiber axis. If these supports were rigid and evenly distributed along the length of the fiber, then the fiber will buckle with multiple zero deflection nodes. A few of these different buckling modes are pictured in Figure 7.6. This concept is of course highly idealized, but if enough is known about the brush construction then this model could give insight into the amount of inter-fiber interaction under load.

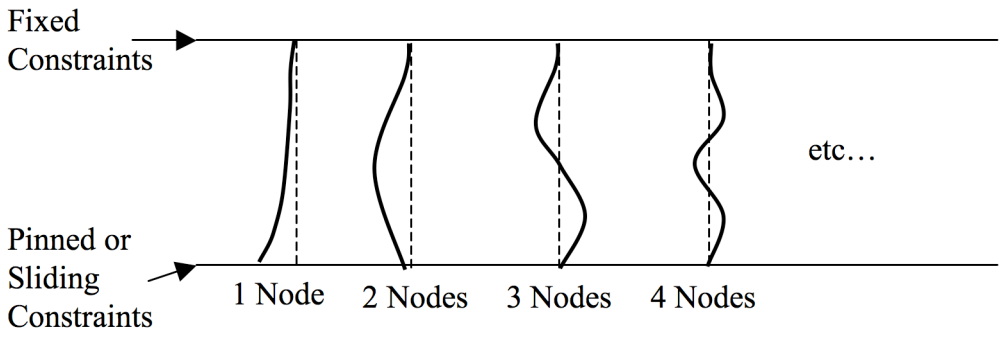


Figure 7.6: Buckled Fiber Mode Shapes

With this conceptual model, a statistical distribution of fiber lengths, and Equations 7.11 and 7.16. it is possible to make a plot of the load-deflection and resistance-deflection curves for a fiber brush with interacting fibers. First, a statistical distribution of fiber lengths is generated, this is plotted in Figure 7.7. This distribution was generated using a gaussian with a standard deviation of $50\,\mu m$, and it is plotted about the average fiber length. The total number of fibers for

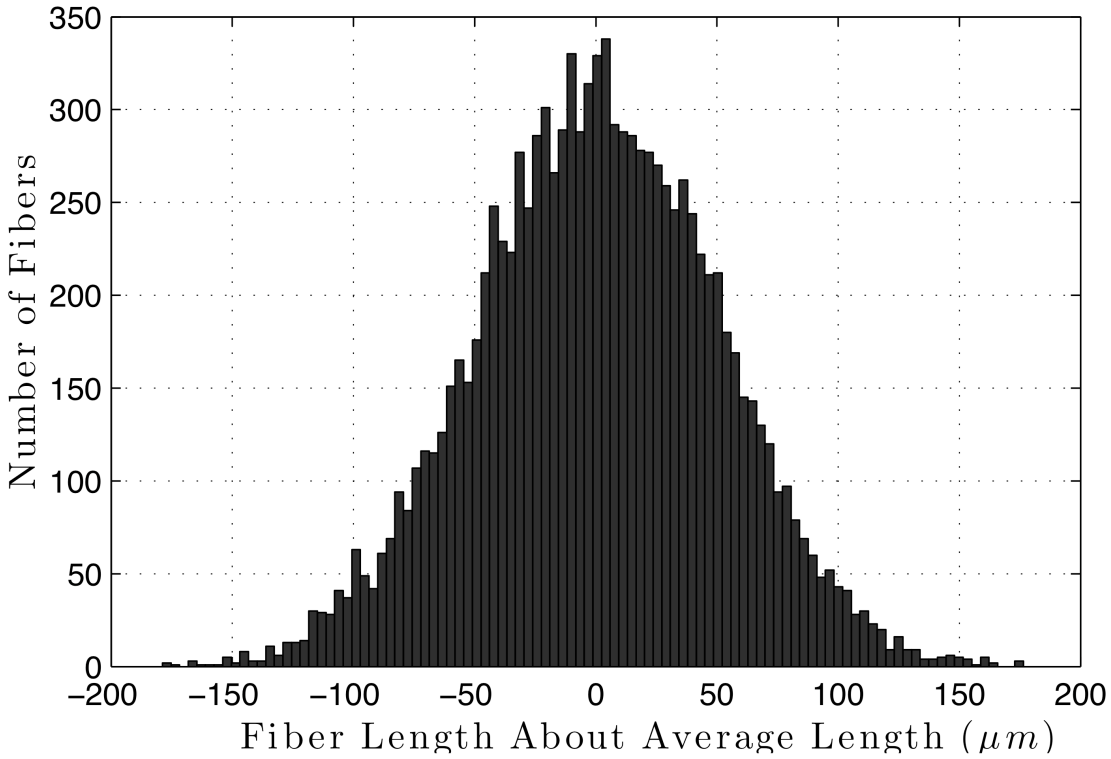


Figure 7.7: Assumed Fiber Length Distribution About Average Length

this distribution is $11,000$. To use equations 7.11 and 7.16 it is necessary to pick values for the fiber geometry and material as well as the stiffness of the fibers. For the sake of putting together an example, values of these parameters were chosen. For the plots in this section the fibers were assumed to be $1\,cm$ in length and have a radius of $70\,\mu m$. The material was assumed to be copper so the density was $8320\,kg/m^3$ and the elastic modulus was $120\,GPa$. The results of this calculation are plotted in Figure 7.8 for various values of $k_b$ including $k_b = 0$.

For this model the low-deflection loads are essentially independent of the buckled fiber stiffness. The stiffness seen in this region is primarily from the $F_{cr}$ term in Equation 7.11. The increases in the force in this region are due to the fact that additional fibers are being brought into contact and then buckled as the brush is compressed. In the large load region, differences are visible between the curves.

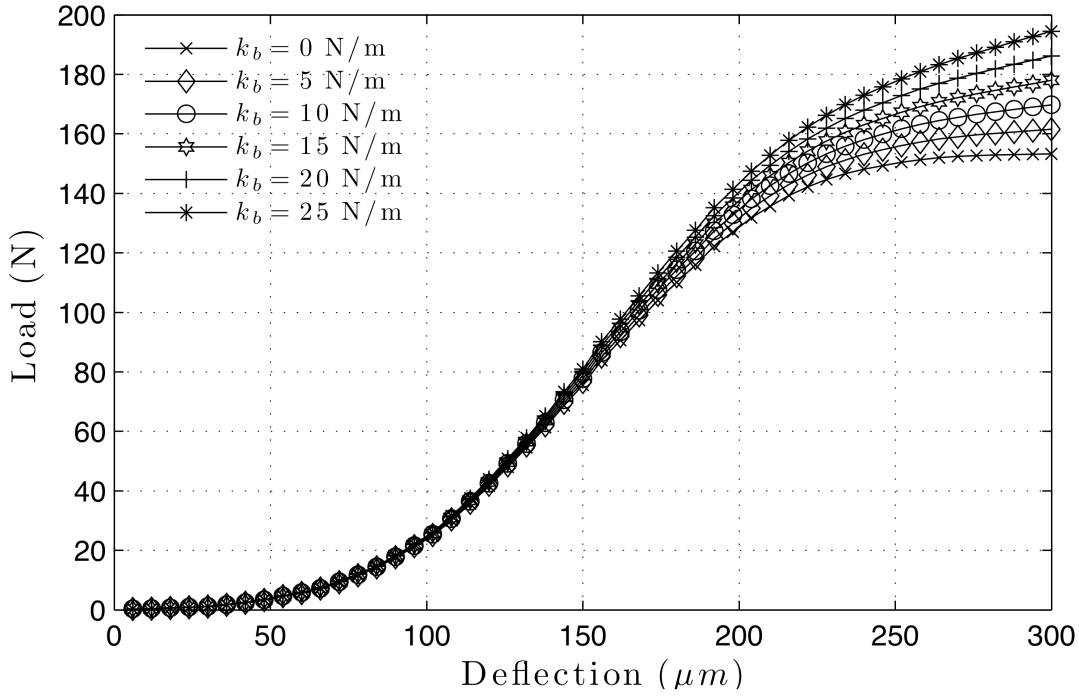


(a) Load Deflection Curve

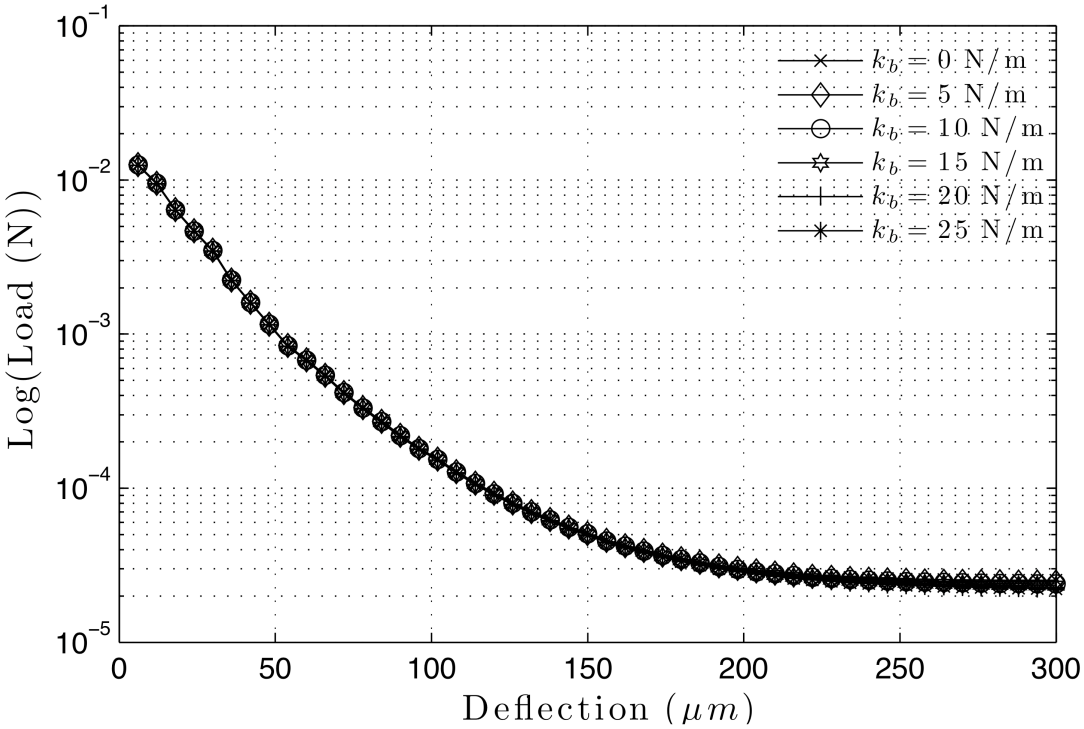


(b) Resistance Deflection Curve

Figure 7.8: Statistical Model With Different Fiber Stiffnesses

The additional stiffness in this region is due to the $k_b$ term in Equation 7.11.

The resistance curve does not show strong dependence on the value of $k_b$ either. It does, however, show strong nonlinearities in the low load region. This indicates that while the structural deformations do affect the overall contact resistance, the resistance curve will not be highly dependent on the specific fiber stiffness.

These observations mean that if this fiber interaction model is correct, it can only be tested for very large loads. Measurements of the load deflection curve for the homopolar motor brushes were taken, but unfortunately, these brushes could not be pushed this hard without being damaged. Only one sample of each brush was available so destructive testing was not an option. The experiments that were attempted will be presented in the next chapter.

# Chapter 8
# Homopolar Motor Brush Experiments

This chapter presents the experimental measurements that were taken with the metal fiber brushes. These consist of both static measurements of the entire brush structure as well as dynamic tests of the individual fibers.

From the static tests it is found that the static mechanical properties of the brush as a whole can vary significantly between different brushes of the same construction. This difference could be due to the differing wear rates of the brushes or uncertainties in the construction process. Either way, the compliance test presented in this section could be used as a quality control test to ensure uniformity of the brushes. Most of the brushes could be characterized by a zero stiffness offset and a linear stiffness constant that essentially constitutes a bilinear spring.

The dynamic tests were performed to see if the fibers of the tangled brush act in any way similar to simple straight fibers. Acoustic emission measurements of the brushes have been taken by researchers at the University of California at San Diego (UCSD) [53] and very high frequency vibrations were measured ($> 100\,kHz$). This section explores the vibrations of a single fiber to characterize the natural frequencies for the fibers in the homopolar motor brushes.

## 8.1 Static Measurements

A device was constructed to measure the stiffness of the electrical brushes. This device consists of a 250 g load cell placed between two different translation stages. The brush is attached to the load cell and then pushed against a flat copper surface. The change in distance between the two stages is measured using a linear variable differential transformer (LVDT). A picture of the device with a brush

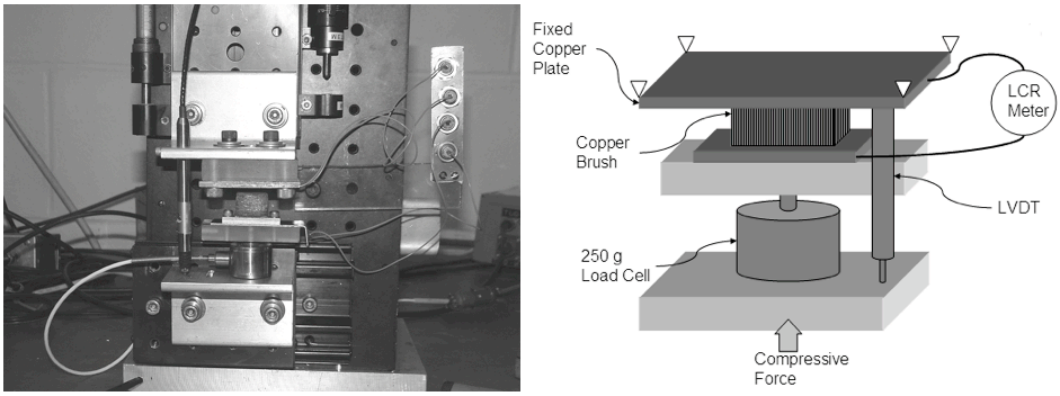


Figure 8.1: Brush Compliance Measurement Device

mounted to it is shown in Figure 8.1. Also included is a sketch of the device to help in illustrating its operation. The copper plate and brush are also attached to a precision inductance-capacitance-resistance (or LCR) meter (HP model number 4284A). This allows for electrical characteristics to be measured along with the mechanical.

Four different brushes were put through this experiment and the results are shown in Figure 8.2. The SSI brushes shown in these plots were new brushes and the hipercon brushes had been used in the General Atomics homopolar motor. Before the test, the copper plate was sanded and cleaned and the brush was very lightly sanded. This was done to try to reduce the effect of surface films on the measurement.

As one can see, the brushes exhibit drastically different load-deflection curves. From these plots it is possible to define an effective gap for each brush. This can be found by drawing a line parallel to the load deflection curve in the large deflection limit and following it down to the deflection axis. The point where it meets the deflection axis is the effective gap. An example of this effective gap is shown for one of the brushes in Figure 8.2. This gap qualitatively represents the width of the distribution of fiber lengths. What is interesting about this data is the

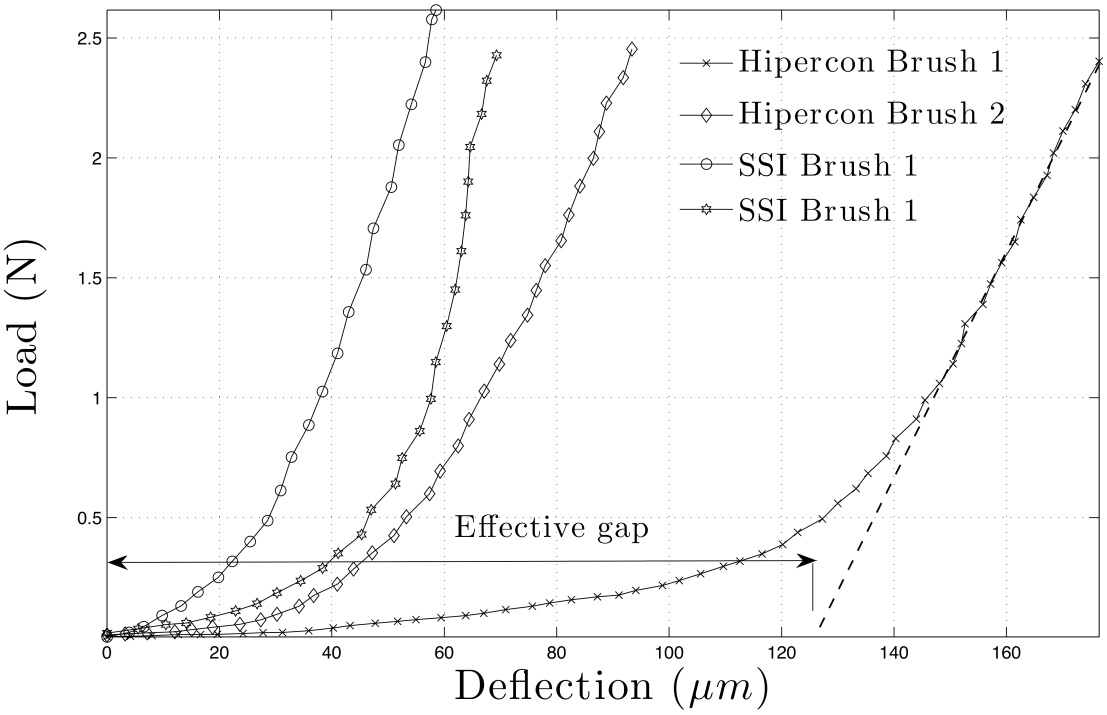


(a) Measured Load Deflection Curve

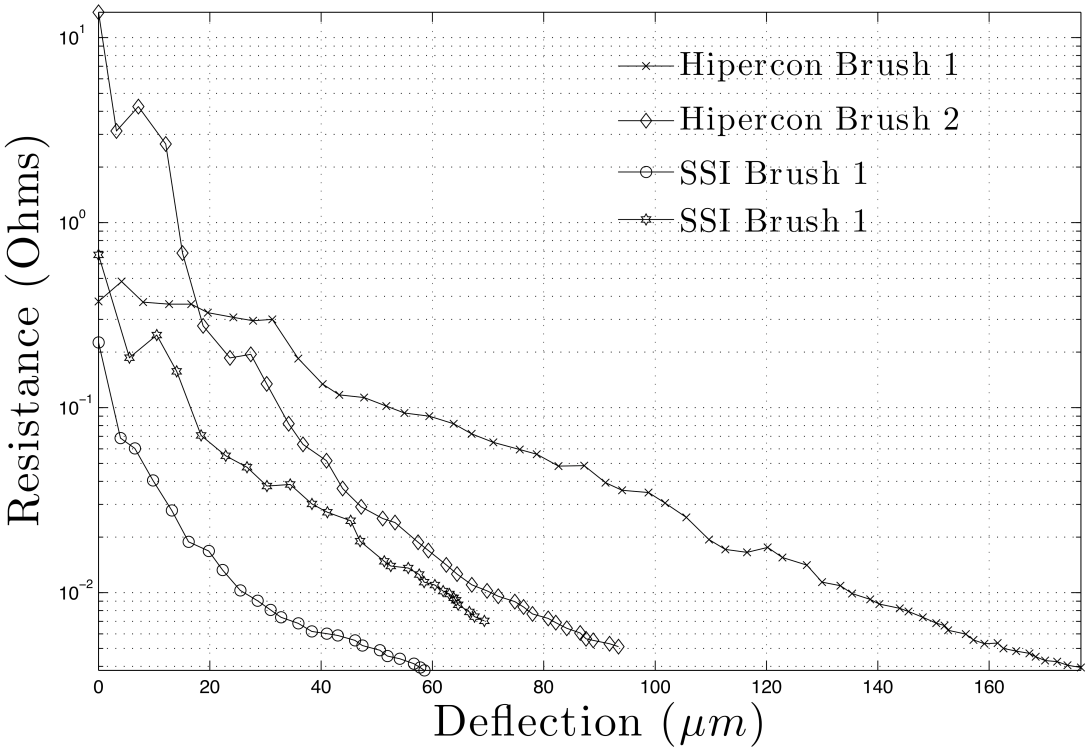


(b) Measured Resistance Deflection Curve

Figure 8.2: Axial Compression Measurement

drastic difference in the effective gaps for each brush. The two Hipercon brushes were made using the same technique and they exhibit drastically different load deflection curves. The only known difference between these two brushes is that one of them was on the positive voltage side of the motor and the other was on the negative side. It is possible that the effective gap difference was caused by the different wear rates on either side of the motor, but since no other brushes were available for testing we were unable to confirm this observation. Even if this is not the case, this measurement could work as a quality control test for the brushes as they are made. The wear rate of each fiber depends on the pressure between the fiber and motor pickup surface so uniformity of the mechanical behavior of the brushes would increase the predictability of the system as well as the repeatability of experiments carried out with the motor.

### 8.1.1 Comparison to Statistical Model

While it is not possible to test the fiber interaction model developed in Section 7.3, it is still useful to try to fit the model to the data for the straight fiber brush. The straight fiber brush is the one labeled SSI Brush 1 in Figure 8.2. This brush has straight, round fibers in contrast to the other brushes which had irregular shaped fibers such as those shown in Figures 7.2-7.3. For this brush, the average fiber length is $17.8\,mm$ and the average fiber diameter is approximately $60\,\mu m$. The spread in the fiber length distribution $\sigma$ was measured under a microscope. This was done by looking at the tips of the fibers from the side and scanning over the surface of the brush. The maximum and minimum fiber length could then be roughly gaged. This process gave value for $\sigma$ of approximately $30\,\mu m$. Since the brush was not pushed hard enough to measure the deflections due to the post-buckled stiffness, the parameter $k_b$ was set to zero for the comparison. These

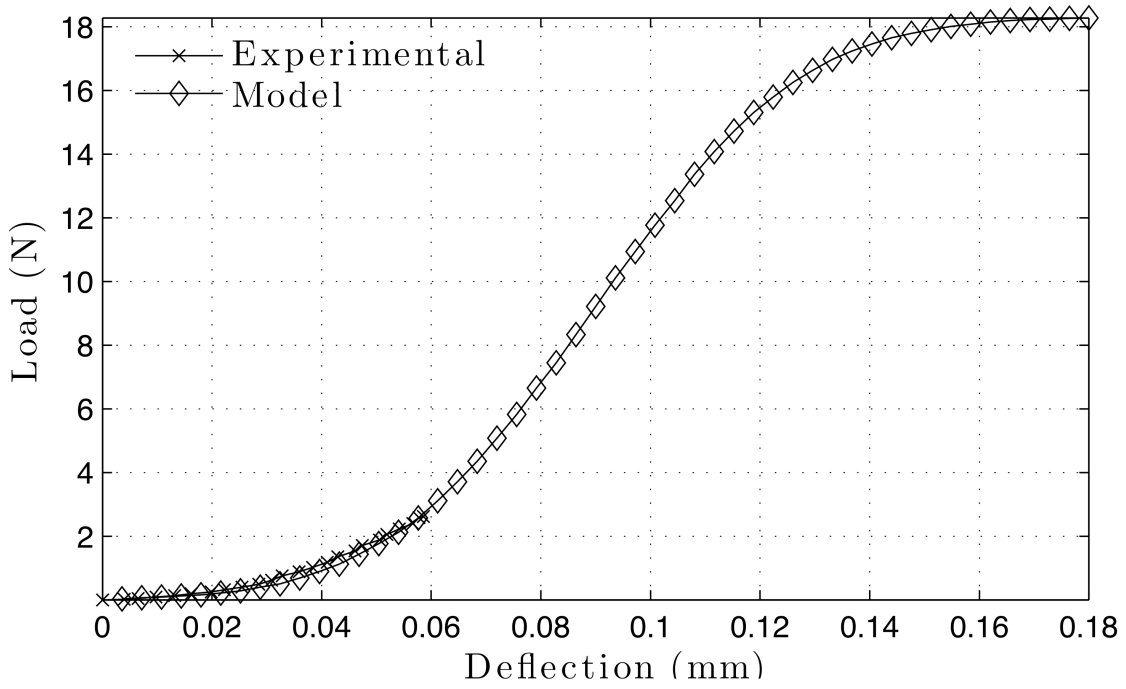


(a) Load Deflection curve

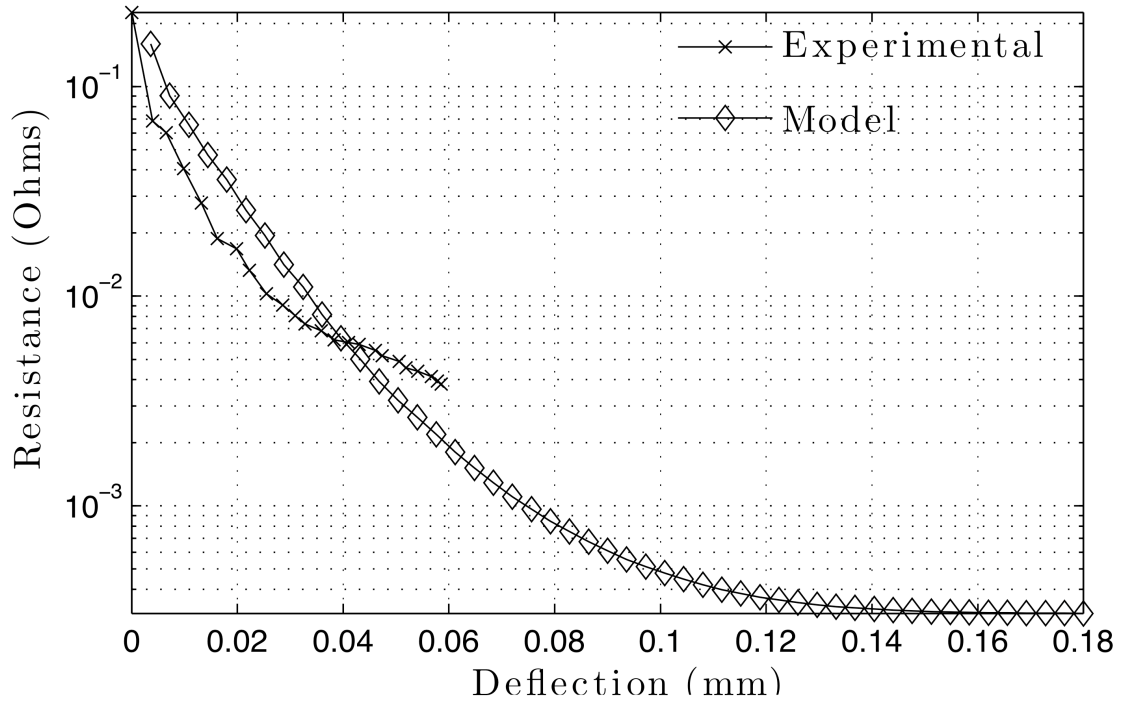


(b) Resistance Deflection Curve

Figure 8.3: Comparison of Theory and Experiment for SSI Brush 1

parameters were plugged into Equation 7.11 and the result is plotted in Figure 8.3. As one can see, the structural model appears to fit pretty well.

The resistance comparison is more difficult to make. This is because two of the parameters are unknown. The parameters that must be approximated include the film resistivity and thickness $\rho t$ and the contact radius $R$. For the film parameters, the value of $\rho t = 1.5 \times 10^{-}12\,\Omega m^2$ from the literature is used [3]. There is no real method for approximating the contact radius $R$. For the plot in Figure 8.3 a value of 1/10th of the fiber radius was found to make the data line up roughly. If the state of the surface films was known then this model could be used to measure the contact radius or vice-versa. The model fits the slope of the experiments at first, but the resistance is higher in the brush at larger deflections. A potential source for this discrepancy is that the shorter fibers could have thicker oxidation films at their tips This could easily happen because when the brushes were sanded, they were only very lightly pressed. Experiments in a controlled atmosphere and a reliable mechanism for cleaning the fibers are needed to make this comparison more quantitative.

## 8.2 Single Fiber Vibration Experiments

Acoustic emission experiments by researchers at the University of California at San Diego found high frequency noise from the brushes in sliding motion operation [53]. It was thought that this vibration motion along with steady sliding might contribute to wear. The purpose of the experiments presented in this section is to measure the natural frequencies of the fibers in the homopolar motor brush. This was done by rigidly clamping one end of the fiber and exciting it using a burst of air. The deflections of the fiber were measured using a non-contacting optical follower camera (Opteron model 5600 Electro-Optical Biaxial Displacement

Follower). A sketch of the set-up is shown in Figure 8.4

The optical device can track vibrations up to 20kHz. Requirements on the scale of the target depend on the optics being used, but it was found that the follower camera could track a copper fiber as small as 30 $\mu m$ in diameter and approximately 1 $mm$ in length. Fibers much smaller than this were very difficult to track. This section will go through the set of experiments performed with this set-up.

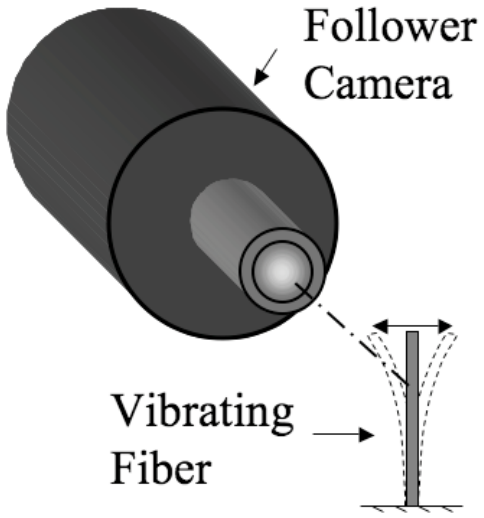


Figure 8.4: Brush Vibration Measurement Setup

### 8.2.1 Individual Fibers

The first step was to measure the vibrations of various fibers taken from one of the copper brushes. These fibers were extracted by cutting the brush in half and then folding the fibers over so that undamaged fibers could be found. Four fibers were pulled out and mounted to tabs of paper. The paper was used to make the small fibers easier to handle, and to make sure that they could be put in a clamp. The free length of the fiber was measured using a dial caliper and the diameter

Table 8.1: Fiber Dimensions

| Fiber | Length | Diameter |
|---|---|---|
| I | 6.27 $mm$ | 73 $\mu m$ |
| II | 6.58 $mm$ | 70 $\mu m$ |
| III | 5.92 $mm$ | 31 $\mu m$ |
| IV | 6.48 $mm$ | 38 $\mu m$ |

was measured under an optical microscope using an objective micrometer. The dimensions of each fiber are shown in Table 8.1. These values are used in the comparisons of the data with the theoretical model from Appendix C.

A small aerosol can of compressed air was then used to excite the fibers and their vibrations were measured. An example of the output of the displacement follower and its Fourier transform is shown in Figure 8.5. The output of the displacement follower was not calibrated since the frequency was all that was of interest. This process was performed for each of the four fibers and the results are shown in Figure 8.6. Also included in these plots are lines from the theoretical model in Appendix C. As one can see, the data from these experiments fits the model very well. This implies that even though these fibers are irregular in nature, their characteristic frequencies can still be approximately calculated as though they were straight, round fibers.

### 8.2.2 Chopped Fiber

The next step in this analysis is to test the frequency response as a function of the length of the fiber. This is done by taking a long fiber and putting it through the same tests as the previous section except that in between each test a small portion of the fiber is cut off and the new length is measured. This gives the frequency response as a function of the length of the fiber.

This experiment was performed both with a fiber from one of the brushes (Fiber

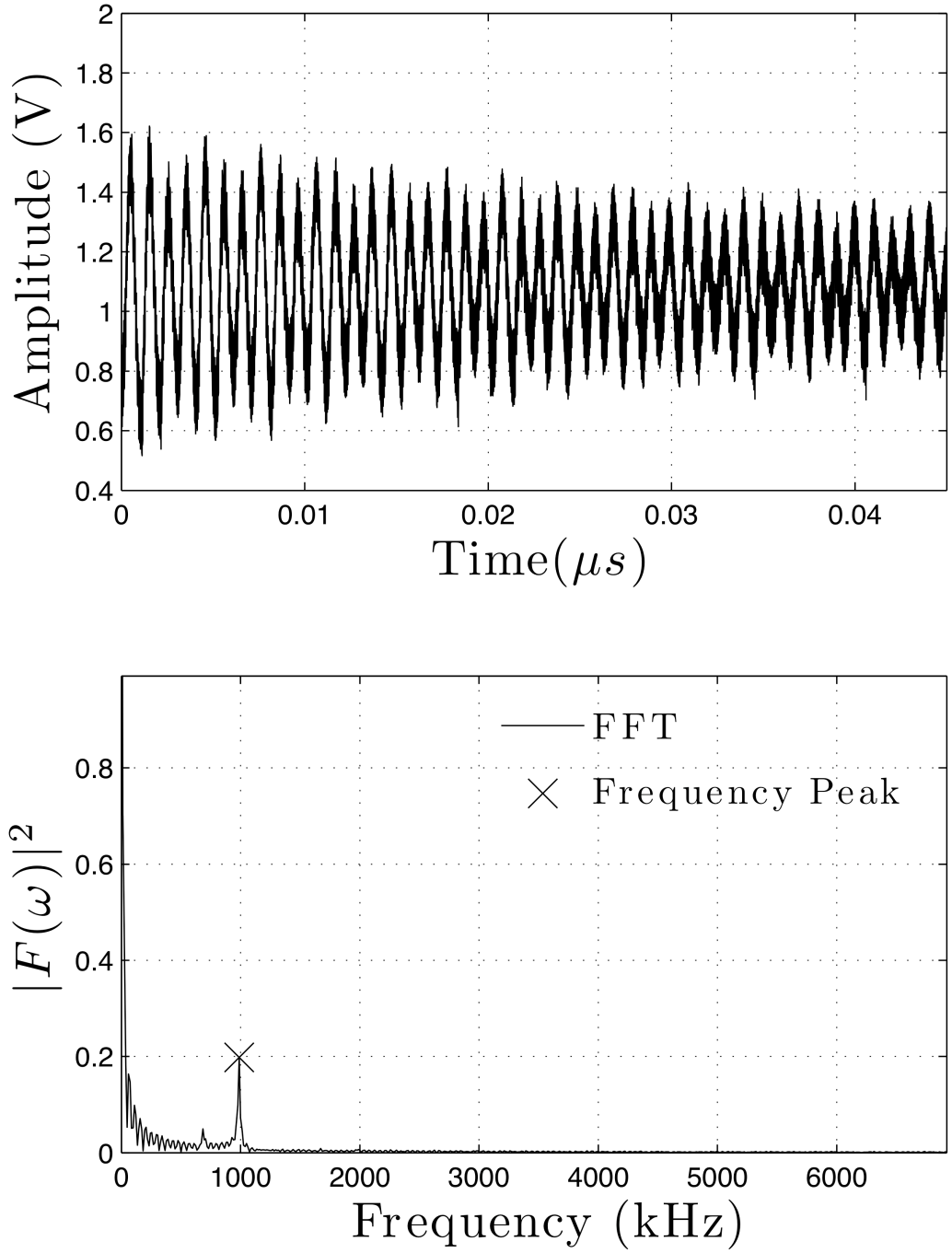


Figure 8.5: Example displacement follower output for fiber II (top) and Fourier transform of signal(bottom).

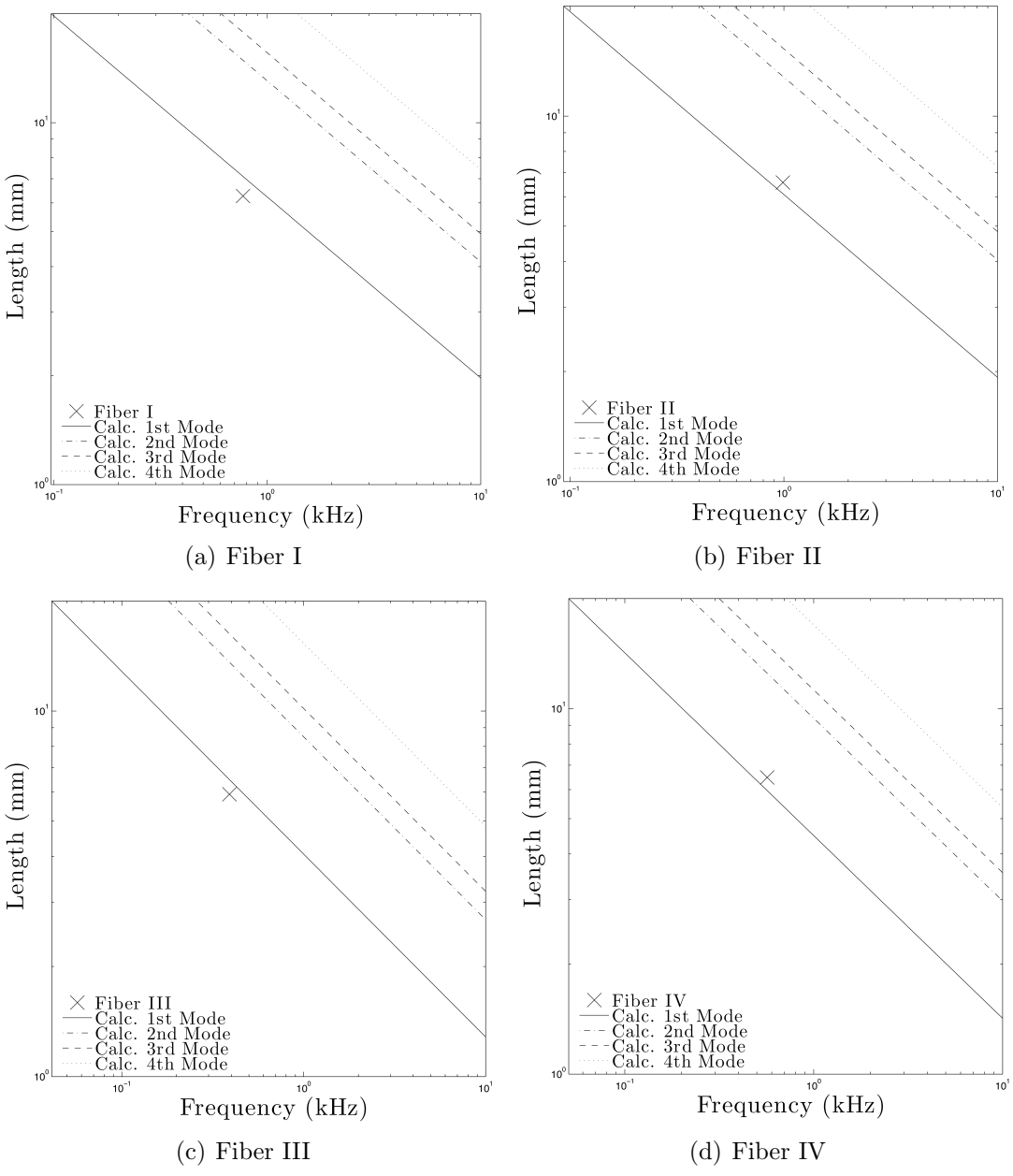


(a) Fiber I (b) Fiber II

(c) Fiber III (d) Fiber IV

Figure 8.6: Characteristic Frequencies of Different Copper Fibers

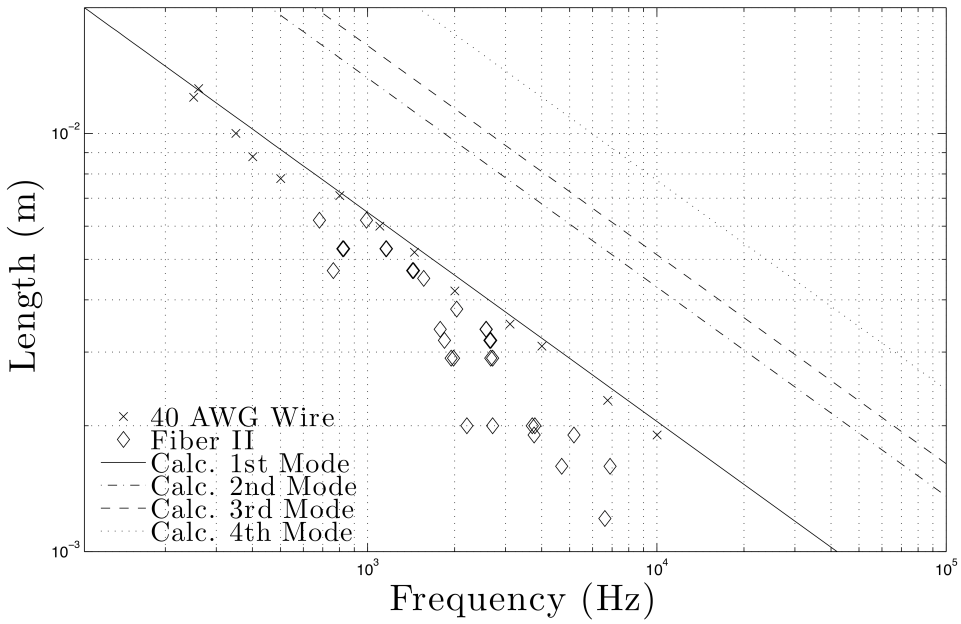


Figure 8.7: Chopped Fiber Vibration

II from the previous section) and with a piece of 40 AWG (diameter $\approx 79\mu m$) uncoated copper wire. The uncoated copper wire was used because it was easier to measure over a wide range of lengths. The results of both of these experiments are shown in Figure 8.7. Also included are plots of modes of the fixed-free beam model in Appendix C. For this comparison, the elastic modulus and density were assumed to have values of $E = 120GPa$ and $\rho = 8320kg/m^3$, and the radius was chosen to match the 40 gage uncoated wire. It is important to state that the theoretical comparison in Figure 8.7 assumes a round fiber cross-section; while this is approximately true, many of the fibers exhibit irregular cross-sectional shapes (see Figure 7.3).

As one can see, they both fit the theoretical model relatively well. The irregular fiber shows a lot more variation and a slight offset. The variation is due to the varying cross section of the brush fiber and the offset is likely due to different material/geometric properties between the fibers and the assumed values for the

model. The important thing to note is that the dependence on the length of the fiber appears to be the same as it is in the theoretical model. This has been verified this down to the 1 mm length scale. This trend should continue until the length of the fiber becomes comparable to it's diameter. This means that the very high frequency vibrations seen in the research from UCSD [53] could be coming from the individual fibers, but only if the effective vibrating length of the fiber is considerably smaller than 1 mm.

# Part IV

# Conclusions and Future Work

# Chapter 9
# Conclusions and Future Work

## 9.1 Electromagnetic Launcher Conclusions and Future Work

This dissertation explored the dynamics of the rails during the launch of an electromagnetic launcher. These dynamics were explored with respect to the contact between the armature and the rails. This interaction can affect friction, wear and the ability to transfer current. It was found that elastic waves and wave radiation can occur at characteristic speeds of the rails of an electromagnetic launcher.

Simulations indicate that the interference of the armature and the elastic waves can cause very large pressures to be generated. These pressures are directly related to the friction during launch and they could potentially affect the wear. In addition to affecting wear and friction, these pressures are large enough to cause macro-scale damage to the rails of the launcher.

A fiber optic strain device was constructed to measure these waves. The experiments conducted with this device show that the velocity and wear of the armature will affect the magnitude of these waves. The shape and magnitude of the measured strains are comparable to the simulations. This means that the reduced order model used in this dissertation is capable of capturing the basic dynamics of the rails during launch.

In addition to the dynamics of the guide way, a simple model for armature stability was presented. Typical launchers use the armature to push the payload down the rails. This puts the center of pressure behind the center of mass and sets up an unstable situation. An unstable armature can vibrate during launch and these vibrations could affect wear and cause damage to the bore of the launcher.

A system for the measurement of in-bore armature velocity was also discussed. This system increases the resolution while decreasing the resources necessary for measuring velocities. While this is an interesting technique, it does not have enough resolution to measure parameters such as friction and mass loss. For these measurements to be taken, more accurate measurements of the armature need to be made during launch.

The essential conclusion one can draw from all of this is that for a launcher design to be successful, it will be necessary to take into account the structural dynamics of the rails as well as the armature. In addition to this, a better understanding of friction and wear of the system is necessary. Further study is necessary on both of these fronts and it is likely that the generation of a successful multi-shot launcher will be highly dependent on both the development of better sensors and simulations.

## 9.2 Homopolar Motor Conclusions and Future Work

In terms of mechanical parameters, the brushes tested in this dissertation show a large variation in compliance. It is unknown if this is a consequence of the asymmetric wear or inconsistency in the brush construction process. Either way, the mechanical tests presented in this dissertation could be used as a quality control test on the uniformity of the brushes.

A statistical model is also considered for the structural and electrical response of these brushes when they are stationary. This model could be used to quantify the amount of fiber to fiber interaction there is as a function of the applied load, but this would require applied loads much greater than the operating loads of the brushes. A lot more could be learned from these tests if they were conducted in a controlled atmosphere and if more brush samples were available.

# APPENDIX A

This appendix presents the full derivations for the differential equations for the Bernoulli-Euler and Timoshenko beam models. These derivations can be found in many sources but they are included here for the sake of completeness

## A.1 Bernoulli-Euler Model

The Bernoulli-Euler beam equation of motion can be derived using both Newton-Euler and Lagrangian methods. A good example of the Lagrangian derivation can be found in the literature [39]. The Newton-Euler derivation, which will be presented here, can also be found in elementary texts on structural dynamics (e.g. see [98]).

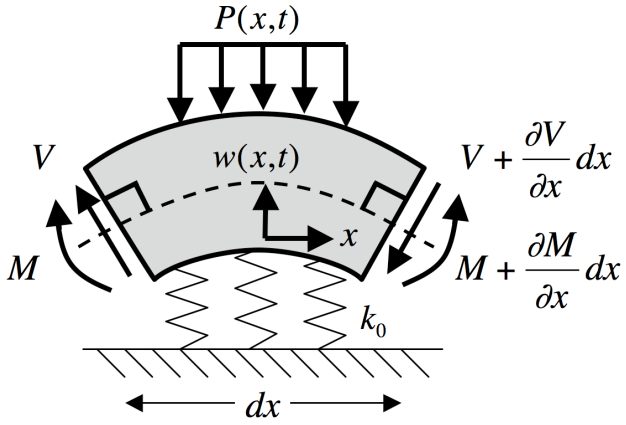


Figure A.1: Differential Element of a Beam on an Elastic Foundation

The first step in deriving the equation of motion is to draw a free body diagram. Figure A.1 shows the free body diagram of a differential element of the beam of length $dx$. The neutral axis of the beam is indicated with a dotted line and the

effective internal moment $M$ and shear $V$ are pictured next to the shear planes. One of the primary assumptions of the Bernoulli-Euler model is that the shear planes remain perpendicular to the neutral axis as shown in Figure A.1. The beam has a density of $\rho$ and a cross-sectional area of $A$. The cross-sectional moment of inertia is represented by the symbol $J$. The loading on the beam element is shown as $P(x,t)$ and the foundation is shown as springs with stiffness per unit area of $k_0$. This means that the stiffness per unit length is $k_0 B$ where $B$ is the width of the beam. The moments and forces must be summed over to get the equations of motion. Summing over the forces on the gives the following equation.

$$\sum F_i = \rho A dx \frac{\partial^2 w(x,t)}{\partial t^2} = V - V - \frac{\partial V}{\partial x} dx + k_0 B w(x,t) dx - P(x,t) dx \quad \text{(A.1)}$$

Which simplifies to the following.

$$\rho A \frac{\partial^2 w(x,t)}{\partial t^2} + \frac{\partial V}{\partial x} + k_0 B w(x,t) = P(x,t) \quad \text{(A.2)}$$

Summing over the moments and neglecting rotary inertia in the beam and moments generated by the applied load gives the following equation.

$$\sum M_i = (M + \frac{\partial M}{\partial x} dx) - M - \frac{V}{2} dx - (\frac{V}{2} + \frac{1}{2} \frac{\partial V}{\partial x} dx) dx = 0 \quad \text{(A.3)}$$

Simplifying and neglecting higher order terms in $dx$ gives the following.

$$V = \frac{\partial M}{\partial x} \quad \text{(A.4)}$$

Equations A.2 and A.4 can then be combined to give the following partial differential equation.

$$\frac{\partial^2 M}{\partial x^2} + \rho A \frac{\partial^2 w(x,t)}{\partial t^2} + k_0 B w(x,t) = P(x,t) \quad \text{(A.5)}$$

All that is needed to get the final form is to relate the moment $M$ to the deflection $w(x,t)$. This can be accomplished by studying Figure A.2. For the Bernoulli-Euler

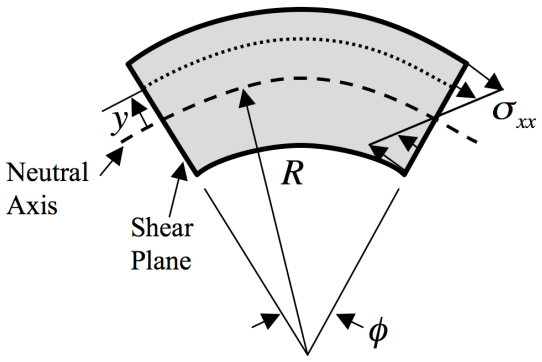


Figure A.2: Stress in a Differential Element of a Beam

beam, the stress normal to the shear plane $\sigma_{xx}$ is assumed to vary linearly across the cross section of the beam. It is also assumed to be zero at the neutral axis of the beam. To calculate the total moment, the stress must be integrated over the beam cross-section.

$$M = -\int y\sigma_{xx}dA \tag{A.6}$$

Re-writing the stress in terms of the strain using the elastic modulus $E$ gives the following.

$$M = -E\int y\epsilon_{xx}dA \tag{A.7}$$

The strain can be re-written by looking at the radius of curvature of the beam element as pictured in Figure A.2. If the differential beam element has a radius of curvature of R and spans an angle of $\phi$ then the unstressed length of the beam at $y$ is equal to $R\phi$ and the stressed length is $(R+y)\phi$. The fractional change in length, or strain, of the beam at $y$ can be written in the following way.

$$\epsilon_{xx} = \frac{R\phi - (R+y)\phi}{R\phi} = -\frac{y}{R} \tag{A.8}$$

Plugging this relationship back into the previous equation for the moment gives the following.

$$M = \frac{E}{R}\left\{\int y^2 dA\right\} \tag{A.9}$$

But the quantity in curly brackets is the definition of the cross-sectional moment $J$ and from elementary calculus it is known that for small slopes $1/R \approx \partial^2 w/\partial x^2$. These observations reduce the moment to the following relationship.

$$M = EJ\frac{\partial^2 w(x,t)}{\partial x^2} \tag{A.10}$$

This can be plugged back into Equation A.5 to get the full differential equation for the Bernoulli-Euler beam on an elastic foundation.

$$EJ\frac{\partial^4 w(x,t)}{\partial x^4} + \rho A\frac{\partial^2 w(x,t)}{\partial t^2} + k_0 B w(x,t) = P(x,t) \tag{A.11}$$

## A.2 Timoshenko Model

The Timoshenko beam equation of motion can also be derived using both Newton-Euler and Lagrangian methods [98],[39]. The Newton-Euler derivation will be shown in this section.

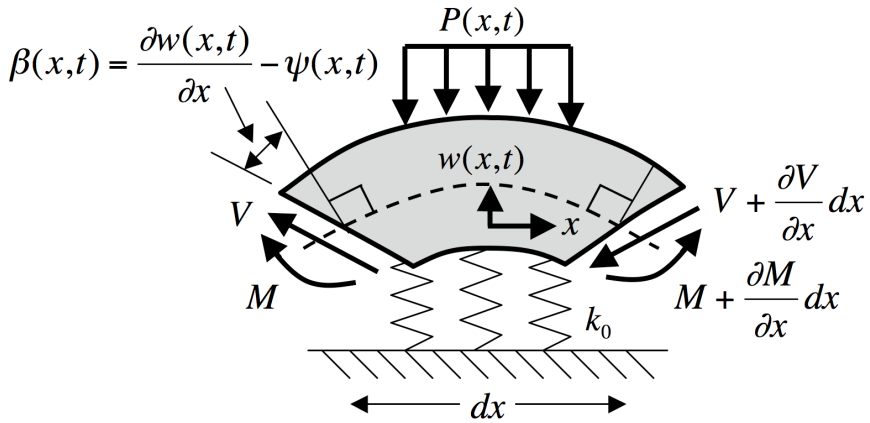


Figure A.3: Differential Element of a Timoshenko Beam on an Elastic Foundation

The free body diagram for the Timoshenko beam on an elastic foundation is shown in Figure A.3. One difference between this model and the Bernoulli-Euler

model is that the shear planes are allowed to rotate relative to their unstressed positions. This is represented by the angle $\beta$ in Figure A.3. The angle of the neutral axis when shear is neglected can be represented by $\psi$. The total slope of the neutral axis is written as the sum of these two angles.

$$\frac{\partial w(x,t)}{\partial x} = \psi(x,t) + \beta(x,t) \tag{A.12}$$

The Timoshenko model also does not neglect rotary inertia in the moment balance equation. This rotary inertia is represented by the second temporal derivative of the slope of the differential beam element. This means that, for the Timoshenko beam, the moment balance equation appears as follows.

$$\sum M_i = (M + \frac{\partial M}{\partial x}dx) - M - \frac{V}{2}dx - (\frac{V}{2} + \frac{1}{2}\frac{\partial V}{\partial x}dx)dx = \rho J \frac{\partial^2 \psi(x,t)}{\partial t^2}dx \tag{A.13}$$

Which simplifies to the following when higher order terms in $dx$ are neglected.

$$\frac{\partial M}{\partial x} - V = \rho J \frac{\partial^2 \psi(x,t)}{\partial t^2} \tag{A.14}$$

The summation over the forces is the same as the Bernoulli-Euler model and reduces to the following.

$$\rho A \frac{\partial^2 w(x,t)}{\partial t^2} + \frac{\partial V}{\partial x} + k_0 B w(x,t) = P(x,t) \tag{A.15}$$

This time the shear and moment need to be calculated to get to the final differential equation. The moment is calculated in the same way as the Bernoulli-Euler beam and is given by the following relationship.

$$M = EJ \frac{\partial \psi(x,t)}{\partial x} \tag{A.16}$$

The shear is calculated by integrating over the shear stress in the shear plane.

$$V = \int \tau dA \tag{A.17}$$

This integral is completed by assuming that the shear stress is proportional to the shear deformation $\beta$ through the shear modulus $G$ and a dimensionless constant $\kappa$ that is called the Timoshenko shear coefficient. The shear coefficient depends on the cross-section of the beam but for a rectangular cross-section it is roughly equal to 5/6 [70],[45]. Taking this assumption into account gives the equation for the shear.

$$V = -\kappa\beta GA = \kappa GA\left(\psi(x,t) - \frac{\partial w(x,t)}{\partial x}\right) \tag{A.18}$$

The final differential equation can now be calculated by plugging Equations A.16 and A.18 into Equations A.14 and A.15. This gives rise to a pair of coupled differential equations that describe the translation and shear deflection of the beam.

$$EJ\frac{\partial^2\psi(x,t)}{\partial x^2} - \kappa GA\left(\psi(x,t) - \frac{\partial w(x,t)}{\partial x}\right) = \rho J\frac{\partial^2\psi(x,t)}{\partial t^2} \tag{A.19}$$
$$\kappa GA\left(\frac{\partial\psi(x,t)}{\partial x} - \frac{\partial^2 w(x,t)}{\partial x^2}\right) + \rho A\frac{\partial^2 w(x,t)}{\partial t^2} + k_0 B w(x,t) = P(x,t)$$

These equations can be combined into one differential equation by eliminating $\psi$. This gives the final differential equation for the Timoshenko beam.

$$\begin{aligned} EJ\frac{\partial^4 w(x,t)}{\partial x^4} - \rho J\left(1 + \frac{E}{\kappa G}\right)\frac{\partial^4 w(x,t)}{\partial x^2\partial t^2} &+ \rho A\frac{\partial^2 w(x,t)}{\partial t^2} \\ +\frac{\rho^2 J}{\kappa G}\frac{\partial^4 w(x,t)}{\partial t^4} &+ k_0 B w(x,t) = P(x,t) \end{aligned} \tag{A.20}$$

# APPENDIX B

The partial differential equation for the deflection of the Timoshenko beam can be solved in closed form for the case of a load moving at a constant velocity on an infinitely long beam. The solution to this problem will be shown in this appendix so that they can be used to verify the beam elements used in this dissertation (see Section 3.3.2). The solutions will be presented here without proof, for the sake of brevity. The full derivation of these results can be found in the text by Frýba [34]. The formulation of this problem with a load moving at velocity $v$ is as follows.

$$\begin{aligned} EJ\frac{\partial^4 w(x-vt)}{\partial x^4} - \rho J(1+\frac{E}{\kappa G})\frac{\partial^4 w(x-vt)}{\partial x^2 \partial t^2} &+ \rho A\frac{\partial^2 w(x-vt)}{\partial t^2} \\ +\frac{\rho^2 J}{\kappa G}\frac{\partial^4 w(x-vt)}{\partial t^4} + k_0 B w(x-vt) &= P\delta(x-vt) \end{aligned} \tag{B.1}$$

Where the solution has been assumed to travel along with the load. The form of the solution of this differential equation depends on the velocity of the load so it is necessary to present the results for all of the different velocity ranges.

For the case of a load moving slower than the critical velocity of the beam, the solution for the deflection is as follows.

$$\begin{aligned} w(s) &= v_0\frac{e^{-b|s|}}{Ab}\left(1+\frac{2m^2(1-\alpha_1^2)}{A}\right)cos(as) \\ &+ v_0\frac{e^{-b|s|}}{Aa}\left(1-\frac{2m^2(1-\alpha_1^2)}{A}\right)sin(a|s|) \end{aligned} \tag{B.2}$$

And for the cross-sectional rotation.

$$\psi(s) = -\frac{2v_0\lambda}{A^2 ab}e^{-b|s|}sin(as) \tag{B.3}$$

Where the constants are defined in terms of the parameters of Table 2.1 as follows.

$$
\begin{aligned}
a^2 = \frac{1}{A}\left(1+\frac{B}{A}\right), \quad b^2 = \frac{1}{A}\left(1-\frac{B}{A}\right) \\
A^2 = (1-\alpha_1^2)(1-\alpha_2^2), \quad B^2 = \alpha^2 - m^2(1-\alpha_1^2) \\
s = \lambda(x-vt), \quad \alpha_1^2 = \frac{\rho v^2}{E}, \quad \alpha_2^2 = \frac{\rho v^2}{\kappa G} \\
m^2 = \frac{\alpha_2^2}{\alpha_1^2} r^2 \lambda^2, \quad \lambda^4 = \left(\frac{k}{4EJ}\right), \quad v_0 = \frac{P}{8\lambda^3 EJ}
\end{aligned}
\tag{B.4}
$$

A plot of this solution can be found in Figure 3.4. The deflection of the rail is very similar to when the load is stationary. This means that below the critical velocity the beam acts nearly statically. This is true in the sense that a dynamic amplification factor does not exist in this region. The load is traveling below the lowest possible unattenuated wave speed, the critical velocity, and so it is not possible for it to generate any waves (in the quasi-static case).

A solution does not exist at the critical velocity. This is, in effect, the mathematical definition of the critical velocity. It is the velocity at which no solution exists to Equation B.1. This represents a point in k-space where attenuated and un-attenuated solutions meet on both sides of the load (see Figure 2.6).

The next region is between the critical velocity and the shear velocity. The solution in this region is as follows.

$$
w(s) = -\frac{4v_0(1+a_1^2m^2(1-\alpha_1^2))}{a_1(A^2a_1^2-2B)} sin(a_1 s) \quad \text{for} \quad s>0 \tag{B.5}
$$

$$
w(s) = \frac{4v_0(1+a_2^2m^2(1-\alpha_1^2))}{a_2(A^2a_2^2-2B)} sin(a_2 s) \quad \text{for} \quad s<0 \tag{B.6}
$$

And for the cross-sectional rotation.

$$
\psi(s) = -\frac{4v_0\lambda}{A^2a_1^2-2B} cos(a_1 s) \quad \text{for} \quad s>0 \tag{B.7}
$$

$$
\psi(s) = \frac{4v_0\lambda}{A^2a_2^2-2B} cos(a_2 s) \quad \text{for} \quad s<0 \tag{B.8}
$$

Where the additional constants are defined as follows.

$$a_1^2 = \frac{2B}{A^2}\left(1+\sqrt{1-\frac{A^2}{B^2}}\right), \quad a_2^2 = \frac{2B}{A^2}\left(1-\sqrt{1-\frac{A^2}{B^2}}\right) \tag{B.9}$$

A representative plot of this solution can be found in Figure 3.5. This solution is different from the last because it shows no attenuation of the rail deflection in front of or behind the load. This means that the load is capable of radiating energy off to infinity in both directions. This is only true for an infinite beam on which the load has been traveling for an infinite time. In a more realistic situation this simply means that the load is capable of radiating energy in both directions in this velocity region.

The next region is above the shear velocity, where the solution is given by the following relationship.

$$w(s) = -\frac{2v_0(1-b^2m^2(1-\alpha_1^2))}{b(A^2b^2+2B)}e^{-bs} \quad \text{for} \quad s>0 \tag{B.10}$$

$$\begin{aligned} w(s) &= \frac{2v_0(1-b^2m^2(1-\alpha_1^2))}{b(A^2b^2+2B)}e^{bs} \\ &+ \frac{4v_0(1+a^2m^2(1-\alpha_1^2))}{a(A^2a^2-2B)}sin(as) \quad \text{for} \quad s<0 \end{aligned} \tag{B.11}$$

And for the cross-sectional rotation.

$$\psi(s) = \frac{2v_0\lambda}{A^2b^2+2B}e^{-bs} \quad \text{for} \quad s>0 \tag{B.12}$$

$$\psi(s) = -\frac{2v_0\lambda}{A^2b^2+2B}e^{bs} + \frac{4v_0\lambda}{A^2a^2-2B}cos(as) \quad \text{for} \quad s<0 \tag{B.13}$$

Where the constants a and b are defined as follows.

$$a^2 = -\frac{2B}{A^2}\left(-1+\sqrt{1-\frac{A^2}{B^2}}\right), \quad b^2 = -\frac{2B}{A^2}\left(1+\sqrt{1-\frac{A^2}{B^2}}\right) \tag{B.14}$$

A representative picture of this solution is shown in Figure 3.6. In this case, the deflection is unattenuated behind the load but completely attenuated in front of the load. This is because the load is now moving faster than the fastest possible wave speed for transverse deflection waves (the shear velocity).

# APPENDIX C

In experiments at General Atomics the individual fibers of the brushes were seen to vibrate during operation. In addition to this, acoustic emission and acoustic emission tests by researchers at UCSD have shown the presence of very high frequency vibrations in the brush fibers during operation [53]. A basic vibrating beam model appears to model the individual fiber dynamics relatively well. The basics of this vibrating beam model are presented here so that they can be used for comparison with measurements presented in Chapter 8.

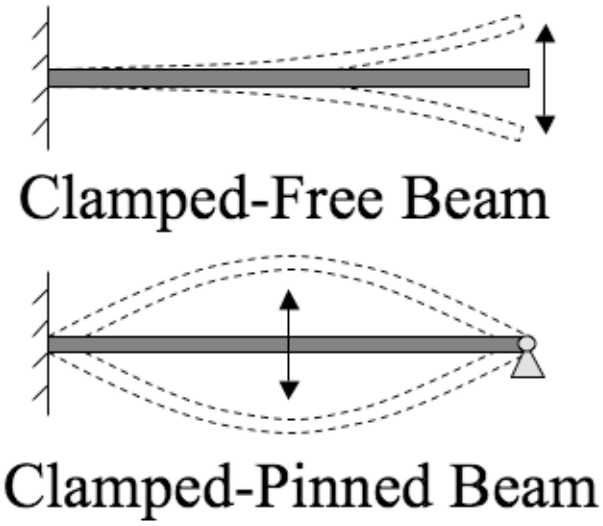


Figure C.1: Vibration Modes for Cantilever Beam

The fibers in the homopolar motor brushes are soldered to a copper plate. This construction makes them similar to a simple cantilever beam with a free end. The shape of the first modes of a cantilever beam are shown in Figure C.1. During operation the fibers in the brushes are in contact with a sliding surface. This means that it is possible for both fixed-free and pinned-free modes to exist. The

equations for both of these modes will be shown in this section. The derivation of these equations can be found in a number of texts, the results are repeated here for convenience [98],[11]. The basic equation for the modes pictured in Figure C.1 is as follows.

$$f_i = \frac{\lambda_i^2}{2\pi L^2}\sqrt{\frac{EJ}{\rho A}}, \quad i = 1, 2, 3... \tag{C.1}$$

Where L is the length of the beam and the other parameters are defined in Table 2.1. The quantity $\lambda_i$ has to be calculated numerically for each mode and is dependent on the boundary conditions. Tabulated values for many different boundary conditions can be found in a book by Robert D. Blevins [11]. The values for the two mode shapes in Figure C.1 are shown in Table C.1. Experiments shown in Section 8.2 test these modes for the fibers in the homopolar motor brushes.

Table C.1: $\lambda_i$ for Cantilever Vibrations

| Quantity | Fixed-Free Modes | Fixed-Pinned Modes |
|---|---|---|
| $\lambda_1$ | 1.875 | 3.927 |
| $\lambda_2$ | 4.694 | 7.069 |
| $\lambda_3$ | 7.855 | 10.210 |
| $\lambda_4$ | 10.996 | 13.352 |
| $\lambda_5$ | 14.137 | 16.493 |
| $\lambda_i$ for $i > 5$ | $(2i-1)\frac{\pi}{2}$ | $(4i+1)\frac{\pi}{4}$ |

# APPENDIX D

The stability model used in Chapter 5 is similar to a model explored by Chu and Moon for the dynamics of magnetically levitated vehicles [16]. For the analysis in this dissertation a change of coordinate system was necessary along with minor changes in notation. It is for this reason that the derivation of the equation of motion for this system will be repeated here.

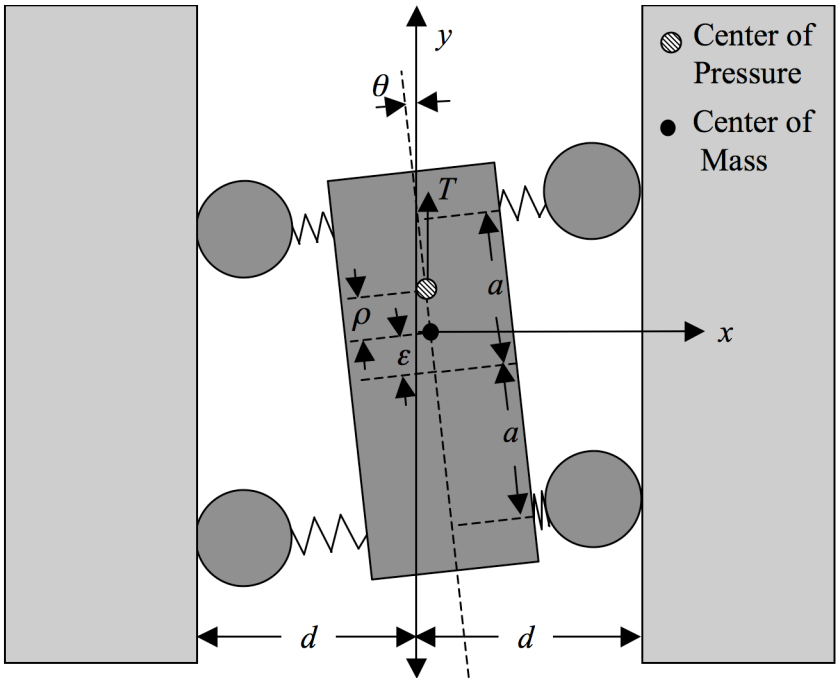


Figure D.1: Armature Model Geometry

The basic geometry of the armature stability model is pictured in Figure D.1. The armature is constrained to travel within a rigid guide way of width 2d. Contact between the armature and guide way is through four sliders on springs. These springs have a stiffness $k$ that is intended to represent the overall compliance of the system. This can include the stiffness of just the armature or the containment structure, or a combination of the two. In either case, a pre-stress of $k\Delta$, where

$\Delta$ is the interference fit of the armature, is assumed to exist in these springs. The center of mass is assumed to be offset from the geometric center of the armature by a distance $\epsilon$ and the propulsion force $T$ is applied at a distance $\rho$ from the center of mass as shown in Figure D.1. The coordinate system describes two degrees of freedom $x$ and $\theta$ which are the deflection and rotation of the armature away from the centerline of the guide way as shown in Figure D.1.

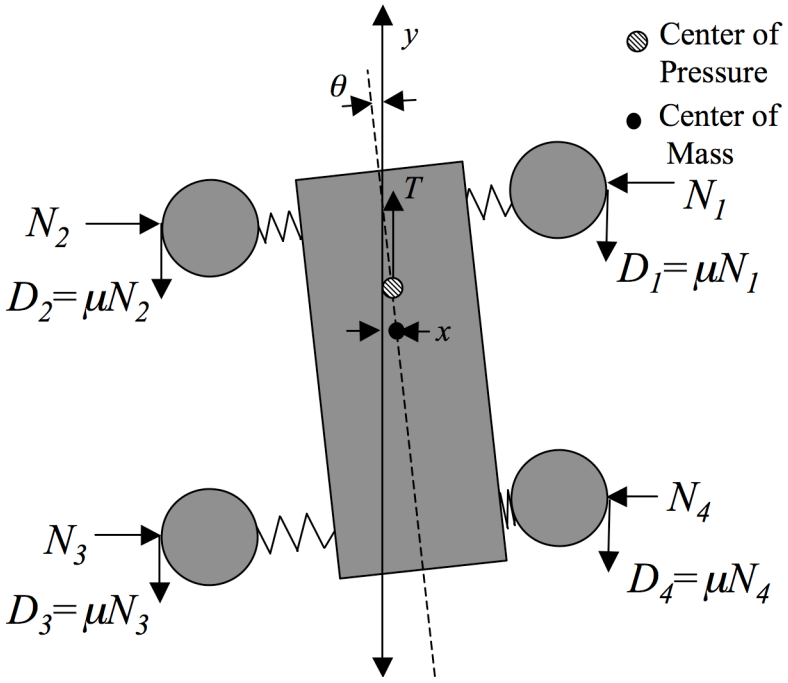


Figure D.2: Armature Free-Body Diagram

The equation of motion for the lateral dynamics of the armature can be derived by summing over the forces and the moments in the free body diagram pictured in Figure D.2. Summing over the forces in the x-direction gives the following equation.

$$\sum F_x = m\ddot{x} = N_2 - N_1 + N_3 - N_4 \tag{D.1}$$

In addition to the lateral force balance, it is important to define the dynamics of the armature along the guide way. The force balance in the y-direction is as

follows.

$$\sum F_y = m\ddot{y} = T - D_1 - D_2 - D_3 - D_4 \tag{D.2}$$

For the stability analysis in this dissertation, the acceleration in the $y$ direction will be assumed to be constant. This sets up a balance between the propulsion force $T$ and the drag forces $D_i$.

$$T = ma_y + D_1 + D_2 + D_3 + D_4 \tag{D.3}$$

Where $a_y$ is the constant acceleration of the armature. This expression will be substituted into the final differential equation. The summation over the moments gives the following relationship.

$$\begin{aligned}\sum M = I_m\ddot{\theta} =&(a-\epsilon)(N_1 - N_2) + (a+\epsilon)(N_3 - N_4) \\ &- D_1(d - (a-\epsilon)\theta) + D_2(d + (a-\epsilon)\theta) \\ &+ D_3(d - (a+\epsilon)\theta) + D_4(d + (a+\epsilon)\theta) - T\rho\theta\end{aligned} \tag{D.4}$$

Where the rotation has been assumed to be small enough that the small angle approximations $sin(\theta) \approx \theta$ and $cos(\theta) \approx 1$ apply. The individual forces at each corner can be written in terms of the stiffness of the springs and the overall deflection of each slider from their non-compressed positions. The lateral forces $N_i$ are written as follows.

$$\begin{aligned}N_1 &= k(\Delta + x - (a-\epsilon)\theta) \\ N_2 &= k(\Delta - x + (a-\epsilon)\theta) \\ N_3 &= k(\Delta - x - (a+\epsilon)\theta) \\ N_4 &= k(\Delta + x + (a+\epsilon)\theta)\end{aligned} \tag{D.5}$$

Where $x$ and $\theta$ are the deflection and rotation of the armature as shown in Figure D.2 and $\Delta$ is the interference fit between the armature and rails. As before, the

rotation has been assumed to be small enough that the small angle approximations $sin(\theta) \approx \theta$ and $cos(\theta) \approx 1$ apply. The corresponding drag terms are dependent on the lateral forces through a friction coefficient as follows.

$$D_i = \mu N_i \quad \text{where} \quad i = 1, 2, 3, 4 \tag{D.6}$$

These equations for the lateral and drag forces can then be plugged into Equation D.1 to give the following differential equation.

$$m\ddot{x} + 4k(x + \epsilon\theta) = 0 \tag{D.7}$$

Equation D.4 and Equation D.3 can be combined with the drag and lateral force equations to give the following differential equation.

$$I_m\ddot{\theta} + 4k(\epsilon + d\mu)x + a_y m\rho\theta + 4k(a^2 + \epsilon^2 + \mu\epsilon(d + \Delta) + \Delta\mu\rho)\theta = 0 \tag{D.8}$$

Equations D.7 and D.8 can be combined by writing them in matrix form.

$$\begin{bmatrix} m & 0 \\ 0 & I_m \end{bmatrix} \begin{bmatrix} \ddot{x} \\ \ddot{\theta} \end{bmatrix} + \begin{bmatrix} 4k & 4k\epsilon \\ 4k(\epsilon + \mu d) & 4k(a^2 + \epsilon^2 + \mu\epsilon(d + \Delta) + \Delta\mu\rho) + a_y m\rho \end{bmatrix} \begin{bmatrix} x \\ \theta \end{bmatrix} = 0 \tag{D.9}$$

This is the equation that is used in Chapter 5 to give a first order approximation to the lateral dynamics of the armature during launch.

# APPENDIX E

The purpose of this appendix is to contain data from additional strain measurements that were taken on the Georgia Tech. launcher. This data is being included in this section for the sake of posterity.

## E.1 Two Gage Single Rail Test 1

The tests in this section were conducted using only two gages attached to one rail. The position of the gages is indicated in Figure E.1. The tests in Figures E.2 and E.3 were both at $800\,m/s$ launch velocity and the test in Figure E.4 was at $1300\,m/s$ launch velocity.

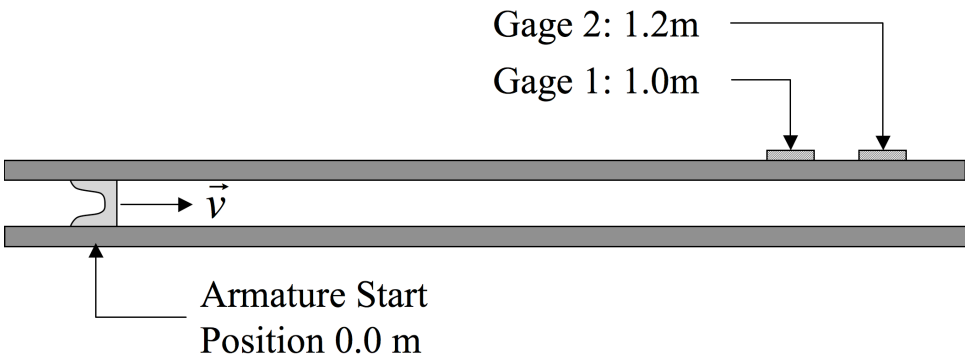


Figure E.1: Positions for Two Gage Single Rail Experiment 1

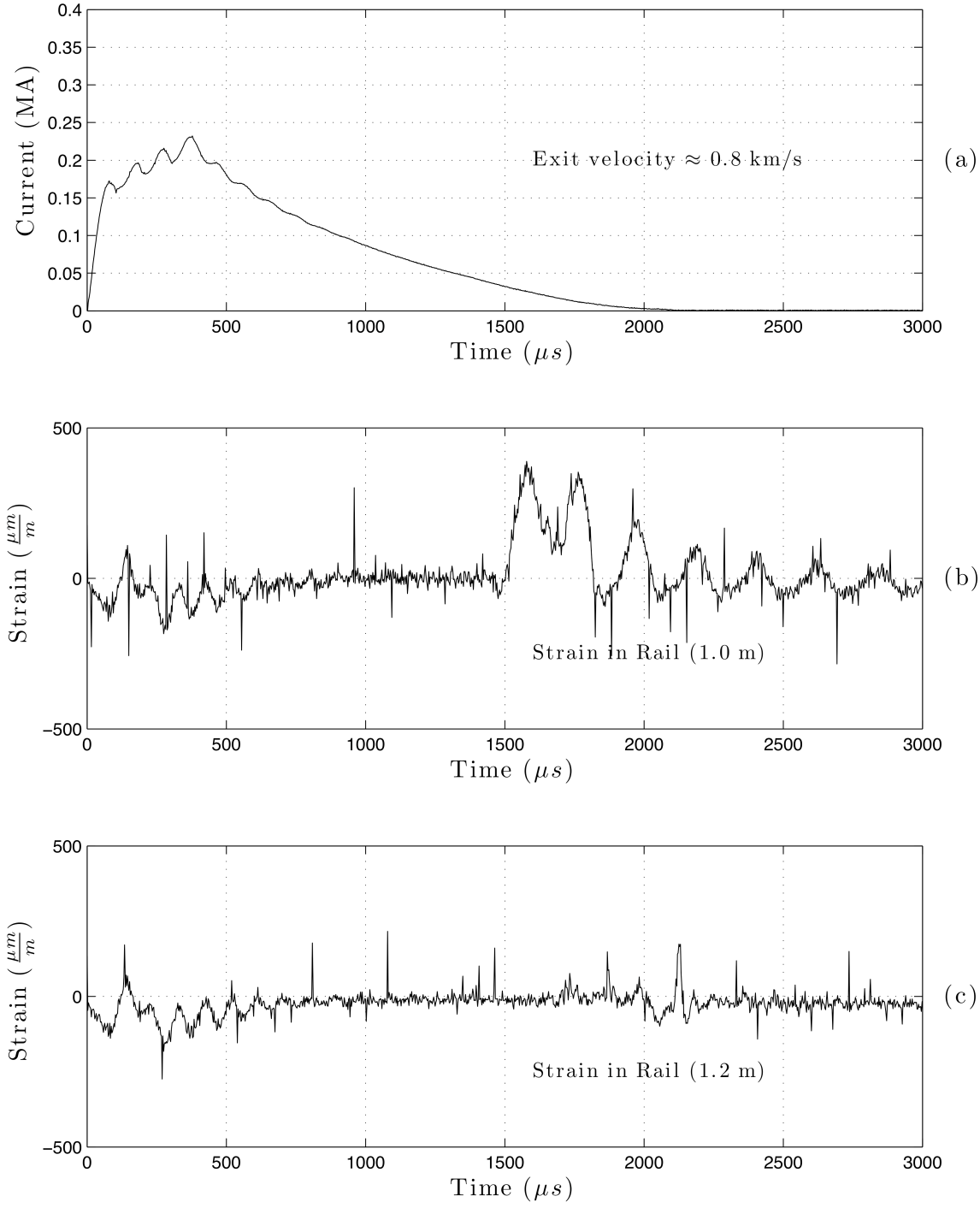


Figure E.2: 800 m/s launch velocity two gage single rail strain experiment 1. (a) Drive current, (b) Strain at 1.0 m in rail, (c) Strain at 1.2 m in rail

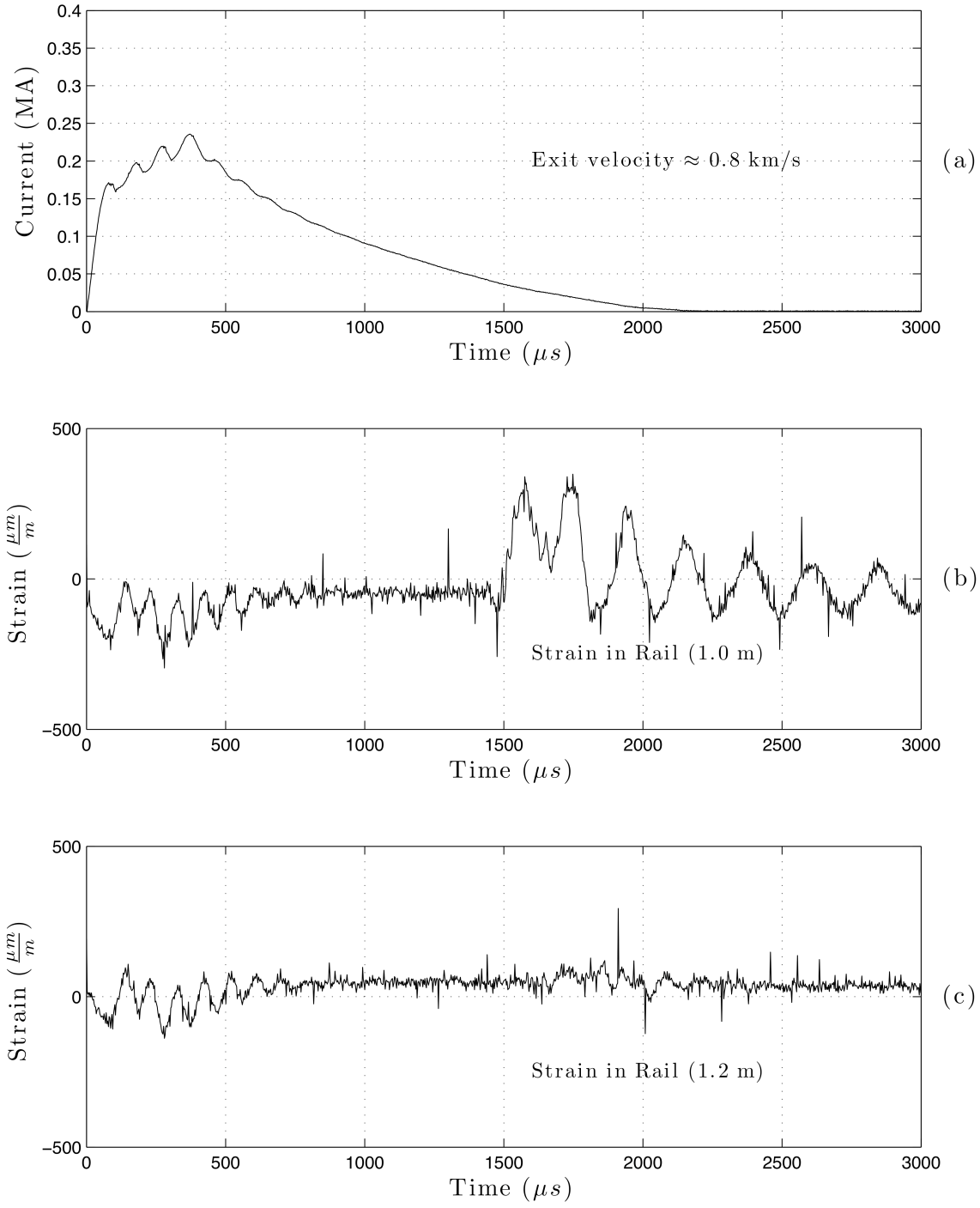


Figure E.3: 800 m/s launch velocity two gage single rail strain experiment 1. (a) Drive current, (b) Strain at 1.0 m in rail, (c) Strain at 1.2 m in rail

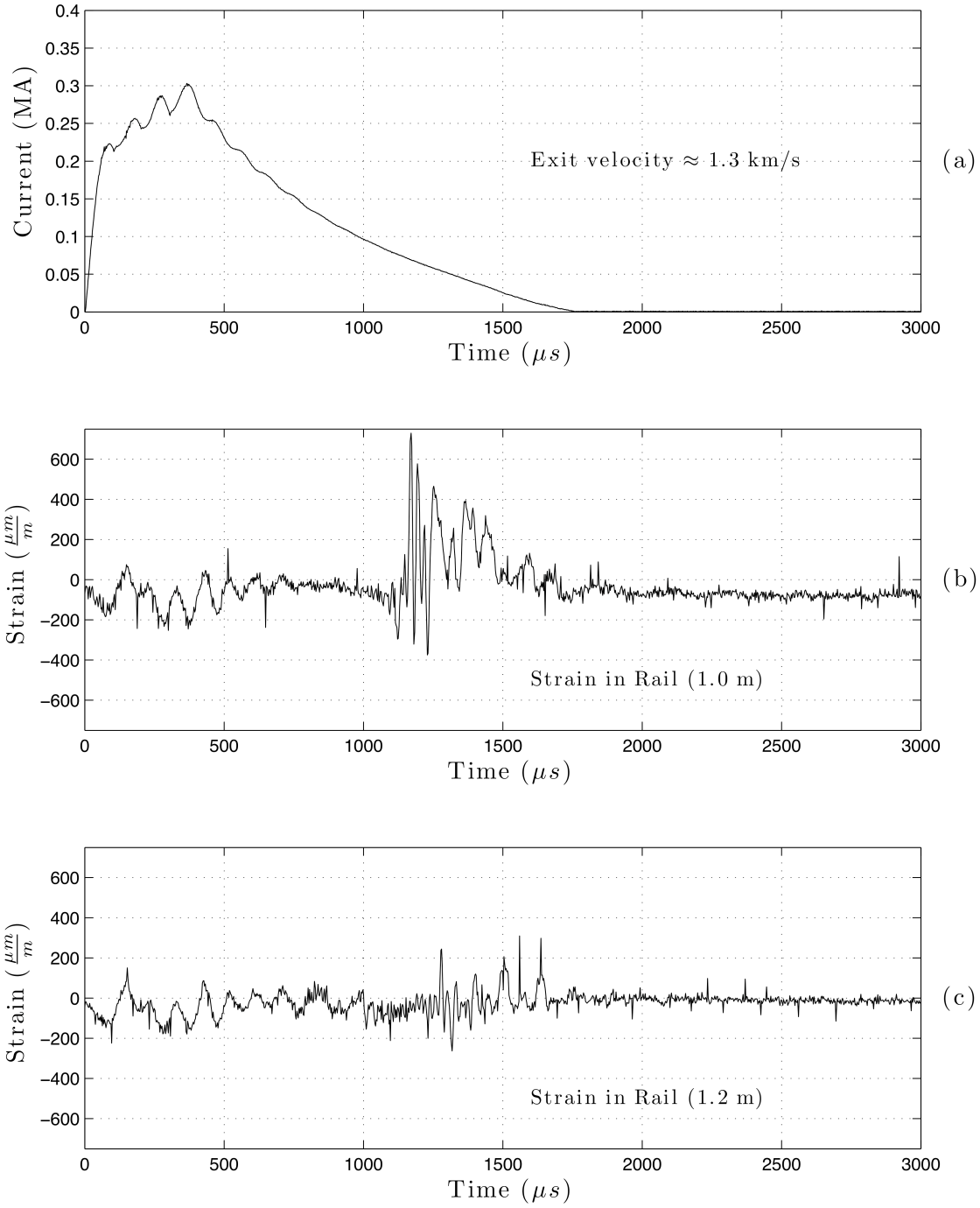


Figure E.4: 1300 m/s launch velocity two gage single rail strain experiment 1. (a) Drive current, (b) Strain at 1.0 m in rail, (c) Strain at 1.2 m in rail

## E.2 Two Gage Single Rail Test 2

The tests in this section were conducted using two gages attached to one rail. The position of the gages is indicated in Figure E.5. This series of tests included four different shots with velocities varying from $800\,m/s$ and $1800\,m/s$. The data from these experiments is shown in Figures E.6-E.9.

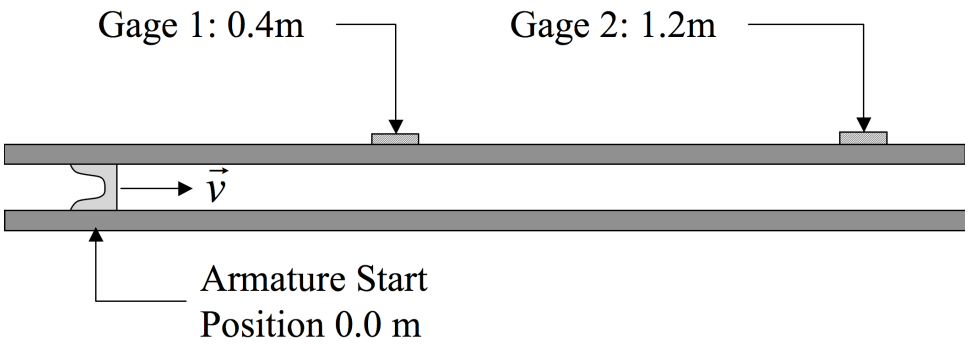


Figure E.5: Positions for Two Gage Single Rail Experiment 2

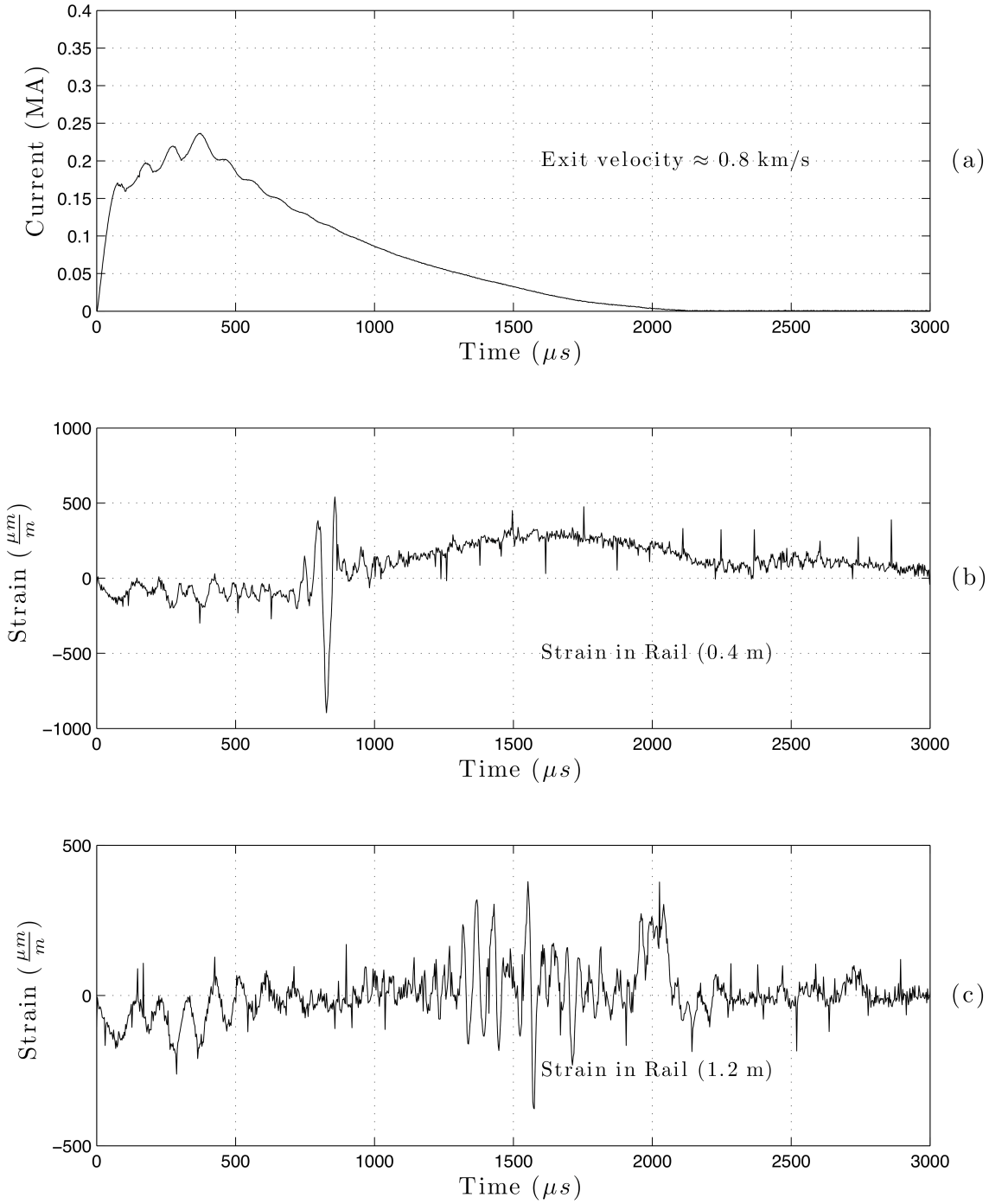


Figure E.6: 800 m/s launch velocity two gage single rail strain experiment 2. (a) Drive current, (b) Strain at 0.4 m in rail, (c) Strain at 1.2 m in rail

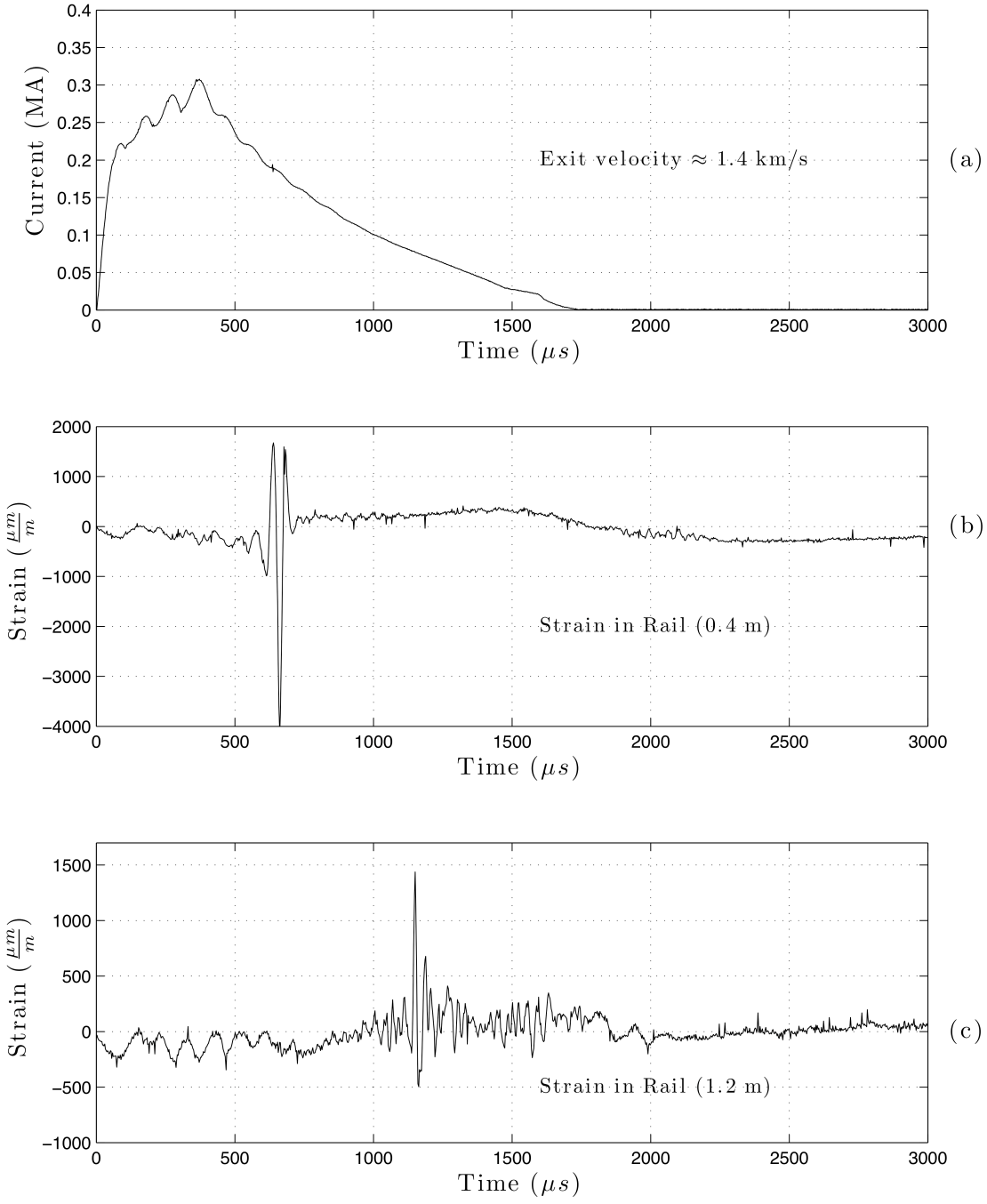


Figure E.7: 1400 m/s launch velocity two gage single rail strain experiment 2. (a) Drive current, (b) Strain at 0.4 m in rail, (c) Strain at 1.2 m in rail

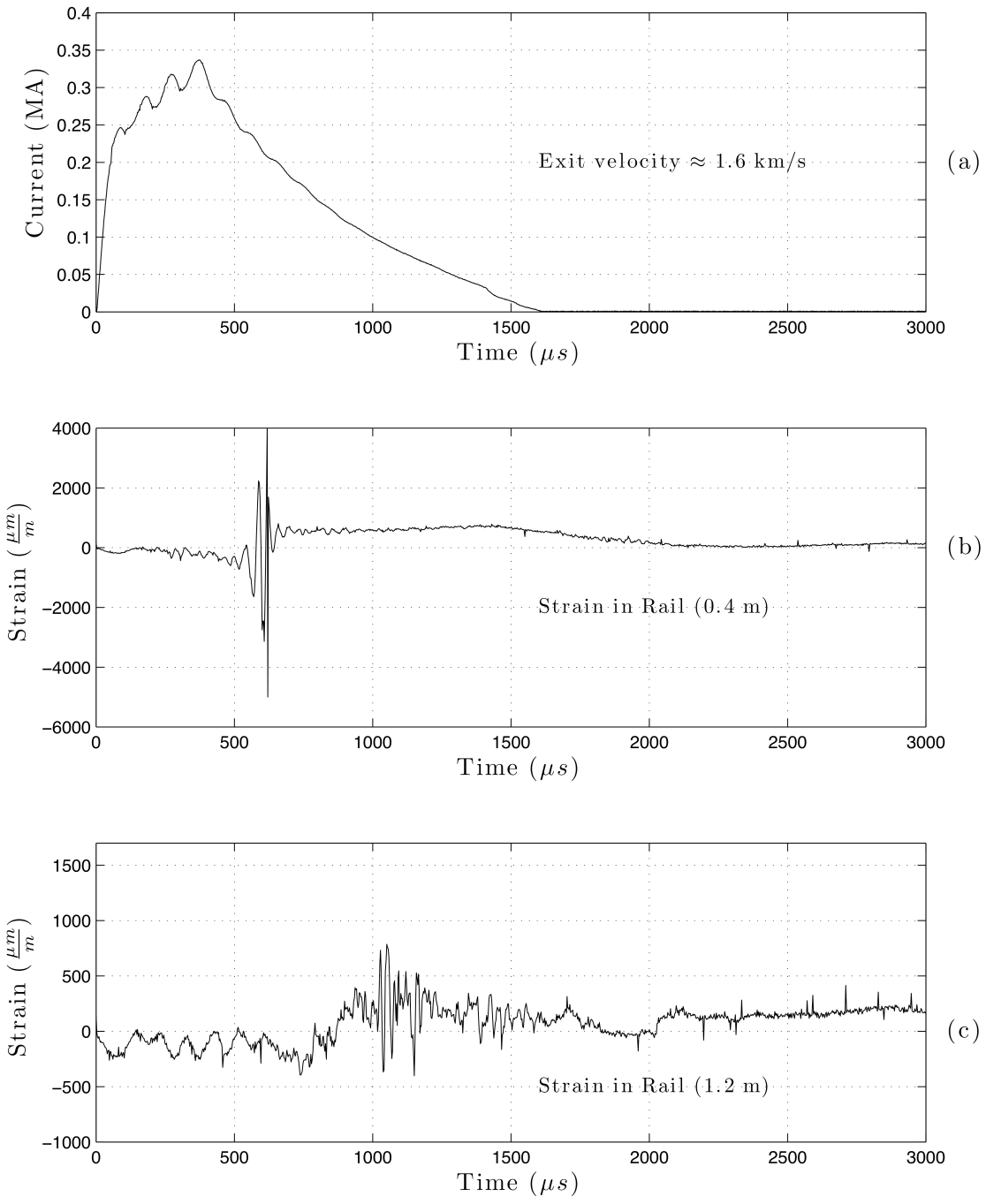


Figure E.8: 1600 m/s launch velocity two gage single rail strain experiment 2. (a) Drive current, (b) Strain at 0.4 m in rail, (c) Strain at 1.2 m in rail

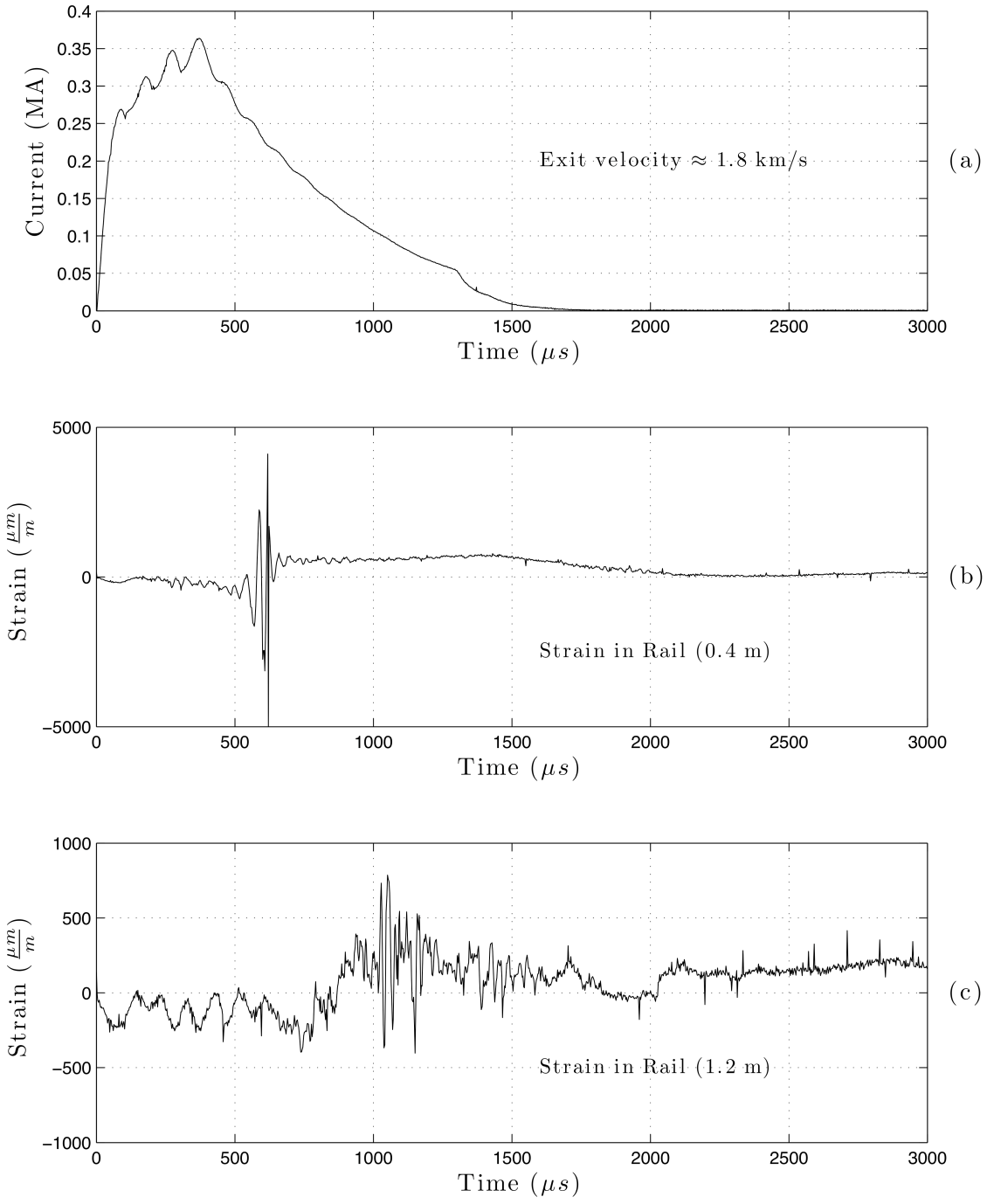


Figure E.9: 1800 m/s launch velocity two gage single rail strain experiment 2. (a) Drive current, (b) Strain at 0.4 m in rail, (c) Strain at 1.2 m in rail

## E.3 Four Gage Single Rail Test

The tests in this section were conducted using four gages attached to one rail. The position of the gages is indicated in Figure E.10. These tests range in launch velocity from $700\,m/s$ to $1200\,m/s$. The data from these experiments is shown in Figures E.11-E.13.

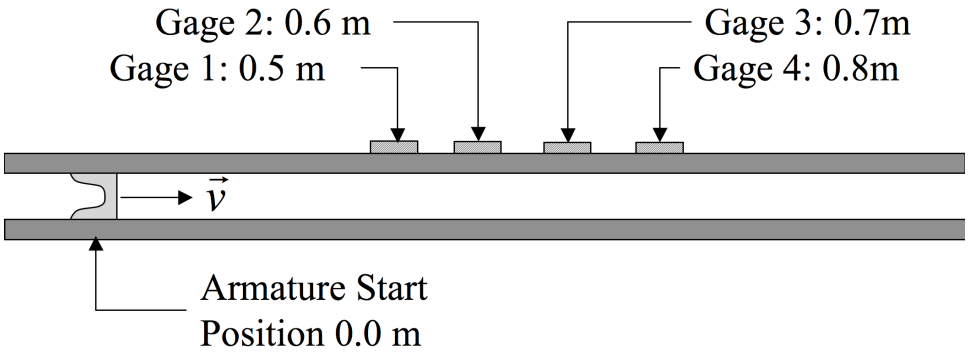


Figure E.10: Positions for Two Gage Single Rail Experiments

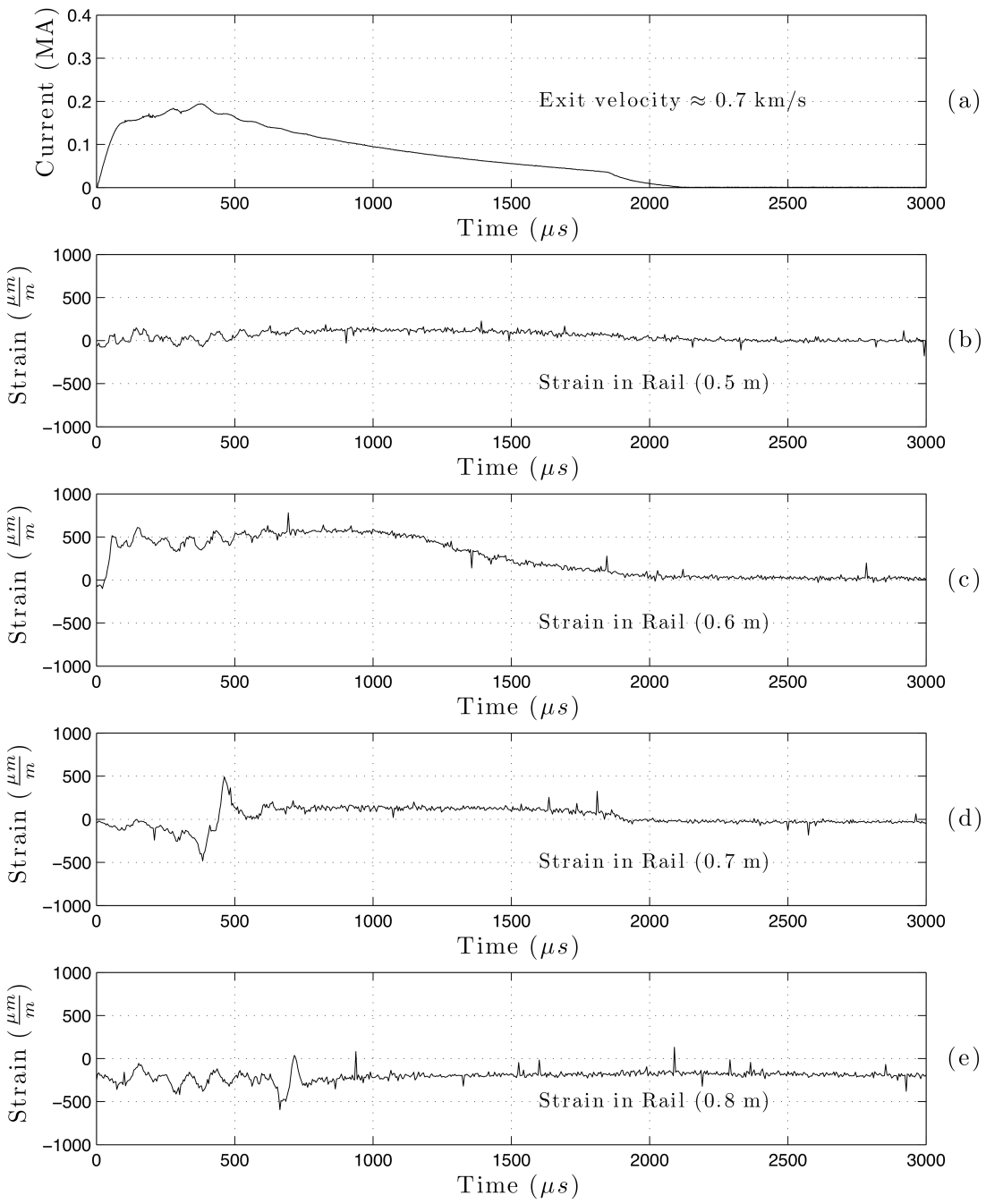


Figure E.11: 700 m/s launch velocity four gage single rail strain test. (a) Drive current, (b) Strain at 0.5 m in rail, (c) Strain at 0.6 m in rail, (c) Strain at 0.7 m in rail, (c) Strain at 0.8 m in rail

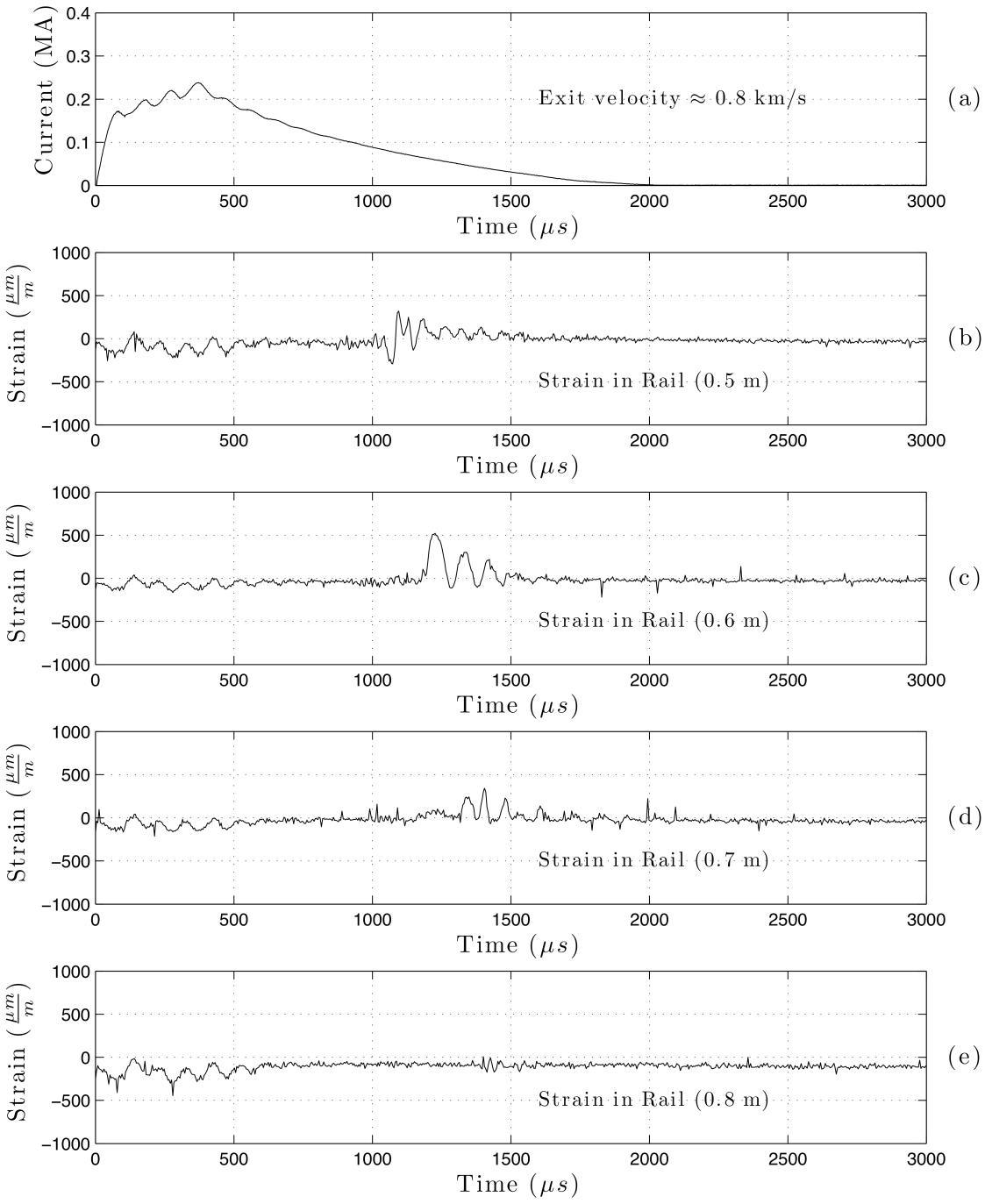


Figure E.12: 800 m/s launch velocity four gage single rail strain test. (a) Drive current, (b) Strain at 0.5 m in rail, (c) Strain at 0.6 m in rail, (c) Strain at 0.7 m in rail, (c) Strain at 0.8 m in rail

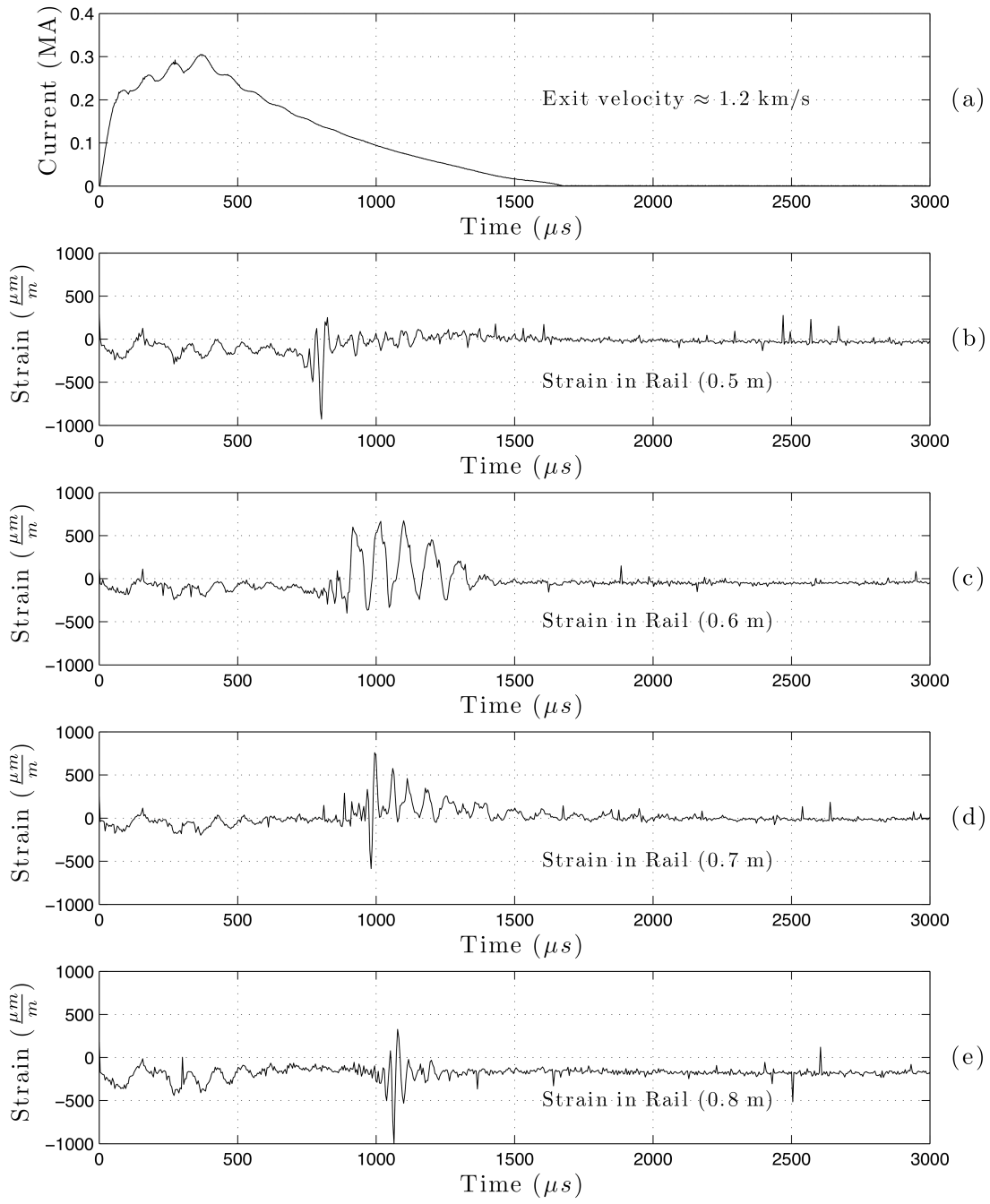


Figure E.13: 1200 m/s launch velocity four gage single rail strain test. (a) Drive current, (b) Strain at 0.5 m in rail, (c) Strain at 0.6 m in rail, (c) Strain at 0.7 m in rail, (c) Strain at 0.8 m in rail

## BIBLIOGRAPHY


[1] J.D. Achenbach and C.T. Sun. Moving Load on a Flexibly Supported Timoshenko Beam. *International Journal of Solids and Structure*, 1:353–370, 1965.

[2] C.M. Adkins and Kuhlman-Wilsdorf. Development of High Performance Metal Fiber Brushes I - Background and Manufacture. *Proceedings of the 25th Holm Conference on Electrical Contacts*, pages 165–169, 1979.

[3] C.M. Adkins and Kuhlman-Wilsdorf. Development of High Performance Metal Fiber Brushes II - Testing and Properties. *Proceedings of the 25th Holm Conference on Electrical Contacts*, pages 171–184, 1979.

[4] Marco Angeli, Ermanno Cardelli, and Bruno Azzerboni. Velocity Skin-Effect Transition Conditions on Metal-to-Metal Sliding Contacts in Muzzle-Fed Railguns. *IEEE Transactions on Magnetics*, 33(1):37–42, January 1997.

[5] J.R. Asay, C.H. Konrad, and C.A. Hall. Continuous Measurements of In-Bore Projectile Velocity. *IEEE Transactions on Magnetics*, 25(1):46–51, January 1989.

[6] N.D. Baker, B.D. McKee, and I.R. McNab. Design of a 40 Megawatt Homopolar Generator. *IEEE Transactions on Magnetics*, 22(6):1386–1388, November 1986.

[7] John P. Barber, B. Challita, B. Maas, and L. Thurmond. Contact Transition in Metal Armatures. *IEEE Transactions on Magnetics*, 27(1):228–232, January 1991.

[8] John P. Barber and McNab I.R. Magnetic Blow-Off in Armature Transition. *IEEE Transactions on Magnetics*, 39(1):42–46, January 2003.

[9] David P. Bauer and Duane C. Newman. High Performance Railgun Barrels for Laboratory Use. *IEEE Transactions on Magnetics*, 29(1):362–367, January 1993.

[10] Bharat Bhushan. *Principles and Applications of Tribology.* Wiley-Interscience, 1999.

[11] Robert D. Blevins. *Formulas for Natural Frequency and Mode Shape.* Van Nostrand Reinhold Company, 1979.

[12] O. Bozic and P. Giese. Aerothermodynamic Aspects of Railgun-Assisted Launches of Projectiles with Sub-Orbital and Low-Earth Orbit Payloads. *IEEE Transactions on Magnetics*, 43(1):491–495, January 2007.

[13] A.L. Brooks, R.S. Hawke, J.K. Scudder, and C.D. Wozynski. Design and Fabricaiton of Large and Small-Bore Railguns. *IEEE Transactions on Magnetics*, MAG-18(1):68–81, January 1982.

[14] Larry Burton. Implications of Rail Straightness for EM-Launched Projectiles. *IEEE Transactions on Magnetics*, 31(1):101–106, January 1995.

[15] Yung-Hsiang Chen and Yen-Hui Huang. Dynamic Stiffness of Infinite Timoshenko Beam on Viscoelastic Foundation in Mooving Co-ordinate. *International Journal for Numerical Methods in Engineering*, 48:1–18, 2000.

[16] Donald Chu and Francis C. Moon. Dynamic Instabilities in Magnetically Levitated Models. *American Institute of Physics*, 54(3):1619–1625, March 1983.

[17] Szu Hsiung Chu. An Approximate Analysis of Balloting Motion of Railgun Projectiles. Technical Report ARFSD-TR-90030, U.S. Army Armament Research, Development and Engineering Center, Picatinny Arsenal, New Jersey, July 1991.

[18] Szu Hsiung Chu. Balloting Motion of SLEKE Launch Packages in EM Railguns. *IEEE Transactions on Magnetics*, 29(1):769–774, January 1993.

[19] A. Cusano, A. Cutolo, J. Nasser, M. Giordano, and A. Calabró. Dynamic Strain Measurements by Fibre Bragg Grating Sensor. *Sensors and Actuators A: Physical*, 110:276–281, 2004.

[20] R.F. Davidson, W.A. Cook, D.A. Rabern, and N.M. Schnurr. Predictions of Bore Deformations and Launcher Stresses in Railguns. *IEEE Transactions on Magnetics*, MAG-22(6):1435–1440, November 1986.

[21] R. Davis, R.D. Henshell, and G.B. Warburton. A Timoshenko Beam Element. *Journal of Sound and Vibration*, 22(4):475–487, 1972.

[22] M.D. Driga, W.F. Weldon, and Woodson H.H. Electromagnetic Induction Launchers. *IEEE Transactions on Magnetics*, MAG-22(6):1453–1458, November 1986.

[23] Alv Egeland. Birkeland's Electromagnetic Gun: A Historical Review. *IEEE Transactions on Magnetics*, 17(2):73–82, April 1989.

[24] Alv Egeland and E. Leer. Professor Kr. Birkeland: His Life and Work. *IEEE Transactions on Plasma Science*, 14(6):666–667, December 1986.

[25] William C. Elmore and Mark A. Heald. *Physics of Waves*. Dover Publications, 1985.

[26] H.D. Fair. Applications of Electric Launch Systems. *IEEE Transactions on Magnetics*, 29(1):342–344, January 1993.

[27] H.D. Fair. Electromagnetic Launch: A Review of the U.S. National Program. *IEEE Transactions on Magnetics*, 33(1):11–16, January 1997.

[28] H.D. Fair. The Science and Technology of Electric Launch: A U.S. Perspective. *IEEE Transactions on Magnetics*, 35(1):11–17, January 1999.

[29] H.D. Fair. Electromagnetic Launch Science and Technology in the United States Enters a New Era. *IEEE Transactions on Magnetics*, 41(1):158–164, January 2005.

[30] H.D. Fair. Progress in Electromagnetic Launch Science and Technology. *IEEE Transactions on Magnetics*, 43(1):93–98, January 2007.

[31] Felszeghy. The Timoshenko Beam on an Elastic Foundation and subject to a Moving Step Load, Part 1: Steady-State Response. *Journal of Vibration and Acoustics*, 118:277–284, July 1996.

[32] Felszeghy. The Timoshenko Beam on an Elastic Foundation and subject to a Moving Step Load, Part 2: Transient Response. *Journal of Vibration and Acoustics*, 118:285–291, July 1996.

[33] A.L. Florence. Traveling Force on a Timoshenko Beam. *Journal of Applied Mechanics*, pages 351–358, June 1965.

[34] Ladislav Frýba. *Vibration of Solids and Structures Under Moving Loads*. Thomas Telford, 3rd edition, 1999.

[35] K Garg, J. Weiss, and R.M. Del Vecchio. A Study of Current Distribution in Electromagnetic Launcher Rails. *IEEE Transactions on Magnetics*, 25(1):193–196, January 1989.

[36] Karl F. Graff. *Wave Motion in Elastic Solids*. Dover Publications, 1991.

[37] Frederick W. Grover. *Inductance Calculations: Working Formulas and Tables*. Dover Publications, 1946.

[38] H.G. Hammon, J. Dempsey, D. Strachan, R. Raos, D. Haugh, F.P. Whitby, M.M. Holland, and P. Eggers. The Kirkcudbright Electromagnetic Launch Facility. *IEEE Transactions on Magnetics*, 29(1):975–979, January 1993.

[39] S.M. Han, Haym Benaroya, and Timothy Wei. Dynamics of Transversely Vibrating Beams using Four Engineering Theories. *Journal of Sound and Vibration*, 225(5):935–988, 1999.

[40] David C. Haugh and Grant M.G. Hainsworth. Why "C" Shaped Armatures Work (and Why they Don't!). *IEEE Transactions on Magnetics*, 39(1):52–55, January 2003.

[41] R.S. Hawke, A.L. Brooks, F.J. Deadrick, J.K. Scudder, C.M. Fowler, R.S. Caird, and D.R. Peterson. Design and Fabricaiton of Large and Small-Bore Railguns. *IEEE Transactions on Magnetics*, MAG-18(1):68–81, January 1982.

[42] Ragnar Holm. *Electrical Contacts: Theory and Application*. Springer Verlag GmbH, 4th edition, 2007.

[43] K. Honig, J. ad Kim. Pellet Acceleration study with a Railgun for Magnetic Fusion Reactor Refueling. *Journal of Vacuum Science and Technology A*, 2(2):641–644, April 1984.

[44] Thomas J.R. Hughes. *The Finite Element Method*. Dover, 2000.

[45] James R. Hutchinson. On Timoshenko Beams of Rectangular Cross-Section. *Journal of Applied Mechanics*, 71:359–367, May 2004.

[46] Scanlon James J. III and Jad H. Batteh. Tactical Applications for Electromagnetic Launchers. *IEEE Transactions on Magnetics*, 31(1):552–557, January 1995.

[47] Robert L. Jackson and Itzhak Green. A Statistical Model of Elasto-Plastic Asperity Contact Between Rough Surfaces. *Tribology International*, 39:906–914, 2006.

[48] Anthony J. Johnson and Francis C. Moon. Elastic Waves and Solid Armature Contact in Electromagnetic Launchers. *IEEE Transactions on Magnetics*, 42(3):422–429, March 2006.

[49] Anthony J. Johnson and Francis C. Moon. Elastic Waves in Electromagnetic Launchers. *IEEE Transactions on Magnetics*, 43(1):141–144, January 2007.

[50] Kanwar K. Kapur. Vibrations of a Timoshenko Beam, Using Finite-Element Approach. *The Journal of the Acoustical Society of America*, 40(5):1058–1063, 1966.

[51] J.T. Kenney. Steady State Vibrations of Beams on Elastic Foundations for Moving Load. *Journal of Applied Mechanics*, 21(4):359–364, 1954.

[52] R.N. Kostoff, Jr. A.T. Peaslee, and F.L. Ribe. Possible application of Electromagnetic Guns to Impact Fusion. *IEEE Transactions on Magnetics*, MAG-18(1):194–196, January 1982.

[53] D.E. Lee, B. Raeymaekers, and F.E. Talke. In-Situ Monitoring of the Brush/Rotor Interface in a Homopolar Motor with Acousitic Emission. *Proceedings of AUSTRIB 06 Conference*, December 2006.

[54] P. Lehmann, B. Reck, M.D. Vo, and J. Behrens. Acceleration of a Suborbital Payload Using an Electromagnetic Railgun. *IEEE Transactions on Magnetics*, 43(1):480–485, January 2007.

[55] K. Lewis and N.V. Nechitalio. Transient Response in Hypervelocity Launchers at Critical Velocities. *IEEE Transactions on Magnetics*, 43(1):157–162, January 2007.

[56] H.P. Liu, Y.L. Ting, and R.C. Zowarka. Electromagnetic and Structural Analyses of an Integrated Launch Package. *IEEE Transactions on Magnetics*, 35(1):74–78, January 1999.

[57] K. Ludwig. Deformation of a Rail Elastically Supported and of Infinite Length by Loads Moving at a constant Horizontal Velocity. *Proceedings of the Fifth International congress of Mechanics*, page 650, 1938.

[58] Richard A. Marshall. Railguns. *American Society of Mechanical Engineers*, pages 361–366, June 1982.

[59] Richard A. Marshall. Railgunnery: Where Have We Been? Where are We Going? *IEEE Transactions on Magnetics*, 37(1):440–444, January 2001.

[60] Richard A. Marshall, C. Persad, A. Jamison, and M.J. Maytac. Observation of Solid Armature Behavior. *IEEE Transactions on Magnetics*, 31(1):214–218, January 1995.

[61] B.D. McKee and I.R. McNab. A 10-MJ Compact Homopolar Generator. *IEEE Transactions on Magnetics*, 22(6):1619–1622, November 1986.

[62] Ian R. Mcnab, Jeff S. Fletcher, Eugene W. Sucov, Pedro L. Rustan, and Michael L. Huebschman. Thunderbolt. *IEEE Transactions on Magnetics*, 27(1):130–135, January 1991.

[63] I.R. McNab. Pulsed High Power Brush Research. *IEEE Transactions on Components, Hybrids and Manufacturing Technology*, CHMT-1(1):30–35, March 1978.

[64] I.R. Mcnab. Homopolar Generators for Electric Guns. *IEEE Transactions on Magnetics*, 33(1):461–467, January 1997.

[65] I.R. McNab. Pulsed Power for Electric Guns. *IEEE Transactions on Magnetics*, 33(1):453–460, January 1997.

[66] I.R. Mcnab. Early Electric Gun Research. *IEEE Transactions on Magnetics*, 35(1):250–261, January 1999.

[67] I.R. Mcnab. A Research Program to Study Airborne Launch to Space. *IEEE Transactions on Magnetics*, 43(1):486–490, January 2007.

[68] I.R. Mcnab and F.C. Beach. Naval Railguns. *IEEE Transactions on Magnetics*, 43(1):463–468, January 2007.

[69] I.R. Mcnab, Frank LeVine, and Manuel Aponte. Experiments with the Green Farm Electric Gun Facility. *IEEE Transactions on Magnetics*, 31(1):338–343, January 1995.

[70] R.D. Mindlin. Timoshenko's Shear Coefficient for Flexural Vibrations of Beams. *Proceedings of the Second U.S. National Congress of Applied Mechanics*, pages 175–178, 1955.

[71] Saeed Moaveni. *Finite Element Analysis: Theory and Applications*. Prentice Hall, 2nd edition, 2003.

[72] Francis C. Moon. *Magneto-Solid Mechanics*. John Wiley and Sons, 1984.

[73] Francis C. Moon. *Applied Dynamics: With Applications to Multibody and Mechatronic Systems*. Wiley-Interscience, 1998.

[74] Francis C. Moon. *Chaotic Vibrations: An Introduction for Applied Scientists and Engineers*. Wiley-Interscience, 2004.

[75] Oliver Nelles. *Nonlinear System Identification: From Classical Approaches to Neural Networks and Fuzzy Models*. Springer, 2001.

[76] J.V. Parker, D.T. Berry, and P.T. Snowden. The IAT Electromagnetic Launch Research Facility. *IEEE Transactions on Magnetics*, 33(1):129–133, January 1997.

[77] J.V. Parker and W.M Parsons. Experimental Measurement of Ablation Effects in Plasma Armature Railguns. *IEEE Transactions on Magnetics*, MAG-22(6):1633–1640, November 1986.

[78] Paul B. Parks. Current Melt-Wave Model for Transitioning Solid Armature. *Journal of Applied Physics*, 67(7):3511–3516, April 1990.

[79] Chadee Persad. A Review of U.S. Patents in Electromagnetic Launch Technology. *IEEE Transactions on Magnetics*, 37(1):493–497, January 2001.

[80] Peter Plostins, Ilmars Celmins, Jonathan Bornstein, and J.E. Diebler. The Effect of Sabot Front Borerider Stiffness on the Launch Dynamics of Fin-Stabilized Kinetic Energy Ammunition. Technical Report ADA213327, Army Ballistic Research Laboratory, Aberdeen Proving Ground, MD, July 1989.

[81] James R. Powell, Wen-shi Yu, John A. Fillo, and John L. Usher. TRAIL: A Tokamak Rail Gun Limiter for Fusion Reactors. *IEEE Transactions on Magnetics*, MAG-18(1):197–208, January 1982.

[82] J.S. Przemieniecki. *Theory of Matrix Structural Analysis*. Dover Publications, 1985.

[83] M. Schneider, D. Eckenfels, and Nezirevic. Doppler Radar: A Possibility to

Monitor Projectile Dynamics in Railguns. *IEEE Transactions on Magnetics*, 39(1):183–187, January 2003.

[84] A.J. Schoolderman, W.A. de Zeeuw, and M. Koops. Electrothermal Design Aspects of Transitioning Solid Armatures. *IEEE Transactions on Magnetics*, 29(1):865–870, January 1993.

[85] Paul G. Slade. *Electrical Contacts: Principles and Applications*. CRC, 1999.

[86] M.L. Sloan. Physics of Rail Gun Plasma Armatures. *IEEE Transactions on Magnetics*, MAG-22(6):1747–1752, November 1986.

[87] William R. Snow and Henry H. Kolm. Electromagnetic Launch of Lunar Material. *Space Resources. Volume 2: Energy, Power and Transport*, 509:117–135, 1992.

[88] Martin T. Soifer and Robert S. Becker. Equations of Projectile Motion in a Flexible Gun Tube. Technical Report ADA127064, Army Ballistic Research Laboratory, Aberdeen Proving Ground, MD, March 1983.

[89] Harold W. Sorenson. *Parameter Estimation Principles and Problems*. Marcel Dekker, Inc., 1980.

[90] C.R. Steele. The Finite Beam With a Moving Load. *Journal of Applied Mechanics*, pages 111–118, January 1967.

[91] C.R. Steele. Nonlinear Effects in the Problem of the Beam on a Foundation With a Moving Load. *International Journal of Solids and Structures*, 3:565–585, 1968.

[92] C.R. Steele. The Timoshenko Beam With a Moving Load. *Journal of Applied Mechanics*, pages 481–488, September 1968.

[93] F. Stefani and J.V. Parker. Experiments to Measure Gouging Threshold Velocity for Various Materials Against Copper. *IEEE Transactions on Magnetics*, 35(1):312–316, January 1999.

[94] Steven H. Strogatz. *Nonlinear Dynamics and Chaos: With Applications to Physics, Biology, Chemistry and Engineering*. Perseus Books Publishing, LLC, 1994.

[95] G.A. Svetsov, V.M. Ermolenko, V.D. Kurguzov, G.V. Ivanov, and S.A. Anisimov. Structural Response of a Railgun Accelerator. *IEEE Transactions on Magnetics*, 31(1):657–660, January 1995.

[96] R.J. Thome, W. Creedon, M. Reed, E. Bowles, and K. Schaubel. Homopolar Motor Technology Development. *IEEE Transactions on Magnetics*, -22(6):1763–1771, November 1986.

[97] D.A. Tidman, S.A. Goldstein, and N.K. Winsor. A Rail Gun Plasma Armature Model. *IEEE Transactions on Magnetics*, MAG-22(6):1763–1771, November 1986.

[98] S. Timoshenko, D.H. Young, and W. Weaver Jr. *Vibration Problems in Engineering*. Wiley-Interscience, 4th edition, 1974.

[99] S.P. Timoshenko. *History of the Strength of Materials*. Dover Publications, 1983.

[100] J.T. Tzeng. Dynamic Response of Electromagnetic Railgun Due to Projectile Movement. *IEEE Transactions on Magnetics*, 39(1):472–475, January 2003.

[101] J.T. Tzeng. Structural Mechanics for Electromagnetic Railguns. *IEEE Transactions on Magnetics*, 41(1):246–250, January 2005.

[102] M. Vaughan. *The Fabry-Perot Interferometer*. Taylor and Francis, 1989.

[103] W.A. Walls, J.H. Gully, W.F. Weldon, and H.H. Woodson. Design of a Homopolar Generator Power Supply System for the IGNITEX Experiment. *Proceedings of the IEEE 13th Symposium on Fusion Engineering*, 1:443–446, October 1989.

[104] S.Y. Wang. The Structural Response of a Rail Accelerator. *IEEE Transactions on Magnetics*, 20(2):356–359, March 1984.

[105] T. Watt and S. Fish. Explanation of High Frequency Contact Chatter in Trailing Arm Armatures. *IEEE Transactions on Magnetics*, 37(1):106–110, January 2001.

[106] T. Yokoyama. Vibrations of a Hanging Timoshenko Beam Under Gravity. *Journal of Sound and Vibration*, 141(2):245–258, 1990.

[107] Bard Yonathan. *Nonlinear Parameter Estimation*. Academic Press, 1974.